Montanuniversität

Dissertation

Application of the configurational forces concept for the design of tough, strong and damage-tolerant composites

MSc. Masoud Sistaninia

Leoben, August 2017

Materials Center Leoben Forschung GmbH
Roseggerstraße 12,
A-8700 Leoben

Erich Schmid Institute of Materials Science
Austrian Academy of Sciences
Jahnstraße 12
A-8700 Leoben

Affidavit

I declare in lieu of oath,
that I wrote this thesis
and performed the associated research myself,
using only literature cited in this volume.

M Sistaninia
………………………………….....………..

Masoud Sistaninia
Leoben, August 2017

Acknowledgements

This thesis has been carried out during my occupation at the Materials Center Leoben (MCL) Forschung GmbH and the Erich Schmid Institute of Materials Science, Austrian Academy of Sciences, and I wish to thank the many people who have supported me on the path towards this dissertation.

Financial support by the Austrian Federal Government and the Styrian Provincial Government within the research activities of the K2 Competence Center on “Integrated Research in Materials, Processing and Product Engineering”, under the frame of the Austrian COMET Competence Center Program, is gratefully acknowledged (strategic projects A4.11-WP2 and A4.20-WP1).

First and foremost I would like to express my sincere gratitude to my advisor Prof. Otmar Kolednik at the Erich Schmid Institute of Materials Science for the continuous support of my Ph.D study. I appreciate all his contributions of time, ideas and valuable discussions to make my Ph.D. experience productive and stimulating.

My sincere thanks also goes to Dr. Prof. Franz Dieter Fischer at the Institute of Mechanics, Montanuniversität Leoben, for helpful discussions.

In addition, I would like to thank my colleagues at the MCL, Dr. Walter Ochensberger, Darjan Kozic, Dr. Ronald Schöngrundner, Stefan Kolitsch, Dr. Jürgen Maierhofer, Dr. Hans-Peter Gänser, Dr. Peter Raninger, for the stimulating discussions and for all the fun we have had in the last years. Particularly, I would like to express my gratitude towards Dr. Werner Ecker, the head of the simulation group of MCL, for letting me be part of his team and for providing excellent conditions for my work. Furthermore, many thanks to Dr. Jozef Predan at Faculty of Mechanical Engineering in University of Maribor who always had an open ear for me to discuss about my findings and many thanks to Dr. Guoxin Shan, Siemens VAI Metals Technologies GmbH, for providing the Python code for the configurational force post-processing.

I also would like to thank the staff of the Erich Schmid Institute, in particular Prof. Reinhard Pippan, Dr. Johannes Zechner, Roland Kasberger and Dr. Andreas Umgeher, for useful discussions.

Last but not the least, I would like to thank my family: my parents and to my brothers and sisters for supporting me spiritually throughout my studied and my life in general.

Masoud Sistaninia, Leoben, August 2017

Abstract

This thesis deals with the application of the concept of configurational forces for the design of novel damage-tolerant and fracture-resistant materials and components.

Recently, numerical modeling with application of the concept of configurational forces has revealed that multilayer structures with thin, compliant interlayers can have highly improved fracture strength and fracture toughness compared to the homogeneous bulk material, if the composite architecture fulfills certain design rules. The reason for this effect is the strong reduction of the crack driving force, if the crack tip is located in the interlayer with low Young's modulus, which can lead to crack arrest.

The aim of the current thesis is to extend the idea of utilizing the material inhomogeneity effect for the enhancement of the fracture toughness and fracture stress to technical elastic–plastic materials. It will be shown that it is possible to improve the strength and the fracture toughness of inherently brittle matrix materials by the introduction of thin interlayers that have the same Young's modulus but lower yield stress than the matrix. The reason is that a crack arrests near the interface to the hard matrix material, caused by the strong decrease of the crack driving force. This effect appears without previous delamination of the interlayer. The effectiveness of soft interlayers as crack arrester is quantified by numerical case studies, based on the application of the configurational forces concept. The decisive parameters influencing the effect are the interlayer spacing (the wavelength of the yield stress variation), the interlayer thickness and the ratio of the yield stress between interlayer- and matrix material. Based on numerical simulations, it is demonstrated how to find, for a given matrix material and load, the architectural parameters of the multilayer in order to enhance the fracture stress and the fracture toughness of the material. An iterative procedure is proposed to find the optimum configuration. It is found that the optimum wavelength is inversely proportional to the square of the applied stress. The design concept presented in this thesis can be applied for different types of multilayers and loading scenarios. Experimental results of fracture tests, conducted on compounds made of high-strength steel as matrix and low-strength steel as interlayer material, confirm the findings.

This thesis also deals with another type of material inhomogeneity, the thermal expansion inhomogeneity effect, which plays a significant role in the thermal behaviors of refractory materials, such as magnesia-spinel refractories. The concept of configurational forces is applied for the investigation of thermal shock resistance of magnesia spinel products during the cooling from the burning temperature. Evaluations provide valuable insights into the behavior of these composites. It is shown that the pronounced damage initiation, in combination with the low crack driving force, is the main reason for the good thermal shock resistance of magnesia spinel refractories.

Content

Part I: Fundamentals of continuum mechanics, fracture mechanics and configurational forces concept

Part II: Design of tough, strong and damage-tolerant composites by utilizing the yield stress inhomogeneity effect

Part III: Physically correct evaluation of the crack driving force in magnesia-spinel refractories with configurational forces concept

Nomenclature

In this thesis, *Scalars* are denoted by lightface letters, *vectors* by lowercase boldface letters and *tensors* by uppercase boldface letters.
A list of Parameters, Symbols and Acronyms used in this thesis are given in the following.

List of parameters

a	crack length
a_0	initial crack length
a_{CA}	length of arrested crack
$a_{\mathrm{n}}^{\mathrm{M}}$	inherent defect size in the matrix material
Δa_{CA}	crack extension into CA position
A	area below load–displacement (F–v) curve
B	specimen thickness
$\mathcal{B}$	body in (deformed) actual configuration
$\mathcal{B}_0$	body in (undeformed) reference configurationan
$\partial\mathcal{B}$	boundary of $\mathcal{B}$
$\mathbf{C}$	(second rank) configurational stress tensor
C_{y}	yield stress gradient term
$\mathrm{C}_{\mathrm{inh}}$	material inhomogeneity term
$\mathrm{C}_{\mathrm{inh1}}$	material inhomogeneity term of IF1
$\mathrm{C}_{\mathrm{inh2}}$	material inhomogeneity term of IF2
C_{IL}	interlayer inhomogeneity term
$C_{\mathrm{inh1}}^{\mathrm{CA}}$	material inhomogeneity term of IF1 for a crack at CA position
$C_{\mathrm{inh2}}^{\mathrm{CA}}$	material inhomogeneity term of IF2 for a crack at CA position
$C_{\mathrm{IL}}^{\mathrm{CA}}$	interlayer inhomogeneity term for a crack at CA position
$\mathcal{D}$	part of deformed body $\mathcal{B}$, e.g. bounded by integration contour Γ
$\mathcal{D}_0$	part of undeformed body $\mathcal{B}_0$
$\mathcal{D}_r$	disk (area) of radius r centered at crack tip
$\mathcal{D}(t)$	migrating control volume in a body
$\partial\mathcal{D}$	boundary of $\mathcal{D}$
$\mathbf{e}$	unit vector in nominal crack growth direction
E	Young's modulus
$\mathbf{f}$	bulk configurational force vector
$\mathbf{f}_{\mathrm{S}}$	surface configurational force
$\mathbf{f}_{\mathrm{tip}}$	configurational force emanating from the crack tip
$\mathbf{f}_{\Sigma}$	configurational force emerging on an interface

$\mathbf{f}^{\mathrm{ep}}$	incremental plasticity bulk configurational force
$\mathbf{f}_{\mathrm{tip}}^{\mathrm{ep}}$	incremental plasticity bulk configurational force emanating from the crack tip
$\mathbf{f}^{\mathrm{nlel}}$	nonlinear elastic configurational force
$\mathbf{F}$	deformation gradient tensor
$\mathbf{F}^{\mathrm{T}}$	transposed of the deformation gradient tensor
f_{K}	dimensionless geometry parameter
G	elastic energy release rate
G_{f}	specific fracture energy
h	height from the crack plane to the upper or lower surface
$\mathbf{I}$	identity tensor
J	conventional J-integral
$\mathbf{J}$	J-integral vector
J_{tip}	near-tip J-integral
$J_{\mathrm{tip}}^{\mathrm{CA}}$	near-tip J-integral for a crack at CA position
$J_{\mathrm{tip,c}}^{\mathrm{CA}}$	crack driving force $J_{\mathrm{tip}}^{\mathrm{CA}}$ at the fracture load
$J_{\mathrm{tip}}^{\mathrm{hom}}$	near-tip J-integral of a homogeneous material
J_{Γ}	J-integral evaluated for an arbitrary contour Γ
J_{far}	far-field J-integral
$J_{\mathrm{far}}^{\mathrm{CA}}$	far-field J-integral for a crack at CA position
$J_{\mathrm{far,c}}^{\mathrm{CA}}$	crack driving force $J_{\mathrm{far}}^{\mathrm{CA}}$ at the fracture load
$J_{\mathrm{far}}^{\mathrm{hom}}$	far-field J-integral of a homogeneous material
J_{PZ}	J-integral evaluated for a contour Γ_{PZ} around the crack tip plastic zone
$J_{\Gamma\mathrm{iDZ}}$	J-integral evaluated for a contour Γ_{iDZ} around the inner damage zone
J^{ep}	incremental plasticity J-integral for elastic–plastic materials
J^{nlel}	nonlinear elastic J-integral
J^{VCE}	ABAQUS J-integral calculated via virtual crack extension method
$J_{\mathrm{c}}^{\mathrm{M}}$	Fracture initiation toughness of the homogeneous matrix material
$J_{\mathrm{c}}^{\mathrm{ML}}$	Fracture toughness of the multilayer material
K	stress intensity factor
$K_{\mathrm{c}}^{\mathrm{M}}$	critical stress intensity factor of the homogeneous matrix material
L_1	distance between the crack tip and IF1
L_2	distance between the crack tip and IF2
$\mathbf{m}$	unit normal vector in the reference configuration
n	average strain hardening exponent
$\mathbf{n}$	unit normal vector in the actual configuration
$\mathbf{n}_{\Sigma}$	unit normal vector to the interface $\sum$ in the reference configuration
N	number of interlayers in the half width of the specimen
$\mathbf{p}$	unit normal vector to the crack flank

$\mathcal{P}$	potential energy
r	distance from the crack tip
r_y	radius of the crack tip plastic zone
r_y^IL	radius of the crack tip plastic zone in the interlayer
r_y^M	radius of the crack tip plastic zone in the matrix
$\left(r_\mathrm{y}^\mathrm{IL}\right)_\mathrm{c}$	radius of the crack tip plastic zone at re-initiation of the arrested crack
R	crack growth resistance
R''''	Hasselman parameter for the characterization of the thermal shock resistance
$\mathbf{S}$	first Piola–Kirchhoff stress
s_f	safety factor
T	temperature
t	interlayer thickness
t_opt	optimum interlayer thickness
$\mathbf{t}$	surface traction vector
$\mathbf{u}$	displacement vector
u_appl	applied vertical displacement
$\mathcal{U}$	strain energy
v	load-line displacement
$\mathbf{v}$	material point velocity in reference configuration
$\mathbf{v}_\mathrm{tip}$	crack tip velocity
$\mathbf{w}$	material point velocity in actual configuration or motion velocity
W	specimen width
$\mathbf{x}$	position vector in the current coordinate system (x, y, z)
$\mathbf{X}$	position vector in the reference coordinate system (X, Y, Z)

Greek symbols

α	thermal expansion coefficient
β	constant related to the radius of the crack tip plastic zone
Γ	arbitrary integration contour for the evaluation of the J-integral
Γ_iDZ	contour around the inner damage zone
Γ_r	contour at distance r around crack tip
Γ_tip	contour around the crack tip
Γ_PZ	contour around the crack tip plastic zone
Γ_far	far-field contour
Γ_int1	contour around interface IF1
Γ_int2	contour around interface IF2
Γ_s	surface energy required to create new surfaces

γ_{s}	specific fracture surface energy
γ_{pl}	specific plastic work for forming the fracture surface
ε	(engineering) strain
ε_{e}	elastic strain
ε_{p}	plastic strain
$\boldsymbol{\varepsilon}$	linear strain tensor
λ	spacing of interlayers, i.e. wavelength of multilayer
λ_{opt}	optimum wavelength of multilayer
ν	Poisson's ratio
σ	(engineering) stress
$\boldsymbol{\sigma}$	Cauchy stress tensor
σ_{appl}	applied global stress
σ_{eq}	equivalent stress or von Mises stress
$\sigma_{\mathrm{fr}}^{\mathrm{M}}$	fracture stress of the matrix material
$\hat{\sigma}_{\mathrm{fr}}^{\mathrm{M}}$	upper limit of fracture stress of the multilayer
σ_{t}	tensile strength
σ_{UTS}	ultimate tensile strength
σ_{y}	yield stress
$\sigma_{\mathrm{y}}^{\mathrm{IL}}$	yield stress of the interlayer
$\sigma_{\mathrm{y}}^{\mathrm{M}}$	yield stress of the matrix
$\left(\sigma_{\mathrm{y}}^{\mathrm{IL}}\right)_{\mathrm{opt}}$	optimum yield stress of the interlayer
ϕ	strain energy density
ϕ_{e}	elastic (reversible) part of strain energy density
ϕ_{p}	plastic (dissipated) part of strain energy density
ψ_{tip}	dissipation due to crack tip propagation
ψ_{bulk}	bulk dissipation per unit volume
$\Psi_{\mathrm{IL}}^{\mathrm{CA}}$	*J*-reduction coefficient of a single interlayer
$\Psi_{\mathrm{ML}}^{\mathrm{CA}}$	*J*-reduction coefficient of the multilayer

Acronyms

CA	critical position for possible crack arrest
CT	Compact Tension (specimen)
CDP	Concrete Damaged Plasticity model
E–PFM	elastic–plastic fracture mechanics
FE	Finite Element
HRR	Hutchinson-Rice-Rosengren (crack tip field)
IF1	first interface of the interlayer

IF2	second interface of the interlayer
LEFM	linear elastic fracture mechanics
MT	Symmetric Middle Crack Tension (specimen)
RVE	2-dimensional representative volume element
SENT	Single Edge Notch Tension (specimen)
ssy	small-scale yielding

“In science one tries to tell people, in such a way as to be understood by everyone, something that no one ever knew before. But in poetry, it’s the exact opposite.”

Paul Dirac
Physicist
1902 –1984

1 Introduction

This thesis was conducted under the frame of a strategic project of the Austrian COMET Competence Center Program, “Integrated Research in Materials, Processing and Product Engineering” (Project A4.20-WP1). The main objective of the project is to derive validated concepts for the optimized design of tough, strong and damage-tolerant materials and components. Theoretical and numerical aspects are utilized in order to reach this aim. The methodological approach consists performing a comprehensive numerical case study, based on the application of the configurational forces concept (Gurtin 2000; Maugin 1995), to work out the effect of soft interlayers on the variation of the crack driving force. The crack driving force is a loading parameter for the crack, trying to extend the crack.

A common feature that is inherent to all classes of multiphase and composite materials is that a spatial variation of material properties in the direction of crack extension influences the crack driving force (Simha et al. 2003; Simha et al. 2005) and thus affects the fracture toughness (Kolednik 2000; Fratzl et al. 2007; Kolednik et al. 2009; Kolednik et al. 2011; Fischer et al. 2012a; Zechner and Kolednik 2013a,b; Kolednik et al. 2014a). This effect is fundamentally different from the effects of crack deflection and interface decohesion that are often observed in composite materials. The crack driving force is reduced when a crack propagates from a material with lower elastic modulus to a material with higher elastic modulus, transition compliant/stiff (Kolednik et al. 2005; Kolednik et al. 2011; Fischer et al. 2012a; Kolednik et al. 2014a). A similar effect appears when a crack propagates from a material with lower strength to a material with higher strength, transition soft/hard (Sugimura et al. 1995; Kolednik 2000; Simha et al. 2005; Predan et al. 2007; Kolednik et al. 2010). In both cases, the material inhomogeneity exerts a shielding effect on the crack tip. This shielding effect results either in a higher apparent fracture toughness of a monotonically loaded specimen, or in a lower growth rate or even arrest of a crack in a cyclically loaded structure (Suresh et al. 1992; Kolednik et al. 2009; Kolednik et al. 2010; Kolednik et al. 2016). For transitions hard/soft or stiff/compliant, anti-shielding occurs: compared to a homogeneous material the crack driving force is enhanced, the apparent fracture toughness reduced, the crack growth rate in fatigue is enhanced.

This effect, which has been denominated "*material inhomogeneity effect*", can be utilized for designing new fracture-resistant and flaw-tolerant materials. Especially interesting for materials design is the introduction of thin, compliant interlayers in high-strength matrix materials with low intrinsic toughness (Kolednik et al. 2011; Zechner and Kolednik 2013a;

Kolednik et al. 2014a). This idea has been basically inspired from nature. In recent years, the unique combination of high stiffness, high strength, and high fracture toughness of certain biological materials, such as the skeleton of deep-sea glass sponges (Fig. 1.1a), has been investigated in great detail (Kamat et al. 2004; Walter et al. 2007; Dunlop and Fratzl 2010; Kolednik et al. 2011). The microstructure of the sponge consists of a layered structure of brittle silica, i.e. bio-glass, connected by thin protein interlayers. Numerical modeling and application of the concept of configurational forces has revealed that the multi-layered structure with strong spatial variation of the Young's modulus between the hard and brittle bio-glass and the thin, compliant protein layers is the dominant mechanism for the high fracture toughness of the glass sponge (Kolednik et al. 2011). The reason is that the crack driving force, expressed in terms of the near-tip J-integral J_{tip}, strongly decreases when the crack enters the compliant interlayer (see Fig. 1.1b). This leads to crack arrest.

The concept of configurational forces, which will be explained later in Section 4, is an appropriate tool for the accurate quantification of the material inhomogeneity effect. This concept enables the evaluation of the crack deriving force without restrictions regarding constitutive assumptions of the material or on the applicability of linear elastic fracture mechanics, see Simha et al. (2003, 2005). Configurational forces (CFs) are thermodynamic forces that act on all types of defects in materials, such as dislocations, cracks, voids, or interfaces (Gurtin 2000; Maugin 1995). Simha et al. (2003, 2005) have worked out the fundamentals for the application of the Configurational forces concept for the description of the behavior of cracks in inhomogeneous materials.

From the results of numerical simulations based on the configurational force concept, see e.g. Kolednik et al. (2011, 2014a), it has been shown that a multilayer composite with compliant interlayers, i.e. a spatial variation in the Young's modulus E, can have a much higher apparent fracture toughness and fracture stress than a comparable homogeneous material, if the architecture of the composite fulfills certain derived criteria.

In the current thesis, it is tried to transfer the idea of enhancing the fracture toughness by introducing compliant interlayers to technical composite materials where both, the matrix and the interlayer material, behave elastic–plastic. Comprehensive numerical case studies based on the configurational force concept are performed to work out the effect of soft interlayers, i.e. interlayers with the same Young's modulus but a lower yield stress than the matrix material, on the variation of the crack driving force. From the results of numerical case studies, it is shown that the influence of soft interlayers on the crack driving force in a multilayer composite (see Fig. 1.2) is a function of the material properties (the yield stress ratio between interlayer and matrix, $\sigma_{\mathrm{y}}^{\mathrm{IL}} / \sigma_{\mathrm{y}}^{\mathrm{M}}$) and the architecture of the composite (interlayer thickness t and -spacing λ).

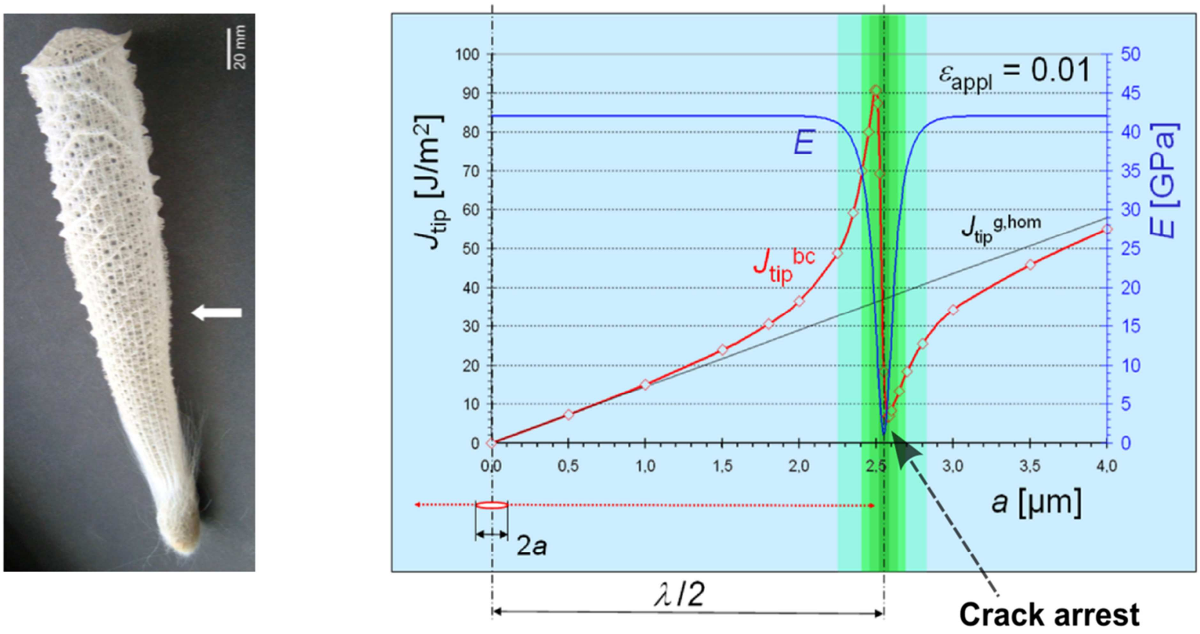

(a) **(b)**

Fig. 1.1 **(a)** Skeleton of the deep sea glass sponge. **(b)** Strong spatial variation of the Young's modulus E between the stiff bio-glass and the compliant protein layers leads to a strong decrease of the crack driving force J_{tip} when the crack enters the interlayer (Kolednik et al. 2011).

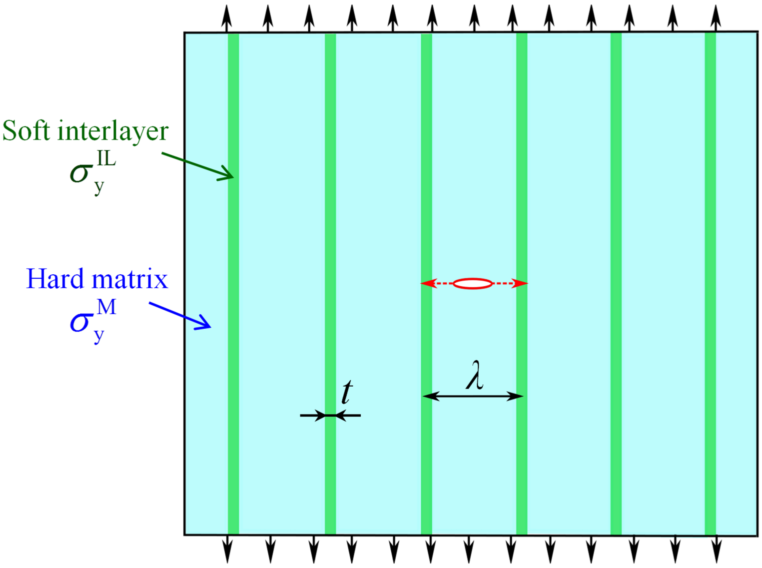

Fig. 1.2 Multilayered composite with thin, soft interlayers. Spatial variations of the yield stress due to soft interlayers have a large influence on the crack driving force. A soft interlayer can work as an efficient crack arrester, if the crack driving force becomes very low in the interlayer.

The main questions the thesis will address are:

1) Can a soft interlayer work as effective crack arrester?

2) How much the crack driving force is reduced by inserting a single, soft interlayer?
3) How to find, for a given matrix material, the optimum interlayer configurations (the thickness and the yield stress of the interlayer), leading to the maximum effectiveness of the soft interlayer as crack arrester?
4) How to find, for a given matrix material, the architectural parameters of the multilayer composite so that the *fracture stress* is greatly improved?
5) How to find, for a given matrix material, the architectural parameters of the multilayer composite so that the *fracture toughness* is greatly improved?

To answer questions 1) – 3), a single-interlayer specimen is considered. Questions 4) and 5) can be answered by considering multilayer configurations with short inherent crack and long crack, respectively.

In another part of the current thesis (Part III), which is an output of a co-operation project with Chair of Ceramics at Montanuniversität Leoben, the thermal shock resistance of magnesia spinel refractories is investigated with the concept of configurational forces. The main objective of this part is to develop a new computational tool for the physically correct evaluation of the crack driving force in coarse grained refractories, in order to characterize the thermal shock resistance.

The methodology consists in numerical simulations based on the applications of the concrete damaged plasticity (CDP) model (see e.g. Lee and Fenves 1998, Lubliner et al. 1989), in order to simulate the damage evolution process in the magnesia matrix during the cooling from the burning temperature, and the configurational forces concept (see e.g. Gurtin 2000, Maugin 1995).

The main question the thesis will address is:

6) Does the combination of CDP-model with configurational forces concept enable the physically correct evaluation of the crack driving force in magnesia-spinel refractories?

In magnesia-spinel refractories, spinel inclusions are embedded in a magnesia matrix in order to increase the thermal shock resistance. Therefore, another main question that this thesis will answer is:

7) What is the main reason for the good thermal shock resistance of magnesia-spinel refractories?

The thesis is structured in three parts: In Part I, first some fundamentals of continuum mechanics, fracture mechanics and configurational forces are presented (in Sections 2–4). In

Part II, first the answers to questions 1) – 3) are worked out in Section 5. This section contains a peer reviewed journal article, Paper I, published in an international journal, *Engineering Fracture Mechanics*. Question 4) is answered in Section 6. Section 6 contains a peer reviewed journal article, Paper II, which has been published in *Acta Materialia*. Section 7 gives the answer to question 5) by a peer reviewed journal article, Paper III, submitted to *Composite Structures*. Part III of the thesis deals with the thermal shock resistance of magnesia-spinel refractories (in Section 8). This part presents the answers to questions 6) and 7) by a peer reviewed journal article, Paper IV, published in the *Journal of the European Ceramic Society*. The numbers of the equations, figures and tables of each paper have been changed according to the section number in the thesis. The reference section of each paper has been removed and included into the reference section of the thesis. Section 9 provides proposals for future research. Section 10 presents a summary of the main conclusions of the thesis.

Part I

Fundamentals of continuum mechanics, fracture mechanics and configurational forces concept

2 Basic continuum mechanical concepts

Before presenting the fundamentals of fracture mechanics and configurational forces it is necessary to set a common continuum mechanical basis. The intention of this chapter is not to present a comprehensive overview of all possible aspects of continuum mechanics, but rather to set a basis necessary for understanding this thesis, particularly for the concept of configurational forces. For a detailed introduction to continuum mechanics many good books are available. For example, please see Bonet and Wood (2008), Chadwick (2012), Gurtin (1982), Malvern (1969), Marsden and Hughes (2012), Rubin et al. (2012), Truesdell and Noll (1965). The notation used here is the same as that used in Gurtin (2000).

2.1 Kinematics

A proper description of the deformation of bodies under stress is fundamental to continuum mechanics. It is important to distinguish between a *reference configuration* and an *actual configuration*. Assume an unloaded body $\mathcal{B}_0$ at initial time $t_0 = 0$, Fig. 2.1a. $\mathcal{B}_0$ is imagined as being an assemblage of material particles, labeled by the coordinates $\mathbf{X}$ with respect to a global Cartesian coordinate basis. If $\mathcal{B}_0$ is subjected to external or internal stresses, it will deform into the body $\mathcal{B}$ at time t (Bonet and Wood 2008). In the body $\mathcal{B}$, the material particles are described by the current position $\mathbf{x}$, see Fig. 2.1a. The unloaded and deformed configurations, $\mathcal{B}_0$ and $\mathcal{B}$, are denoted as reference and actual configuration. It is important to note that deformation is seen in the actual configuration, whereas the movement of a defect is seen in the reference configuration.

The motion can be mathematically described by a mapping $\mathbf{x}(\mathbf{X},t)$ between reference and actual particle positions as (Bonet and Wood 2008),

$$\mathbf{x} = \mathbf{x}(\mathbf{X},t)\,. \tag{2.1}$$

For a fixed value of t the above equation represent a mapping between the undeformed and deformed bodies.

Taking the material time derivative, denoted by a superposed dot of the actual position $\mathbf{x}$, defines the velocity $\mathbf{w}$ of a material particle,

$$\mathbf{w} = \frac{\partial \mathbf{x}}{\partial t} = \dot{\mathbf{x}}\,. \tag{2.2}$$

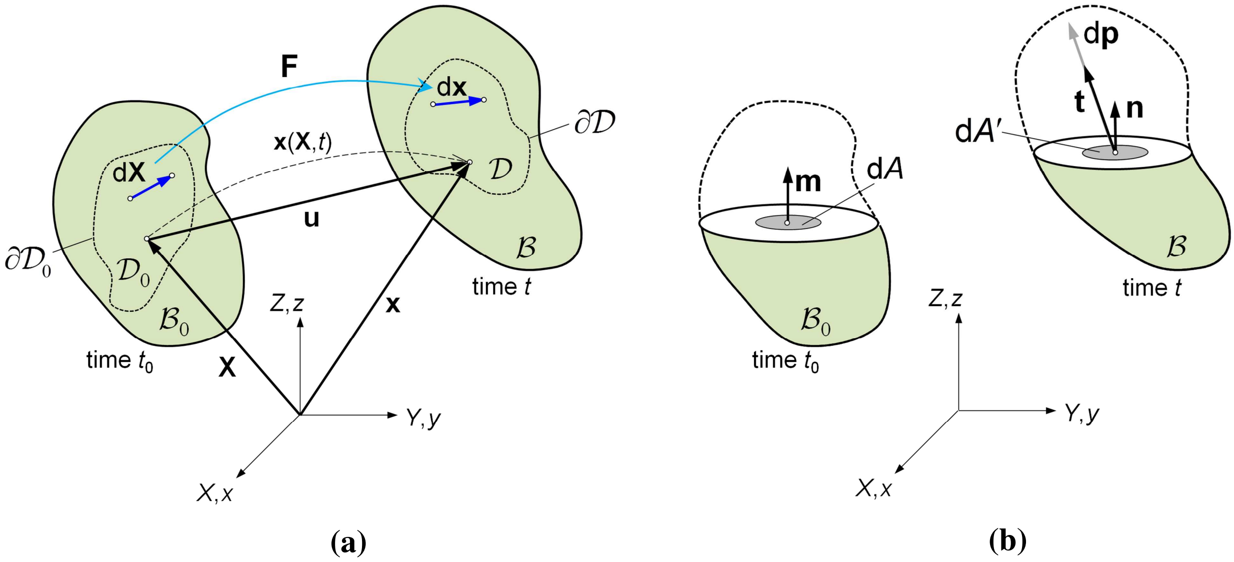

Fig. 2.1 (**a**) Reference configuration $\mathcal{B}_0$ and actual configuration $\mathcal{B}$ of a deformable body. The motion can be mathematically described by a mapping $\mathbf{x}=\mathbf{x}(\mathbf{X},t)$ between reference and actual particle positions. The deformation gradient tensor **F** maps vectors of $\mathcal{B}_0$ onto deformed vectors of $\mathcal{B}$ via $\mathrm{d}\mathbf{x}=\mathbf{F}\,\mathrm{d}\mathbf{X}$. (**b**) Cut-off parts of $\mathcal{B}_0$ and $\mathcal{B}$. Reaction force d**p** acts on the cut surface of $\mathcal{B}$ in order to fulfill the state of static equilibrium.

The velocity of the same material particle in the reference configuration is given by

$$\mathbf{v}=\frac{\partial\mathbf{X}}{\partial t}=\dot{\mathbf{X}}\,. \tag{2.3}$$

2.2 *Deformation gradient*

A key quantity in deformation analysis is the deformation gradient **F**, which is involved in all equations relating quantities before deformation to corresponding quantities after (or during) deformation. The deformation gradient tensor enables the relative spatial position of two neighboring particles after deformation, d**x**, to be described in terms of their relative position before deformation, d**X**, (see Fig. 2.1a). The vectors d**x** and d**X** are related by the deformation gradient tensor **F** (Bonet and Wood 2008),

$$\mathbf{F}=\frac{\partial\mathbf{x}}{\partial\mathbf{X}}=\mathbf{1}+\nabla\mathbf{u}\,. \tag{2.4}$$

In the above equation, the symbol ∇ is the Lagrangian gradient operator and $\nabla\mathbf{u}$ denotes the gradient of the displacement $\mathbf{u}=\mathbf{x}-\mathbf{X}$ (see Fig. 2.1a) with respect to **X**.

F is also needed to describe the transformation of surface elements, denoted by $\mathbf{n}\mathrm{d}A'$, see Fig. 2.1b. The following relations can be derived (Chadwick 2012),

$$\begin{aligned} \mathbf{n}\,\mathrm{d}A' &= J\,\mathbf{F}^{-\mathrm{T}}\mathbf{m}\,\mathrm{d}A \\ \mathrm{d}v &= J\,\mathrm{d}V \end{aligned} \quad . \tag{2.5}$$

J denotes the determinant of the deformation gradient tensor **F**, $J = \det(\mathbf{F})$, and $\mathbf{F}^{-\mathrm{T}}$ the transposed of the inverse of **F**. In the above equation, $\mathrm{d}A$ and $\mathrm{d}A'$ are the area elements of the reference and actual configurations, respectively. **n** denotes the outward unit normal vector to $\mathrm{d}A'$ and **m** the outward unit normal vector to $\mathrm{d}A$. The volumes of the actual and reference configurations are v and V, respectively.

2.3 Stress measures

Stress can be defined in the actual configuration $\mathcal{B}$ in the standard way as force per unit area. This leads to the well-known Cauchy stress tensor. Consider a cut-off part of body $\mathcal{B}$, Fig. 2.1b, and a region $\mathrm{d}A'$ located on the cut surface. In order to develop the concept of stress, it is necessary to study the action of the forces applied on the region $\mathrm{d}A'$; external forces acting on a body produce internal forces so that each part of the body is in a state of static equilibrium (Bonet and Wood 2008). If the resultant force on the area $\mathrm{d}A'$ is d**p**, the surface traction vector **t** is given by the limit of the ratio $\mathrm{d}\mathbf{p}/\mathrm{d}A'$ as $\mathrm{d}A'$ tends to zero (Bonet and Wood 2008). The Cauchy stress tensor $\boldsymbol{\sigma}$ defines the stress state of a material point in the actual configuration. $\boldsymbol{\sigma}$ is also called the true stress and it is a symmetric quantity, $\boldsymbol{\sigma} = \boldsymbol{\sigma}^{\mathrm{T}}$. The relationship between the Cauchy stress tensor $\boldsymbol{\sigma}$ and the surface traction vector **t** can be derived,

$$\mathbf{t} = \boldsymbol{\sigma}\mathbf{n}\,. \tag{2.6}$$

The surface traction vector **t** can also be derived with respect to the reference configuration $\mathcal{B}_0$. The first Piola–Kirchhoff stress **S** relates the force vector d**p** in the actual configuration to the undeformed area element of the reference configuration, dA (Fig. 2.1b). The traction is obtained by

$$\mathbf{t} = \mathbf{S}\mathbf{m}\,, \tag{2.7}$$

where **m** is the unit normal vector to the area element dA in the reference configuration. With the help of Eq. (2.5), the transformation between the two stress tensors, the first Piola–Kirchhoff stress tensor and the Cauchy stress tensor, can be established (Bonet and Wood 2008) as

$$\mathbf{S} = J\boldsymbol{\sigma}\mathbf{F}^{-\mathrm{T}}\,. \tag{2.8}$$

The symmetry of the Cauchy stress tensor results in the following identity,

$$\mathbf{S}\mathbf{F}^{\mathrm{T}} = \mathbf{F}\mathbf{S}^{\mathrm{T}}. \tag{2.9}$$

It should be noted that the second Piola–Kirchhoff stress tensor **T**, which is a symmetric stress tensor, relates forces in the reference configuration to areas in the reference configuration, d*A*. However, it must be mentioned that **T** has no real physical meaning. The second Piola–Kirchhoff stress tensor **T** can be defined by,

$$\mathbf{T} = \mathbf{F}^{-1}\mathbf{S} = J\,\mathbf{F}^{-1}\boldsymbol{\sigma}\mathbf{F}^{-\mathrm{T}} \tag{2.10}$$

2.4 Balance laws

Essential in the understanding of continuum mechanics and the theory of configurational forces is the concept of balance laws. There exist five balance laws in continuum mechanics: the balance of mass, linear momentum, angular momentum, the first and the second law of thermodynamics (Chadwick 2012).

The balance laws are only presented for the reference configuration $\mathcal{B}_0$. However, the transformation between first Piola–Kirchhoff stress and Cauchy stress, Eq. (2.8), leads to equivalent relations for the actual configuration.

Balance of mass:

The balance of mass, or better the conservation of mass, is expressed in the global and local forms in the reference configuration by (Chadwick 2012),

$$\frac{\mathrm{d}}{\mathrm{d}t}\int_{\mathcal{D}_0} \rho_0 \,\mathrm{d}V = 0, \; \dot{\rho}_0 = 0, \tag{2.11}$$

where ρ_0 represents the mass density in the reference configuration and $\mathcal{D}_0$ is an arbitrary part of the reference configuration $\mathcal{B}_0$ (Fig. 2.1a). Since the mass of a closed system cannot change, if there is no transfer of mass (or energy) across the system boundary, one can write

$$\int_{\mathcal{D}_0} \rho_0 \,\mathrm{d}V = \int_{\mathcal{D}} \rho \,\mathrm{d}v \;, \tag{2.12}$$

where ρ is the mass density in the actual configuration and $\mathcal{D}$ the corresponding part in the actual configuration $\mathcal{B}$. With the help of Eq. (2.5), Eq. (2.12) can be defined in its local form as $\rho_0 = \rho J$.

Balance of linear momentum:

Consider the arbitrary part $\mathcal{D}_0$ of the body $\mathcal{B}_0$ (Fig. 2.1a) acted by two types of forces, i.e. traction forces **t**, on the boundary $\partial\mathcal{D}_0$ of $\mathcal{D}_0$, and body forces $\rho_0\mathbf{b}$ per unit volume of the reference configuration and **b** per unit mass. The rate of change of the total momentum of the part $\mathcal{D}_0$ is $\mathrm{d}/\mathrm{d}t\int_{\mathcal{D}_0}\rho_0\mathbf{v}\,\mathrm{d}V$. The momentum balance can be then expressed, in the global form, as (see Malvern 1969, Chadwick 2012),

$$\frac{\mathrm{d}}{\mathrm{d}t}\int_{\mathcal{D}_0}\rho_0\mathbf{v}\,\mathrm{d}V=\int_{\partial\mathcal{D}_0}\mathbf{S}\mathbf{m}\,\mathrm{d}A+\int_{\mathcal{D}_0}\rho_0\,\mathbf{b}\,\mathrm{d}V\,. \tag{2.13}$$

Eq. (2.13) can be written in its local form by using Gauss theorem (or divergence theorem) (Malvern 1969), yields,

$$\rho_0\dot{\mathbf{v}}=\nabla\cdot\mathbf{S}+\rho_0\mathbf{b}\qquad\text{at each point in the body }\mathcal{D}_0\,. \tag{2.14}$$

$\nabla\cdot$ denotes the divergence operator.

If the velocity field is zero (in the static case), or constant so that $\dot{\mathbf{v}}=0$, the momentum balance, Eq. (2.14), reduces to the equilibrium equation as

$$\nabla\cdot\mathbf{S}+\rho_0\mathbf{b}=0\,. \tag{2.15}$$

If body forces are ignored, the equilibrium equation (in the local form) is written as

$$\nabla\cdot\mathbf{S}=0, \tag{2.16}$$

and the equilibrium equation in the global form can be written as

$$\int_{\partial\mathcal{D}_0}\mathbf{S}\mathbf{m}\,\mathrm{d}A=0\ . \tag{2.17}$$

Balance of angular momentum:

Angular momentum is the moment of the linear momentum (or rotational momentum) with respect to some point. The rotational equilibrium of $\mathcal{D}_0$ (Fig. 2.1a) leads to the symmetry of the Cauchy stress, $\boldsymbol{\sigma}=\boldsymbol{\sigma}^{\mathrm{T}}$, and results in Eq. (2.9); the first Piola–Kirchhoff stress is, in general, not symmetric (see e.g. Malvern 1969).

Balance of energy:

Consider the part $\mathcal{D}_0$ in the reference configuration which is acted by traction forces **t** and body forces $\rho_0\mathbf{b}$ per unit volume. The kinetic energy of this part can be defined as $\mathcal{K}(\mathcal{D}_0)=1/2\int_{\mathcal{D}_0}\rho_0\,\mathbf{v}.\mathbf{v}\,\mathrm{d}V$. The mechanical power (or the working rate of applied forces) is defined as

$$\mathcal{W}(\mathcal{D}_0)=\int_{\partial\mathcal{D}_0}(\mathbf{S}\mathbf{m}).\mathbf{v}\,\mathrm{d}A+\int_{\mathcal{D}_0}(\rho_0\,\mathbf{b}).\mathbf{v}\,\mathrm{d}V\,. \tag{2.18}$$

The balance of energy for the control volume $\mathcal{D}_0$ is given by Malvern (1969) as

$$\frac{\mathrm{d}}{\mathrm{d}t}(\mathcal{K}+\mathcal{U})=\mathcal{W}+\mathcal{H} \ , \tag{2.19}$$

where $\mathcal{U}$ is the strain energy[1] and $\mathcal{H}$ the heating rate. Eq. (2.19) can also be given as (see Malvern 1969)

$$\frac{\mathrm{d}\mathcal{E}}{\mathrm{d}t}=\frac{\mathrm{d}\mathcal{A}}{\mathrm{d}t}+\frac{\mathrm{d}\mathcal{Q}}{\mathrm{d}t}, \tag{2.20}$$

$\mathcal{E}$ denotes the total stored energy in the system and is a summation of kinetic energy and internal energy[1]. The quantity $\mathcal{A}$ denotes the mechanical energy or work of the applied traction forces and body forces. $\mathcal{Q}$ is the inserted or removed energy by heat. The energy balance in Eq. (2.20), which expresses the first law of thermodynamics, will be used later in order to define the criteria for crack growth and the crack driving force.

The second law of thermodynamics should be introduced in order to identify the direction, in which thermodynamic process takes place. According to this law, the dissipation, $\Psi(\mathcal{D}_0)$, cannot be negative for each part $\mathcal{D}_0$ of a body. Under consideration of isothermal state changes, the dissipation can be expressed in the global form by the relation (Malvern 1969, Gurtin 2000),

$$\Psi(\mathcal{D}_0)=\mathcal{W}-\frac{\mathrm{d}\mathcal{E}}{\mathrm{d}t}\geq 0 . \tag{2.21}$$

If the kinetic energy is ignored, $\mathcal{E}$ equals the strain energy $\mathcal{U}$, and Eq. (2.21) can be defined in its local form as

$$\psi_{\mathrm{bulk}}=\mathbf{S}\cdot\dot{\mathbf{F}}-\dot{\phi}\geq 0 \qquad \text{at each point in the body } \mathcal{D}_0\subset\mathcal{B}_0, \tag{2.22}$$

which is termed "bulk dissipation per unit volume" (e.g. Simha et al. 2003). In Eq. (2.22), $\dot{\phi}$ denotes the time derivative of the (Helmholtz) free energy ϕ per volume in the reference configuration, which is identical to the strain energy density (it is defined later).

According to Eq. (2.22), if $\psi_{\mathrm{bulk}}=0$ (if dissipative processes do not occur in the material), ϕ is a single valued function of deformation and ϕ serves as a potential for the stresses,

$$\mathbf{S}=\frac{\mathrm{d}\phi(\mathbf{F})}{\mathrm{d}\mathbf{F}}. \tag{2.23}$$

---

[1] In our cases the strain energy $\mathcal{U}$ reflects the internal energy.

On the contrary, if dissipative processes occur in the material, $\psi_{\text{bulk}} > 0$, ϕ is not a single valued function of deformation and Eq. (2.23) is not valid any more.

2.5 Small strain setting

Although the elementary continuum mechanical basics are set up to understand the basic concepts of configurational forces in the large strain setting, in many applications the use of small strain setting is accurate enough, and it is not necessary to use the large strain formulations. In small strain setting the displacement **u** is assumed to be in the limit infinitesimally small. For infinitesimal small deformations of a continuum, the magnitude of the displacement gradient $\nabla\mathbf{u}$ is small compared to unity, $\|\nabla\mathbf{u}\| \ll 1$. This means that reference- and actual configurations are (approximately) the same. In the large strain formulations, a material particle is identified by its position in the reference position **X**, but in small strain formulations material particles can be characterized only by **x** (Malvern 1969).

In small strain formulations all strain and stress measures coincide. The displacement **u** is the essential kinematic descriptor for infinitesimal deformations and, in this case, the linearized strain tensor $\boldsymbol{\varepsilon}$ is defined as a function of $\nabla\mathbf{u}$ by

$$\boldsymbol{\varepsilon} = \frac{1}{2}\left(\nabla\mathbf{u} + \left(\nabla\mathbf{u}\right)^{\mathrm{T}}\right), \tag{2.24}$$

where the stress tensor is given by the Cauchy stress tensor $\boldsymbol{\sigma}$.

The balance of linear momentum, Eqs. (2.16) and (2.17), reads now

$$\int_{\partial\mathcal{D}} \boldsymbol{\sigma}\mathbf{n}\,\mathrm{d}A' = 0,\ \nabla.\boldsymbol{\sigma} = 0, \tag{2.25}$$

in global and local forms. The dissipation inequality, Eq. (2.22), becomes now

$$\psi_{\text{bulk}} = \boldsymbol{\sigma}\cdot\dot{\boldsymbol{\varepsilon}} - \dot{\phi} \geq 0 \quad \text{at each point in the body } \mathcal{D}. \tag{2.26}$$

If dissipative processes do not occur in the material, ϕ is a single valued function of $\boldsymbol{\varepsilon}$ and it leads to the conclusion that

$$\boldsymbol{\sigma} = \frac{\mathrm{d}\phi(\boldsymbol{\varepsilon})}{\mathrm{d}\boldsymbol{\varepsilon}}. \tag{2.27}$$

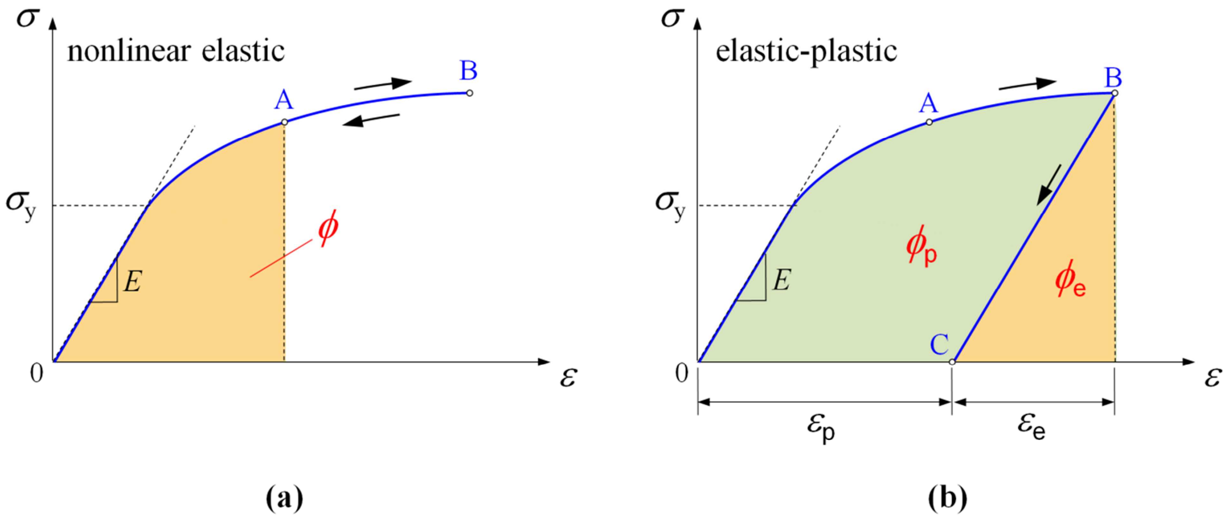

Fig. 2.2 Stress–strain relationship in **(a)** a nonlinear elastic material and **(b)** an elastic–plastic material. Nonlinear elastic and elastic–plastic materials exhibit different stress–strain curves during unloading. Deformation theory of plasticity treats the elastic–plastic material as being nonlinear elastic. In this case the total strain energy density $\phi = \phi_e + \phi_p$ is reversible. However, only the elastic part ϕ_e of the total strain energy density $\phi = \phi_e + \phi_p$ is recoverable in an elastic–plastic material following the incremental theory of plasticity.

2.6 *Strain energy density*

Since the strain energy density ϕ plays an important role in the derivation of the *J*-integral as crack driving force parameter in elastic–plastic materials, we briefly present an overview of the strain energy density ϕ in elastic–plastic materials, when *deformation*- and *incremental theory of plasticity* are applied.

If an elastic–plastic material is loaded beyond the yield stress σ_y, it will deform plastically. If small strain theory is considered, the total strain $\boldsymbol{\varepsilon}$ can be split into elastic and plastic parts, $\boldsymbol{\varepsilon} = \boldsymbol{\varepsilon}_e + \boldsymbol{\varepsilon}_p$ (Fig. 2.2b). Two theories, deformation- and incremental theory of plasticity, can be applied for the description of the relationship between the stresses $\boldsymbol{\sigma}$ and total strains $\boldsymbol{\varepsilon}$. Readers are referred to textbooks (see e.g. Malvern 1969, Marsden and Hughes 2012, Truesdell and Noll 1965) for a deeper understanding.

2.6.1 *Deformation theory of plasticity*

The deformation theory of plasticity, proposed by (Hencky 1924), actually does not describe irreversible plastic deformations as in the "incremental theory of plasticity" of Von Mises, Prandtl and Reuss. This theory treats elastic–plastic materials as non-linear elastic (Fig. 2.2a). Deformation theory of plasticity can be applied for elastic–plastic materials, if the conditions of proportional loading are fulfilled, that is, if no unloading processes occur in the material. In this case, the non-linear elastic and the elastic–plastic body will exhibit the same stress–strain curves; compare Figs. 2.2a and b. Therefore, deformation theory of plasticity is not applicable for crack extension and for cyclic loading.

When the conditions of proportional loading are fulfilled, the stress $\boldsymbol{\sigma}$ depends only on the current deformation $\boldsymbol{\varepsilon}$, but not on the deformation history. In this case, ψ_{bulk} = 0, Eq. (2.26), and ϕ is a single valued function of strain, $\phi = \phi(\boldsymbol{\varepsilon})$, as the area below the $\sigma - \varepsilon$-curve in Fig. 2.2a, given by

$$\phi(\boldsymbol{\varepsilon}) = \int_{\mathbf{0}}^{\boldsymbol{\varepsilon}} \boldsymbol{\sigma} \cdot \mathrm{d}\boldsymbol{\varepsilon} . \tag{2.28}$$

Based on deformation theory of plasticity, the plastic strain $\boldsymbol{\varepsilon}_{\text{p}}$ is a function of the deviatoric stresses, $\boldsymbol{\varepsilon}_{\text{p}} \sim \mathbf{s}$ (Lubliner 2013). It is noted that stresses can be decomposed into hydrostatic stresses, $\boldsymbol{\sigma}_{\text{m}} = 1/3\sigma_{kk}\mathbf{I}$, with $\mathbf{I}$ as unit tensor, and deviatoric stresses, $\mathbf{s} = \boldsymbol{\sigma} - \boldsymbol{\sigma}_{\text{m}}$. Plastic deformation is caused only due to deviatoric stresses. Note that, since the equivalent stress σ_{eq} is a function of the deviatoric stresses, the plastic strain $\boldsymbol{\varepsilon}_{\text{p}}$ is also a function of the equivalent stress. It is important to note that, based on deformation theory of plasticity, the total strain energy density $\phi = \phi_{\text{e}} + \phi_{\text{p}}$ is reversible.

The severest restriction for the application of the conventional *J*-integral results from the assumed existence of a strain energy density as a potential for the stresses (Rice 1968b,c). This assumption relies on the application of the deformation theory of plasticity (Rice and Rosengren 1968).

2.6.2 *Incremental theory of plasticity*

The incremental theory of plasticity is required for a realistic description of the behavior of elastic–plastic materials, even under strongly non-proportional loading conditions (see e.g. Newman 1976, Yuan and Brocks 1989, Li and Chandra 2003, Simha et al. 2008). The incremental theory of plasticity describes the increment of plastic strain $\mathrm{d}\boldsymbol{\varepsilon}_{\text{p}}$ as a function of the deviatoric stresses, $\mathrm{d}\boldsymbol{\varepsilon}_{\text{p}} \sim \mathbf{s}$. The total strain increment is a linear combination of the elastic and plastic increments, i.e. $\mathrm{d}\boldsymbol{\varepsilon} = \mathrm{d}\boldsymbol{\varepsilon}_{\text{e}} + \mathrm{d}\boldsymbol{\varepsilon}_{\text{p}}$. The elastic strain increment $\mathrm{d}\boldsymbol{\varepsilon}_{\text{e}}$ is related to the stresses by Hooke's law.

In an elastic–plastic material, after loading to point B (see Fig. 2.2b), the total strain energy density $\phi = \phi_{\text{e}} + \phi_{\text{p}}$ is not fully reversible any more. The elastic part of the strain energy density ϕ_{e} is reversible; the plastic part of the strain energy density ϕ_{p} has been dissipated already. Therefore, point C (Fig. 2.2b) is reached after unloading from B.

In Part II of this thesis the deformation theory is used for calculating the configurational forces and the material inhomogeneity effect (the total strain energy density $\phi = \phi_{\text{e}} + \phi_{\text{p}}$ is taken)[2], since there are no real crack extension and cyclic loading. In Part III of this thesis the incremental theory of plasticity is used for calculating the configurational forces and the crack driving force in the magnesia-spinel refractory, since the material is under strongly non-proportional loading conditions due to the damage evolution process in the magnesia matrix (see Section 8).

---

[2] Von Mises plasticity model is used.

3 Fundamentals of fracture mechanics

An introduction into the principles of fracture mechanics, as a continuum mechanics tool for the description of the behavior of cracks in materials and components, is given in this chapter. For a comprehensive survey on fracture mechanics, see e.g. Anderson (2005), Gross and Seelig (2007) and the review given by Kolednik (2012).

This chapter concentrates on the fundamental understanding of the various parameters that are applied to characterize the crack driving force and the fracture resistance and outlines their physical meanings. The emphasis is laid on the J-integral concept, i.e. the common approach in the regime of elastic–plastic fracture mechanics.

3.1 Crack driving force and crack growth resistance

Fracture mechanics is used to describe fracture processes in materials that are already containing cracks by the use of concepts of continuum mechanics. Fracture mechanics concepts differ between linear–elastic and elastic–plastic fracture mechanics. In both cases it is possible to determine the criterion for the growth of cracks by two parameters, i.e. the *crack driving force*, which tries to extend the crack, and the *crack growth resistance*, which hinders crack extension. A major problem in fracture mechanics is that different parameters are used for the description of the crack driving force and the crack growth resistance (Kolednik 2012). Therefore, here we present the crack driving force and the crack growth resistance in their generalized form.

Consider a crack of initial length a_0 in a loaded body (Fig. 3.1a). The crack will extend if the generalized crack driving force D_{gen} becomes equal or larger than the generalized crack growth resistance R_{gen} (Kolednik 2012),

$$D_{\mathrm{gen}} \geq R_{\mathrm{gen}}, \tag{3.1}$$

see Fig. 3.1b. The crack driving force D_{gen} is a loading parameter for the crack; it originates from the work of the applied forces and/or the stored strain energy in the body. The crack growth resistance R_{gen} is a function of the material, the crack extension Δa, and the geometry of the body. If D_{gen} is smaller than R_{gen}, the crack cannot extend. If D_{gen} equals R_{gen}, “equilibrium crack growth” prevails. If D_{gen} is larger than R_{gen}, we have “unstable crack growth”.

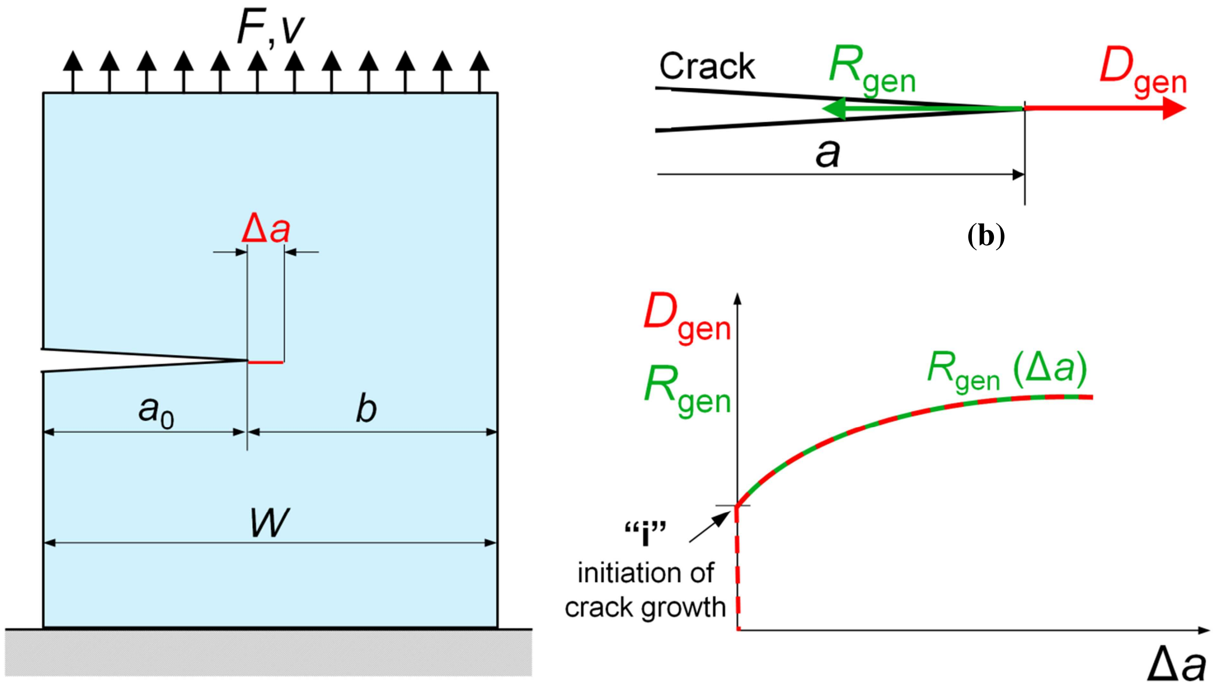

(b)

(a) **(c)**

Fig. 3.1 **(a)** Loaded body with an initial crack of length a_0. **(b)** The crack starts to grow, if the generalized crack driving force D_{gen} is equal or larger than the generalized crack growth resistance R_{gen}. **(c)** Crack growth resistance curve, where D_{gen} and R_{gen} are plotted against the crack extension Δa. The point, marked by ''i'', characterizes the initiation of crack growth.

The fracture toughness of a material can be determined by conducting a fracture mechanics experiment. A specimen with a sharp crack of initial length a_0 is loaded. The load F, the load point displacement v and the crack extension Δa are measured during testing, Fig. 3.1a. The crack driving force D_{gen} is determined from the resulting $F–v$ curve, the actual crack length a and the geometry of the body. Fig. 3.1c shows a crack growth resistance curve, i.e. a curve where R_{gen} is plotted against the crack extension Δa. The crack driving force D_{gen} increases with increasing load. When $D_{\text{gen}} = R_{\text{gen}}$, the first step of crack extension occurs; this point is marked by "i" in Fig. 3.1c. The value of R_{gen} at this point, $R_{\text{gen,i}}$, gives the fracture initiation toughness of the material (Kolednik 2012). The crack growth resistance $R_{\text{gen}}(\Delta a)$ can be determined during the equilibrium crack growth, since $D_{\text{gen}} = R_{\text{gen}}$. The $R_{\text{gen}}–\Delta a$ curve in Fig. 3.1c is known as the *crack growth resistance curve* or the so-called *R–curve* (Anderson 2005).

3.2 Regimes of fracture mechanics

Various parameters are used for the characterization of the crack driving force and the crack growth resistance, see (Kolednik 2012). The reason is due to the different regimes of fracture mechanics, i.e. linear elastic fracture mechanics and elastic–plastic- or non-linear fracture mechanics.

Linear elastic fracture mechanics describes fracture processes by using a small strain setting within the frame work of linear elasticity. Since this is appropriate particularly for brittle fracture, linear fracture mechanics also is understood as brittle fracture mechanics (Gross and Seelig 2007). Linear elastic fracture mechanics is applied when crack growth is accompanied by zero or limited plastic deformation, i.e. the radius of the plastic zone r_{pl} is very small compared to the crack length a and the ligament length b (Fig. 3.2a), yielding

$$r_{\mathrm{pl}} \ll a, b \,. \tag{3.2}$$

This regime of fracture mechanics under *small-scale yielding* (ssy) conditions is denominated as “LEFM”.

In contrast, elastic–plastic- or non-linear fracture mechanics characterizes fracture processes in presence of significant plastic deformation, i.e. if *large-scale yielding* (lsy) or *general yielding* (gy) conditions prevail (Fig. 3.2b)[3], or when the material, as a general, exhibits non-linear behavior (Gross and Seelig 2007; Kolednik 2012). This regime of fracture mechanics under lsy or gy conditions is denominated as “E–PFM”.

In the LEFM regime, it is easy to describe fracture processes, since the crack growth resistance R_{gen} is a material constant; the R_{gen}–Δa curve in Fig. 3.1c, R−curve, becomes relatively flat (Anderson 2005)[4]. On the contrary, the situation is much more complex in the E–PFM regime. In this case, the crack growth resistance depends not only on the crack extension Δa, but also on the geometry and size of the considered structure (Kolednik 2012).

3.3 Energy balance during crack extension

A definition of the crack driving force and crack growth resistance originates from the balance of energy during an increment of equilibrium crack extension $\mathrm{d}(\Delta a)$. Based on Griffith’s idea (Griffith 1920), an existing crack can grow only if the total energy of the system decreases or remains constant. Thus the critical condition for fracture can be defined for the situation where the crack growth occurs in case of equilibrium conditions, with no net change in total energy (Anderson 2005). Assume an elastic–plastic body of thickness B with a crack during an increment of equilibrium crack extension $\mathrm{d}(\Delta a)$ (Fig. 3.1a). The balance of energy can be expressed as (e.g. Kolednik 2012)

---

[3] Lsy-conditions start when the crack tip plastic zone is large compared to the crack length and the ligament length. Gy-conditions prevail when plasticity spreads over the whole ligament.

[4] R-curve cannot be exactly flat due to toughening mechanisms, e.g. transformation toughening in ceramics. In this case, the material exhibits an R-curve effect (i.e. the crack growth resistance increases with crack extension).

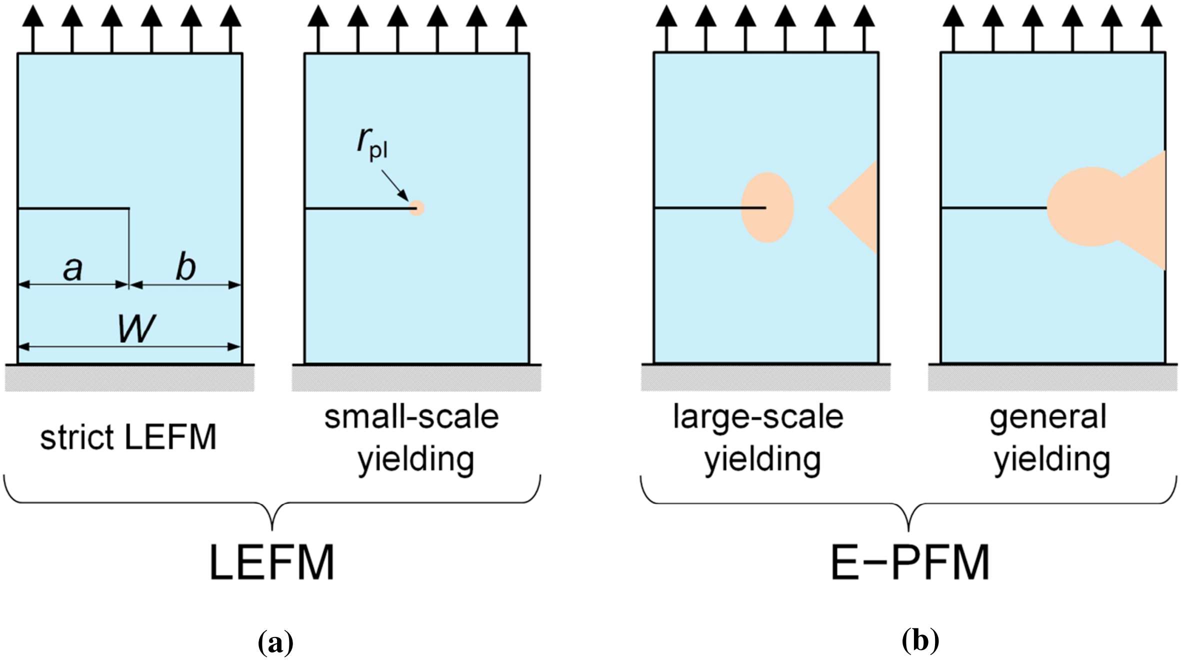

Fig. 3.2 Regimes of fracture mechanics. **(a)** linear elastic fracture mechanics (LEFM) is applied if linear elastic (strict LEFM) or small-scale yielding conditions prevail. **(b)** elastic–plastic fracture mechanics (E–PFM) is applied if large-scale- or general yielding conditions prevail.

$$\mathrm{d}\mathcal{A} = \mathrm{d}\mathcal{U}_{\mathrm{el}} + \mathrm{d}\mathcal{U}_{\text{non-rev}} + \mathrm{d}\Gamma_{\mathrm{s}}\,, \tag{3.3}$$

where $\mathcal{A}$ denotes the work of the applied forces, $\mathcal{U}_{\mathrm{el}}$ the reversible (elastic) strain energy, $\mathcal{U}_{\text{non-rev}}$ the non-reversible (i.e. dissipated) energy, and Γ_{s} the surface energy, which reflects the work required to create new surfaces (Anderson 2005). Since the formation of a crack requires the creation of two fracture surfaces, Γ_{s} is given by

$$\Gamma_{\mathrm{s}} = 2aB\gamma_{\mathrm{s}}\,, \tag{3.4}$$

where γ_{s} is the specific surface energy of the material. In Eq. (3.3), the term $\mathcal{U}_{\text{non-rev}}$ contains all dissipative processes that appear in the body during the crack extension, which is mainly the plastic strain energy $\mathcal{U}_{\mathrm{pl}}$. Note that $\mathcal{U}_{\text{non-rev}}$ may include also other energy terms, e.g. for phase transformation in transformation toughening ceramics, for fiber pull-out in short fiber reinforced composites, and etc., see (Kolednik 2012). Re-arrangement of Eq. (3.3) and division by the increased crack area, $B\,\mathrm{d}(\Delta a)$, leads to

$$\underbrace{D \equiv -\frac{1}{B}\frac{\mathrm{d}\mathcal{U}_{\mathrm{el}} - \mathrm{d}\mathcal{A}}{\mathrm{d}(\Delta a)} = -\frac{1}{B}\frac{\mathrm{d}\mathcal{P}}{\mathrm{d}(\Delta a)}}_{\text{crack driving force}} = \underbrace{\frac{1}{B}\frac{\mathrm{d}\mathcal{U}_{\text{non-rev}} + \mathrm{d}\Gamma_{\mathrm{s}}}{\mathrm{d}(\Delta a)} \equiv R}_{\text{crack growth resistance}}\,. \tag{3.5}$$

Eq. (3.5) is a special form of Eq. (3.1) for equilibrium crack growth. In Eq. (3.5), $\mathcal{P} = \mathcal{U}_{\mathrm{el}} - \mathcal{A}$ denotes the total potential energy that is supplied by the internal elastic strain energy and the work of the external force; $\mathrm{d}\mathcal{P} = \mathrm{d}\mathcal{U}_{\mathrm{el}} - \mathrm{d}\mathcal{A}$ is the change in potential energy of the body during crack extension. If crack extension occurs at constant load point displacement *v*, the work of the applied forces $\mathrm{d}\mathcal{A} = 0$ and the change in potential energy equals the change in stored elastic strain energy, $\mathrm{d}\mathcal{P} = \mathrm{d}\mathcal{U}_{\mathrm{el}}$ (Anderson 2005; Kolednik 2012).

The term on the left of Eq. (3.5) is identical to the crack driving force, i.e. the potential energy released per unit crack extension. The term on the right side of Eq. (3.5) describes the crack growth resistance, i.e. the non-reversible energy is required to produce an increment of crack area, see Griffith (1920), Eftis and Liebowitz (1975), Kolednik (1991), Kolednik (1993), Turner and Kolednik (1994).

Irwin defined the *energy release rate G*, which is a measure of the energy available for an increment of crack extension (Irwin 1956). The elastic energy release rate *G* characterizes the crack driving force *D* in the regime of LEFM. The stress intensity factor *K* (Irwin 1957), which is presented in Section 3.4, is also applied for the characterization of the crack driving force in the regime of LEFM. The parameters *G* and *K* are related in the regime of LEFM; both concepts are in principle equivalent (Anderson 2005; Gross and Seelig 2007).

In the regime of E–PFM, two approaches are widely used to characterize the crack driving force and the crack growth resistance in elastic–plastic materials. The first is the crack tip opening displacement concept (CTOD-concept), proposed by Wells (1961, 1963), where plastic deformation at the crack tip leads to blunting of the initially sharp crack tip. The second is the *J*-integral concept introduced to describe the thermodynamic crack driving force for nonlinear elastic bodies (Rice 1968b; Rice 1968c); this concept is explained in Section 3.5. The *J*-integral concept is widely used in this thesis for the numerical and experimental investigations of the fracture behavior of inhomogeneous materials.

For ideally brittle materials, the crack growth resistance *R* equals twice the specific surface energy, $R = 2\gamma_{\mathrm{s}}$, compare Eqs. (3.4) and (3.5). For ssy conditions where the plastic zone is very small and remains constant during crack extension, *R* equals twice the summation of the specific surface energy γ_{s} and a specific plastic work γ_{pl}, $R = 2\left(\gamma_{\mathrm{s}} + \gamma_{\mathrm{pl}}\right)$. The specific plastic work γ_{pl} is the plastic work required to create a unit area of fracture surface, see Anderson (2005), Kolednik (2012). Note that $\gamma_{\mathrm{pl}} \gg \gamma_{\mathrm{s}}$. In this case, the crack growth resistance *R* is independent of crack extension Δa (Kolednik 1993; Kolednik 2012).

In the regime of E–PFM, for lsy and gy conditions, the crack growth resistance *R* depends on the crack extension Δa, on the geometry and size of the considered structure. In this case, *R* is denominated often as energy dissipation rate (Turner 1990) or total crack growth resistance (Kolednik et al. 1997). The crack growth resistance curve for lsy and gy conditions is determined by recording the load–displacement curve, *F*–*v* curve, versus the crack extension Δa, as described in the section titled “Experimental *J*-integral”.

3.4 The Stress Intensity Concept

This section describes the stress intensity approach to linear fracture mechanics. The stress intensity factor *K* will be used later in Section 6.

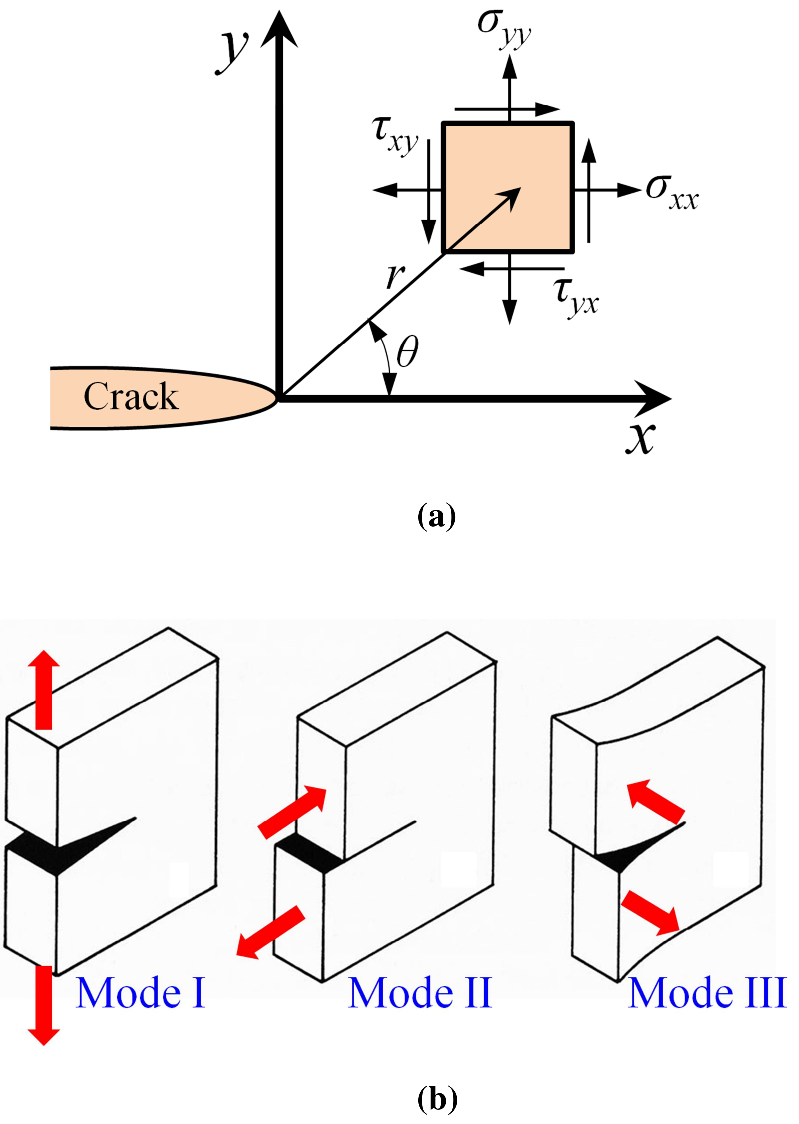

Fig. 3.3 **(a)** Stresses at a point with polar coordinates (r, θ) with respect to the crack tip. **(b)** Three types of loading that a crack can experience.

Classical fracture mechanics defines three basic modes of deformation, see Fig. 3.3b. Mode I is the tensile or opening mode, in which the crack faces separate in a direction normal to the crack plane without any sliding. Mode II is the shear mode, in which the crack faces slide normal to the crack front. Mode III is the tearing or out-of-plane shear mode, in which the crack faces slide parallel to the crack front. A mixed-mode loading occurs when more than one loading mode is present, e.g. the mixed mode I/II loading occurs when the crack faces are subjected to opening and sliding modes. Usually, fracture mechanics tests are performed under Mode I loading, since this mode is the most critical loading mode (Anderson 2005).

Fig. 3.3a schematically shows an element near the tip of a crack, together with the in-plane stresses on this element. The stresses in a linear elastic body were derived from complex stress functions (Westergaard 1939; Irwin 1957; Williams 1957). The elastic stresses at a point around the crack tip with polar coordinates (r, θ), Fig. 3.3a, are written as an infinite series expansion by the relation,

$$\sigma_{ij} = \frac{K}{\sqrt{2\pi r}} f_{ij}\left(\theta\right) + \text{nonsingular terms}\,. \tag{3.6}$$

The first term of stresses in Eq. (3.6) is the singular stress term of the order $r^{-1/2}$ which is dominant in the vicinity of the crack tip, for small r. The nonsingular stress terms, terms of the order r^0, $r^{1/2}$, and so on, can be neglected near the crack tip. Therefore, the stress intensity factor K determines the intensity of the near-tip stress field. f_{ij} is a function only of the crack plane angle θ. Each mode of loading, Fig. 3.3b, produces a singularity at the crack tip. The components of the stresses and displacements for the three crack opening modes are given in fracture mechanics textbooks (see e.g. Anderson 2005, Gross and Seelig 2007).

The stress intensity factor K is a loading parameter for the crack which depends on the applied load, the crack length a, and the geometry of the body (compare Fig. 3.1a),

$$K = \sigma_{\text{appl}} \sqrt{\pi a} f_K \left(\frac{a}{W}\right), \tag{3.7}$$

where σ_{appl} denotes the applied global stress, and f_K is a dimensionless geometry parameter. It should be mentioned that the first term of Eq. (3.6) is independent of the crack length and the geometry of the considered body. Therefore, only a single parameter, K, determines all the stress and strain components near the crack tip. In the stress intensity concept, the crack starts to grow if a critical stress intensity of the crack tip field, K_i, is reached (Irwin 1957),

$$K \geq K_\text{i}\,. \tag{3.8}$$

K_i is the stress intensity of the crack tip field at the point of fracture initiation, the point “i” in Fig. 3.1c. Often it is difficult to determine the point of fracture initiation accurately. Then a substitute value is taken, K_c. K_i or K_c values are denoted as *critical stress intensity factors* of the crack tip field, see e.g. Anderson (2005).

3.5 The *J*-integral concept

The J-integral describes the crack driving force for nonlinear elastic bodies. The J-integral also characterizes the intensity of the crack tip field for nonlinear elastic materials (HRR field), similar as K and G do for the linear elastic case (Hutchinson 1968; Rice and Rosengren 1968).

3.5.1 Definition and properties

Rice (1968b,c) presented a contour integral for the analysis of cracks. He showed that the value of this integral, which is called J-integral, is equal to the energy release rate in a nonlinear elastic body that contains a crack. Assume a homogeneous, nonlinear elastic body as illustrated in Fig. 3.4b. The J-integral can express the change in potential energy $\mathrm{d}\mathcal{P}$ released during an incremental crack extension $\mathrm{d}a$,

$$-\frac{1}{B}\frac{\mathrm{d}\mathcal{P}}{\mathrm{d}a}=\int_{\Gamma}\left(\phi\,\mathrm{d}y-\mathbf{t}\cdot\frac{\partial\mathbf{u}}{\partial x}\mathrm{d}s\right)\equiv J\,. \tag{3.9}$$

The crack length a has the meaning of an internal variable. In Eq. (3.9), $\mathrm{d}s$ denotes an increment of the integration path Γ, drawn from the lower to the upper crack flank in counterclockwise direction around a crack (see Fig. 3.4b). The strain energy density ϕ and the traction vector $\mathbf{t}$ have been already introduced in Section 2.

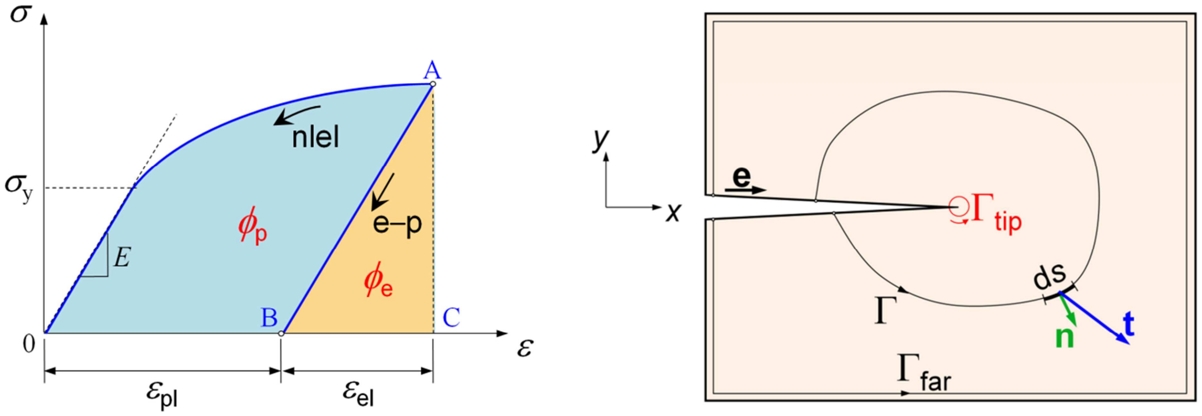

(a) **(b)**

Fig. 3.4 **(a)** Nonlinear elastic (nlel) and elastic–plastic (e–p) materials exhibit different stress–strain curves during unloading. **(b)** Homogeneous, nonlinear elastic body with a crack. The magnitude of the J-integral is independent of the integration path Γ.

If the material inside the arbitrary contour Γ is homogeneous and nonlinear elastic, the *J*-integral becomes *path independent*. In this case, $J_{\text{tip}} = J_{\Gamma} = J_{\text{far}}$, see Fig. 3.4b. This path independency of the *J*-integral is an important advantage. The reason is that a direct evaluation of the energy released at the crack tip, characterized by the near-tip *J*-integral J_{tip}, is often difficult. However, since $J_{\text{tip}} = J_{\text{far}}$, the magnitude of J_{tip} can readily be determined by the far-field *J*-integral J_{far}.

It is noted that in the regime of LEFM, *J*-integral is identical to the elastic energy release rate *G*, and it is related to the stress intensity factor *K* by the following relation (Anderson 2005; Gross and Seelig 2007; Kolednik 2012),

$$J = G = \frac{K^2}{E'}, \tag{3.10}$$

where $E' = E$ for plane stress conditions and $E' = E/(1-\nu^2)$ for plane strain conditions.

3.5.2 *Restrictions of J-integral in elastic–plastic materials*

It should be emphasized that the *J*-integral does not characterize the crack driving force for elastic–plastic materials. The application of the *J*-integral for elastic–plastic (e–p) materials lies in the assumption that deformation theory of plasticity can be used (see Section 2.6), i.e. if the elastic–plastic material is characterized by nonlinear elastic behavior (see Fig. 3.4a). The reason is that the meaning of a crack driving force term, Eq. (3.9), and the path independence of *J* can be shown only if the strain energy density ϕ exhibits the properties of a potential so that Eq. (2.27) is valid.

Fig. 3.4a shows the stress–strain ($\sigma - \varepsilon$) curve of a nonlinear elastic and an elastic–plastic material that exhibit the same stress–strain-curves where no unloading occurs in the material: When the conditions of *proportional loading* are fulfilled. In this case, the deformation theory of plasticity can be correctly used for elastic–plastic (e–p) materials (Rice 1968b,c; Kolednik et al. 2014b); the stress $\boldsymbol{\sigma}$ depends only on the current deformation $\boldsymbol{\varepsilon}$, but not on the deformation history. In this case, $\psi_{\text{bulk}} = 0$, Eq. (2.26), and ϕ is a single valued function of strain, $\phi = \phi(\boldsymbol{\varepsilon})$. Deformation plasticity presumes the total strain energy density ϕ to be fully reversible (see Section 2.6).

On the contrary, incremental theory of plasticity describes the increment of plastic strain as a function of the equivalent stress, $\mathrm{d}\boldsymbol{\varepsilon}_{\text{p}} \sim \sigma_{\text{eq}}$, which is the correct description for elastic–plastic materials, see Section 2.6. It can be seen from the stress–strain curve of a material point near the crack tip, Fig. 3.4a, that deformation theory predicts wrong total strains, if the unloading process occurs such as in cyclic loading and crack extension, i.e. if the conditions of proportional loading are violated. In an elastic–plastic material, the total strain energy density $\phi = \phi_e + \phi_p$ is not fully reversible. The elastic part of the strain energy density ϕ_e is reversible. The plastic part of the strain energy density ϕ_p has been dissipated already and is not available for driving crack extension. Eq. (3.9) cannot be derived for incremental plasticity, since ϕ is not a thermodynamic potential, hence, Eq. (2.27) is invalid (e.g. Anderson 2005). This is the reason why the *J*-integral does not characterize the crack driving force for elastic–plastic materials.

It should be remarked that, if the stress and strain analyses are performed based on the incremental theory of plasticity, e.g. by finite element (FE) computations, and deformation plasticity is implicitly assumed in the evaluation of the *J*-integral, Eq. (3.9), the physical meaning of the crack driving force still remains unclear for incremental plasticity (Simha et al. 2008; Kolednik et al. 2014b; Ochensberger and Kolednik 2014; Ochensberger and Kolednik 2015).

A possible solution of these problems originates from the application of the concept of configurational forces, since it enables the derivation of the *J*-integral without restrictions regarding the constitutive relations of the material, see Simha et al. (2008), Kolednik et al. (2014b). The concept of configurational forces will be presented in Section 4.

3.5.3 Experimental J-integral

The most widely used *J*-integral testing technique was introduced in (Rice et al. 1973) and allows the calculation of a *J*-value at a certain load or displacement from the load–displacement curve of a single specimen. This method is also the basis of most standards for fracture mechanical testing, e.g. (ESIS P2-92 1992) or (ASTM E1820-05 2005). The magnitude of the *J*-integral, which is given in Eq. (3.9), can be determined by fracture mechanics experiments from the area *A* below the *F*–*v* curve, *A* denotes the work of the applied loading system, by the relation (Rice et al. 1973),

$$J^{(\exp)} = \frac{\eta A}{bB}, \tag{3.11}$$

where *b* is the ligament length ($b = W - a$), *W* and *a* as the width of the specimen and the crack length, respectively. The dimensionless geometry factor $\eta(a/W)$ depends on the specimen type and the ratio a/W.

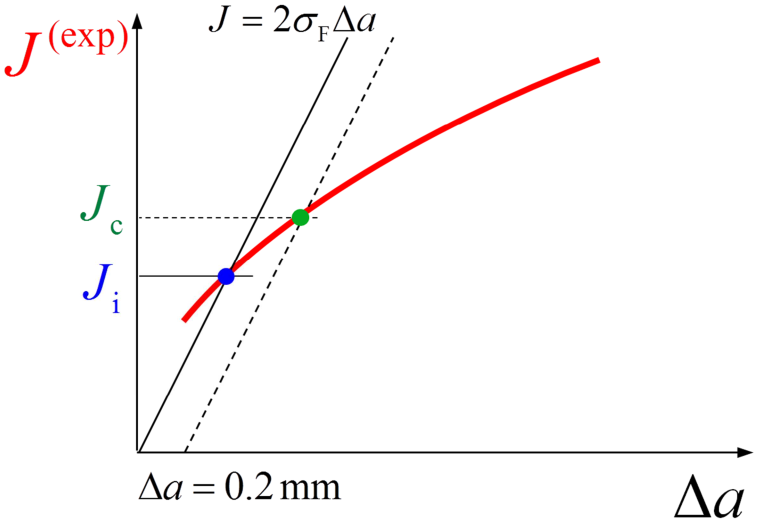

Fig. 3.5 Schematic of the experimental J-integral vs. crack extension Δa, $J^{(\mathrm{exp})} - \Delta a$, curve. It is also called crack growth resistance curve in terms of the experimental J-integral.

$J^{(\mathrm{exp})}$ can be determined from Eq. (3.11) by loading the fracture mechanics specimen and measuring the average crack extension Δa. Then the $J^{(\mathrm{exp})} - \Delta a$ curve is plotted, Fig. 3.5, which describes the behavior for stable crack extension. Extrapolation and intersection of this curve with the blunting line, given by the equation $J = 2\sigma_F \Delta a$, with σ_F as average flow stress, yields the J-integral at the initiation of crack growth point, J_i. Since the $J^{(\mathrm{exp})} - \Delta a$ curve is often inaccurate for very small Δa values, an engineering approximation of the fracture initiation point is determined by drawing a 0.2 mm offset line parallel to the blunting line (see e.g. ASTM E1820-05 2005, Anderson 2005); intersection with the $J^{(\mathrm{exp})} - \Delta a$ curve gives the fracture initiation toughness J_c, see Fig. 3.5.

For a LEFM case, where the crack growth resistance equals the fracture initiation toughness ($R = J_i$), the experimental J-integral is constant, $J^{(\mathrm{exp})} = R = J_i$. For lsy or gy conditions, the crack growth resistance is usually much larger than the fracture initiation toughness ($R \gg J_i$), see e.g. Kolednik (2012). In the case of lsy or gy conditions and when the change in the elastic strain energy is small, the crack growth resistance is proportional to the slope of the $J^{(\mathrm{exp})} - \Delta a$ curve (Kolednik 1991). Therefore, an increasing of this curve does not necessarily mean that the crack growth resistance increases.

It is worth noting that Eq. (3.11) and Eq. (3.9) yield identical J-values, $J^{\mathrm{exp}} = J$, for a monotonically loaded, stationary crack in an elastic–plastic material with incremental plasticity (Kolednik 1991; Kolednik 2012; Rice et al. 1973).

3.6 Crack tip plastic zone

An important length parameter, which is used widely in this work, is the radius of the *crack tip plastic zone*. Therefore, it is useful to show how the radius of the crack tip plastic zone can be estimated in an elastic–plastic material.

It is recognized that plastic deformation appears at the crack tip as a result of the high stresses that are generated by the stress concentration near the crack tip. Based on Irwin's model (Irwin 1961), for small-scale yielding conditions, the radius of the crack tip plastic zone, r_{y}, can be estimated as,

$$r_{\mathrm{y}} = \beta \left(\frac{K}{\sigma_{\mathrm{y}}} \right)^2 , \tag{3.12}$$

where σ_{y} is the yield stress of the material, and $\beta = 1/(6\pi)$ for plane strain conditions and $\beta = 1/(2\pi)$ for plane stress conditions. In the *J*-integral concept, the radius of the crack tip plastic zone can be determined by inserting the relation between *J*-integral and stress intensity factor *K*, Eq. (3.10), into Eq. (3.12), yielding

$$r_{\mathrm{y}} = \beta \frac{J\,E'}{\sigma_{\mathrm{y}}^2} , \tag{3.13}$$

where $E' = E$ for plane stress conditions and $E' = E/(1-\nu^2)$ for plane strain conditions. Since the radius of the plastic zone r_{y} depends linearly on *J*-integral, it can be considered as a loading parameter of the crack.

A shortcoming of Irwin's model is that it assumes a circular plastic zone with its center at the crack tip. In reality, the plastic zone has a more complicated shape with a forward orientation, e.g. with a maximum extension at an angle of $\theta = 70^\circ$ with respect to the crack plane for plane strain conditions (Anderson 2005). In an inhomogeneous material, the angle θ changes, depending on the material inhomogeneity, its distance to the crack tip and the load, see Sections 5–7.

3.7 Cracks in inhomogeneous materials

Inhomogeneous materials can be divided into two major categories: graded materials and multilayered materials. This thesis deals with the fracture behavior of multilayer materials and, therefore, this section only concentrates on multilayer materials.

Multilayer composites are a unique form of composite materials in which layers are bonded together with discrete interfaces. Laminated composites can dramatically improve many properties. For example, numerous studies have illustrated the benefits to the fracture toughness that can be achieved via the creation of a layered structure (Lesuer et al. 1996). Toughening in layered structures can arise from many different sources. Ritchie (1988) showed that toughening in materials can result from two different types of mechanisms, intrinsic and extrinsic. Intrinsic toughening results from the inherent resistance of the microstructure to crack growth and, thus, is influenced by such microstructural characteristics as grain size, particle spacing, particle size, etc. On the other hand, extrinsic toughening results from mechanisms that reduce the local stress intensity at the crack trip and thus the local "driving force" for crack growth. Multilayer structures toughen materials by various extrinsic mechanisms. The most relevant mechanisms are discussed in the following.

3.7.1 Interface delamination

The improvement of the fracture- or impact toughness can be achieved by the introduction of weak interfaces in front of the crack tip, caused by the delamination of interfaces.

When a weak interface is located in front of the crack tip, the high stress triaxiality near the crack tip leads to decohesion and opening of the interface (Hertzberg 1976). The delamination generates an internally free surface, see Fig. 3.6a, which reduces strongly the crack tip triaxiality as the stress component acting normal to the free surface has to be zero. Additionally, the sharpness of the crack tip is lost when the crack grows into the delaminated interface, which also reduces the local stress intensity, see Fig. 3.6b. Caused by the delamination, the crack can arrest at the interface and has to be re-initiated in the adjacent layer, which consumes a high amount of energy and can markedly increase the fracture toughness (Cook and Gordon 1964; Embury et al. 1967; Lesuer et al. 1996; Tariolle et al. 2005; Wang et al. 2000). Note that the increase in fracture toughness is especially high for a crack arrester configuration, i.e. when the interfaces are perpendicular to the nominal crack plane (Kolednik 2012).

3.7.2 Crack deflection

In many multilayer structures, the local interface delaminations (Fig. 3.7a) can result in crack deflection which can significantly reduce the mode I component of the local stress intensity factor because of the large deviations in crack path, see Fig. 3.7b. These crack path deviations cause the crack to move away from the plane experiencing maximum stress. Consequently, the crack deflection can significantly enhance the fracture toughness (Faber and Evans 1983; Suresh 1983; Suresh 1985; Lesuer et al. 1996).

An expression has been derived in (Suresh 1983) for the effective local stress intensity resulting from deflected cracks that can be applied to laminated composites.

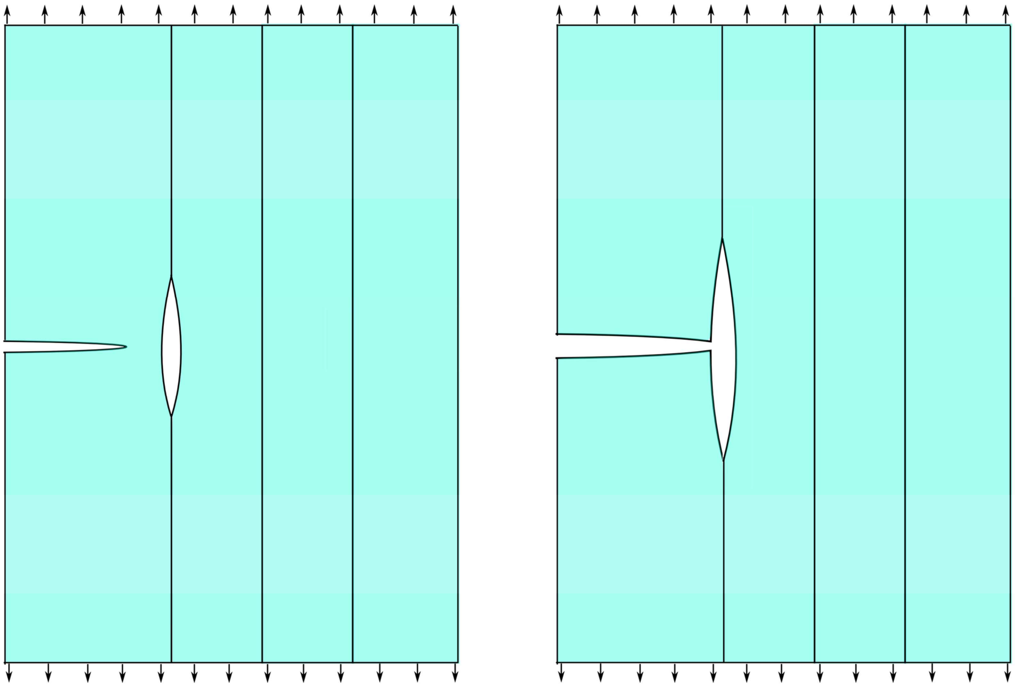

Fig. 3.6 Decohesion and opening of weak interfaces can lead to a reduction of the hydrostatic stress state due to the free surfaces. **(a)** Delamination ahead of the crack tip and **(b)** crack tip blunting.

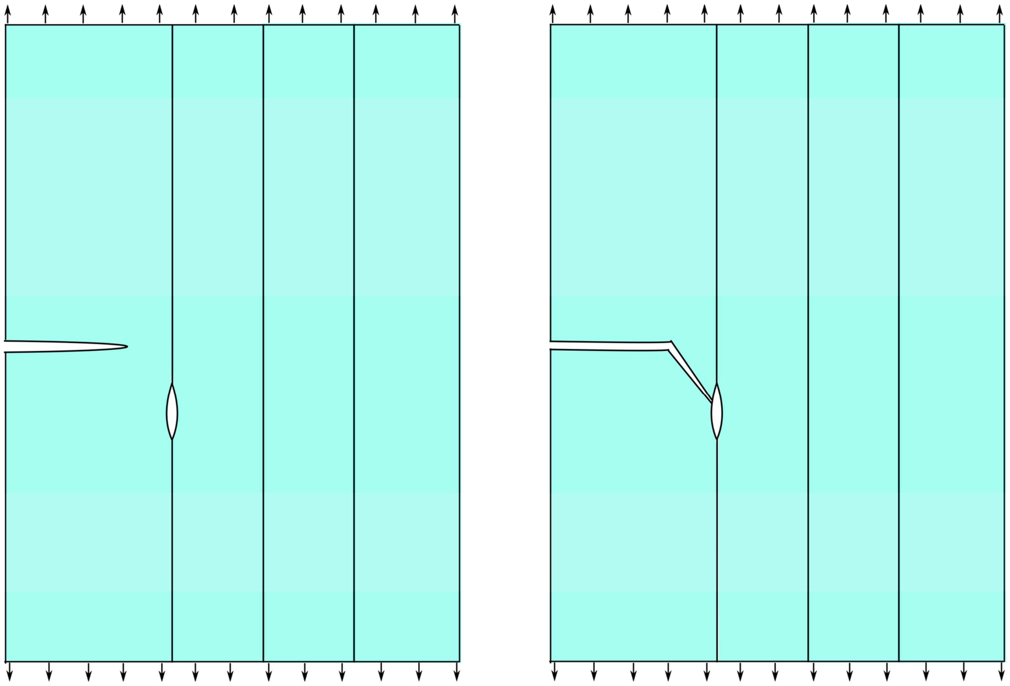

Fig. 3.7 **(a)** Local interface delaminations can result in crack deflection. **(b)** Crack deflection can significantly reduce the mode I component of the local stress intensity factor, because of the large deviations in crack path, and enhances the fracture toughness.

3.7.3 Compressive residual stresses

Residual stresses in laminates can influence fracture toughness and fatigue crack growth rates. Residual stresses can be introduced in individual layers by thermal expansion mismatch between layers produced during rapid cooling from the processing temperature. In the crack arrester configuration when the crack propagates from one layer to the next, layers that have compressive residual stresses experience a decrease in the crack driving force, leading to great improvement of fracture toughness. In contrast, layers with tensile residual stresses experience an increase in the crack driving force (Lesuer et al. 1996; Lugovy et al. 2005; Chen et al. 2007).

3.7.4 Effect of material property variations on crack driving force

A common feature that is inherent to all classes of multilayered materials is that a spatial variation of material properties in the direction of crack extension influences the crack driving force and thus affects the behavior of cracks. This effect, denominated material inhomogeneity effect, occurs independently of the toughening mechanisms presented above, interface delamination, crack deflection and residual stresses.

As it has been explained in Section 3.5, in a homogenous material under monotonic loading, the J-integral is path independent and the near-tip J-integral J_{tip} is equal to the far-field J-integral J_{far}, $J_{\mathrm{tip}} = J_{\mathrm{far}}$, see Fig. 3.8a. J_{tip} denotes the crack driving force in terms of the J-integral, which is a loading parameter. The far-field J-integral J_{far} represents the driving force that is inserted by the applied load into the specimen.

In an inhomogeneous material, e.g. a bimaterial specimen shown in Fig. 3.8b, the far-field J-integral J_{far} differs from the crack driving force J_{tip}, $J_{\mathrm{tip}} \neq J_{\mathrm{far}}$ (Kolednik 2012). Therefore, in inhomogeneous materials, the scalar J-integral of Eq. (3.9) becomes path dependent, as soon as the material properties exhibit a variation in the direction of crack growth along the integration path. As it will be seen in Section 4, the reason is that a material inhomogeneity can be considered as an additional defect in the material, which induces an additional contribution to the crack driving force J_{tip}. In an inhomogeneous material, e.g. a bimaterial specimen in Fig. 3.8b, the crack driving force J_{tip} is a function of the properties of Materials 1 and 2, the crack length, the distance between crack tip and interface and the load.

Numerous researchers have shown that the variations of material properties in the direction of the crack extension can significantly affect the crack driving force. A brief survey of those studies will be given in Section 5, Paper I. Most analytical papers consider cracks near interfaces using the stress intensity K-field formulation, which is applicable for linear elastic fracture mechanics, see e.g. Zak and Williams (1963), Cook and Erdogan (1972), Erdogan and Biricikoglu (1973), Romeo and Ballarini (1995). The most relevant results from these studies are in the following. The stress intensity approach holds as long as the elastic

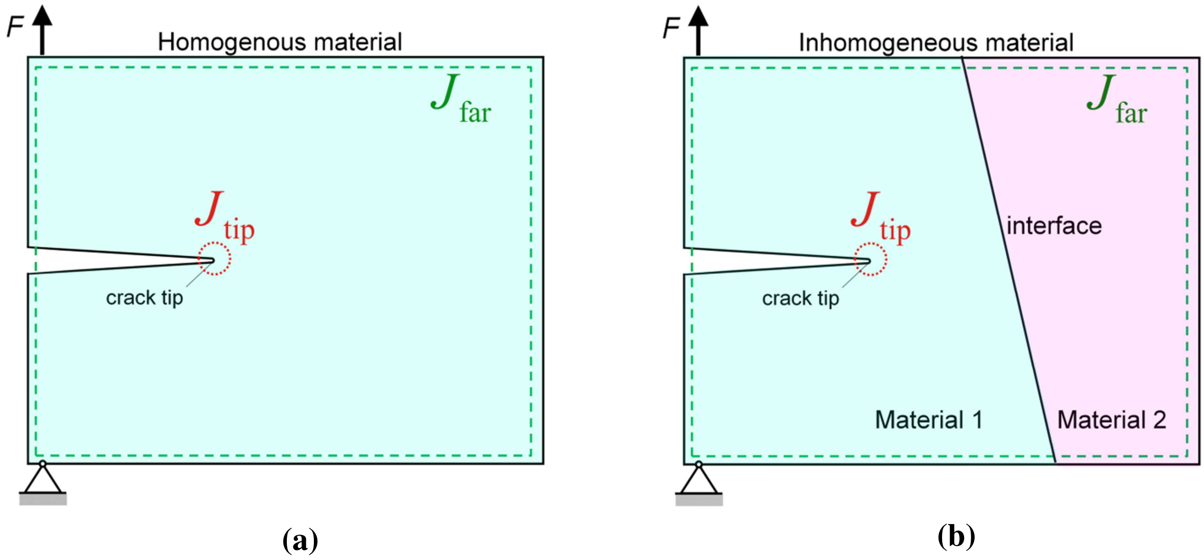

Fig. 3.8 **(a)** In a homogeneous material with a crack, $J_{\text{tip}} = J_{\text{far}}$. **(b)** In a bimaterial body containing a crack and a sharp interface, $J_{\text{tip}} \neq J_{\text{far}}$. In this case, the crack driving force J_{tip} is a function of the properties of Materials 1 and 2, the crack length, the distance between crack tip and interface and the load.

properties is piecewise continuous and differentiable. When a crack lying in the elastically weaker material approaches a bimaterial interface to a stiffer material, the (local) stress intensity decreases and reaches zero directly at the interface. For a crack in the stiffer material, the stress intensity increases to infinity at the interface. A variation of the Poisson's ratio has approximately no effect.

A large number of numerical studies have been performed for evaluating the crack driving force in many types of inhomogeneous materials, see e.g. Delfin et al. (1995), Sugimura et al. (1995), Kim et al. (1997), Joyce et al. (2003), Hattiangadi and Siegmund (2004), Prechtel et al. (2011). Various other methods have been proposed for evaluating the crack driving force in inhomogeneous materials (see e.g. Maugin and Epstein 1991, Weichert and Schulz 1993, Miyazaki and Nakagaki 1995).

New insight into the behavior of cracks in inhomogeneous materials has been gained by adopting the concept of configurational forces. This concept, which will be explained in the next section, has proven to be a very efficient tool to determine the crack driving force in inhomogeneous materials, see e.g. Simha et al. (2003, 2005), Kolednik et al. (2011, 2014a). By applying the concept of configurational forces, it has been found that the material inhomogeneity effect can be applied as an innovative and efficient method for designing new fracture-resistant and flaw-tolerant multilayer composites (e.g. Fratzl et al. 2007; Kolednik et al. 2010; Kolednik et al. 2011; Kolednik et al. 2014a); this will be explained in Section 4.5.

4 Configurational forces concept

The theory of configurational forces, which is based on ideas by Eshelby (1951, 1970), provides a convenient method for the quantitative description of the behavior of various types of defects in materials, such as voids, dislocations, cracks, interfaces or phase boundaries (e.g. Maugin 1995, Gurtin 2000). Configurational forces are thermodynamic forces that are responsible for the motion of defects in materials, e.g. crack growth. The concept of configurational forces has been frequently applied in the fields of fracture mechanics (see e.g. Maugin and Trimarco 1992, Gurtin and Podio-Guidugli 1996, Honein and Herrmann 1997, Steinmann 2000, Gross et al. 2003, Simha et al. 2003, Kolednik et al. 2005, Simha et al. 2008, Kolednik et al. 2009, Kolednik et al. 2010, Fischer et al. 2012a,b, Kolednik et al. 2014a,b, Fischer et al. 2014, Sistaninia and Kolednik 2014). The significant advantage of this concept is that it enables the derivation of driving forces on defects in materials without making any assumptions about the constitutive nature of the material. The purpose of this chapter is to present a brief introduction to the concept of configurational forces. For general information on the topic the reader is referred to books and articles, e.g., by Gurtin (1995), Maugin (1995), Gurtin (2000), Kienzler and Herrmann (2000), Maugin (2011).

4.1 Initial motivation

A configurational force at a defect appears, if the total energy of the system varies for different positions of the defect in the material. According to the second law of thermodynamics, the driving force tries to move a defect in such a way that the total potential energy of the system decreases (see Fig. 4.1). Driving forces are formulated with respect to a motion of the defect in the reference configuration (Gurtin 1995; Gurtin 2000). Crack growth is defined as the movement of the crack tip from one material point to another in the reference configuration.

4.1.1 Derivation of Eshelby's tensor

The basic idea of the configurational forces concept was introduced by Eshelby (1951). His objective was to quantify the change in energy in a body due to the change in position of a defect. As the idea is essential to understand the relevance of this theory to investigate fracture, the derivation proposed by Eshelby is recalled here. The derivation was proposed for small strain, and the extension of the theory to large strain was proposed in (Eshelby 1975).

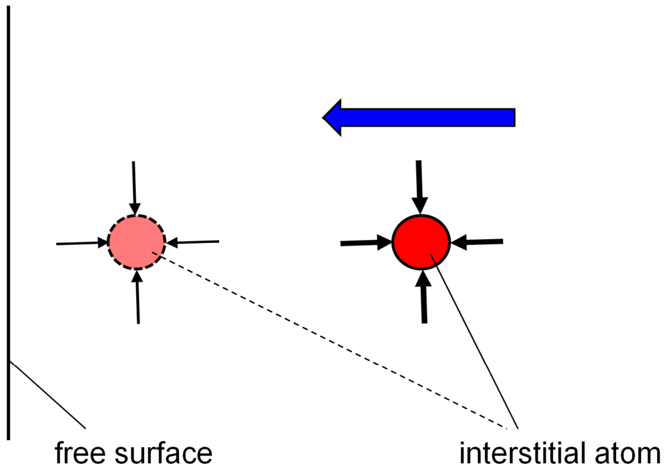

Fig. 4.1 A configurational force at a defect (e.g. an interstitial atom) arises, if the total potential energy of the system varies for different positions of the defect in the material.

The derivation is explained in Fig. 4.2. Consider a body in a given reference configuration, which contains a crack, as shown in Fig. 4.2a. Under loading, the body deforms as shown in Fig. 4.2b. We focus on the calculation of the change in potential energy induced by the crack extension Δa in the reference configuration. In this way, based on the principle of virtual work, we should slightly move the crack tip in material and find out how the potential energy changes in this virtual material motion. Following Eshelby, an arbitrary contour Γ_0 surrounding the crack tip is considered before the motion occurs (Fig. 4.2a). Similarly, consider a replica of the body with another contour Γ_0' that surrounds the crack tip as shown in Fig. 4.2a′. The contour Γ_0' is obtained by giving Γ_0 a vector displacement $-\delta\mathbf{U}$ in the undeformed (reference) configuration of the body. The aim is to compute the energy change from this virtual material displacement $-\delta\mathbf{U}$.

First, the difference in the internal energy $\mathcal{E}$ of the contour between the body and its replica should be determined. The strain energy reflects the internal energy. Therefore, the difference in the internal energy can be determined as (see Eshelby 1975),

$$\delta\mathcal{E} = \mathcal{E}(\Gamma_0') - \mathcal{E}(\Gamma_0) = -\delta\mathbf{U}\int_{\Gamma_0} \phi\mathbf{m}\,\mathrm{d}s\,. \tag{4.1}$$

In Eq. (4.1), ϕ is the strain energy density, $\mathrm{d}s$ an increment of the integration path Γ_0, $\mathbf{m}$ the unit normal vector to $\mathrm{d}s$. By following the idea of Eshelby, we consider the following steps:

- In the deformed configuration of Fig. 4.2b, the surface of the contour Γ (deformed counterpart of Γ_0) is cut out and discarded from the body, thus creating the hole Γ. Suitable tractions are applied to the surface of the hole to prevent matter relaxation.

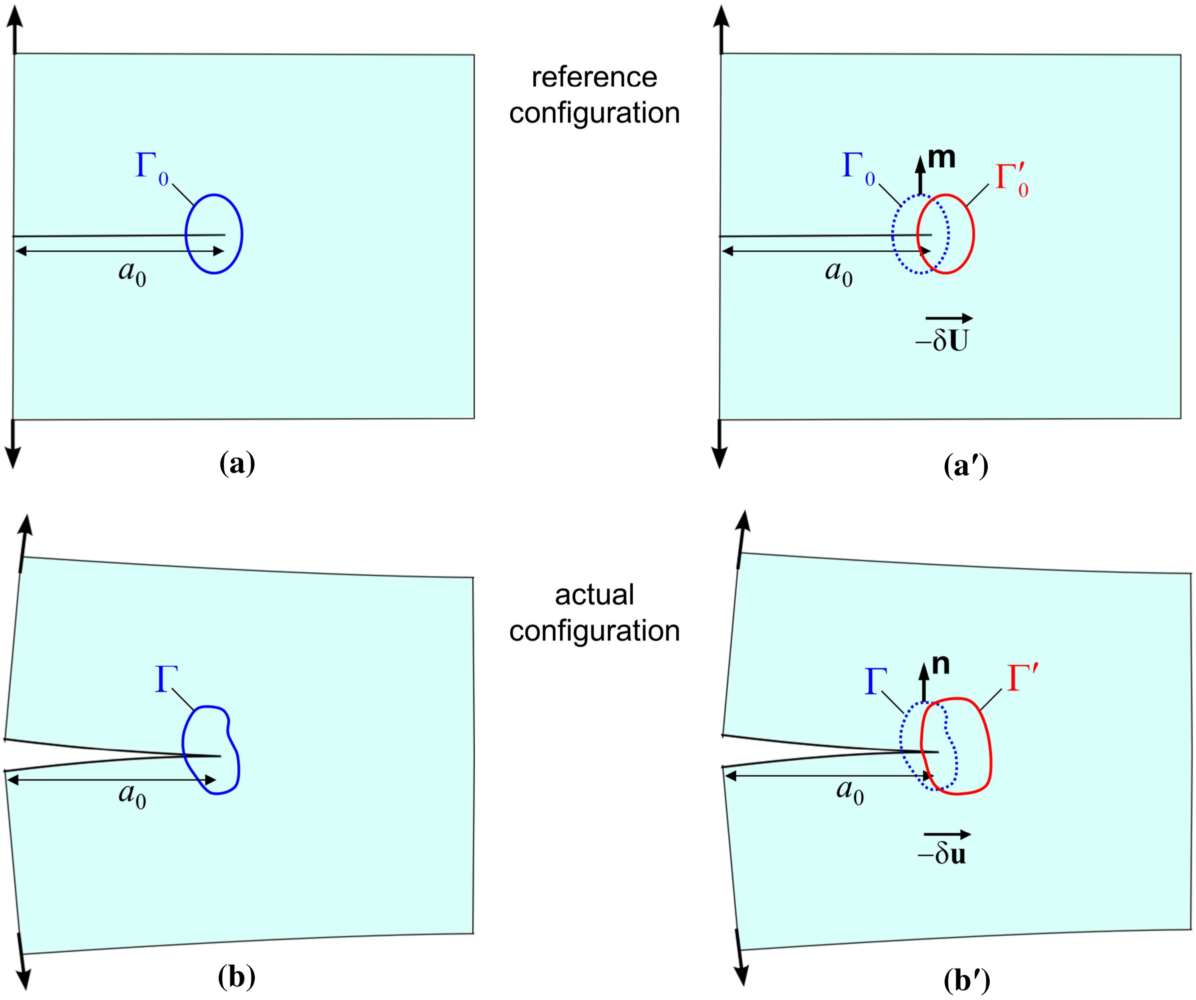

Fig. 4.2 The Eshelby problem.

- A similar procedure is applied to the replica in the deformed configuration of Fig. 4.2b′.
- Finally, the part of the body bounded by the contour Γ' (deformed counterpart of Γ'_0) is fitted into the hole Γ.

Clearly, the deformed surfaces Γ and Γ' do not coincide by a simple translation in the reference configuration. Indeed, the displacement field $\delta\mathbf{u}$ ($\mathbf{u}=\mathbf{x}-\mathbf{X}$, see Section 2.2) must be applied to the surface of the hole to make Γ and Γ' coincident. $\delta\mathbf{u}$ can be related to $\delta\mathrm{U}$ by,

$$\delta\mathbf{u}=-\frac{\partial\mathbf{u}}{\partial\mathbf{X}}\delta\mathrm{U}=-(\mathbf{F}-\mathbf{I})\,\delta\mathrm{U}\,; \tag{4.2}$$

F is the deformation gradient tensor and **I** the identity tensor, see Section 2.2. Applying this displacement field on the boundary of the hole leads to the following amount of work,

$$\delta P=-\int_\Gamma \delta\mathbf{u}.\mathbf{t}\,\mathrm{d}s=-\int_\Gamma \delta\mathbf{u}.\boldsymbol{\sigma}\,\mathbf{n}\,\mathrm{d}s\,, \tag{4.3}$$

where **t** is the surface traction acting on the surface Γ, **σ** the Cauchy stress tensor and **n** the unit normal vector to the contour in the deformed configuration, see Sections 2.1–2.3. By inserting Eq. (4.2) into Eq. (4.3) and considering the relation between **σ** and **S** in Eq. (2.8) (**S** is the first Piola–Kirchhoff stress tensor, see Section 2.3) one can write,

$$\delta P = \delta \mathbf{U}\left(\int_{\Gamma_0} \mathbf{F}^{\mathrm{T}}\,\mathbf{S}\,\mathbf{m}\,\mathrm{d}s - \int_{\Gamma_0} \mathbf{S}\,\mathbf{m}\,\mathrm{d}s\right). \tag{4.4}$$

We are now in the situation where the system is as in the beginning with except that the crack tip has been shifted by the material displacement $+\delta\mathbf{U}$, $\Delta a = \delta\mathbf{U}$. The associated change of potential energy $\delta\mathcal{P}$ is the sum of $\delta\mathcal{E}$ and δP, Eqs. (4.1) and (4.4), respectively, that is

$$\delta\mathcal{P} = -\delta\mathbf{U}.\int_{\Gamma_0} \left(\phi\mathbf{I} - \mathbf{F}^{\mathrm{T}}\mathbf{S}\right)\mathbf{m}\,\mathrm{d}s\,. \tag{4.5}$$

So, the change in energy is completely defined by a tensor, denoted **C** in the following as

$$\mathbf{C} = \phi\mathbf{I} - \mathbf{F}^{\mathrm{T}}\mathbf{S}\ , \tag{4.6}$$

which is referred to as the Eshelby stress tensor or the configurational stress tensor, or also the energy momentum tensor, see Eshelby (1951, 1970, 1975).

4.2 Configurational force framework

In the previous section, the configurational stress tensor was introduced by following the derivation of Eshelby (1951, 1970, 1975). The configurational force framework is now briefly presented. There are three main steps in the derivation of the configurational framework: formulation of (i) balance of deformational forces, (ii) balance of configurational forces, and (iii) dissipation inequality for the body under consideration (Simha et al. 2003; Simha et al. 2008).

4.2.1 Deformational and configurational force balances

In the configurational forces approach two systems of forces are presented: the classical deformational forces that act in the actual configuration, e.g. gravity, and a new system of forces, called configurational forces, which act in the reference configuration. The configurational forces are responsible for kinematic changes in the reference configuration, e.g. the movement of point defects, the propagation of phase boundaries or crack growth. Deformational and configurational force balances can be obtained by considering a body in the current- and reference configuration (Simha et al. 2003).

In the following we apply a simple two-dimensional setting in absence of inertia, heating and body forces. Fig. 4.3a shows a homogeneous body $\mathcal{B}$ with a sharp crack in the reference configuration. The only deformational force acting on $\mathcal{D}$ is the traction force due to the bulk stress **S**, which act on the boundary Γ. Thus, the global balance of the deformational forces reads,

$$\int_{\Gamma} \mathbf{S}\,\mathbf{m}\,\mathrm{d}s = \mathbf{0} \qquad \text{for every subregion } \mathcal{D}, \tag{4.7}$$

see Section 2.4; **m** the unit normal vector to Γ.

Since the bulk stresses can be singular at the crack-tip, we need to be careful in localizing these balance laws. Therefore, the divergence theorem must be modified in order to account for singular stresses at the crack tip: a disk $\mathcal{D}_r$ of radius r centered at the crack tip is removed and then the usual divergence theorem is applied in the domain $\mathcal{D} \backslash \mathcal{D}_r$ where r tends to zero (Fig. 4.3a). After localizing the deformational force balances, one obtains (Simha et al. 2003),

$$\nabla \cdot \mathbf{S} = \mathbf{0} \quad \text{at each point in } \mathcal{D}, \tag{4.8}$$

$$[\![\mathbf{S}]\!]\,\mathbf{p} = \mathbf{0} \quad \text{on the crack flanks,} \tag{4.9}$$

$$\lim_{r \to 0} \int_{\Gamma_r} \mathbf{S}\mathbf{m}\,\mathrm{d}s = \mathbf{0} \quad \text{at the crack tip.} \tag{4.10}$$

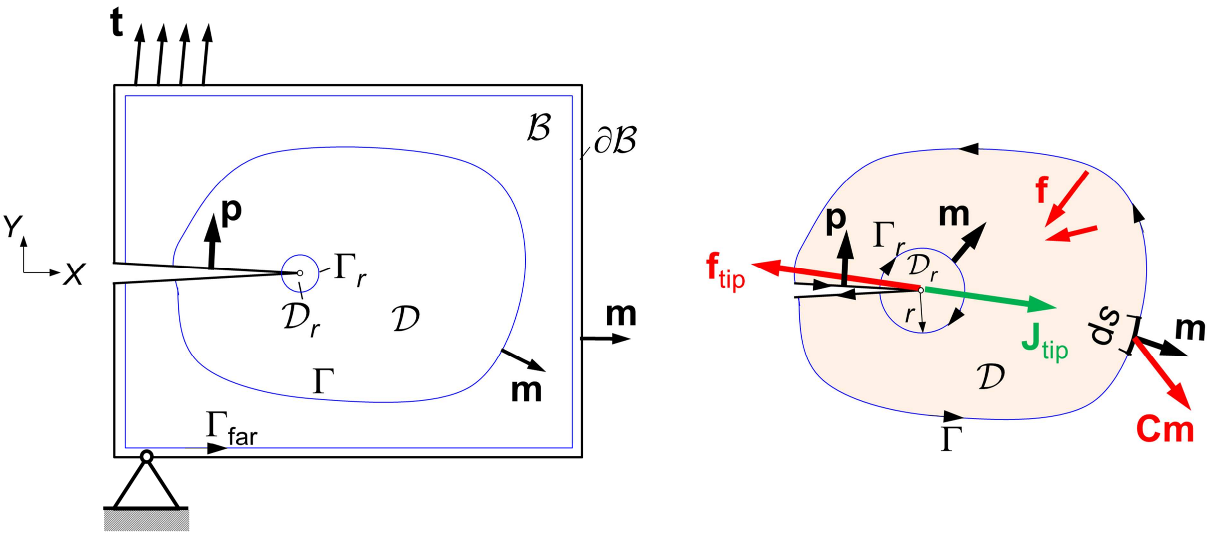

(a) **(b)**

Fig. 4.3 **(a)** Homogeneous body $\mathcal{B}$ with a sharp crack in the reference configuration. The area $\mathcal{D}$ is a part of the body $\mathcal{B}$ that contains the crack tip. Region $\mathcal{D}_r$ of radius r is centered at the crack tip. **p** is the normal vector to the crack flanks. **(b)** Free body diagram for the configurational force system; internal body forces **f** and a driving force $\mathbf{f}_{\mathrm{tip}}$ emanating from the crack tip. The near-tip J-integral vector equals the negative configurational force at the crack tip.

Eq. (4.8) is the translational equilibrium condition of continuum mechanics, see Section 2.4. Eq. (4.9) is trivially satisfied since the crack faces are traction free; $[\![\,]\!]$ denotes the jump of a quantity, **p** is the unit normal to the crack flank (see Fig. 4.3a). Eq. (4.10) describes the limit value of the singular stress field at the crack tip; Γ_r is a contour with radius *r* around the crack tip. It shall be noted that Eqs. (4.8)–(4.10) are satisfied by the stress intensity (*K*-) field of LEFM (Simha et al. 2003).

Fig. 4.3b shows configurational forces **f** acting in an arbitrary region $\mathcal{D}$ containing the crack tip with a driving force $\mathbf{f}_{\text{tip}}$ emanating from the crack tip. The contact force due to the bulk configurational stress **C** acting on the boundary Γ, the body force **f** as well as the force at the crack tip $\mathbf{f}_{\text{tip}}$ (Fig. 4.3b) contribute to the balance of configurational forces (Gurtin 1995; Gurtin 2000; Simha et al. 2003),

$$\int_{\Gamma} \mathbf{C}\mathbf{m}\,\mathrm{d}s + \int_{\mathcal{D}} \mathbf{f}\,\mathrm{d}A + \mathbf{f}_{\text{tip}} = \mathbf{0} \qquad \text{for every subregion } \mathcal{D}. \tag{4.11}$$

As explained in Section 4.1.1, **C** is the bulk configurational stress or Eshelby tensor, compare Eq. (4.6). The configurational traction force $\mathbf{Cm}$ acts on Γ, analogously to the traction stress in the deformational force system.

Analogously to Eqs. (4.8)–(4.10), the following equations can be derived for the configurational force system (e.g. Simha et al. 2003):

$$\nabla\cdot\mathbf{C} + \mathbf{f} = \mathbf{0} \quad \text{at each point in } \mathcal{D}, \tag{4.12}$$

$$[\![\mathbf{C}]\!]\mathbf{p} = \mathbf{0} \quad \text{on the crack flanks}, \tag{4.13}$$

$$\lim_{r\to 0}\int_{\Gamma_r} \mathbf{C}\mathbf{m}\,\mathrm{d}s + \mathbf{f}_{\text{tip}} = \mathbf{0} \quad \text{at the crack tip.} \tag{4.14}$$

From Eqs. (4.12) and (4.14) we can define the configurational forces in the bulk and at the crack tip, $\mathbf{f}$ and $\mathbf{f}_{\text{tip}}$, respectively.

By inserting the configurational stress **C** from Eq. (4.6) into Eqs. (4.12) and (4.14), the configurational forces in the bulk and at the crack tip, $\mathbf{f}$ and $\mathbf{f}_{\text{tip}}$, can be expressed in the forms, see Simha et al. (2003), as

$$\mathbf{f} = -\nabla\cdot\mathbf{C} = -\nabla\cdot\left(\phi\mathbf{I} - \mathbf{F}^{\mathrm{T}}\mathbf{S}\right), \tag{4.15}$$

$$\mathbf{f}_{\text{tip}} = -\lim_{r\to 0}\int_{\Gamma_r}\left(\phi\mathbf{I} - \mathbf{F}^{\mathrm{T}}\mathbf{S}\right)\mathbf{m}\,\mathrm{d}s\,. \tag{4.16}$$

Eqs. (4.15) and (4.16) show that a configurational force $\mathbf{f}$ appears in the body where the divergence of the configurational stress tensor **C** does not vanish, which is at the position of a defect. The vector **f** determines magnitude and direction of the driving force on a defect, e.g. $\mathbf{f}_{\text{tip}}$ for the crack tip.

As one can observe, the derivation of **C,** and consequently of $\mathbf{f}$ and $\mathbf{f}_{\text{tip}}$, has been done without any assumption regarding the constitutive nature of the material. Therefore, the derivations of Eqs. (4.15) and (4.16) are valid for real elastic–plastic (e–p) materials (Gurtin 1995; Simha et al. 2008; Kolednik et al. 2014b).

4.3 Configurational forces and J-integrals

4.3.1 Definition of the crack driving force

The dissipation inequality for a cracked body leads to the definition of the crack driving force, see (Simha et al. 2003). The total dissipation $\Psi(\mathcal{D})$ in any part of the body $\mathcal{D}$ containing the crack tip, see Fig. 4.3a, is given by (Gurtin and Podio-Guidugli 1996),

$$\Psi(\mathcal{D}) = \Psi_{\text{bulk}} + \Psi_{\text{tip}} = \int_{\mathcal{D}} \left(\mathbf{S} \cdot \dot{\mathbf{F}} - \dot{\phi}\right) \mathrm{d}A + \left(-\mathbf{f}_{\text{tip}}\right) \cdot \mathbf{v}_{\text{tip}} \geq 0 . \tag{4.17}$$

$\dot{\mathbf{F}}$ denotes the time derivative of **F** (at fixed points in the reference configuration) and $\mathbf{v}_{\text{tip}}$ is the crack tip velocity (in the reference configuration). The total dissipation $\Psi(\mathcal{D})$, Eq. (4.17), is a summation of the dissipation in the bulk, including plastic dissipation, and the dissipation due to the crack tip propagation (in the reference configuration) with the velocity $\mathbf{v}_{\text{tip}}$. The Clausius–Duhem inequality (second law of thermodynamics) requires that the dissipation $\Psi(\mathcal{D})$ be non-negative for every part of the body $\mathcal{D}$.

According to the bulk dissipation inequality at each material point, $\Psi_{\text{bulk}} \geq 0$ (see Eq. (2.22)), a sufficient condition to fulfill $\Psi(\mathcal{D}) \geq 0$ is that the dissipation due to the movement of the crack tip should be non-negative (Simha et al. 2003),

$$\Psi_{\text{tip}} = \left(-\mathbf{f}_{\text{tip}}\right) \cdot \mathbf{v}_{\text{tip}} \geq 0 . \tag{4.18}$$

In the case of $\Psi_{\text{bulk}} = 0$, Eq. (4.18) becomes a necessary condition in order to fulfill $\Psi(\mathcal{D}) \geq 0$, see Eq. (4.17).

Since the crack tip velocity $\mathbf{v}_{\text{tip}}$ can be considered as the rate of an internal variable (which is the position vector of the crack tip), the conjugate force term to $\mathbf{v}_{\text{tip}}$ in the dissipation $\left(-\mathbf{f}_{\text{tip}}\right)$ is identified by common thermodynamic reasoning as the crack driving force (Kolednik et al. 2014b; Simha et al. 2008),

$$\mathbf{J}_{\text{tip}} = \left(-\mathbf{f}_{\text{tip}}\right), \tag{4.19}$$

see Fig. 4.3b. This corresponds to the criterion in Hellen and Blackburn (1975) that the crack grows into the direction of the near-tip *J*-integral vector, $\mathbf{J}_{\text{tip}}$.

In order to get the common scalar J-integral, the J-integral vector must be projected into the nominal crack growth direction $\mathbf{e} = \mathbf{v}_{\mathrm{tip}} / |\mathbf{v}_{\mathrm{tip}}|$. The near-tip J-integral J_{tip} by Rice (1968b,c), see Section 3.5, is expressed by the relation (Simha et al. 2003)

$$J_{\mathrm{tip}} = \mathbf{e} \cdot \mathbf{J}_{\mathrm{tip}} = \mathbf{e} \cdot \lim_{r \to 0} \int_{\Gamma_r} \left(\phi \mathbf{I} - \mathbf{F}^{\mathrm{T}} \mathbf{S} \right) \mathbf{m} \, \mathrm{d}s \,. \tag{4.20}$$

The configurational force balance for a region, which does not contain the crack tip, is used to relate the near-tip and far-field J-integrals. Consider the region $\mathcal{D} \setminus \mathcal{D}_r$ between the contours Γ and Γ_r (Fig. 4.3b). This region does not include the crack tip. Furthermore, no forces acting on the crack flanks are assumed. Thus only the configurational body force and contact forces act on this region, so the statement of configurational force balance for region $\mathcal{D}$ reads as

$$\int_{\mathcal{D} \setminus \mathcal{D}_r} \mathbf{f} \, \mathrm{d}A + \int_{\Gamma} \mathbf{C} \mathbf{m} \, \mathrm{d}s + \int_{\Gamma_r} \mathbf{C}(-\mathbf{m}) \, \mathrm{d}s = \mathbf{0} \,. \tag{4.21}$$

For a detailed discussion see Simha et al. (2008). Since $\mathcal{D}_r$ and Γ_r tend to zero, the balance can be written in the form

$$\lim_{r \to 0} \int_{\Gamma_r} \mathbf{C} \mathbf{m} \, \mathrm{d}s - \int_{\Gamma} \mathbf{C} \mathbf{m} \, \mathrm{d}s = \int_{\mathcal{D} \setminus \mathcal{D}_r} \mathbf{f} \, \mathrm{d}A \,. \tag{4.22}$$

The scalar product of this equation with **e** yields (Simha et al. 2008)

$$J_{\mathrm{tip}} - J_{\Gamma} = \mathbf{e} \cdot \int_{\mathcal{D} \setminus \mathcal{D}_r} \mathbf{f} \, \mathrm{d}A \,, \tag{4.23}$$

with

$$J_{\Gamma} = \mathbf{e} \cdot \int_{\Gamma} \left(\phi \mathbf{I} - \mathbf{F}^{\mathrm{T}} \mathbf{S} \right) \mathbf{m} \, \mathrm{d}s \,. \tag{4.24}$$

Let us Γ becoming a contour adjacent to the external boundary of the cracked body, Fig. 4.3a, then the far-field J-integral J_{far} can be determined as

$$J_{\mathrm{far}} = \mathbf{e} \cdot \mathbf{J}_{\mathrm{far}} = \mathbf{e} \cdot \int_{\Gamma_{\mathrm{far}}} \left(\phi \mathbf{I} - \mathbf{F}^{\mathrm{T}} \mathbf{S} \right) \mathbf{m} \, \mathrm{d}s \,. \tag{4.25}$$

The physical meaning of J_{far} is that of the driving force inserted into the body by the applied load (Simha et al. 2008; Sistaninia and Kolednik 2014). Considering the contour Γ_{far} in Eq. (4.23) leads to

$$J_{\mathrm{tip}} - J_{\mathrm{far}} = \mathbf{e} \cdot \int_{\mathcal{B} \setminus \mathrm{tip}} \mathbf{f} \, \mathrm{d}A \,. \tag{4.26}$$

The right hand side of Eq. (4.26) can be used, e.g., to evaluate the influence of plasticity on the crack driving force, see Simha et al. (2008). If the right hand side of Eq. (4.26) is zero, then the configurational body force vanishes and Eq. (4.26) implies the path-independence of the *J*-integral, $J_{\text{tip}} = J_{\text{far}}$. In contrast, when the right hand side of Eq. (4.26) is non-zero, the *J*-integral becomes path dependent, $J_{\text{tip}} \neq J_{\text{far}}$.

4.3.2 Numerical implementation of configurational forces into finite elements

Here the numerical computation of configurational forces by the finite element method (FEM) is briefly discussed. For general information on this topic the reader is referred to the literature, e.g. see Müller et al. (2002), Müller and Maugin (2002), Denzer et al. (2003), Müller et al. (2004).

In the following we consider homogeneous bodies without body forces. In order to compute discrete configurational forces, a weak formulation is presented that is consistent with the implementation of the standard forces. Multiplying the balance law in Eq. (4.12) with a vectorial test function $\boldsymbol{\eta}$ and integrating over the domain $\mathcal{B}$ gives, see Müller et al. (2002) or Müller and Maugin (2002),

$$\int_{\mathcal{B}} (\nabla \cdot \mathbf{C} + \mathbf{f}) \boldsymbol{\eta} \, \mathrm{d}V = 0 . \tag{4.27}$$

By integrating by parts, Eq. (4.27) can be transformed to (Müller and Maugin 2002),

$$-\int_{\mathcal{B}} (\mathbf{C} \cdot D(\boldsymbol{\eta})) \mathrm{d}V + \int_{\mathcal{B}} (\mathbf{f} \cdot \boldsymbol{\eta}) \mathrm{d}V = 0 , \tag{4.28}$$

where $D(\boldsymbol{\eta})$ denotes the derivative of the test function $\boldsymbol{\eta}$. As usual in the FE method, an element-wise interpolation of the test function $\boldsymbol{\eta}$ is introduced,

$$\boldsymbol{\eta} = \sum_{\mathrm{I}} \mathbf{N}^{\mathrm{I}} \boldsymbol{\eta}^{\mathrm{I}} , \tag{4.29}$$

where $\boldsymbol{\eta}^{\mathrm{I}}$ are the nodal values of the test function and $\mathbf{N}^{\mathrm{I}}$ are the shape functions corresponding to the node I. The derivative of the test function $\boldsymbol{\eta}$ is introduced as

$$D(\boldsymbol{\eta}) = \sum_{\mathrm{I}} D(\mathbf{N}^{\mathrm{I}}) \boldsymbol{\eta}^{\mathrm{I}} , \tag{4.30}$$

where $D(\mathbf{N}^{\mathrm{I}})$ denotes the derivative of the element shape functions $\mathbf{N}^{\mathrm{I}}$. Using Eqs. (4.29) and (4.30), Eq. (4.28) can be evaluated for each element of area $V^{(e)}$ as,

$$\sum_{\mathrm{I}} \left[\int_{V^{(e)}} \left(\mathbf{C} \cdot D(\mathbf{N}^{\mathrm{I}}) - \mathbf{N}^{\mathrm{I}} \mathbf{f} \right) \mathrm{d}V \right] \boldsymbol{\eta}^{\mathrm{I}} = 0 . \tag{4.31}$$

As Eq. (4.31) must be true for all values of the test function $\boldsymbol{\eta}^{\mathrm{I}}$ the term in the brackets has to be zero, which defines the *nodal* configurational force **f**-vector, $\mathbf{f}^{\mathrm{I}}$,

$$\mathbf{f}^{\mathrm{I}} = \int_{V^{(e)}} \mathbf{C} \cdot D\left(\mathbf{N}^{\mathrm{I}}\right) \mathrm{d}V , \tag{4.32}$$

where the integration is performed numerically using a Gauß quadrature, under consideration of $\mathrm{d}V = B\,\mathrm{d}A$; B is the element thickness.

Once the stresses and displacements are known from the FE analysis, the configurational stress tensor **C** can readily be computed for each integration point in the FE-mesh. Here, it should be remarked that the deformation gradient tensor **F** needs to be calculated from Eq. (2.4), since **F** is not provided by most of commercial FE packages, and the first Piola–Kirchhoff stresses **S** should be determined from the Cauchy stresses $\boldsymbol{\sigma}$ according to Eq. (2.8). Then, the nodal configurational force $\mathbf{f}^{\mathrm{I}}$ is evaluated for each integration point of a single element *e* by Eq. (4.32). Finally, the configurational forces $\mathbf{f}^{\mathrm{I}}$ of all elements adjacent to one node *n* need to be summed up to get the resulting **f**-vector at this node (Müller et al. 2002; Müller and Maugin 2002),

$$\mathbf{f}^{(n)} = \sum_{\mathrm{I} \in n} \mathbf{f}^{\mathrm{I}} . \tag{4.33}$$

In this thesis, the configurational forces, and the resulting *J*-integrals, are computed by a post-processing routine after a conventional finite element (FE) stress and strain analysis. For the FE program, the commercial software ABAQUS/Standard (see http://www.simulia.com/products/abaqus_ fea.html) is used. The post-processing routine is written in the scripting language of ABAQUS, Python programming language, based on Müller et al. (2002, 2004) and Denzer et al. (2003). After stress and strain analysis the configurational force **f**-vector is computed for all nodes in the body by Eq. (4.33). Fig. 4.4 shows, for example, the distribution of the configurational force vectors, computed for all nodes by Eq. (4.33), in a square plate with a circular hole. The side length of the plate is 10 mm and the diameter of the hole 4 mm. The plate is loaded by a vertical displacement of 5 mm at the upper boundary, and the lower boundary is fixed.

Here it shall be also outlined how the scalar *J*-integral is determined after the configurational force computations. The scalar *J*-integral can be evaluated on specific contours Γ around the crack tip, by a summation of configurational forces emanating from all nodes that lie within the area $\mathcal{D}$ bounded by the contour Γ, see Eq. (4.24),

$$J_{\Gamma} = \sum_{\text{nodes within}\,\Gamma} -\left(\mathbf{e} \cdot \mathbf{f}^{(n)}\right) \Delta A_{n} . \tag{4.34}$$

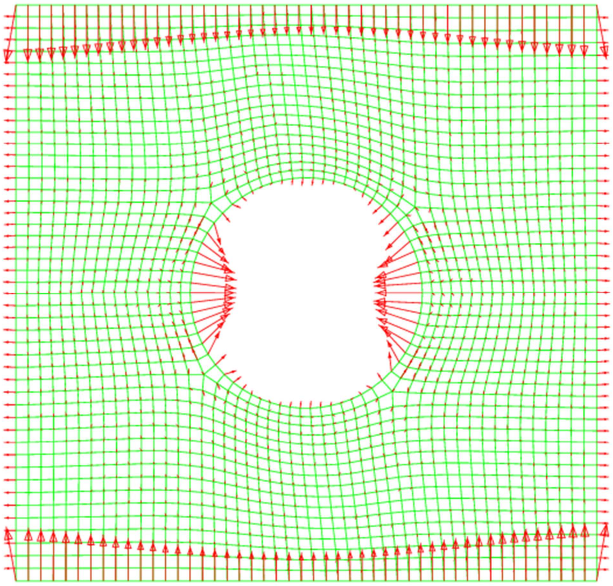

Fig. 4.4 Distribution of the configurational force **f**-vectors in a square plate with a circular hole (Shan 2005).

In Eq. (4.34), the quantity ΔA_n is the element area corresponding to a certain node *n*. Since the magnitude of the $\mathbf{f}$-vector at one node is a contribution from all elements adjacent to that node, the integration contour Γ always crosses the middle of the elements (Kolednik et al. 2014b).

In our post-processing the configurational forces are computed for deformation plasticity $\mathbf{f}^{\text{def.pl}}$ and for incremental plasticity $\mathbf{f}^{\text{ep}}$; in the next section we explain both.

4.4 Configurational forces and J-integrals in elastic–plastic materials

The great advantage of the configurational force concept is that it enables the derivation of the *J*-integral without restrictions regarding the constitutive relations of the material. Therefore, the configurational force concept can provide an actual thermodynamic driving force term in elastic–plastic materials with *incremental theory of plasticity*, since the second law of thermodynamics has been invoked in the derivation (Simha et al. 2008). This is in contrast to the classical *J*-integral which is based on *deformation theory of plasticity*, see Section 3.5. The derivation of the *J*-integral in elastic–plastic materials with incremental theory of plasticity becomes important as soon as the conditions of proportional loading are violated. The nonlinear elastic and the elastic–plastic body exhibit different stress–strain and load–displacement curves, see Section 2.6.

First, assume that body $\mathcal{B}$, Fig. 4.5a, consists of an elastic–plastic material described with deformation theory of plasticity. The total strain energy density ϕ is reversible in this case.

The configurational force at a material point for deformation plasticity can be determined from Eq. (4.15) as

$$\mathbf{f}^{\mathrm{nlel}} = -\nabla \cdot \mathbf{C} = -\nabla \cdot \left(\phi \mathbf{I} - \mathbf{F}^{\mathrm{T}} \mathbf{S} \right). \tag{4.35}$$

Now let us to determine the scalar *J*-integral for the desired contour Γ in Fig. 4.5a. Eqs. (4.23) and (4.35) provide the scalar *J*-integral for the desired contour Γ for deformation plasticity, $J_{\Gamma}^{\mathrm{nlel}}$,

$$J_{\Gamma}^{\mathrm{nlel}} = -\mathbf{e} \cdot \left(\mathbf{f}_{\mathrm{tip}}^{\mathrm{nlel}} + \int_{\mathcal{D}\setminus\mathrm{tip}} \mathbf{f}^{\mathrm{nlel}} \, \mathrm{d}A \right) = J_{\mathrm{tip}}^{\mathrm{nlel}} + \mathbf{e} \cdot \int_{\mathcal{D}\setminus\mathrm{tip}} \nabla \cdot \left(\phi \mathbf{I} - \mathbf{F}^{\mathrm{T}} \mathbf{S} \right) \mathrm{d}A \,, \tag{4.36}$$

where $\mathcal{D}$ is the region inside the contour Γ, and the region $\mathcal{D}\setminus\mathrm{tip}$ does not include the crack tip. The non-linear elastic *J*-integral deduced from configurational forces $J_{\Gamma}^{\mathrm{nlel}}$ is identical to the conventional *J*-integral derived by Rice (1968b,c), Section 3.5.

In an elastic–plastic material, described with deformation theory of plasticity, the bulk dissipation is equal to zero, $\Psi_{\mathrm{bulk}}(\mathcal{B}) = 0$, see Section 2.6. Therefore, the crack tip is the single source of dissipation, and bulk configurational forces do not exist, $\mathbf{f}^{\mathrm{nlel}} = \mathbf{0}$. Only a single configurational force emerges from the crack tip $\mathbf{f}_{\mathrm{tip}}^{\mathrm{nlel}}$ (Fig. 4.5a). It should be remarked that the bulk configurational forces appear in a small region around the crack tip due to the discretization problem. Consequently, the non-linear elastic *J*-integral is path-independent, $J_{\mathrm{tip}}^{\mathrm{nlel}} = J_{\Gamma}^{\mathrm{nlel}} = J_{\mathrm{far}}^{\mathrm{nlel}}$ (Simha et al. 2008; Kolednik et al. 2014b). As it will be discussed later, this is not so for incremental plasticity; in this case, the magnitude of the *J*-integral J_{Γ} and its path dependence are intimately connected to the configurational force distribution in the body.

It should be noted that, as soon as the conditions of proportional loading are disturbed, e.g. for cyclic loading or crack extension, the bulk configurational forces appear in the body, which do not have any physical meaning. As it was shown in (Kolednik et al. 2014b), the bulk configurational forces for deformation plasticity appear on positions with a gradient in plastic strain; the bulk configurational force is proportional to the gradient of the plastic strain, see Simha et al. (2008).

Now let us to assume that $\mathcal{B}$ consists of an elastic–plastic material described with incremental theory of plasticity. Then incremental theory of plasticity is required for a realistic modeling of the behavior of elastic–plastic materials. Only the elastic part of the strain energy density ϕ_{el} is recoverable in a real, elastic–plastic material. Therefore, the elastic part of the strain energy density ϕ_{el} is considered in Eq. (4.15) for the determination of the configurational force at a material point, yielding

$$\mathbf{f}^{\mathrm{ep}} = -\nabla \cdot \mathbf{C} = -\nabla \cdot \left(\phi_{\mathrm{el}} \mathbf{I} - \mathbf{F}^{\mathrm{T}} \mathbf{S} \right). \tag{4.37}$$

The scalar J-integral for a desired contour Γ based on incremental plasticity, J_{Γ}^{ep}, can be evaluated from Eqs. (4.23), where ϕ_{el} is considered instead of ϕ, and (4.37),

$$J_{\Gamma}^{\mathrm{ep}} = -\mathbf{e} \cdot \left(\mathbf{f}_{\mathrm{tip}}^{\mathrm{ep}} + \int_{\mathcal{D} \setminus \mathrm{tip}} \mathbf{f}^{\mathrm{ep}} \, \mathrm{d}A \right) = J_{\mathrm{tip}}^{\mathrm{ep}} + \mathbf{e} \cdot \int_{\mathcal{D} \setminus \mathrm{tip}} \nabla \cdot \left(\phi_{\mathrm{el}} \mathbf{I} - \mathbf{F}^{\mathrm{T}} \mathbf{S} \right) \mathrm{d}A \,. \tag{4.38}$$

When an elastic–plastic material is modeled with incremental theory of plasticity, the bulk dissipation is non-zero, $\Psi_{\mathrm{bulk}} \left(\mathcal{B} \right) \neq 0$. Therefore, the crack tip is not the single source of dissipation, and bulk configurational forces appear in the plastically deformed regions of the material, $\mathbf{f}^{\mathrm{ep}} \neq 0$, see Fig. 4.5b. Consequently, the elastic–plastic J-integral J^{ep} is path-dependent, $J_{\mathrm{tip}}^{\mathrm{ep}} \neq J_{\Gamma}^{\mathrm{ep}} \neq J_{\mathrm{far}}^{\mathrm{ep}}$ (Simha et al. 2008; Kolednik et al. 2014b). In this case, the magnitude of the J-integral J_{Γ}^{ep} is connected to the configurational force distribution in the

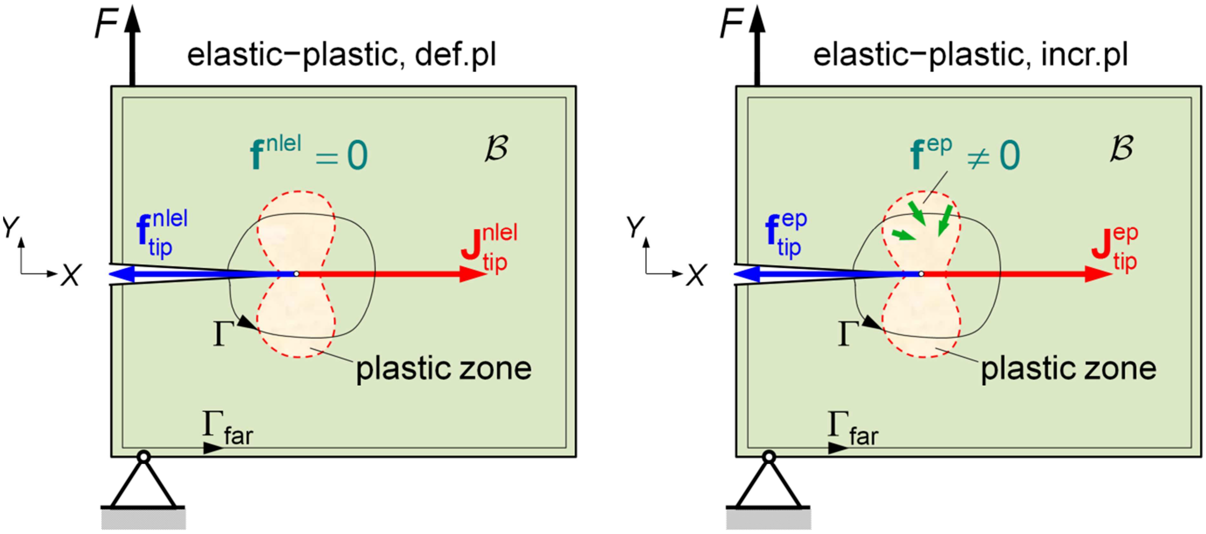

(a) **(b)**

Fig. 4.5 Homogeneous body made of an elastic–plastic material. **(a)** elastic–plastic material described with deformation plasticity (def.pl). In this case no bulk configurational forces exist in the body, $\mathbf{f}^{\mathrm{nlel}} = 0$, the non-linear elastic J-integral is path-independent, $J_{\mathrm{tip}}^{\mathrm{nlel}} = J_{\Gamma}^{\mathrm{nlel}} = J_{\mathrm{far}}^{\mathrm{nlel}}$. **(b)** elastic–plastic material described with incremental plasticity (incr.pl). In this case, bulk configurational forces appear in the body, $\mathbf{f}^{\mathrm{ep}} \neq 0$. The path dependence of the J-integrals, J_{Γ}^{ep}, is connected to the appearance of configurational forces in the body: if the integration contour Γ increases from the crack tip, more and more configurational forces become included, so that the magnitude of the J-integral changes.

body. If the integration contour Γ increases with deviating from the crack tip, more and more contributions by configurational forces become included, so that the magnitude of the J-integral J_{Γ}^{ep} changes, see Fig. 4.5b.

In order to show how the crack driving force should be correctly evaluated for an elastic–plastic material modeled with incremental theory of plasticity, an example is presented here. Fig. 4.6a shows the spatial distribution of plasticity for the compact tension (CT) specimen with a stationary crack after loading to a load-line displacement $v_{\mathrm{LL}} = 0.1$ mm (under lsy condition). Figure 4.6b shows the distribution of incremental plasticity configurational forces $\mathbf{f}^{\mathrm{ep}}$ in the crack tip plastic zone and the back face region. Note that in Fig. 4.6b two inclined partial configurational forces appear on the crack tip node due to the coinciding master and slave nodes of the lower and upper specimen half. The resulting configurational force vector at the crack tip, $\mathbf{f}_{\mathrm{tip}}^{\mathrm{ep}}$, is the sum of the two partial configurational forces and has only an x-component. Note that only the x-component of the configurational force vectors, i.e. the components along crack growth direction $\mathbf{e}$, contribute to the scalar J-integral. The $\mathbf{f}^{\mathrm{ep}}$ vectors point into the direction of the gradient of the plastic equivalent strain, see (Kolednik et al. 2014b). The far-field J-integral $J_{\mathrm{far}}^{\mathrm{ep}}$, which measures the driving force induced by the applied loads into the specimen, is the summation of all configurational forces over the whole body. Indeed, $J_{\mathrm{far}}^{\mathrm{ep}}$ is calculated by the summation of configurational forces along the rectangular contour Γ_{far} (see Fig. 4.6a). The crack driving force is explained below.

The J-integral describes the driving force for the simultaneous translational movement of all defects enclosed by the integration contour Γ (Kolednik et al. 2014b). The physical meaning of the near-tip J-integral $J_{\mathrm{tip}}^{\mathrm{ep}}$ is that of the driving force for the movement of the crack tip. However, in an elastic–plastic material, it is impossible that crack extension occurs without simultaneous movement of the plastic zone around the crack tip (Fig. 4.6a). The J-integral $J_{\mathrm{PZ}}^{\mathrm{ep}}$ as the J-integral for an integration path Γ_{PZ} encloses the crack tip and the crack tip plastic zone (Fig. 4.6a), has consequently the physical meaning of the driving force for the common movement of the crack tip plus the crack tip plastic zone. Thus, $J_{\mathrm{PZ}}^{\mathrm{ep}}$ is the appropriate driving force parameter for a stationary crack in an elastic–plastic material (Kolednik et al. 2014b). It should be mentioned that the J-integrals J^{nlel} and J^{ep} on the path Γ_{PZ} (see Fig. 4.6a), are approximately equal in magnitude, $J_{\mathrm{PZ}}^{\mathrm{ep}} \approx J_{\mathrm{PZ}}^{\mathrm{nlel}} = J^{(\mathrm{exp})}$, and they reflect the value of the experimental J-integral, Eq. (3.11), see (Kolednik et al. 2014b).

The physical meaning of the driving force for crack growth and cycling loading has been presented in detail in (Ochensberger 2015; Ochensberger and Kolednik 2014; Ochensberger and Kolednik 2015).

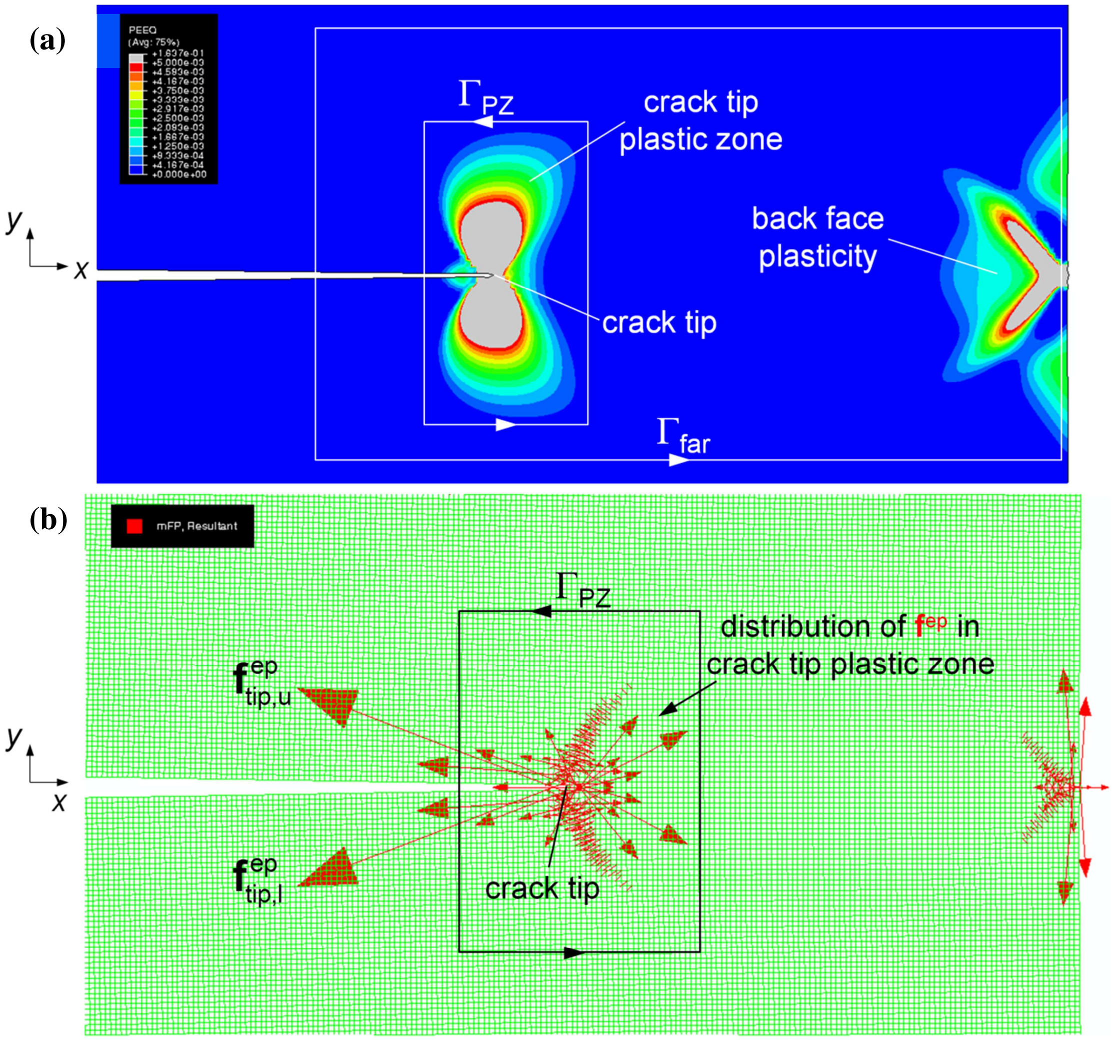

Fig. 4.6 Elastic–plastic C(T)-specimen described with incremental theory of plasticity. **(a)** Distribution of the accumulated plastic strain PEEQ at $v_{LL} = 0.1$ mm (large-scale yielding). Γ_{PZ} and Γ_{far} denote the crack tip plastic zone and far-field *J*-integral contours. **(b)** Distribution of the incremental plasticity configurational forces $\mathbf{f}^{ep}$ in the crack tip plastic zone. The configurational force at the crack tip $\mathbf{f}^{ep}_{tip}$ is the vector sum of the two partial configurational forces $\mathbf{f}^{ep}_{tip,u}$ and $\mathbf{f}^{ep}_{tip,l}$ of the upper and lower specimen half.

4.5 *Configurational forces and J-integrals in inhomogeneous materials*

The purpose of this section is to present the configurational forces in inhomogeneous materials, and to elucidate how the *J*-integral for inhomogeneous materials has been derived by Simha et al. (2003, 2005).

Configurational forces have been proven to be very useful to analyze the behavior of cracks in inhomogeneous materials. The configurational force concept treats a *material inhomogeneity* also like a defect. For inhomogeneous materials, configurational forces $\mathbf{f}_{\Sigma}$ are induced along the interface Σ where the material properties exhibit a change. These configurational forces $\mathbf{f}_\Sigma$ can be used to evaluate a “material inhomogeneity term” which enables an explanation of the effect of inhomogeneities on the crack driving force; the details are given in the following.

The balance laws for the configurational forces within a body in the reference configuration provide all the relations relevant for studying cracks in inhomogeneous bodies. Consider the simple setting of a two-dimensional body $\mathcal{B}$ containing a crack in the reference configuration with no heat conduction and no inertia. The body also contains a sharp interface Σ, where the material properties exhibit a jump, with unit normal $\mathbf{n}_\Sigma$ (see Fig. 4.7a).

The average of a quantity **a** across the interface is denoted as $\langle \mathbf{a} \rangle = (\mathbf{a}^+ + \mathbf{a}^-)/2$. The jump of a quantity **a** at the interface is denoted as $[[\mathbf{a}]] = (\mathbf{a}^+ - \mathbf{a}^-)$, where $\mathbf{a}^+$ and $\mathbf{a}^-$ denote the limiting values of the quantity on either side of the interface. The jump of **a**.**b** (the product of quantities **a** and **b**) at the interface is defined as

$$[[\mathbf{a}.\mathbf{b}]] = [[\mathbf{a}]]\langle \mathbf{b} \rangle + \langle \mathbf{a} \rangle [[\mathbf{b}]]. \tag{4.39}$$

The balance of deformational force can be written as Eqs. (4.8)–(4.10), including the following equation (Simha et al. 2005),

$$[[\mathbf{S}]]\mathbf{n}_\Sigma = 0 \quad \text{at the sharp interface } \Sigma, \tag{4.40}$$

where $[[\mathbf{S}]]$ is the jump in **S** at the interface Σ. In other words, the local traction vector at an interface must not show a jump in the static case (no momentum). Analogously to Eq. (4.11), the balance of configurational forces leads to,

$$\int_\Gamma \mathbf{C}\mathbf{m}\, \mathrm{d}s + \int_{\mathcal{D}} \mathbf{f}\, \mathrm{d}A + \int_\Sigma \mathbf{f}_\Sigma\, \mathrm{d}s + \mathbf{f}_{\mathrm{tip}} = \mathbf{0} \quad \text{for every subregion } \mathcal{D}, \tag{4.41}$$

where $\mathbf{f}_\Sigma$ is the configurational force which emerges at the interface Σ, see Fig. 4.7b. Applying Eqs. (4.12)–(4.14), the following equation can be obtained from Eq. (4.41) for the configurational force system (Simha et al. 2003) as

$$[[\mathbf{C}]]\mathbf{n}_\Sigma + \mathbf{f}_\Sigma = 0. \tag{4.42}$$

In Eq. (4.42), $[[\mathbf{C}]]$ denotes the jump in the configurational stress **C** at the interface Σ. By inserting the configurational stress **C**, Eq. (4.6), into Eq. (4.42), the configurational force at the interface Σ can be derived as

$$\mathbf{f}_\Sigma = -[[\phi\mathbf{I} - \mathbf{F}^{\mathrm{T}}\mathbf{S}]]\mathbf{n}_\Sigma = -\left([[\phi]]\mathbf{I} - [[\mathbf{F}^{\mathrm{T}}\mathbf{S}]]\right)\mathbf{n}_\Sigma. \tag{4.43}$$

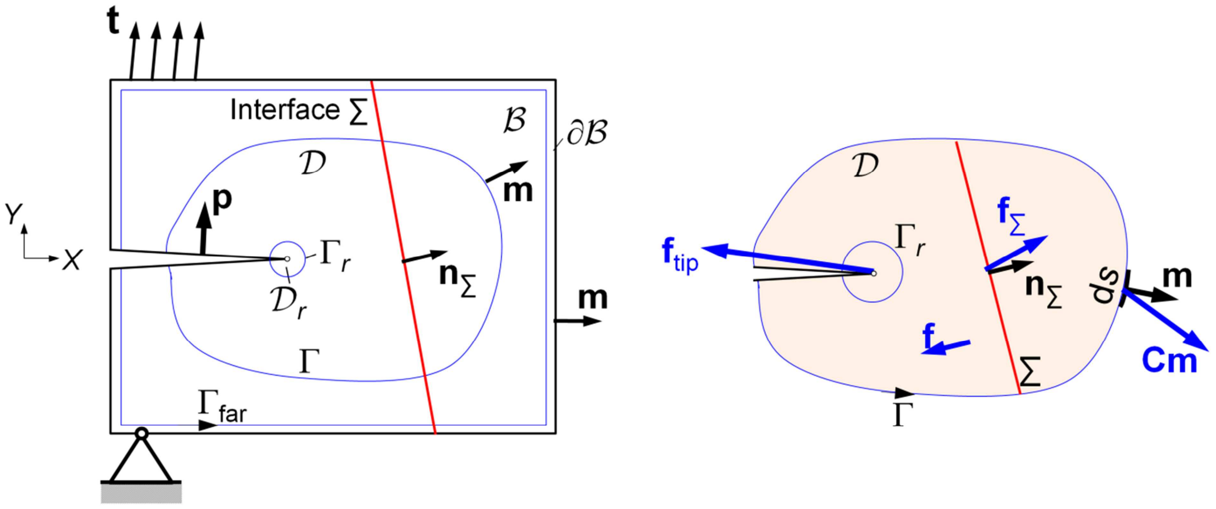

(a) **(b)**

Fig. 4.7 **(a)** A two-dimensional body $\mathcal{B}$ containing a crack and a sharp interface Σ in the reference configuration. The (unit) normal to the interface is $\mathbf{n}_\Sigma$. The direction of crack growth is $\mathbf{e}$. Region $\mathcal{D}_r$ of radius r is centered at the crack tip. **(b)** Configurational forces acting on subregion $\mathcal{D}$.

From the traction continuity in Eq. (4.40) and the identity, Eq. (4.39), one can write

$$[[\mathbf{F}^{\mathrm{T}}\mathbf{S}]]\mathbf{n}_\Sigma = \left([[\mathbf{F}]]^{\mathrm{T}}\langle\mathbf{S}\rangle + \langle\mathbf{F}^{\mathrm{T}}\rangle[[\mathbf{S}]]\right)\mathbf{n}_\Sigma = \left([[\mathbf{F}]]^{\mathrm{T}}\langle\mathbf{S}\rangle\right)\mathbf{n}_\Sigma\,. \tag{4.44}$$

By inserting Eq. (4.44) into Eq. (4.43), the configurational force at the interface Σ can be finally derived as

$$\mathbf{f}_\Sigma = -\left([[\phi]]\mathbf{I} - [[\mathbf{F}]]^{\mathrm{T}}\langle\mathbf{S}\rangle\right)\mathbf{n}_\Sigma\,. \tag{4.45}$$

Therefore, the configurational interface force $\mathbf{f}_\Sigma$ is the negative of the jump of the normal component of the Eshelby tensor $\mathbf{C}$. Now, since the configurational interface force $\mathbf{f}_\Sigma$ is known, the effect of inhomogeneities on the crack driving force can be expressed after rearrangement of the balance of configurational forces.

The configurational force balance for a region, which does not contain the crack tip, is used to relate the near-tip and far-field J-integrals. Consider the region $\mathcal{D}$ between a circle close to the tip $\mathcal{D}_r$ and another contour Γ (Fig. 4.7b). Thus only the configurational body force and the configurational interface force act on this region, so the statement of configurational force balance for region $\mathcal{D}$ reads as (Simha et al. 2005)

$$\int_{\mathcal{D}\setminus\mathcal{D}_r} \mathbf{f}\,\mathrm{d}A + \int_\Sigma \mathbf{f}_\Sigma\,\mathrm{d}s + \int_\Gamma \mathbf{C}\mathbf{m}\,\mathrm{d}s + \int_{\Gamma_r} \mathbf{C}(-\mathbf{m})\,\mathrm{d}s = \mathbf{0}\,. \tag{4.46}$$

Since r tends to zero, the balance can be written as,

$$\lim_{r\to 0}\int_{\Gamma_r}\mathbf{C}\mathbf{m}\,\mathrm{d}s-\int_{\Gamma}\mathbf{C}\mathbf{m}\,\mathrm{d}s=\int_{\mathcal{D}\setminus\mathcal{D}_r}\mathbf{f}\,\mathrm{d}A+\int_{\Sigma}\mathbf{f}_{\Sigma}\,\mathrm{d}s\,. \tag{4.47}$$

The scalar product of this equation with **e** yields,

$$J_{\text{tip}}-J_{\Gamma}=\mathbf{e}\cdot\int_{\mathcal{D}\setminus\mathcal{D}_r}\mathbf{f}\,\mathrm{d}A+\mathbf{e}\cdot\int_{\Sigma}\mathbf{f}_{\Sigma}\,\mathrm{d}s\,. \tag{4.48}$$

If we let Γ become a contour adjacent to the external boundary of the cracked body ($\Gamma=\Gamma_{\text{far}}$), $J_{\Gamma}=J_{\text{far}}$. Then Eq. (4.48) can be rewritten as,

$$J_{\text{tip}}-J_{\text{far}}=\mathbf{e}\cdot\int_{\mathcal{B}\setminus\text{tip}}\mathbf{f}\,\mathrm{d}A+\mathbf{e}\cdot\int_{\Sigma}\mathbf{f}_{\Sigma}\,\mathrm{d}s\,. \tag{4.49}$$

The right hand side of Eq. (4.49) can be used to evaluate the influence of plasticity and inhomogeneities on the crack driving force. If it is assumed that the influence of plasticity vanishes, e.g. in the case of linear elastic or nonlinear elastic materials, Eq. (4.49) is written in the form

$$J_{\text{tip}}=J_{\text{far}}+\mathbf{e}\cdot\int_{\Sigma}\mathbf{f}_{\Sigma}\,\mathrm{d}s\,. \tag{4.50}$$

Finally, from Eq. (4.50), the effect of inhomogeneities on the crack driving force follows with Eq. (4.45) as (Simha et al. 2003; Simha et al. 2005)

$$J_{\text{tip}}=J_{\text{far}}+C_{\text{inh}}\,, \tag{4.51}$$

where

$$C_{\text{inh}}=-\mathbf{e}\cdot\int_{\Sigma}\left([[\phi]]\mathbf{I}-[[\mathbf{F}]]^{\mathrm{T}}\langle\mathbf{S}\rangle\right)\mathbf{n}_{\Sigma}\,\mathrm{d}s\,. \tag{4.52}$$

Based on the concept of configurational forces, a material inhomogeneity is considered as an additional defect in the material, which induces an additional contribution to the crack driving force. The effect of all inhomogeneities in the body inside the contour Γ_{far} has been called the material inhomogeneity term or C_{inh} (Eq. (4.52)). Indeed, the material inhomogeneity term or the scalar quantity C_{inh} represents the projection of the configurational forces induced along the interface, $\mathbf{f}_{\Sigma}$, into the direction of the crack growth. It shall be noted that Eq. (4.52) gives the the material inhomogeneity term due to the *sharp interface*. In the case of a *continuous inhomogeneity*, the material inhomogeneity term can be determined according to (Simha et al. 2003,2005) as

$$C_{\mathrm{inh}} = -\mathbf{e} \cdot \int_{\mathcal{D}} \nabla_{\mathrm{x}} \phi(\mathbf{F}, \mathbf{X}) \, \mathrm{d}A \, . \tag{4.53}$$

The integral in the right-hand side of Eq. (4.53) is a vector representing the total material force due to inhomogeneities in the control volume $\mathcal{D}$. It is noted that this thesis only deals with sharp inhomogeneities.

4.5.1 An intuitive explanation of the material inhomogeneity effect

For a better understanding of the material inhomogeneity effect, presented in the previous section, an intuitive explanation for the effect should be given here. This energy-based explanation was presented in detail in Kolednik et al. (2011).

An elastically inhomogeneous bimaterial body with a straight crack and a sharp interface is assumed where a jump from a high Young's modulus to a low Young's modulus occurs, $E_{\mathrm{L}} > E_{\mathrm{R}}$, a stiff/compliant transition (see Fig. 4.8a). The crack is assumed lying perpendicular to the interface and the crack tip approaches the interface from the left. Before crack extension the strain energy density ϕ_{L} is stored at a material point with polar coordinates (r, θ) with respect to the crack tip during an increment of crack extension. In a homogeneous material, its strain energy density ϕ_{L} will not change during an increment of crack extension; the whole crack driving force must be delivered by the external forces. If, upon crack extension, the point crosses the interface, the stored strain energy density decreases from ϕ_{L} to ϕ_{R}, see Fig. 4.8a. The energy difference, $\phi_{\mathrm{L}} - \phi_{\mathrm{R}}$, becomes available, and so the crack driving force increases. This corresponds to the anti-shielding effect of the stiff/compliant transition at the interface. This will be explained in more detail in the next section by a numerical case study.

Now, let us assume the opposite case: An elastically bimaterial body with a crack and a sharp interface where a jump from a low Young's modulus to a high Young's modulus occurs, $E_{\mathrm{L}} < E_{\mathrm{R}}$, a compliant/stiff transition (see Fig. 4.8b). For the compliant/stiff transition, if the point crosses the interface, the strain energy density of the point increases from ϕ_{L} to ϕ_{R}. Therefore, an additional amount of energy ($\phi_{\mathrm{R}} - \phi_{\mathrm{L}}$) is needed for the movement of the crack tip field, which is not available for extending the crack. Consequently, the crack driving force is decreased. In this case, the interface shields the crack tip.

4.5.2 Influence of a sharp bimaterial interface

Assume an elastically inhomogeneous bimaterial body with a crack and a sharp interface.
Several numerical studies, see e.g. Kolednik et al. (2005) and Simha et al. (2003), show that C_{inh} for a crack propagating from a material with higher Young's modulus to one with lower

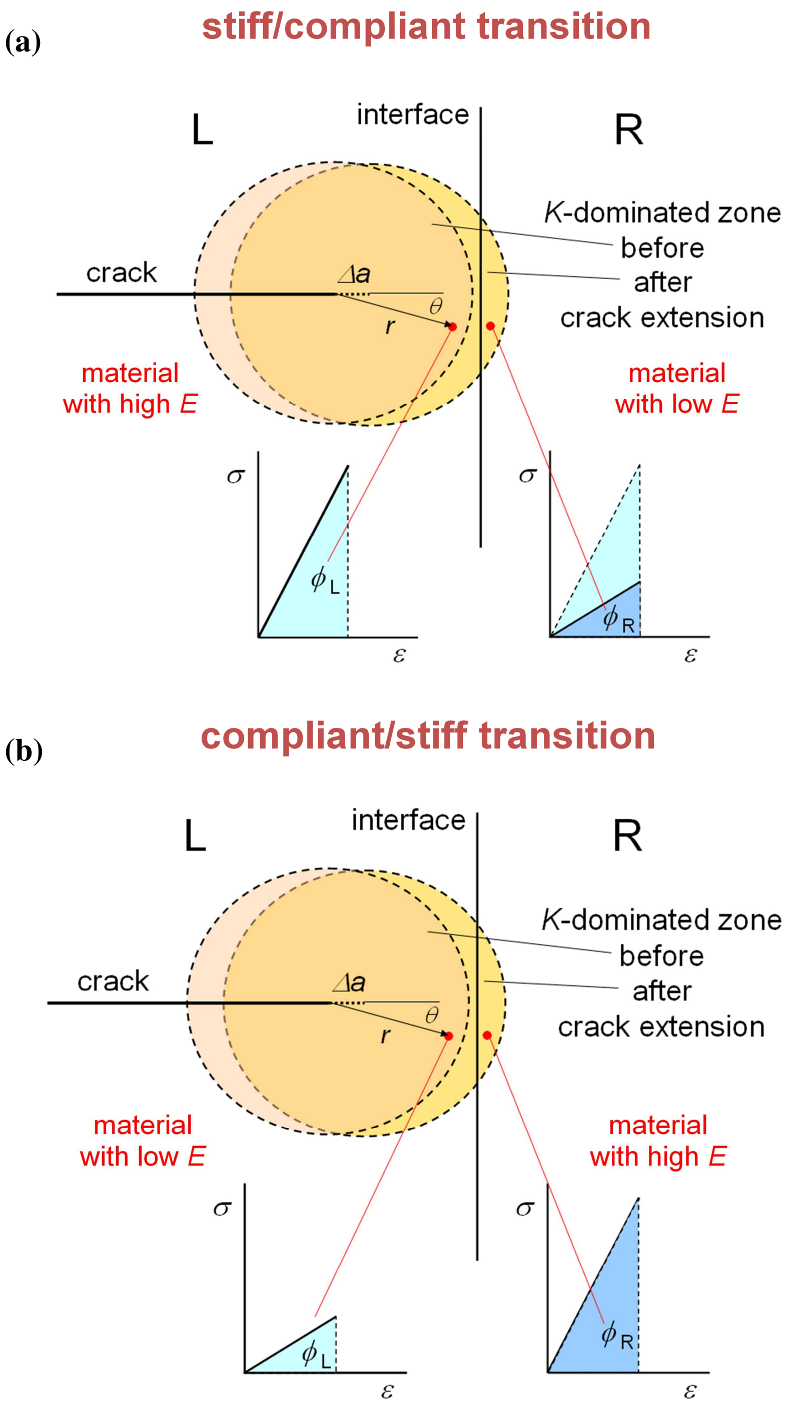

Fig. 4.8 Explanation for the influence of a sharp interface on the crack driving force. Consider the strain energy density of a point with polar coordinates (r, θ). Crack perpendicular to a bimaterial interface for a **(a)** stiff/compliant and **(b)** compliant/stiff transition, (Kolednik et al. 2011).

Young's modulus, $E_{\mathrm{L}} > E_{\mathrm{R}}$, is positive and thus, according to Eq. (4.51), the crack driving force J_{tip} becomes larger than the applied far-field crack driving force or, in other words, a stiff/compliant transition provides a crack tip anti-shielding effect. The anti-shielding effect of

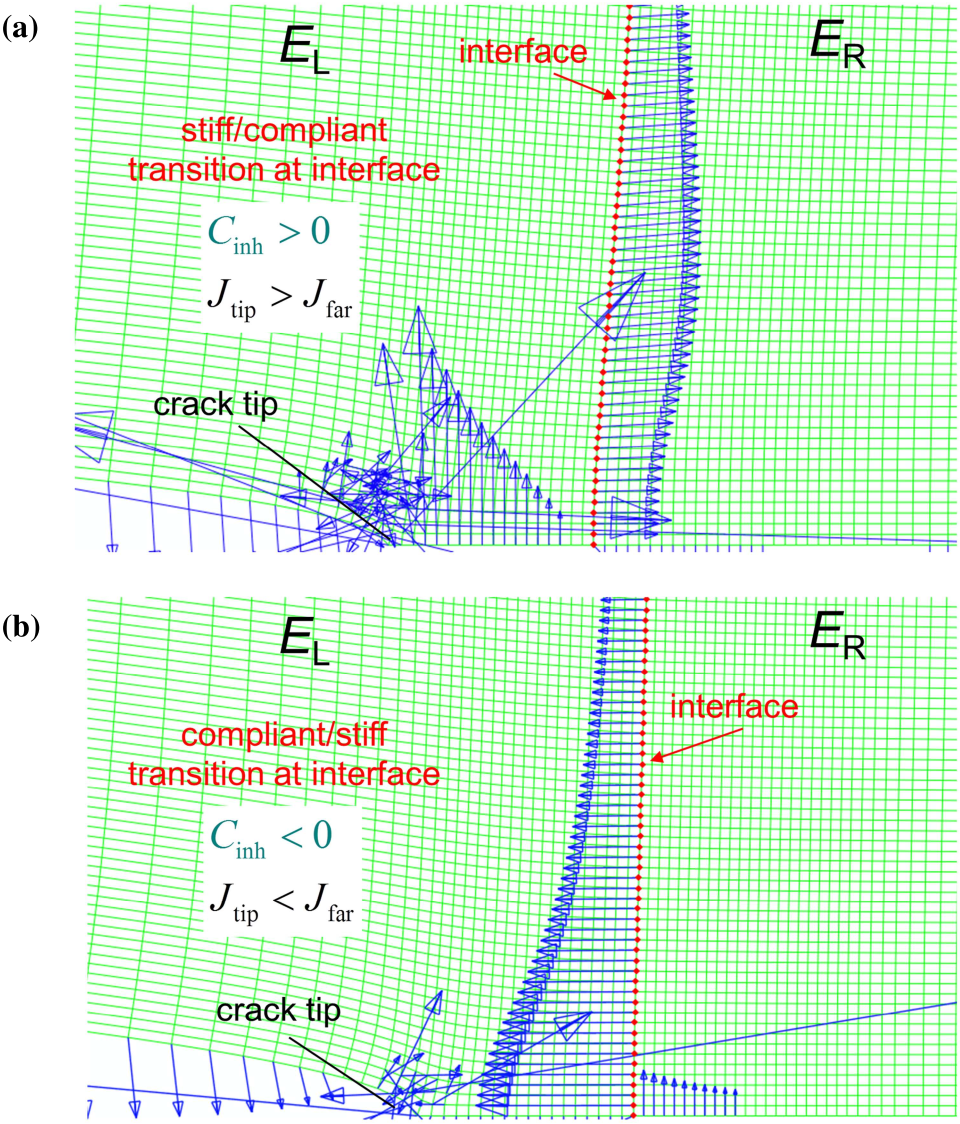

Fig. 4.9 Configurational force distribution near the crack tip and along the interface for an elastically inhomogeneous bimaterial CT specimen at a load line displacement v_{LL} = 0.5 mm, where the distance between crack tip and interface is L_1 = 0.15 mm. **(a)** Stiff/compliant transition at the interface. **(b)** Compliant/stiff transition at the interface.

the interface with a stiff/compliant transition can be observed in Fig. 4.9a. Fig. 4.9a presents the configurational force distribution near the crack tip and along the interface for a bimaterial CT specimen with the Young's modulus ratio $E_R/E_L = 1/3$ and a load line displacement v_{LL} = 0.5 mm, where the distance between crack tip and interface is L_1 = 0.15 mm. Note that due to symmetry only the upper half of the specimen is modeled. The interface configurational forces point into the direction of the crack growth direction. According to Eqs. (4.50) and (4.52), C_{inh} becomes positive and leads to a crack tip anti-shielding effect; $J_{tip} > J_{far}$. Numerical case studies, based on the application of the configurational forces concept, have indicated that when a crack approaches the interface with a stiff/compliant transition, the crack driving force increases to infinity at the interface (Simha et al. 2003; Kolednik et al. 2005).

In the opposite case, C_{inh} for a crack propagating from a material with lower Young's modulus to one with higher Young's modulus, $E_{\text{L}} < E_{\text{R}}$, is negative and, according to Eq. (4.51), the crack driving force J_{tip} becomes smaller than the applied far-field crack driving force; a compliant/stiff transition provides a crack tip shielding effect. Fig. 4.9b presents the according configurational force distribution near the crack tip and along the interface for a bimaterial CT specimen with the Young's modulus ratio $E_{\text{R}}/E_{\text{L}} = 3$ and a load line displacement $v_{\text{LL}} = 0.5$ mm. According to Eqs. (4.50) and (4.52), C_{inh} becomes negative and leads to a crack tip shielding effect; $J_{\text{tip}} < J_{\text{far}}$. Numerical case studies, based on the application of the configurational forces concept, in Kolednik et al. (2005) have indicated that the crack driving force decreases when a crack approaches the interface from an elastically weaker material to a stiffer material, and reaches zero at the interface.

Not only the variation of Young's modulus, but also the yield stress variation can affect the crack driving force. Monotonically loaded cracks, which perpendicularly approach interfaces between two materials with the same elastic properties but different yield stresses, experience decreased or increased values of the near-tip J-integral J_{tip} as a result of the interaction of the crack-tip plastic zone with the interface, e.g. see Kolednik (2000), Kolednik et al. (2010). If the crack propagates from a material with a higher yield stress to a material with a lower yield stress (hard/soft transition), C_{inh} is positive and J_{tip} becomes larger than J_{far}, which leads to an anti-shielding effect. A crack tip shielding effect occurs when the crack propagates from a material with a lower yield stress to a material with a higher yield stress (soft/hard transition). In this case, C_{inh} is negative and J_{tip} becomes smaller than J_{far}.

4.6 Multilayer composites with thin compliant interlayers

4.6.1 Influence of a thin, compliant interlayer on the crack driving force

As discussed above, a spatial variation of material properties in the direction of crack extension leads to a spatial variation of the crack driving force and, thus, affects the fracture toughness. For this reason, the material inhomogeneity effect can be applied as a new method for the design of tough and damage-tolerant materials by inserting compliant and/or soft interlayers in materials. In this section, the influence of a single compliant interlayer on the crack driving force is explained.

Assume a CT specimen (Fig. 4.10a) that has a compliant interlayer with two sharp interfaces, interface 1 (IF1) and interface 2 (IF2), where the Young's modulus exhibits jumps. For a crack growing from the matrix material towards the compliant interlayer, see Fig. 4.10a, a combination of the two transitions discussed above occurs. The interlayer material has a lower Young's modulus than the matrix material, $E^{\mathrm{IL}} < E^{\mathrm{M}}$. A straight crack is assumed lying perpendicular to the interlayer; L_1 is the distances between the crack tip and IF1. When the crack tip is situated left of IF1, L_1 is negative. The crack driving force J_{tip} can be determined from the relation,

$$J_{\mathrm{tip}} = J_{\mathrm{far}} + C_{\mathrm{inh1}} + C_{\mathrm{inh2}}, \tag{4.54}$$

where the parameters C_{inh1} and C_{inh2} are the material inhomogeneity terms of the interfaces IF1 and IF2, respectively. Fig. 4.10b shows the configurational force distribution near the crack tip and along the interfaces for a single interlayer CT specimen (evaluated by FE computations), where $E^{\mathrm{IL}} = 50$ GPa, $E^{\mathrm{M}} = 200$ GPa, the interlayer thickness $t = 0.3$ mm and $L_1 = 0.15$ mm. Due to a stiff/compliant transition at IF1, C_{inh1} is positive; the configurational forces at IF1 point into the direction of the crack growth direction. However, C_{inh2} is negative due to a compliant/stiff transition at IF2; the configurational forces at IF2 point into the opposite direction of the crack growth direction. Fig. 4.10c shows the variation of the crack driving force J_{tip} for constant loading, i.e. a constant value of J_{far}, and different crack tip positions. If the crack tip approaches the interface from the left, J_{tip} first increases, due to anti-shielding effect of IF1, and then decreases due to the shielding effect of IF2. The maximum reduction of the crack driving force J_{tip} is reached at IF2. This position is the critical position for possible crack arrest (CA), and it is referred to in the following as the "CA position".

A compliant interlayer works as a very efficient crack arrester in materials, if the crack driving force becomes very low at the second interface. The interesting idea for materials design is the introduction of thin, compliant interlayers in high-strength matrix materials. Kolednik et al. (2011, 2014a) showed that, if the material properties and the spacing of the interlayers are appropriately chosen, the strong decrease of the crack driving force in the interlayer leads to crack arrest, and fracture toughness and strength of the composite become much higher than the values of the homogeneous matrix material. The findings of Kolednik et al. (2011, 2014a) are briefly presented below.

4.6.2 Strength and fracture toughness of composites with thin compliant interlayers

Kolednik et al. (2011) performed finite element analysis on a composite resembling the structure of a deep-sea glass sponge, with a periodical variation of the Young's modulus E, see Fig. 4.11a. The stiff layers in the deep-sea sponge consist of bioglass with $E = 42$ GPa. The compliant, thin interlayer is a protein with $E = 1$ GPa. The stiff and compliant layers of the composite have thicknesses of 5 μm and 0.1 μm, respectively. The interfaces between the layers are modeled as perfect, i.e. no delamination can occur. The variation of the crack driving force J_{tip} in the composite with a short crack is numerically evaluated. Fig. 4.11b shows the variation of J_{tip} plotted versus the crack length in the vicinity of an interlayer. In homogeneous bioglass, J_{tip} increases linearly with increasing crack length, which is plotted in Fig. 4.11b. First, J_{tip} of the composite increases much stronger than that of homogeneous bioglass due to the anti-shielding effect of the first interface of the interlayer. Then, the crack driving force strongly decreases inside the interlayer. Due to the low J_{tip} inside the interlayer, the crack is arrested and cannot grow into the next layer. Therefore, the strength of the structure is remarkably improved. The strength, i.e. the fracture stress of intrinsically brittle materials in a tensile test, is determined by the initiation and growth of small defects.

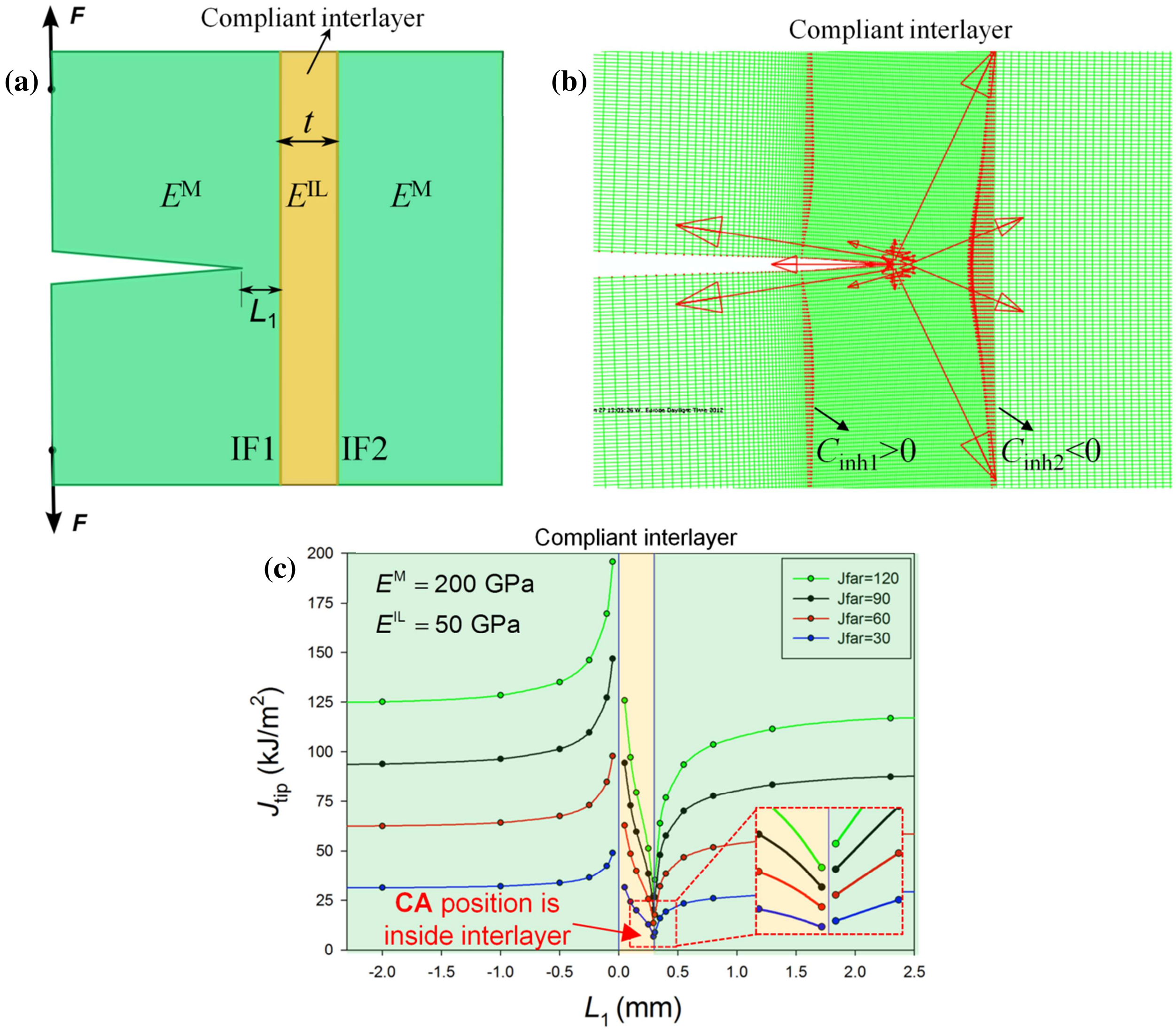

Fig. 4.10 **(a)** Fracture mechanics specimen with a long crack and a single, compliant interlayer with interfaces, IF1 and IF2, perpendicular to the crack plane. **(b)** Configurational force distribution (evaluated by FE computations) near the crack tip and along the interfaces. **(c)** The crack driving force J_{tip} reaches a minimum value at IF2.

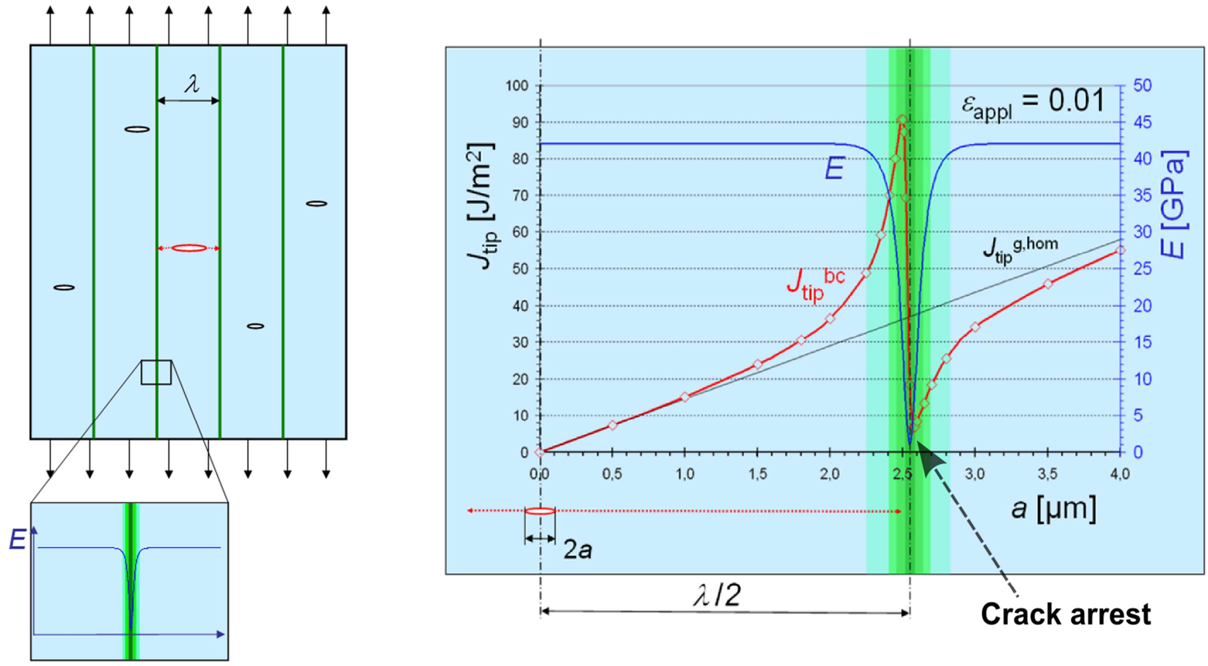

(a) **(b)**

Fig. 4.11 **(a)** Layered structure with spatial variations in Young's modulus and a short crack. **(b)** Strong spatial variation of the Young's modulus between the stiff bio-glass and the compliant protein layers leads to a strong decrease of the crack driving force when the crack enters the interlayer (Kolednik et al. 2011).

The composite will exhibit a higher fracture stress than the homogeneous matrix material, if the applied load at the re-initiation of crack growth of the arrested crack is higher than the load required to initiate a short inherent crack with length $2a_\mathrm{n}$ in the homogeneous material. Kolednik et al. (2011) derived the ratio of the fracture strength of the multilayer composite $\sigma_\mathrm{fr}^\mathrm{ML}$ to the fracture strength of the homogeneous matrix material $\sigma_\mathrm{fr}^\mathrm{M}$ as

$$\frac{\sigma_\mathrm{fr}^\mathrm{ML}}{\sigma_\mathrm{fr}^\mathrm{M}} \approx \sqrt{\frac{1}{\varPsi}\frac{2a_\mathrm{n}}{\lambda}\frac{E^\mathrm{M}}{E^\mathrm{IL}}}, \tag{4.55}$$

where λ is the wavelength of the composite (see Fig. 4.11a), and $\varPsi$ is a dimensionless parameter, which must be determined by FE computations for each specific crack configuration (in the order of magnitude as $\varPsi = 5$). The inherent defect size a_n in the homogeneous matrix material can be determined as (Kolednik et al. 2011),

$$a_\mathrm{n} = \frac{1}{\pi}\left(\frac{K_\mathrm{c}^\mathrm{M}}{\sigma_\mathrm{fr}^\mathrm{M}}\right)^2, \tag{4.56}$$

where K_c^M is the critical stress intensity factor of the homogeneous matrix material, see Section 3.4. Eq. (4.55) is based on the assumption that the interlayer material has the same crack growth resistance as the homogeneous material. If this is not so, the right hand side of Eq. (4.55) has to be multiplied by the term $\sqrt{R^{\mathrm{IL}}/R^{\mathrm{M}}}$ with R^{M} as the crack growth resistance of the matrix material, and R^{IL} the crack growth resistance of the interlayer material.

Eq. (4.55) can be used as an architectural criterion for the design of strong multilayered composites. Based on this criterion, a multilayer composite with large ratio $E^{\mathrm{M}}/E^{\mathrm{IL}}$ and small wavelength λ has a much higher fracture stress than the homogeneous material.

Eq. (4.55) yields very high fracture stresses for small wavelengths of the multilayer. An upper limit of the fracture stress of the multilayer, $\hat{\sigma}_{\mathrm{fr}}^{\mathrm{ML}}$, was derived in Kolednik et al. (2014a) for inherently brittle matrix materials, based on the weakest link concept,

$$\hat{\sigma}_{\mathrm{fr}}^{\mathrm{ML}} \approx \sigma_{\mathrm{fr}}^{\mathrm{M}} \left(\frac{W}{\lambda} \right)^{\frac{1}{M}}, \tag{4.57}$$

where the parameter M denotes the Weibull modulus of the matrix (Weibull 1951). Eq. (4.57) assumes two tensile specimens of same thickness B, width W, and height H. One specimen consists of homogeneous matrix material, the other one of a multilayer with the wavelength λ.

Kolednik et al. (2014a) showed that not only the fracture stress, but also the fracture toughness of inherently brittle materials can be significantly improved by the introduction of compliant interlayers; note that fracture toughness is determined on specimens with long cracks. They showed that the maximum possible fracture toughness of a multilayer composite can be determined, in term of the J-integral, by the following equation,

$$J_{\max}^{\mathrm{ML}} = \frac{\eta}{2} H \left(\frac{W}{\lambda} \right)^{\frac{2}{M}} \frac{\left(\sigma_{\mathrm{fr}}^{\mathrm{M}}\right)^2}{E^{\mathrm{M}}}, \tag{4.58}$$

where η is the dimensionless geometry factor, see Section 3.5. Inserting the relation between the stress intensity factor K and J-integral, Eq. (3.10), the maximum possible fracture toughness of a multilayer composite can be written in term of the stress intensity factor as

$$K_{\max}^{\mathrm{ML}} = \sqrt{\frac{\eta}{2} H} \left(\frac{W}{\lambda} \right)^{\frac{1}{M}} \sigma_{\mathrm{fr}}^{\mathrm{M}}. \tag{4.59}$$

In Sections 5–7, this thesis shows that a soft interlayer, i.e. an interlayer with the same Young's modulus but a lower yield stress than the matrix material, also works as effective crack arrester. Furthermore, it is shown that the strength and the fracture toughness of inherently brittle matrix materials can be greatly improved by the introduction of thin, soft interlayers, if the architectural parameters of the multilayer fulfill the derived design rules.

“Science doesn't purvey absolute truth. Science is a mechanism. It's a way of trying to improve your knowledge of nature. It's a system for testing your thoughts against the universe and seeing whether they match. And this works, not just for the ordinary aspects of science, but for all of life.”

Isaac Asimov
Professor of biochemistry at Boston University
1919–1992

Part II

Design of tough, strong and damage-tolerant composites by utilizing the yield stress inhomogeneity effect

5 Effect of a single soft interlayer on the crack driving force

In subsequent papers, e.g. Kolednik et al. (2011, 2014a), the concept of configurational forces (see Section 4.5) has been applied in order to evaluate the crack driving force and to predict the behavior of cracks in various types of inhomogeneous materials. It has been demonstrated that multilayer structures with thin, compliant interlayers can have highly improved fracture strength and fracture toughness compared to the homogeneous bulk material, if the multilayer architecture fulfills certain design rules, see Section 4.6.

The idea of enhancing the fracture stress and the fracture toughness by introducing compliant interlayers shall be transferred to technical materials where both, the hard and the soft material, behave elastic-plastic. However, a problem is that the available criteria proposed by Kolednik et al. (2011, 2014a), see Section 4.6, for the design of strong and tough multilayer composites can be only used for elastic materials. In order to work out design rules of tough, strong and damage tolerant elastic–plastic multilayer composites, it is necessary to quantify the influence of a single soft interlayer on the crack driving force.

Paper I performs a comprehensive case study for a fracture mechanics specimen with a single soft interlayer, which has equal elastic properties as the matrix but a lower yield stress, see Fig. 5.0. The concept of configurational forces, in combination with a finite element (FE) stress and strain analysis, is used to evaluate the variation of the crack driving force J_{tip} for various positions of the crack tip with respect to the interlayer, for various loads and for various variations of the yield stress. It is noted that since the proportional loading conditions are not disturbed, the evaluation of the crack driving force J_{tip} is performed with deformation theory of plasticity, see Section 4. The results are then used to find, for a given matrix material and load, the optimum thickness (t) and yield stress of the soft interlayer ($\sigma_{\mathrm{y}}^{\mathrm{IL}}$) so that a maximum reduction of the crack driving force is achieved. The most important findings of this paper can be highlighted as:

- The material inhomogeneity effect due to a single interlayer on the crack driving force, which is called the interlayer inhomogeneity term C_{IL}, can be quantified by the summation of the material inhomogeneity terms of the first and second interfaces of the interlayer, C_{inh1} and C_{inh2}.
- The normalized material inhomogeneity term, $C_{\mathrm{inh}}/J_{\mathrm{far}}$, of each interface is a function of two dimensionless terms, the ratio of the yield stresses of the

interlayer and matrix materials, $\sigma_{\mathrm{y}}^{\mathrm{IL}}/\sigma_{\mathrm{y}}^{\mathrm{M}}$, and the ratio of the radius of the crack tip plastic zone in the interlayer material to the distance between crack tip and interface, $L_1/r_{\mathrm{y}}^{\mathrm{IL}}$, see Fig. 5.0.

- The normalized interlayer inhomogeneity term, $C_{\mathrm{IL}}/J_{\mathrm{far}}$, is additionally dependent on a third dimensionless term, which is the interlayer thickness related to the plastic zone size in the interlayer, $t/r_{\mathrm{y}}^{\mathrm{IL}}$.
- It is observed that the crack driving force becomes a minimum immediately after the crack has crossed the second interface of the soft interlayer (IF2). This position is the critical position for possible crack arrest (CA-position).
- Conditions for maximum effectiveness of a soft interlayer as crack arrester are derived, i.e. for a given matrix material and load, the magnitudes of thickness and yield stress of the soft interlayer are determined so that the maximum reduction of the crack driving force at the CA-position appears. These conditions are: (i) $\sigma_{\mathrm{y}}^{\mathrm{IL}}/\sigma_{\mathrm{y}}^{\mathrm{M}} \le 0.2$, and (ii) $t \cong r_{\mathrm{y}}^{\mathrm{IL}}$.
- By inserting a soft interlayer with the derived conditions, the crack driving force of a bulk material can be reduced by a factor of 10, which is the maximum possible reduction of the crack driving force.

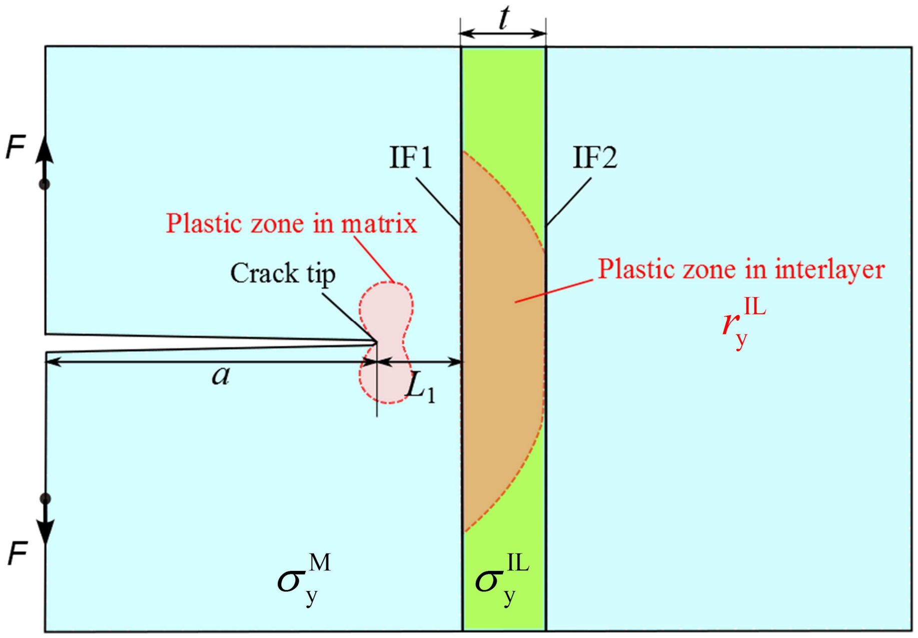

Fig. 5.0 Fracture mechanics specimen with a single, soft interlayer with interfaces, IF1 and IF2, perpendicular to the crack plane.

Paper I:

Effect of a single soft interlayer on the crack driving force

M. Sistaninia, O. Kolednik

published in

Engineering Fracture Mechanics (2014) 130:21–41

https://doi.org/10.1016/j.engfracmech.2014.02.026

Abstract

It has recently been shown that a strong spatial variation of the Young's modulus can improve greatly the fracture resistance and the fracture strength of an inherently brittle material. In this paper, using numerical modeling and application of the concept of the configurational forces, it is shown that spatial variations of the yield stress can also improve the fracture resistance. The reason is that, when the crack has crossed the soft interlayer, the crack driving force strongly decreases and the crack is arrested by the soft interlayer; this effect appears without previous delamination of the interlayer. Furthermore, "optimum interlayer configurations" are derived, i.e. for a given matrix material and load, the magnitude of the thickness and the yield stress of the soft interlayer are derived so that the crack driving force exhibits a minimum. Such optimum configurations can be used for the design especially fracture resistant materials and components.

Keywords: Crack driving force; Configurational forces; Finite element method; Fracture toughness; Crack tip plastic zone.

5.1 Introduction

Most of the newly designed engineering materials need to be reinforced against fracture and fatigue. For instance, the Al–Zn–Mg–Cu alloys have the highest strength to weight ratio of all aluminum alloys and are candidates for lightweight constructions. However, they have inherently low resistance to fracture. Silicon nitride has a high potential for its combination of strength, hardness, and chemical and thermal durability. But the low fracture resistance of this ceramic material limits its applications (Liu et al. 1996). Generally, there exists a rule that increasing strength leads to a decrease in fracture toughness, this rule applies for many materials and alloys. To overcome this problem, trends to design "damage-tolerant" materials have been in the focus of researchers in the past decades, e.g. Sglavo and Bertoldi (2006), Bermejo et al. (2007). In particular, layered structures have been proposed as an efficient way for the design of more fracture resistant materials. A very strong increase of fracture resistance compared to the homogenous bulk material can be achieved by introducing soft or weak interlayers (Cook and Gordon 1964; Embury et al. 1967; Taylor and Ryder 1976; Suresh et al. 1993; Lesuer et al. 1996; Tariolle et al. 2005; Fratzl et al. 2007; Kolednik et al. 2011). Two basic mechanisms behind these multilayered structures shall be highlighted.

On the one hand, multilayered structures with weak interlayers (weak interfacial bonding) have been designed to yield significant enhanced failure resistance and *R*-curve behavior through interface delamination (Cook and Gordon 1964; Embury et al. 1967; Taylor and Ryder 1976; Lesuer et al. 1996; Wang et al. 2000; Tariolle et al. 2005; Anderson 2005; Ceylan and Fuierer 2007; Tomaszewski et al. 2007; Bermejo and Danzer 2010). When the crack grows into the delaminated area, the hydrostatic stress state strongly decreases and the crack tip becomes blunted, which leads to a higher fracture resistance. For example, the fracture toughness of layered ceramic composite silicon nitride with interlayers of boron nitride (Si_3N_4-BN) is much higher than that of the homogenous Silicon nitride material (Wang et al. 2000), and also the fracture toughness of ceramic SiC can be improved by a factor of 5 using weak graphite interlayers (Tariolle et al. 2005). In both examples, the fracture resistance of the materials is strongly improved due to the interface delamination.

A problem of this mechanism is that the tensile strength of the composites perpendicular to the interfaces is strongly reduced due to weak interfacial bonding. An interesting idea was proposed by Atkins and co-workers (Atkins 1974; Marston et al. 1974; Atkins 1975) in order to increase the fracture resistance of fiber reinforced composites without significant loss of tensile strength and stiffness. By intermittent coating of the filaments, alternating regions with high and low interfacial bonding were produced.

On the other hand, multilayer structures with soft interlayers can reach very high fracture resistance compared to the homogenous material, due to spatial variations of the mechanical properties (Suresh et al. 1993; Kolednik 2000; Fratzl et al. 2007; Kolednik et al. 2011; Fischer et al. 2012a). The reason for the effect is that in materials with spatial variations of the mechanical properties, the crack driving force is locally reduced, compared to a homogenous material, which leads to a strong increase of the fracture resistance. It is worth to mention that this effect occurs independently of delaminating interfaces.

Many fracture resistant biological materials, such as the skeleton of deep-sea glass sponges, nacre and bone, have a hierarchical structure. Nacre and bone have the brick-and-mortar type structures that allow surprisingly large inelastic deformations due to sliding of the mineral tablets, which leads to an increased work of fracture and, therefore, to an increased fracture toughness (Espinosa et al. 2009; Dunlop and Fratzl 2010; Shao et al. 2012). Such a mechanism cannot occur in the skeleton of deep-sea glass sponges, which have a structure made of cylindrical layers of brittle bioglass with thin, soft protein layers in between (Kamat et al. 2004; Aizenberg 2010; Dunlop and Fratzl 2010; Kolednik et al. 2011). Numerical modeling and application of the concept of configurational forces has recently revealed that the strong spatial variation of the Young's modulus between the hard and brittle bio-glass and the thin, soft protein layers is the dominant mechanism for the high fracture resistance of the skeleton of deep-sea glass sponges (Kolednik et al. 2011). The reason is that the crack driving force strongly decreases when the crack enters the soft layer. It has been shown that the fracture resistance of a composite becomes much higher than that of the homogenous material, if the composite architecture fulfills certain design rules, which were derived in (Kolednik et al. 2011).

The idea of enhancing the fracture resistance by introducing soft interlayers shall be transferred to engineering materials where both the hard and the soft material behaves elastic–plastic. A problem is, however, that the criterion proposed by Kolednik et al. (2011) for the design of fracture resistant layered composites can be only used for elastic materials. In order to work out design rules of more fracture resistant elastic–plastic multilayered materials, it is necessary to quantify the influence of a single soft interlayer on the crack driving force.

The present paper performs a comprehensive case study for a fracture mechanics specimen with a single soft interlayer with yield stress inhomogeneity. The concept of configurational forces, in combination with a finite element (FE) stress and strain analysis, is used to evaluate the variation of the crack driving force for various positions of the crack tip with respect to the interlayer, for various loads and for various variations of the yield stress. The results are used to find, for a given material and load, the optimum thickness and yield stress of the soft interlayer so that the crack driving force exhibits a minimum. We consider here only the effect of an inhomogeneity in the yield stress. The other case, the influence of an interlayer with elastic inhomogeneity on the crack driving force will be considered in a separate paper.

The current paper is structured as follows: In Section 5.2 a literature review on related experimental, analytical and numerical investigations is given. Section 5.3 explains the application of the configurational forces concept for determining the crack driving force in inhomogeneous materials. In Section 5.4, a short overview is given about the numerical modeling and some computational aspects. In Section 5.5, case studies are presented in order to examine the variation of the crack driving force. In Section 5.6, the influence of dimensionless effective parameters on the normalized material inhomogeneity terms are discussed. Finally, the certain conditions for achieving the maximum effectiveness of a soft interlayer are derived in Section 5.7.

5.2 Background

Numerous researchers have shown in theoretical, numerical and experimental studies that the variations of material properties in the direction of the crack extension can significantly affect the growth or arrest of cracks. In the following, a brief survey of those studies will be given.

5.2.1 Theoretical studies

Most analytical papers consider cracks near interfaces using the stress intensity *K*-field formulation, which is applicable for linear elastic fracture mechanics. Numerous publications, see e.g. Zak and Williams (1963), Cook and Erdogan (1972), Erdogan and Biricikoglu (1973), Romeo and Ballarini (1995), have reported elastic analyses of the fracture characteristics and near-tip field quantities for cracks that perpendicularly approach interfaces. They showed that when a crack approaches the interface from an elastically weaker material to a stiffer material, the local stress intensity decreases and reaches zero at the interface. For a crack lying in the stiffer material approaches the interface to a compliant material, the local stress intensity increases to infinity at the interface. Gao (1991) presented a first-order moduli-perturbation algorithm based on the Bueckner-Rice weight function theory for fracture analysis of inhomogeneous materials. The perturbation algorithm was applied to calculate the stress intensity factors for several crack problems involving spatially varying material moduli. Muju (2000) extended the moduli perturbation approach by Gao (1991) for the study of the inhomogeneity effect on a crack propagating through an interface in elastic multilayered composites. Fratzl et al. (2007) analyzed analytically the crack driving force in a composite with periodically varying Young’s modulus. In Fischer et al. (2012a) two semi-analytical approximation concepts based on either the configurational forces concept or the moduli perturbation concept were introduced to assess the crack driving force in periodically heterogeneous elastic materials.

The plasticity aspects of a crack lying perpendicularly near an interface have been taken into account in papers by Shih (1991) and Wang and Ståhle (1998). These papers obtained small scale yielding solutions for the stress and deformation fields of cracks at interfaces between materials with different elastic properties. In another paper by Riemelmoser and Pippan (2000), the Dugdale model was applied to calculate the crack tip opening displacement and the J-integral for cracks perpendicular to an interface of materials with equal elastic properties but different yield stresses under monotonic and cyclic loading.

In Kolednik (2000) an analytical model based on global energy considerations was presented to quantify the influence of the yield stress variation on the crack driving force in non-hardening inhomogeneous materials under small-scale yielding conditions. It was demonstrated that an additional crack driving force term, the so-called yield stress gradient term C_y, appears in materials with a smooth gradient in yield stress or a jump in yield stress at a sharp interface. The crack driving force, written in terms of the near-tip J-integral J_tip, is evaluated by the sum of the yield stress gradient term and the nominally applied far-field driving force, J_far,

$$J_\mathrm{tip} = J_\mathrm{far} + C_\mathrm{y} . \tag{5.1}$$

The yield stress gradient term C_y is positive and enhances the effective crack driving force when the yield stress decreases in the crack growth direction. On the contrary, if the yield stress increases in the crack growth direction, C_y is negative and reduces the effective crack driving force. The analytical expressions for the magnitude of the yield stress gradient term near bimaterial interfaces and near interlayers were developed for small-scale yielding conditions and non-hardening materials. For an elastic interlayer in an elastic–plastic matrix, the ratio of the yield stress gradient term vs. the far-field driving force, J_far, can be determined from

$$\frac{C_\mathrm{y}^\mathrm{M}}{J_\mathrm{far}} = -\frac{1}{2\pi}\left\{\mathrm{Re}\left(\operatorname{arctanh}\sqrt{1-\left(\frac{L_1}{r_\mathrm{y}^\mathrm{M}}\right)^2}\right) - \mathrm{Re}\left(\operatorname{arctanh}\sqrt{1-\left(\frac{L_1-t}{r_\mathrm{y}^\mathrm{M}}\right)^2}\right)\right\}, \tag{5.2}$$

and for an elastic–plastic interlayer in an elastic matrix, the ratio of the yield stress gradient term vs. the far-field driving force, J_far, can be determined from

$$\frac{C_\mathrm{y}^\mathrm{IL}}{J_\mathrm{far}} = \frac{1}{2\pi}\left\{\mathrm{Re}\left(\operatorname{arctanh}\sqrt{1-\left(\frac{L_1}{r_\mathrm{y}^\mathrm{IL}}\right)^2}\right) - \mathrm{Re}\left(\operatorname{arctanh}\sqrt{1-\left(\frac{L_1-t}{r_\mathrm{y}^\mathrm{IL}}\right)^2}\right)\right\}, \tag{5.3}$$

where L_1 is the distance between the crack tip and the first interface of the interlayer, t the interlayer thickness, r_{y} the radius of the plastic zone, and Re is the real part of the expression (). The superscripts IL and M refer to the interlayer and matrix, respectively. The sign of the distance L_1 is negative when the crack tip is located left of the first interface, and L_1 is positive for the crack tip situated right of the first interface; note that a different notation was used in Kolednik (2000). The radius of the crack tip plastic zone, r_{y}, can be determined by Irwin's model (Irwin 1961) as

$$r_{\mathrm{y}} = \beta \frac{J_{\mathrm{far}} E}{\sigma_{\mathrm{y}}^2 (1-\nu^2)}, \tag{5.4}$$

where E is the Young's modulus, σ_{y} the yield stress, ν Poisson's ratio, and $\beta = 1/6\pi$ for plane strain conditions. In general, when both the matrix and the interlayer deform plastically, the ratio of the yield stress gradient term vs. J_{far} can be determined as the summation of Eq. (5.2) and Eq. (5.3),

$$\begin{aligned} \frac{C_{\mathrm{y}}}{J_{\mathrm{far}}} = \frac{C_{\mathrm{y}}^{\mathrm{IL}}}{J_{\mathrm{far}}} + \frac{C_{\mathrm{y}}^{\mathrm{M}}}{J_{\mathrm{far}}} = -\frac{1}{2\pi} \left\{ \mathrm{Re}\left(\operatorname{arctanh}\sqrt{1-\left(\frac{L_1}{r_{\mathrm{y}}^{\mathrm{M}}}\right)^2} \right) - \mathrm{Re}\left(\operatorname{arctanh}\sqrt{1-\left(\frac{L_1-t}{r_{\mathrm{y}}^{\mathrm{M}}}\right)^2} \right) \right\} + \\ + \frac{1}{2\pi} \left\{ \mathrm{Re}\left(\operatorname{arctanh}\sqrt{1-\left(\frac{L_1}{r_{\mathrm{y}}^{\mathrm{IL}}}\right)^2} \right) - \mathrm{Re}\left(\operatorname{arctanh}\sqrt{1-\left(\frac{L_1-t}{r_{\mathrm{y}}^{\mathrm{IL}}}\right)^2} \right) \right\}. \end{aligned} \tag{5.5}$$

Due to the simplifications of the model, Eq. (5.5) does not provide quantitatively correct results, see Section 5.6.2. Nevertheless, it correctly shows that the crack driving force increases near the first interface and decreases near the second interface for a soft interlayer, and vice versa for a hard interlayer.

5.2.2 *Numerical studies*

The yield stress variation effect on the crack driving force was analyzed by conducting finite element (FE) computations in Kim et al. (1997) and Sugimura et al. (1995). They showed that monotonically loaded stationary cracks, which perpendicularly approach interfaces between two materials with the same elastic properties but different yield stresses, can experience decreased or increased values of the near-tip J-integral as a result of the interaction of the crack-tip plastic zone with the interface. Similar studies were also presented in Joyce et al. (2003).

In recent papers (Honein and Herrmann 1997; Simha et al. 2003; Simha et al. 2005; Chen et al. 2007; Kolednik et al. 2009; Rakin et al. 2009; Kolednik et al. 2010; Kolednik et al. 2011), numerical modeling with application of the concept of configurational forces has been applied for determining the crack driving force in inhomogenous materials. Based on the concept of configurational forces, an additional crack driving force term, the so-called material inhomogeneity term, C_{inh}, appears in materials when the material properties vary in the direction of the crack extension. The material inhomogeneity term, C_{inh}, is evaluated by a post-processing procedure, following a conventional finite element stress analysis. It was demonstrated in (Honein and Herrmann 1997; Simha et al. 2003; Simha et al. 2005; Chen et al. 2007; Kolednik et al. 2009; Rakin et al. 2009; Kolednik et al. 2010; Kolednik et al. 2011) that if the crack propagates from a material with a higher yield stress or Young's modulus to a material with a lower yield stress or Young's modulus (hard/soft or stiff/compliant transition), C_{inh} is positive and J_{tip} becomes larger than J_{far}, which leads to an anti-shielding effect. A crack tip shielding effect occurs when the crack propagates from a material with a lower yield stress or Young's modulus to a material with a higher yield stress or Young's modulus (soft/hard or compliant/stiff transition). In this case, C_{inh} is negative and J_{tip} becomes smaller than J_{far}.

The concept of configurational forces is shortly explained in Section 3.

5.2.3 Experimental studies

In (Suresh et al. 1992; Suresh et al. 1993) fatigue crack growth experiments were conducted on explosion clad bimaterial specimens consisting of ferritic and austenitic steel. The two steels had approximately the same Young's modulus, similar yield strengths, but the strain hardening exponent and the ultimate tensile strength of the austenitic steel were significantly larger than those of the ferritic steel. The crack growth rate was measured for cracks perpendicular to the interface and it was shown that, when a fatigue crack approached the interface from the softer side, it arrested some distance before the interface. When a fatigue crack approached the interface from the harder side, the crack growth rate increased slightly some distance before the interface.

A shortcoming of the experimental investigation in (Suresh et al. 1992; Suresh et al. 1993) was that the thermal residual stresses were not taken into account. Residual stresses appear due to the different values of the coefficient of thermal expansion (CTE) of the ferritic and austenitic steels during the cooling from the annealing temperature to the room temperature, the specimens were annealed for stress relief at $860\ ^{\circ}\mathrm{C}$. For this reason Pippan et al. (2000) conducted similar experiments on bimaterial specimens consisting of technically pure (ARMCO) iron and the steel SAE 4340 where this problem does not appear, because the materials have the same CTE. They reached similar conclusions as in (Suresh et al. 1992;

Suresh et al. 1993). In Kolednik et al. (2009) FE analysis with application of the concept of configurational forces was performed to describe the behavior of fatigue cracks in experiments conducted in Pippan et al. (2000). It was seen that FE results were in good agreement with the experimental results.

Recently, Zechner and Kolednik (2013a) investigated experimentally the influence of compliant interlayers on the fracture resistance of multilayer composites. The experimental tests were conducted on multilayer single edge notch tension specimen consisting of the high-strength aluminum alloy Al7075-T6 and thin, soft polymer interlayers. The specimens were built in two different configurations, crack divider and crack arrester configurations. The experimental results showed that the layered composite in the crack arrester configuration exhibited a significantly improved fracture resistance compared to the homogeneous aluminum alloy. The reason is that cracks are completely arrested in the compliant interlayers, they become ineffective and the specimen behaves like a tensile specimen. Consequently, the crack growth resistance increases tremendously. The crack arrest in the compliant interlayer of the crack arrester configuration originates from the strong inhomogeneity in the mechanical properties between bulk material and polymer interlayers. It was observed that this effect occurs independently from the delamination of the interfaces.

The influence of compliant interlayers on the fracture resistance of multilayer composites was experimentally investigated in another paper by Zechner and Kolednik (2013b). They conducted experimental tests on multilayers made of commercially available printing paper with air as interlayer material. Multilayer specimens were manufactured in both crack arrester and crack divider configuration. It was demonstrated that paper multilayers in crack arrester configuration can reach very high fracture toughness, comparable to that of steel.

In order to experimentally investigate the influence of the yield stress variation on the fracture resistance of multilayered composites, Zechner and Kolednik (to be published) conducted experimental tests on multilayer specimens consisting of the high-strength aluminum alloy Al7075 and pure aluminum interlayers (Al7075 and pure aluminum have the same elastic properties, but very different yield stresses). They observed that this composite structure can reach a high fracture resistance, compared to the homogenous Al7075, due to the soft pure aluminum interlayers.

All these experiments show that it is possible to strongly increase the fracture- and fatigue resistance of materials or components by introducing compliant or soft interlayers that are able to provide sufficient crack arrest. Moreover, these materials become also flaw-tolerant, i.e. insensitive to initial notches or cracks, see also Kolednik et al. (2014a).

5.3 The concept of configurational forces for the evaluation of crack driving force in inhomogenous materials

The concept of configurational forces, which is based on ideas by Eshelby (1970), is explained in books by Maugin (1993) and Gurtin (2000). The concept of configurational forces is appropriate for analyzing the behavior of all kinds of inhomogeneities in materials, such as point defects, dislocations, cracks, interfaces, phase boundaries, inclusions or voids. According to this concept, configurational forces act at defects and try to move them in such a way that the total potential energy of the system decreases. In terms of the concept of the configurational forces, a material inhomogeneity is considered as an additional defect in the material, which induces an additional contribution to the crack driving force. This additional contribution has been called the material inhomogeneity term, C_{inh}. As explained in (Simha et al. 2003; Simha et al. 2005; Kolednik et al. 2010), for a body containing a crack and a sharp interface Σ where the material properties exhibit a jump, the material inhomogeneity term, which represents the sum of the configurational forces induced along the interface, can be calculated for small strain theory by

$$C_{\text{inh}} = -\mathbf{e} \cdot \int_{\Sigma} \left([[\phi]]\mathbf{I} - \langle \boldsymbol{\sigma} \rangle \cdot [[\boldsymbol{\varepsilon}]] \right) \mathbf{n} \, dl. \tag{5.6}$$

where ϕ is the strain energy density, $\mathbf{I}$ the identity tensor, $\boldsymbol{\sigma}$ the Cauchy stress tensor, $\boldsymbol{\varepsilon}$ the strain tensor, $\mathbf{e}$ the unit vector in the direction of crack extension, $\mathbf{n}$ the unit vector normal to the interface Σ, and dl is an increment of the interface Σ. In Eq. (5.6), the jump of a quantity $\mathbf{a}$ at the interface is denoted as $[[\mathbf{a}]] = \left(\mathbf{a}^{+} - \mathbf{a}^{-}\right)$ and the average of a quantity $\mathbf{a}$ across the interface is denoted as $\langle \mathbf{a} \rangle = \left(\mathbf{a}^{+} + \mathbf{a}^{-}\right)/2$, where $\mathbf{a}^{+}$ and $\mathbf{a}^{-}$ denote the limiting values of the quantity on either side of the interface. C_{inh} is a scalar quantity, denoting the energy that is released during a unit crack extension due to the material inhomogeneity at the interface.

The crack driving force, expressed in terms of the near-tip J-integral J_{tip}, is the sum of the far-field J-integral J_{far} and the material inhomogeneity term,

$$J_{\text{tip}} = J_{\text{far}} + C_{\text{inh}} \,. \tag{5.7}$$

The far-field J-integral J_{far}, which is a loading parameter, measures the driving force induced by the applied loads into the specimen. Indeed, J_{far} is the summation of all configurational forces over the whole body, including the configurational forces acting at the crack tip and the interface. In a homogenous material $C_{\text{inh}} = 0$ and $J_{\text{tip}} = J_{\text{far}}$, i.e. the J-integral is path independent. In a hard/soft or stiff/compliant transition, C_{inh} becomes positive and leads to a crack tip anti-shielding effect. In the opposite case, in a soft/hard or compliant/stiff transition, C_{inh} becomes negative and leads to a crack tip shielding effect.

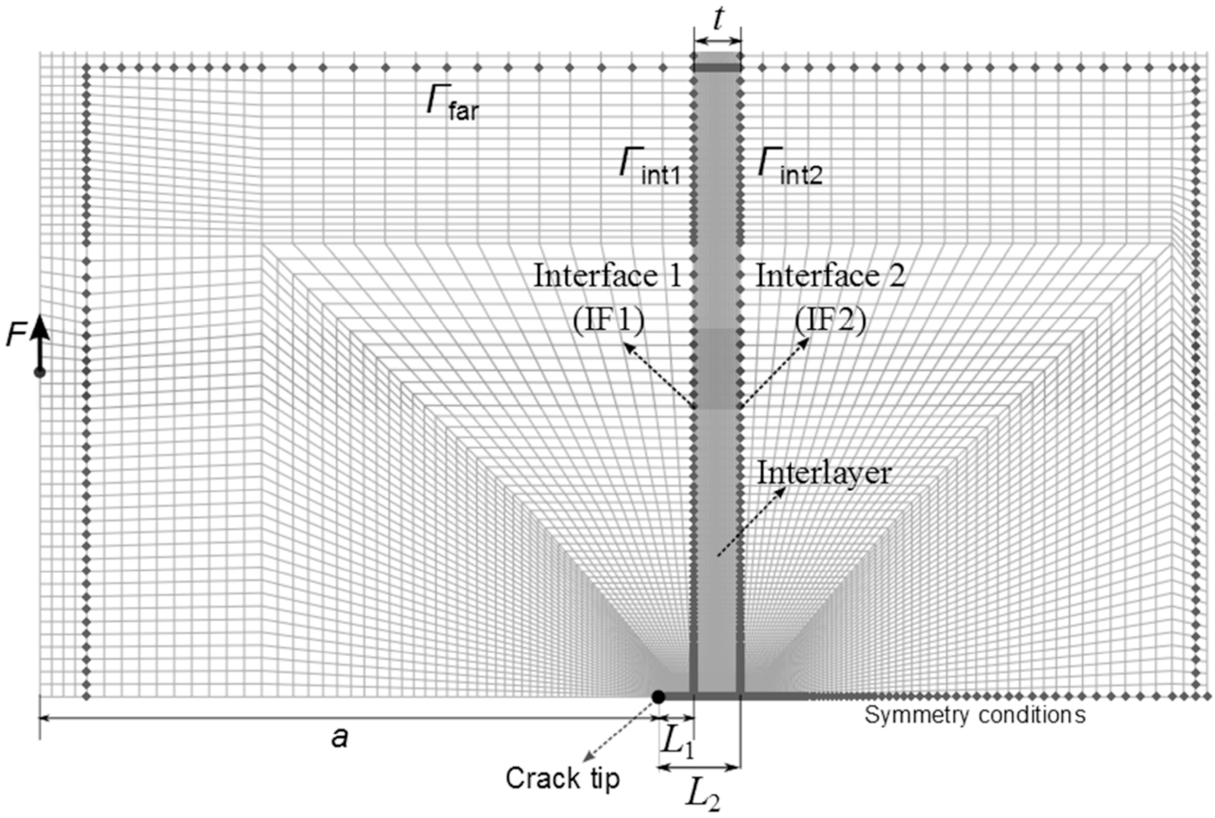

Fig. 5.1 Finite element mesh of the CT-specimen with an interlayer (two sharp interfaces) perpendicular to the crack. The paths for evaluating the far-field *J*-integral and the material inhomogeneity terms, C_{inh1} and C_{inh2}, are indicated. L_1 and L_2 are the distances between crack tip and IF1 and IF2, respectively.

It is noted that when deformation theory of plasticity is used, ϕ is taken as the total strain energy density for calculating the material inhomogeneity term by Eq. (5.6). When incremental theory of plasticity is applied, ϕ is taken as the elastic part of the strain energy density in Eq. (5.6). The physical meaning of the *J*-integral as crack driving force term for deformation- and incremental theory of plasticity and for stationary and growing cracks is discussed in a recent paper by Kolednik et al. (2014b).

5.4 Numerical modeling

The FE analyses are implemented for a standard Compact Tension specimen (Fig. 5.1) that has an interlayer with two sharp interfaces, interface 1 (IF1) and interface 2 (IF2), where the material properties exhibit a jump. Both the base material and the interlayer are assumed to be isotropic elastic–plastic materials with ideally plastic behavior (without hardening), and the bonding at the interfaces is assumed to be perfect. The specimen width is $W = 50$ mm, the height from the crack plane to the upper or lower surface is $h = 30$ mm, the specimen thickness is B = 25 mm, and the crack length a = 29 mm. A straight crack is assumed lying perpendicular to the interfaces, where L_1 and L_2 are the distances between the crack tip and IF1 and IF2, respectively. When the crack tip is situated left of an interface, L (the distance between the crack tip and the interface) is negative. A positive L denotes that the crack tip is situated right of an interface. For example, L_1 and L_2 are negative in the situation depicted in Fig. 5.1. L_1 and L_2 are related by

$$L_2 = L_1 - t, \tag{5.8}$$

where t is the interlayer thickness. For evaluating the variation of the crack driving force for various positions of the crack tip with respect to the interlayer, the crack length is kept constant and the position of the interlayer in the specimen is varied. No real crack extension is modeled and instead of that, specimens with stationary cracks are modeled.

The numerical analyses are performed with a commercial implementation of the finite element method (ABAQUS, http://www.simulia.com/products/abaqus_fea.html). The analyses are performed for two-dimensional FE models under the assumption of plane strain condition. Both small strain and large strain formulations can be considered. For several cases, comparisons have been made between the results of small strain and large strain formulations, and we found that the use of small strain theory is accurate enough for our analyses. Therefore, small strain formulations are generally adopted. 4 node elements are used for discretizing the FE models. The minimum mesh size, which is near to the crack tip, depends on the distance between the crack tip and the interface. In order to get sufficient accuracy, at least 10 elements lie between the crack tip and the interface (Fig. 5.1 shows the mesh of the specimen).

In the FE-modeling, the elastic–plastic materials are modeled using the incremental plasticity model provided by ABAQUS and the loading is controlled by prescribing the load-line displacement. After the FE analysis, the material inhomogeneity term, C_{inh}, by Eq. (5.6) and the far-field J-integral, J_{far}, are evaluated for each increment of displacement by a post-processing process. It should be noted that in order to calculate the material inhomogeneity term, C_{inh}, by Eq. (5.6) and the far-field J-integral, J_{far}, ϕ is taken as the total strain energy density. Therefore, deformation theory of plasticity is used in the post-processing procedure, i.e. the material is treated as if it were non-linear elastic. Such a treatment is conventionally used when applying the J-integral concept to elastic–plastic materials. Non-negligible differences may appear between C_{inh}-values calculated from deformation theory of plasticity and incremental theory of plasticity if the conditions of proportional loading are violated (Schöngrundner 2011).

After evaluating the configurational body force at each node using post processing, J_{far} is calculated by the summation of all configurational forces along the rectangular contour Γ_{far} (see Fig. 5.1) in the direction of crack extension. Γ_{far} is taken so that it lies one element inside the outer boundary of the specimen, and the region around the load application points is excluded (Kolednik et al. 2010; Simha et al. 2003; Simha et al. 2005). It is worth noting that J_{far} can also be calculated by the summation of configurational forces along the boundary of the specimen (Fischer et al. 2012b). The material inhomogeneity term of IF1, C_{inh1}, and the material inhomogeneity term of IF2, C_{inh2}, are calculated by the sum of the configurational forces on IF1 and IF2, respectively. It has been found that the configurational forces appear not only directly at nodes on the interface, but also at nodes adjacent to the interface. Therefore, in order to accurately compute the material inhomogeneity term from Eq. (5.6), the integration should be performed around a region consisting all nodes on and adjacent to the interface. It is recommended to see (Kolednik et al. 2010; Simha et al. 2003; Simha et al. 2005) for more information regarding the numerical evaluation of J_{far} and C_{inh}. Once the far-field J-integral and material inhomogeneity terms are calculated for each crack tip position, the crack driving force can be determined from the relation

$$J_{\mathrm{tip}} = J_{\mathrm{far}} + C_{\mathrm{inh1}} + C_{\mathrm{inh2}}. \tag{5.9}$$

It is noted that the virtual crack extension method of ABAQUS (Parks 1977) can also be applied for calculating the far-field J-integral and material inhomogeneity terms. Using this method, the far-field J-integral can be calculated by evaluation of the J-integral around the rectangular contour Γ_{far}. The material inhomogeneity term is determined by evaluation of the J-integral around the interface (J_{int}), $C_{\mathrm{inh}} = -J_{\mathrm{int}}$ (Simha et al. 2005). J_{int} can be readily evaluated by specifying the set of nodes on the interface as virtual crack tip nodes.

5.5 *The material inhomogeneity effect due to a single soft interlayer on the crack driving force*

In this section, the influence of the yield stress variation due to a single soft interlayer on the crack driving force is demonstrated. This is done by considering a CT specimen made of the matrix and interlayer with the same elastic properties, Young's modulus E = 70 GPa and Poisson's ratio ν = 0.3, but different yield stresses. The yield stresses of the matrix and interlayer are 500 MPa and 200 MPa, respectively. In the current paper, this material combination is referred to as "standard material combination". The interlayer thickness is t = 0.3 mm.

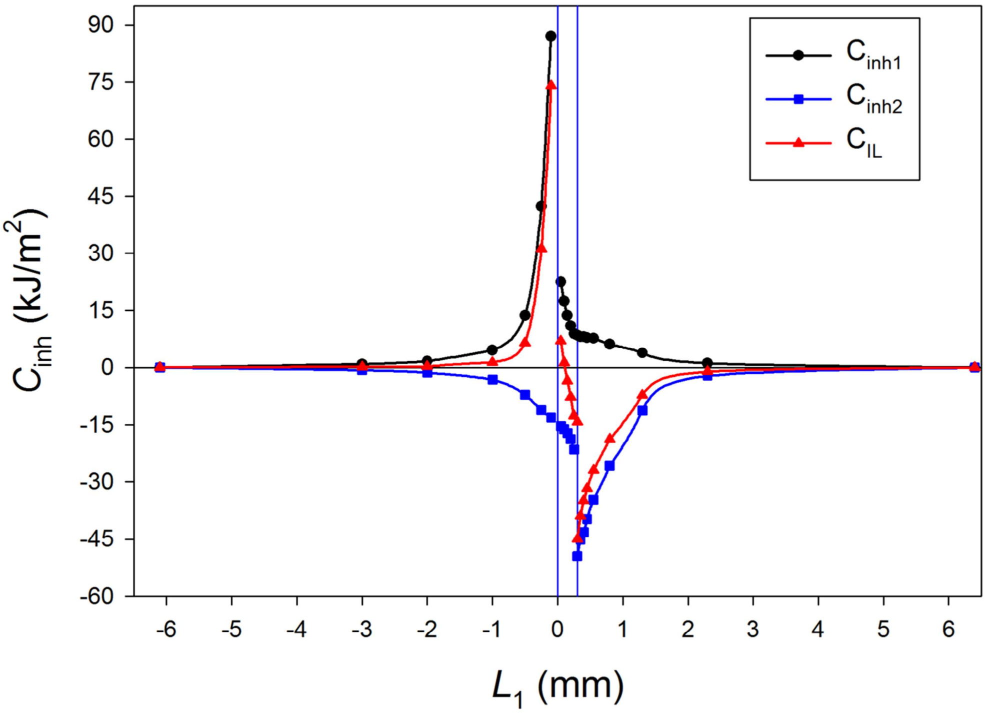

Fig. 5.2 C_{inh1}, C_{inh2} and C_{IL} plotted against L_1 for an elastic–plastic single interlayer specimen with $t = 0.3$ mm and at $J_{far} = 60$ kJ/m^2.

The material inhomogeneity terms of IF1 and IF2, C_{inh1} and C_{inh2}, the far-field J-integral, J_{far}, and the resulting crack driving force are evaluated, as explained in Section 5.4, for various positions of the crack tip with respect to the interlayer and for various loads. 20 different crack tip positions are evaluated where L_1 varies between $-6.1 \leq L_1 \leq 6.4$ mm. Fig. 5.2 shows, as an example, the material inhomogeneity term of IF1, C_{inh1}, and the material inhomogeneity term of IF2, C_{inh2}, plotted against L_1 for a constant value of the far-field J-integral, $J_{far} = 60$ kJ/m^2. As it can be seen, C_{inh1} is zero when $L_1 \leq -6.1$ mm, because the crack tip plastic zone does not touch IF1. However, C_{inh1} becomes non-zero when the plastic zone starts to interact with IF1, the radius of the plastic zone in the interlayer calculated by Eq. (5.4) is 6.1 mm for $J_{far} = 60$ kJ/m^2. Due to a hard/soft transition at IF1, C_{inh1} is positive as long as the plastic zone touches IF1, which leads to an anti-shielding effect on the crack tip. C_{inh1} first increases with decreasing $|L_1|$ and reaches its maximum value when $L_1 \rightarrow 0$, and then after the crack has crossed IF1, C_{inh1} drops immediately. Then, C_{inh1} decreases slowly with L_1 and becomes zero at distance of $L_1 = 6.1$ mm or larger; the plastic zone does not touch IF1 when L_1 is larger than 6.1 mm.

The variation of C_{inh} can be explained by considering Eq. (5.6). The results show that the first term in Eq. (5.6), which describes the contribution of the jump of the strain energy density along the interface to the material inhomogeneity term, is the dominant term and the second term gives only a small contribution. As long as the crack tip plastic zone interacts with the interface, the strain energy density exhibits a jump at the interface and C_{inh} becomes effective. As explained in Simha et al. (2003), in a hard/soft transition, the jump of the strain energy density at the interface in the crack growth direction is negative, $[[\phi]] < 0$, and leads to $C_{\text{inh}} > 0$. This is why C_{inh1} is positive. According to the HRR-field solution[5] (Hutchinson 1968; Rice 1968a; Rice and Rosengren 1968), the strain energy density is inversely proportional to the distance to the crack tip. Therefore, when the crack approaches IF1, the absolute value of the jump of the strain energy density strongly increases and leads to a strong increase of C_{inh1}. After the crack has crossed IF1, the size of the plastic zone at the interface strongly decreases, due to the forward orientation of the plastic zone, and hence C_{inh1} drops immediately. The plastic zone is not circular and it has a complicated shape with its maximum extension at a certain angle ($\theta \approx 70^\circ$ for a homogeneous material) with respect to the crack plane.

There is a soft/hard transition at IF2 and C_{inh2} is zero or negative in Fig. 5.2, IF2 has a shielding effect on the crack tip. As it can be seen, C_{inh2} is first zero until the crack tip reaches a distance of about −6.1 mm from IF2. At this point the plastic zone in the soft interlayer reaches IF2 and a jump in the strain energy density appears. With further decreasing $|L_2|$, the absolute value of C_{inh2} increases. The reason is that with decreasing $|L_2|$, the strain energy density and its jump at the interface increases. Immediately after the crack has crossed IF2, the absolute value of C_{inh2} makes a jump, which is due to the forward orientation of the plastic zone in the matrix. Later, the absolute value of C_{inh2} decreases with L_2 and it becomes zero approximately at L_2 = 6.1 mm, at this point the interlayer does not exhibit plastic deformation.

The material inhomogeneity effect due to the interlayer on the crack driving force can be quantified by the summation of the material inhomogeneity term of IF1 and IF2,

$$C_{\text{IL}} = C_{\text{inh1}} + C_{\text{inh2}} . \tag{5.10}$$

We call this the "interlayer inhomogeneity term", C_{IL}. By inserting Eq. (5.10) into Eq. (5.9), the crack driving force can be determined from

$$J_{\text{tip}} = J_{\text{far}} + C_{\text{IL}} . \tag{5.11}$$

---

[5] Although the HRR-field solution relies on the existence of strain hardening, it contains the elastic-ideally plastic material as a limiting case (Rice 1968a).

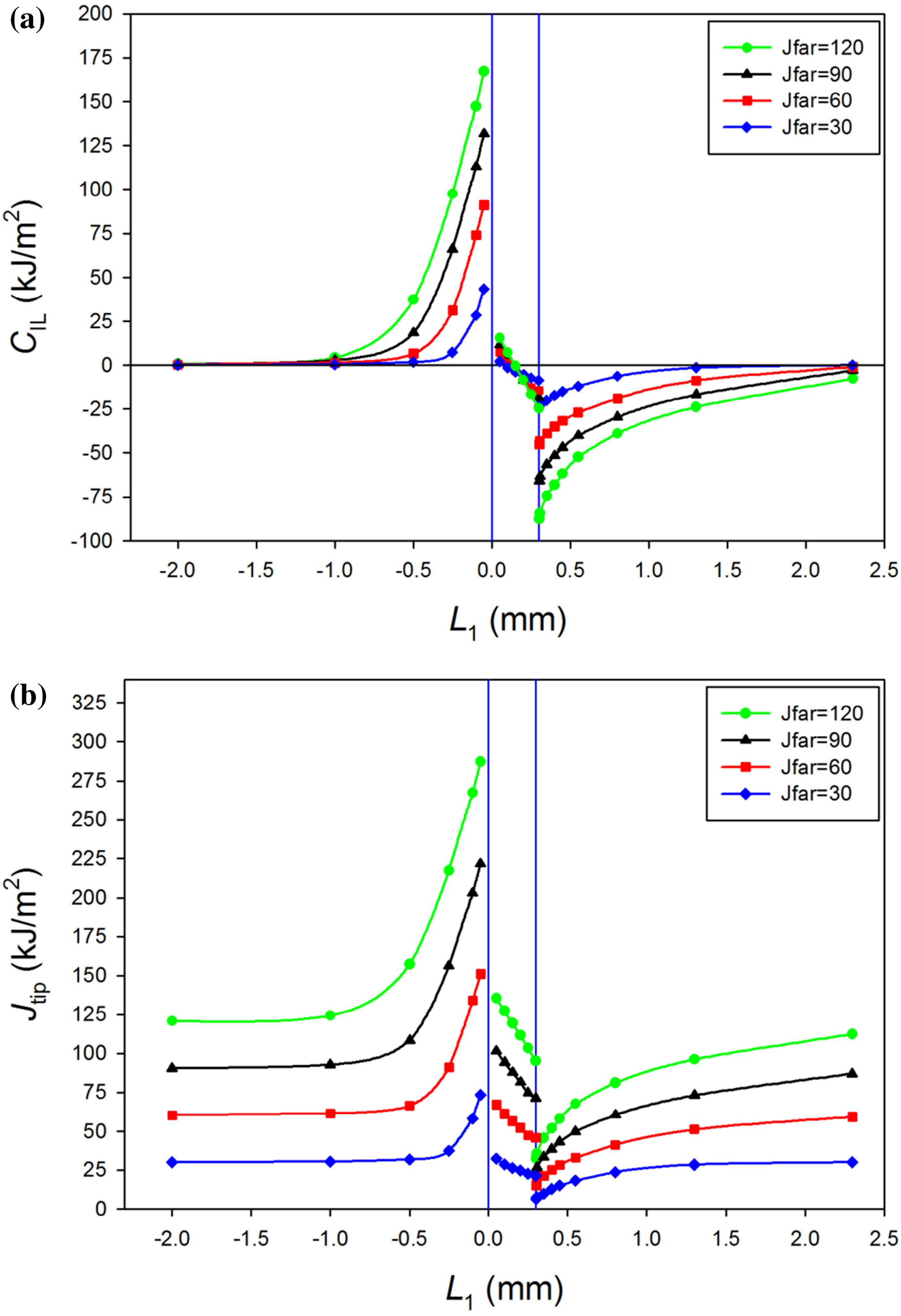

Fig. 5.3 C_{IL} and J_{tip} plotted against L_1 for an elastic–plastic single interlayer specimen with four different values of J_{far}.

Depending on the crack tip position, the interlayer can exert a shielding or anti-shielding effect on the crack tip. If C_{IL} is negative, the interlayer exerts a shielding effect on the crack tip and if C_{IL} is positive, an anti-shielding effect occurs. The magnitude of the interlayer inhomogeneity term, C_{IL}, for $J_{\mathrm{far}} = 60$ kJ/m^2 is also plotted in Fig. 5.2. C_{IL} first is positive and steeply increasing when the crack tip approaches IF1. After the crack has crossed IF1, C_{IL}

drops sharply, but it is still positive. C_{IL} decreases with L_1 and it becomes zero at a distance near the middle of the interlayer where C_{inh1} becomes identical to $|C_{\mathrm{inh2}}|$. With further increasing L_1, C_{IL} becomes negative. Immediately, when the crack tip re-enters the matrix, C_{IL} steeply drops and reaches its minimum value at this point. With increasing L_2, the absolute value of C_{IL} decreases until it becomes zero.

The influence of the magnitude of the load on the interlayer inhomogeneity term, C_{IL}, is shown in Fig. 5.3a. The absolute size of the interlayer inhomogeneity term, $|C_{\mathrm{IL}}|$, increases with J_{far} because, according to the HRR-field solution, the strain energy density is proportional to J_{far}. As it can be seen, C_{IL} becomes zero when the crack tip is located in the interlayer at a distance which depends on J_{far}, i.e. for small J_{far}-values, C_{IL} is zero at a distance close to IF1, but it becomes zero near to the middle of the interlayer for high J_{far}-values.

Fig. 5.3b shows the variation of the crack driving force, J_{tip}, for four different values of J_{far} between 30 and 120 kJ/m^2. As it can be seen, when the crack approaches the soft interlayer, the crack driving force first increases at IF1 and then decreases at IF2. The minimum value of J_{tip} is reached immediately when the crack has crossed IF2. This position is the critical position for possible crack arrest. The J_{tip}-values at the critical position are 6.6, 13.2, 19.8 and 26.4 kJ/m^2 for $J_{\mathrm{far}} = 30$, 60, 90 and 120 kJ/m^2, respectively. Consequently, a soft interlayer works as a very efficient crack arrester in materials, if the crack driving force becomes very low at the second interface. In Section 5.7, we explore the optimum thickness and yield stress of the soft interlayer so that the maximum reduction of the crack driving force can be achieved.

5.6 Normalization of material inhomogeneity terms

The material inhomogeneity terms of IF1 and IF2, C_{inh1} and C_{inh2}, and the resulting interlayer inhomogeneity term, C_{IL}, and the crack driving force, J_{tip}, are dependent on the magnitude of J_{far}, the distance between crack tip and interface, the material properties and the interlayer thickness. In order to provide a better understanding of the effective influence parameters on the material inhomogeneity terms, it is better to work with normalized data. The aim of this section is to find the effective dimensionless parameters on the normalized material inhomogeneity terms and to quantify their influences. It will be seen that if the material inhomogeneity terms, C_{inh1} and C_{inh2}, are expressed in a dimensionless form, they become dependent only on two dimensionless parameters.

5.6.1 Normalization of the material inhomogeneity terms of interfaces 1 and 2

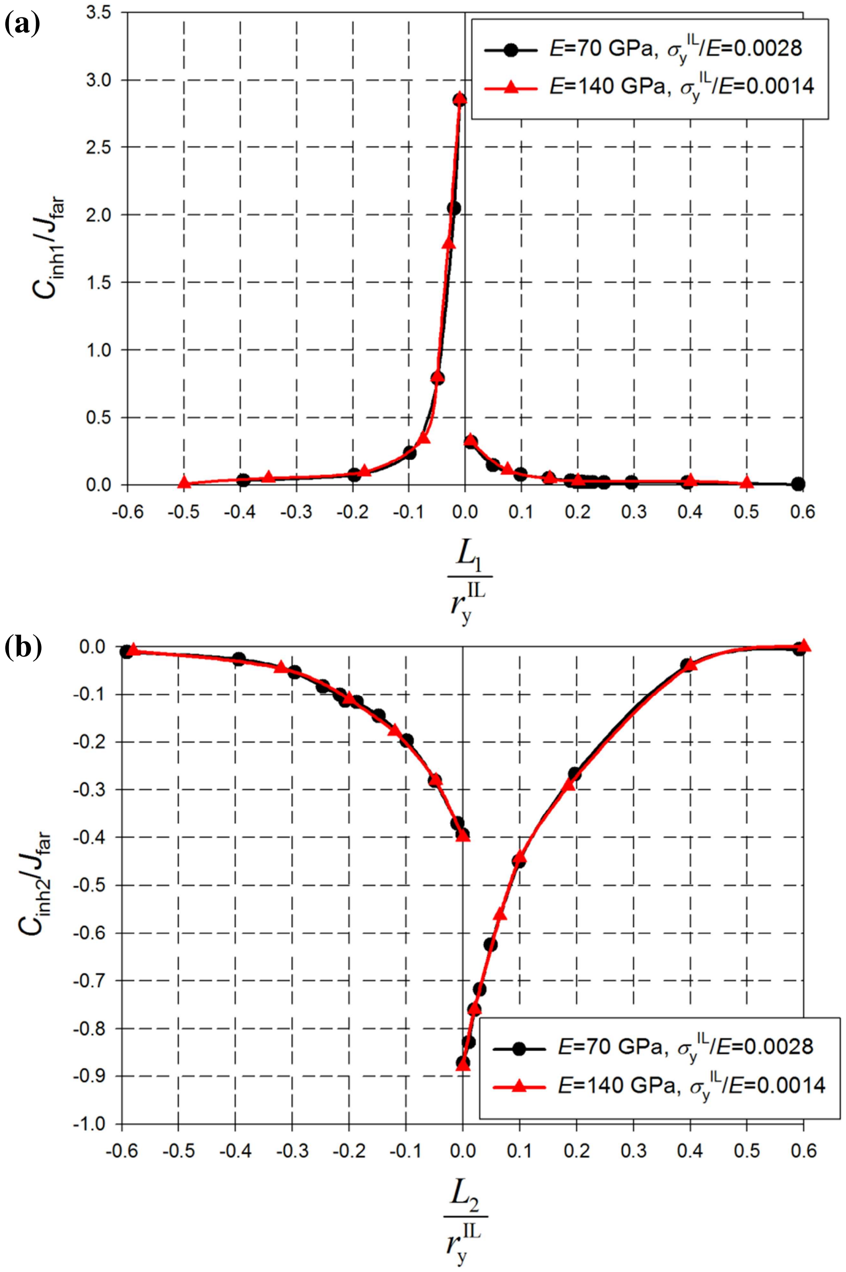

Fig. 5.4 Normalized material inhomogeneity terms plotted against the normalized distance $L / r_{\mathrm{y}}^{\mathrm{IL}}$ for elastic–plastic single interlayer specimens with two different Young's modulus, E = 70 and 140 GPa. **(a)** $C_{\mathrm{inh1}}/J_{\mathrm{far}}$ vs. $L_1 / r_{\mathrm{y}}^{\mathrm{IL}}$, **(b)** $C_{\mathrm{inh2}}/J_{\mathrm{far}}$ vs. $L_2 / r_{\mathrm{y}}^{\mathrm{IL}}$. Dimensionless parameter $\sigma_{\mathrm{y}}^{\mathrm{IL}} / E$ does not have an influence on the normalized material inhomogeneity terms.

The analytical model in Kolednik (2000), Eq. (5.2) and Eq. (5.3), gives the functional relationship of the normalized crack driving force $J_{\mathrm{tip}}/J_{\mathrm{far}}$ for a bimaterial specimen (which is made of materials 1 and 2) in the form,

$$\frac{J_{\text{tip}}}{J_{\text{far}}} = F\left(\frac{L}{r_{\text{y1}}}, \frac{r_{\text{y1}}}{r_{\text{y2}}}\right) = g\left(\frac{L}{r_{\text{y1}}}, \frac{\sigma_{\text{y2}}}{\sigma_{\text{y1}}}\right), \tag{5.12}$$

where the subscripts 1 and 2 refer to the softer and harder materials, respectively, and the radius of the plastic zone is given by Eq. (5.4). By substituting Eq. (5.7), the functional relationship of the normalized material inhomogeneity term $C_{\text{inh}}/J_{\text{far}}$ for a bimaterial can be written as

$$\frac{C_{\text{inh}}}{J_{\text{far}}} = f\left(\frac{L}{r_{\text{y1}}}, \frac{\sigma_{\text{y2}}}{\sigma_{\text{y1}}}\right). \tag{5.13}$$

Eq. (5.13) shows that the normalized material inhomogeneity term $C_{\text{inh}}/J_{\text{far}}$ is related directly to the term r_{y1}/L and the yield stress ratio $\sigma_{\text{y1}}/\sigma_{\text{y2}}$. The term r_{y1}/L is a measure of the plastic zone size relative to L and is a loading parameter since r_{y} is directly proportional to J_{far}, see Eq. (5.4).

For an interlayer with two sharp interfaces where the matrix and interlayer are elastically homogenous, but have different yield stresses, the two material inhomogeneity terms C_{inh1} and C_{inh2} can be presented in a dimensionless form as Eq. (5.13) as long as the interlayer thickness t is so large that the plasticity in the interlayer is not confined by the interfaces. If this condition is not fulfilled, one would expect that $t / r_{\text{y}}^{\text{IL}}$ should appear as third dimensionless parameter. We will see later that this parameter has only very little influence on the dimensionless material inhomogeneity terms so that it is negligible. The functional relationship of the normalized material inhomogeneity terms at the interlayer can be written as

$$\begin{aligned} \frac{C_{\text{inh1}}}{J_{\text{far}}} &= f_1\left(\frac{L_1}{r_{\text{y}}^{\text{IL}}}, \frac{\sigma_{\text{y}}^{\text{IL}}}{\sigma_{\text{y}}^{\text{M}}}\right) \\ \frac{C_{\text{inh2}}}{J_{\text{far}}} &= f_2\left(\frac{L_2}{r_{\text{y}}^{\text{IL}}}, \frac{\sigma_{\text{y}}^{\text{IL}}}{\sigma_{\text{y}}^{\text{M}}}\right), \end{aligned} \tag{5.14}$$

where the superscripts IL and M refer to the interlayer and matrix, respectively.

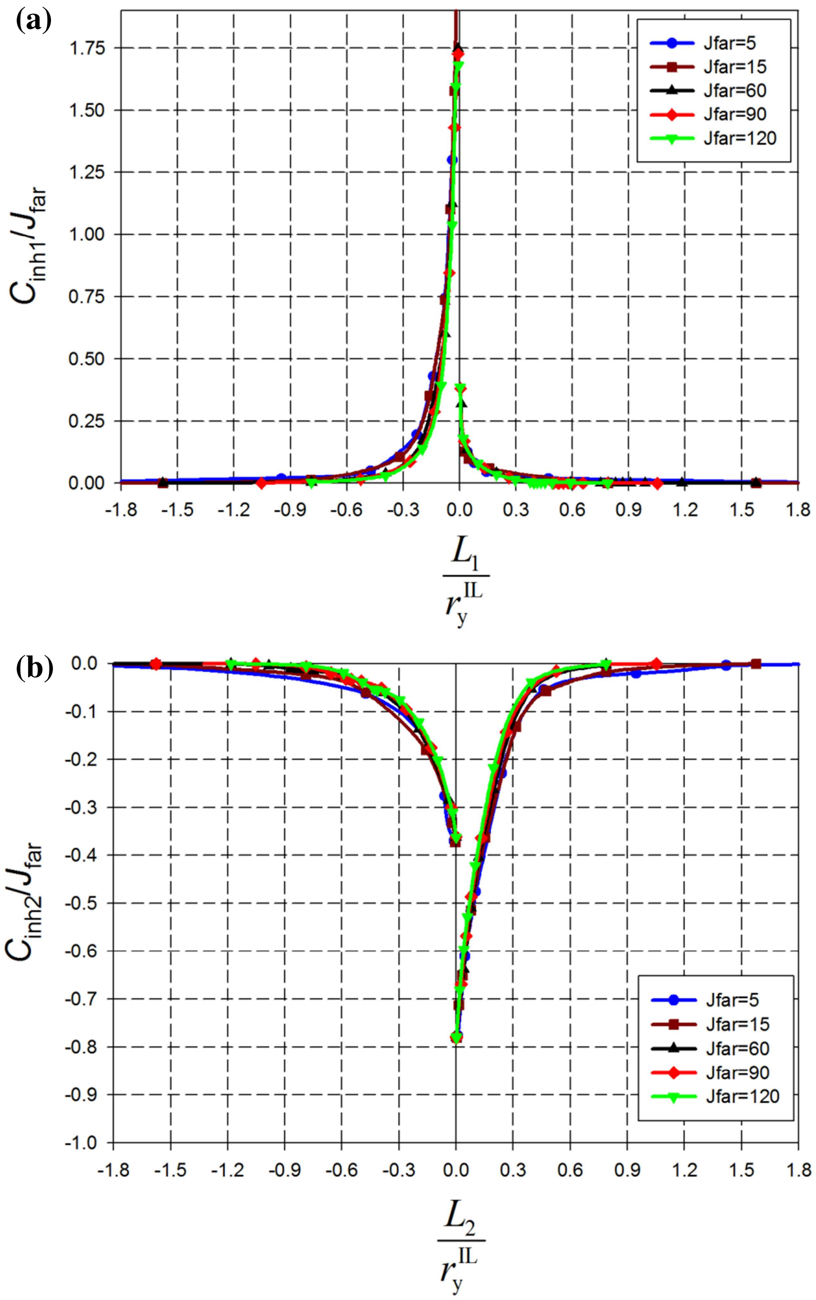

Fig. 5.5 Normalized material inhomogeneity terms plotted against the normalized distance between crack tip and the two interfaces for five different values of J_{far} between 5 kJ/m^2 and 120 kJ/m^2. **(a)** $C_{\mathrm{inh1}}/J_{\mathrm{far}}$ plotted against L_1 / r_y^{IL}, **(b)** $C_{\mathrm{inh2}}/J_{\mathrm{far}}$ plotted against L_2 / r_y^{IL}. The curves for different J_{far}-values coincide well.

Sugimura et al. (1995) and Kim et al. (1997) included additionally a term σ_{y1} / E into Eq. (5.12). Therefore, we perform a check whether σ_{y1} / E has an influence on the normalized material inhomogeneity term $C_{\mathrm{inh}}/J_{\mathrm{far}}$. Fig. 5.4 shows the normalized material inhomogeneity terms of IF1 and IF2, $C_{\mathrm{inh1}}/J_{\mathrm{far}}$ and $C_{\mathrm{inh2}}/J_{\mathrm{far}}$, plotted against the normalized distance between crack tip and the two interfaces, L_1 / r_y^{IL} and L_2 / r_y^{IL}, for single interlayer specimens with two different values of Young's modulus, E = 70 and 140 GPa. The yield stress of the matrix and soft interlayer are 900 and 200 MPa, respectively, and t = 0.3 mm. It can be seen that the curves ($C_{\mathrm{inh1}}/J_{\mathrm{far}}$ vs. $L_1 / r_{\mathrm{y}}^{\mathrm{IL}}$ and $C_{\mathrm{inh2}}/J_{\mathrm{far}}$ vs. $L_2 / r_{\mathrm{y}}^{\mathrm{IL}}$) for $\sigma_{\mathrm{y}}^{\mathrm{IL}} / E = 0.0028$ coincide with the curves for $\sigma_{\mathrm{y}}^{\mathrm{IL}} / E = 0.0014$. Therefore, it is concluded that the term $\sigma_{\mathrm{y}}^{\mathrm{IL}} / E$ does not have an influence on the normalized material inhomogeneity terms and Eq. (5.14) is correct.

Fig. 5.5 displays the normalized material inhomogeneity terms $C_{\mathrm{inh1}}/J_{\mathrm{far}}$ and $C_{\mathrm{inh2}}/J_{\mathrm{far}}$ plotted against $L_1 / r_{\mathrm{y}}^{\mathrm{IL}}$ and $L_2 / r_{\mathrm{y}}^{\mathrm{IL}}$, respectively, for five different values of J_{far} between 5 kJ/m^2 and 120 kJ/m^2 where t = 0.3 mm and the specimen is made of the standard material combination. The curves $C_{\mathrm{inh1}}/J_{\mathrm{far}}$ versus $L_1 / r_{\mathrm{y}}^{\mathrm{IL}}$ and $C_{\mathrm{inh2}}/J_{\mathrm{far}}$ versus $L_2 / r_{\mathrm{y}}^{\mathrm{IL}}$ are not symmetric with respect to the line $L_1 / r_{\mathrm{y}}^{\mathrm{IL}} = 0$ and $L_2 / r_{\mathrm{y}}^{\mathrm{IL}} = 0$, respectively. As explained before, the strong non-symmetry of $C_{\mathrm{inh1}}/J_{\mathrm{far}}$ and $C_{\mathrm{inh2}}/J_{\mathrm{far}}$ with respect to IF1 and IF2 occurs because of the forward orientation of the plastic zone. As it can be seen in Figs. 5.5a and 5.5b, the curves $C_{\mathrm{inh1}}/J_{\mathrm{far}}$ versus $L_1 / r_{\mathrm{y}}^{\mathrm{IL}}$ and $C_{\mathrm{inh2}}/J_{\mathrm{far}}$ versus $L_2 / r_{\mathrm{y}}^{\mathrm{IL}}$ for different values of J_{far} coincide and it shows that the normalized material inhomogeneity terms, $C_{\mathrm{inh1}}/J_{\mathrm{far}}$ and $C_{\mathrm{inh2}}/J_{\mathrm{far}}$, are independent of the J_{far} values if the dimensionless parameter $L / r_{\mathrm{y}}^{\mathrm{IL}}$ is kept constant.

In Fig. 5.6, the normalized material inhomogeneity terms $C_{\mathrm{inh1}}/J_{\mathrm{far}}$ and $C_{\mathrm{inh2}}/J_{\mathrm{far}}$ plotted against the normalized distance between crack tip and the two interfaces, $L_1 / r_{\mathrm{y}}^{\mathrm{IL}}$ and $L_2 / r_{\mathrm{y}}^{\mathrm{IL}}$, where t = 0.3 mm and E = 70 GPa. The two curves correspond to two different yield stress combinations, $\sigma_{\mathrm{y}}^{\mathrm{IL}} = 200$ MPa, $\sigma_{\mathrm{y}}^{\mathrm{M}} = 900$ MPa and $\sigma_{\mathrm{y}}^{\mathrm{IL}} = 400$ MPa, $\sigma_{\mathrm{y}}^{\mathrm{M}} = 1800$ MPa, but the yield stress ratio is constant, $\sigma_{\mathrm{y}}^{\mathrm{IL}} / \sigma_{\mathrm{y}}^{\mathrm{M}} = 0.22$. It can be seen that the curves coincide when the yield stress ratio is identical. Figs. 5.6a and 5.6b show that, by keeping constant the values of $L_1 / r_{\mathrm{y}}^{\mathrm{IL}}$ and $L_2 / r_{\mathrm{y}}^{\mathrm{IL}}$, the normalized material inhomogeneity terms $C_{\mathrm{inh1}}/J_{\mathrm{far}}$ and $C_{\mathrm{inh2}}/J_{\mathrm{far}}$ do not depend on absolute values of the yield stresses, but are dependent on the yield stress ratio.

Fig. 5.7 shows the normalized material inhomogeneity terms of IF1 and IF2, $C_{\mathrm{inh1}}/J_{\mathrm{far}}$ and $C_{\mathrm{inh2}}/J_{\mathrm{far}}$, plotted against the normalized distance between crack tip and the two interfaces, $L_1 / r_{\mathrm{y}}^{\mathrm{IL}}$ and $L_2 / r_{\mathrm{y}}^{\mathrm{IL}}$, for single interlayer specimens made of the standard material combination with three different interlayer thicknesses, t = 0.1, 0.3 and 1 mm. As it can be seen, the curves $C_{\mathrm{inh1}}/J_{\mathrm{far}}$ versus $L_1 / r_{\mathrm{y}}^{\mathrm{IL}}$ and $C_{\mathrm{inh2}}/J_{\mathrm{far}}$ versus $L_2 / r_{\mathrm{y}}^{\mathrm{IL}}$ for different interlayer thicknesses coincide well. Therefore, the normalized material inhomogeneity terms $C_{\mathrm{inh1}}/J_{\mathrm{far}}$ and $C_{\mathrm{inh2}}/J_{\mathrm{far}}$ do not depend on the interlayer thickness. The reason is that the plastic zone sizes at the left and right sides of each interface are not dependent on the interlayer thickness; they depend on the normalized distance between crack tip and interface $L / r_{\mathrm{y}}^{\mathrm{IL}}$ and $L / r_{\mathrm{y}}^{\mathrm{M}}$. Fig. 5.8 shows the shape of the plastic zone at J_{far} = 5.5 kJ/m^2 ($r_{\mathrm{y}}^{\mathrm{IL}}$ = 0.56 mm) for interlayer specimens made of the standard material combination with constant L_1, L_1 = −0.1 mm and $L_1 / r_{\mathrm{y}}^{\mathrm{IL}} = -0.178$, but three different interlayer thicknesses t = 0.1, 0.3 and 1 mm (L_2 = −0.2, −0.4 and −1.1 mm). As it is shown, the plastic zone sizes at both sides of IF1 are constant for

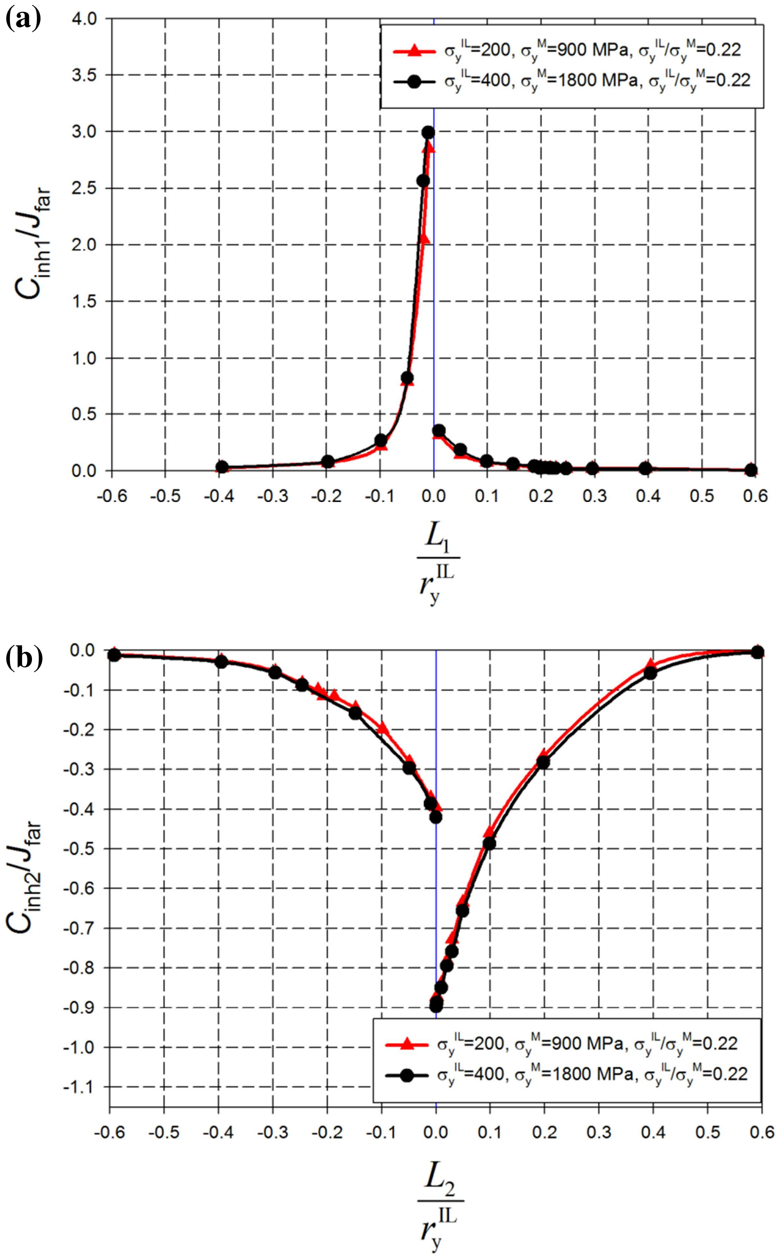

Fig. 5.6 Normalized material inhomogeneity terms plotted against the normalized distance L/r_y^{IL} for elastic–plastic single interlayer specimens with constant yield stress ratio. **(a)** C_{inh1}/J_{far} vs. L_1/r_y^{IL}, **(b)** C_{inh2}/J_{far} vs. L_2/r_y^{IL}. The curves coincide when the yield stress ratio is constant.

three different interlayer thicknesses (the plastic zone sizes at the left and right sides are 0.18 and 0.91 mm, respectively). C_{inh1} is calculated to be constant for three different interlayer thicknesses (C_{inh1} = 0.95 kJ/m^2) which is reasonable, since the plastic zone sizes at both sides of IF1 are constant for different interlayer thicknesses. It is mentioned that C_{inh2} is not constant for three different interlayer thicknesses, because the value of L_2/r_y^{IL} differs.

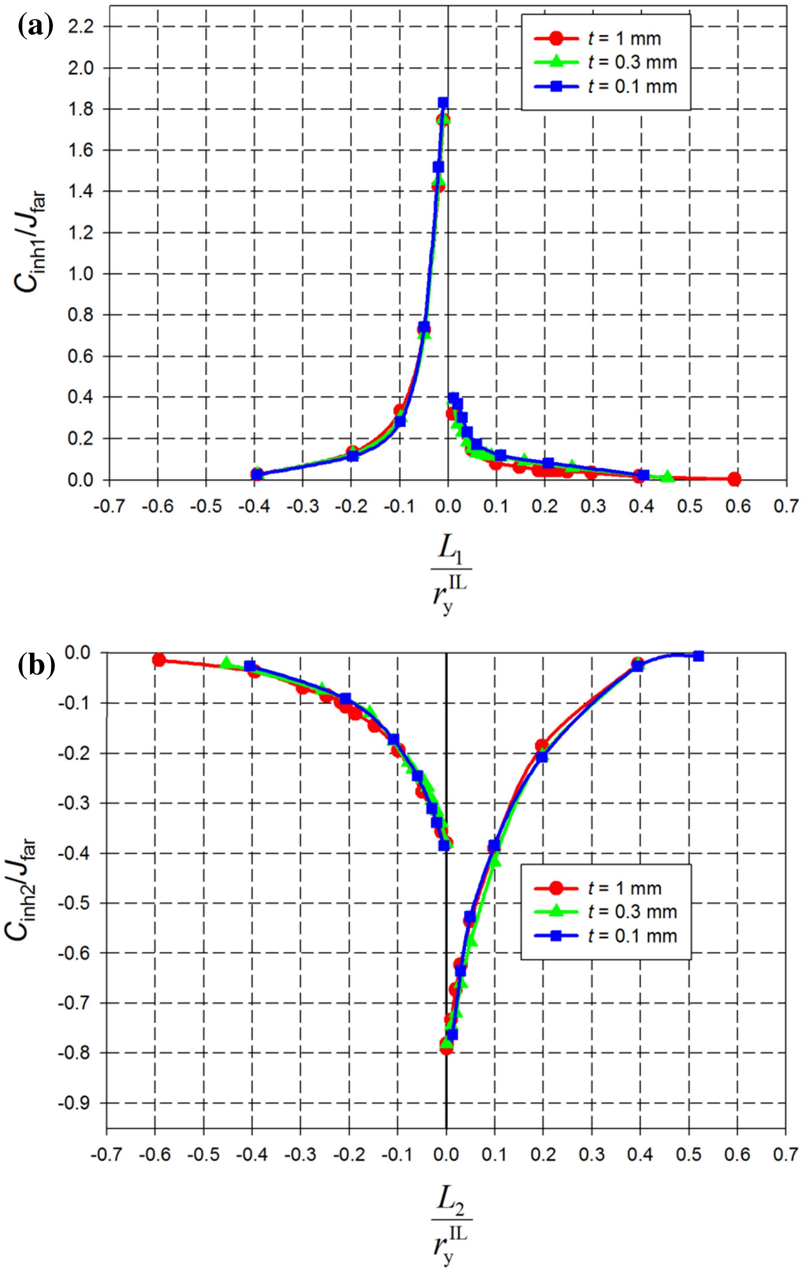

Fig. 5.7 Normalized material inhomogeneity terms plotted against the normalized distance L/r_y^{IL} for elastic–plastic single interlayer specimens with three different values of t. **(a)** $C_{\text{inh1}}/J_{\text{far}}$ vs. L_1/r_y^{IL}, **(b)** $C_{\text{inh2}}/J_{\text{far}}$ vs. L_2/r_y^{IL}. The interlayer thickness does not have an influence on the normalized material inhomogeneity terms.

Figs. 5.4–5.7 show that the normalized material inhomogeneity terms are only a function of the two dimensionless parameters L/r_y^{IL} and $\sigma_y^{\text{IL}}/\sigma_y^{\text{M}}$. Fig. 5.9 shows the influence of the yield stress ratio $\sigma_y^{\text{IL}}/\sigma_y^{\text{M}}$ on the normalized material inhomogeneity terms $C_{\text{inh1}}/J_{\text{far}}$ and $C_{\text{inh2}}/J_{\text{far}}$. $C_{\text{inh1}}/J_{\text{far}}$ and $C_{\text{inh2}}/J_{\text{far}}$ are plotted against L_1/r_y^{IL} and L_2/r_y^{IL}, respectively, for a single interlayer specimen with t = 0.3 mm, $\sigma_y^{\text{IL}} = 200$ MPa, and four different yield stress ratios $\sigma_y^{IL}/\sigma_y^{M}$ between 0.8 and 0. The later value is related to the case of an elastic–plastic interlayer in an elastic matrix. It can be seen that the C_{inh1}/J_{far} and $|C_{inh2}/J_{far}|$ values increase with decreasing $\sigma_y^{IL}/\sigma_y^{M}$. The reason is that the jump of the strain energy density at the two interfaces increases. For $L_1 < 0$, the yield stress ratio has a significant effect on the C_{inh1}-values and they increase considerably with decreasing $\sigma_y^{IL}/\sigma_y^{M}$. For example, for $L_1/r_y^{IL} = -0.015$, the term C_{inh1}/J_{far} is 5 for $\sigma_y^{IL}/\sigma_y^{M} \to 0$, but it is 0.7 for $\sigma_y^{IL}/\sigma_y^{M} = 0.67$. The curve C_{inh2}/J_{far} for each $\sigma_y^{IL}/\sigma_y^{M}$ reaches its minimum value where $L_2/r_y^{IL} \to 0$ and the crack tip is located at the right side of IF2. For $L_2 > 0$, the curves for IF2 show that the term C_{inh2}/J_{far} becomes approximately constant, if $\sigma_y^{IL}/\sigma_y^{M}$ is smaller than 0.22.

5.6.2 Normalization of the interlayer inhomogeneity term

The normalized crack driving force for a single interlayer specimen can be determined from

$$\frac{J_{tip}}{J_{far}} = 1 + \frac{C_{IL}}{J_{far}} = 1 + \frac{C_{inh1}}{J_{far}} + \frac{C_{inh2}}{J_{far}}. \tag{5.15}$$

By inserting Eq. (5.14) and Eq. (5.8), the functional relationship of the normalized crack driving force can be expressed as

$$\frac{J_{tip}}{J_{far}} = f\left(\frac{L_1}{r_y^{IL}}, \frac{L_2}{r_y^{IL}}, \frac{\sigma_y^{IL}}{\sigma_y^{M}}\right) = f\left(\frac{L_1}{r_y^{IL}}, \frac{L_1 - t}{r_y^{IL}}, \frac{\sigma_y^{IL}}{\sigma_y^{M}}\right). \tag{5.16}$$

Eq. (5.16) shows that the interlayer thickness has an influence on the normalized crack driving force. The normalized crack driving force, or the normalized interlayer inhomogeneity term, is a function of the three dimensionless parameters L_1/r_y^{IL}, t/r_y^{IL} and $\sigma_y^{IL}/\sigma_y^{M}$.

It is interesting to compare the solution of the analytical model of Kolednik (2000) to the FE results. Note that the term C_y in Eq. (5.5) corresponds to the interlayer inhomogeneity term C_{IL}, Eq. (5.10). The normalized material inhomogeneity terms of IF1 and IF2 can be derived analytically as,

$$\begin{aligned}
\frac{C_{inh1}}{J_{far}} &= \frac{1}{2\pi}\left\{\mathrm{Re}\left(\mathrm{arctanh}\sqrt{1-\left(\frac{L_1}{r_y^{IL}}\right)^2}\right) - \mathrm{Re}\left(\mathrm{arctanh}\sqrt{1-\left(\frac{L_1}{r_y^{IL}}\right)^2\left(\frac{\sigma_y^{M}}{\sigma_y^{IL}}\right)^4}\right)\right\} \\
\frac{C_{inh2}}{J_{far}} &= \frac{1}{2\pi}\left\{\mathrm{Re}\left(\mathrm{arctanh}\sqrt{1-\left(\frac{L_2}{r_y^{IL}}\right)^2\left(\frac{\sigma_y^{M}}{\sigma_y^{IL}}\right)^4}\right) - \mathrm{Re}\left(\mathrm{arctanh}\sqrt{1-\left(\frac{L_2}{r_y^{IL}}\right)^2}\right)\right\}.
\end{aligned} \tag{5.17}$$

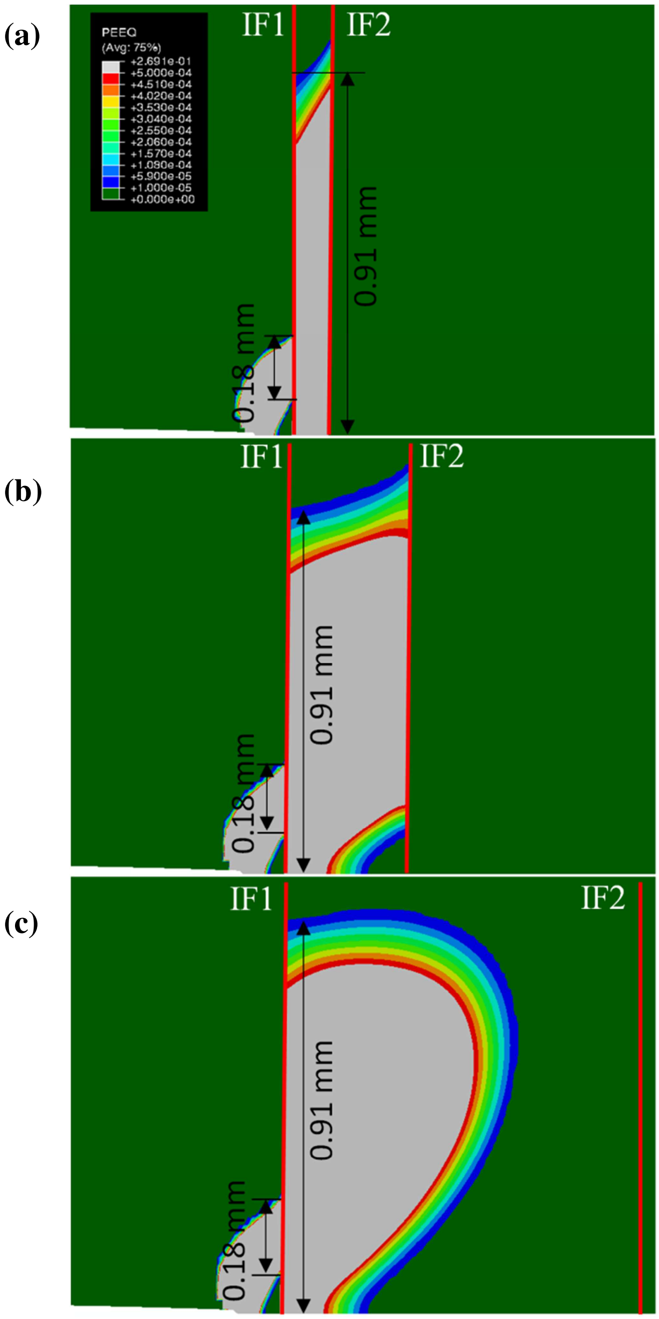

Fig. 5.8 The shape of the plastic zone at $J_{\mathrm{far}} = 5.5$ kJ/m^2 for interlayer specimens with $L_1 = -0.1$ mm and three different interlayer thicknesses. **(a)** $t = 0.1$ mm, **(b)** $t = 0.3$ mm and **(c)** $t = 1$ mm.

Fig. 5.10 compares $J_{\mathrm{tip}}/J_{\mathrm{far}}$ estimated by the analytical model to those obtained by the FE computations for a single interlayer specimen at $J_{\mathrm{far}} = 1$ kJ/m^2 with the standard material combination and $t = 0.3$ mm. As it can be seen, there are deviations between the analytical predictions and the FE results. Possible reasons have been discussed already in Kolednik (2000): Assumption of small-scale yielding condition, neglect of misfit strains, and use of the

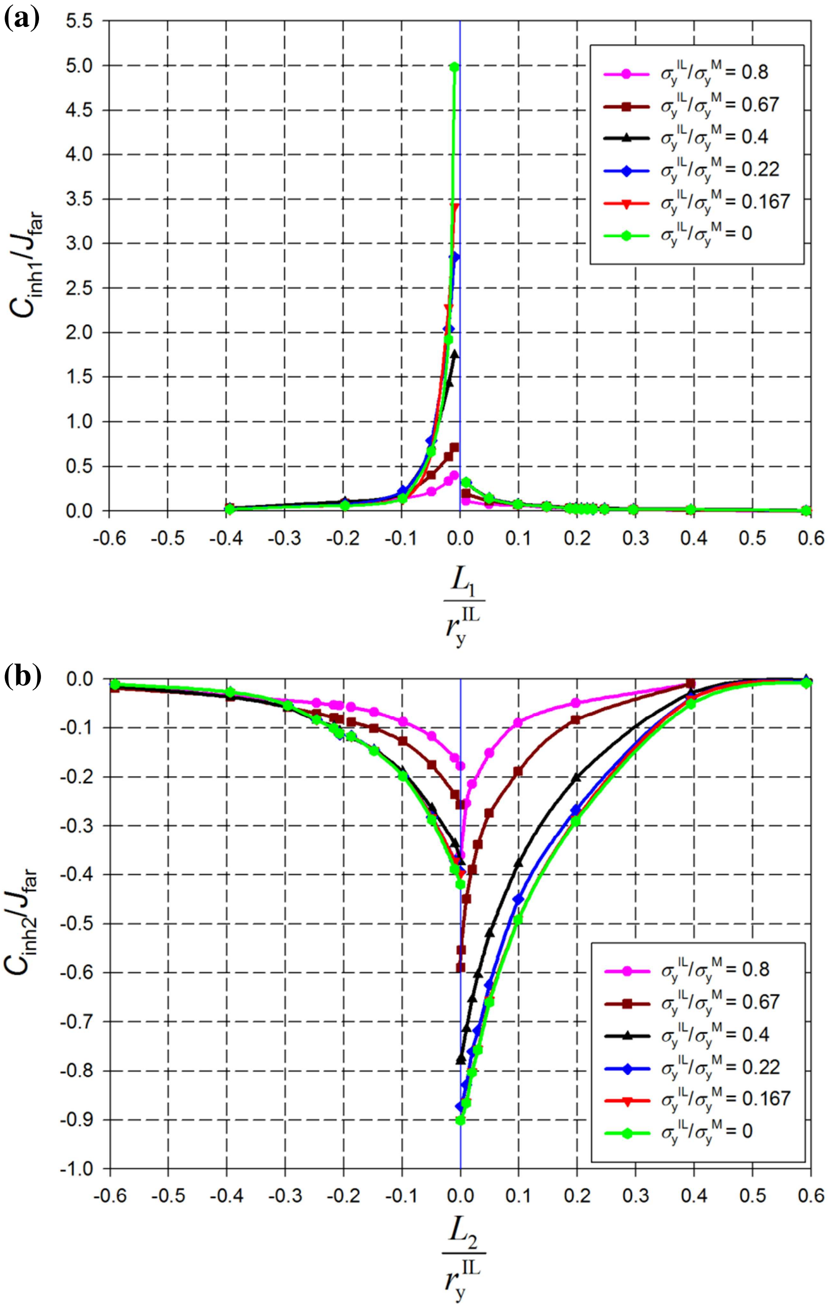

Fig. 5.9 Normalized material inhomogeneity terms plotted against the normalized distance L / r_y^{IL} for an elastic–plastic single interlayer specimen with four different yield stress ratios $\sigma_y^{IL} / \sigma_y^M$ between 0 and 0.8. **(a)** C_{inh1}/J_{far} vs. L_1 / r_y^{IL}, **(b)** C_{inh2}/J_{far} vs. L_2 / r_y^{IL}.

circular plastic zones. The analytical model tends to underestimate J_{tip}/J_{far}-values when the crack tip is located at the matrix and close to IF1, and it tends to overestimate J_{tip}/J_{far}-values when the crack tip is situated at the critical position for possible crack arrest. As can be seen, the minimum value of J_{tip}/J_{far} is overestimated by a factor of 1.44 compared to the FE results.

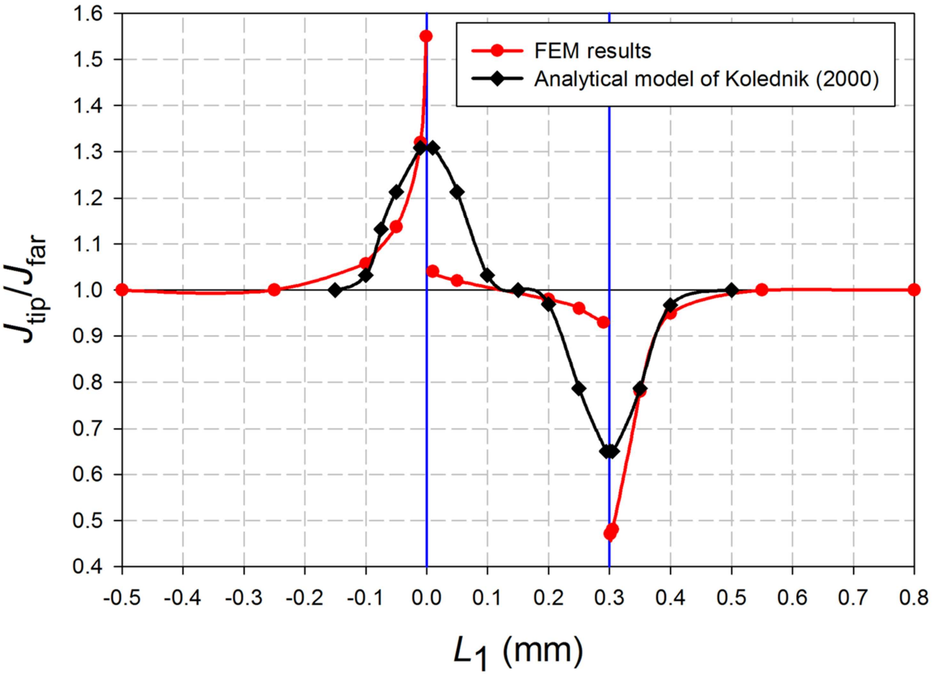

Fig. 5.10 Comparison between the predictions of the analytical model and FE computations for a single interlayer specimen. J_{tip}/J_{far} is plotted against L_1.

The results presented in this section demonstrate that a soft interlayer can act as a crack arrester, since the crack driving force is considerably reduced when the crack has crossed the second interface of the soft interlayer.

5.7 Optimum effectiveness of a soft interlayer

A general criterion for initiation of crack growth is that the crack driving force equals or exceeds the crack growth resistance R of the material,

$$J_{tip} \geq R. \tag{5.18}$$

The negative interlayer inhomogeneity term C_{IL}, especially near IF2, results in the decrease of the crack driving force J_{tip}, and a higher applied load is needed for initiation of crack growth, compared to the case of a homogenous bulk material. Therefore, by a decrease of the minimum crack driving force due to insertion of a soft interlayer, a material can become fracture resistant. The aim of this section is to find a soft interlayer with the maximum effectiveness, that is, to find for a given material and load, the magnitudes of thickness and yield stress of the soft interlayer so that the maximum reduction of the crack driving force is achieved.

As explained before, the critical position for possible crack arrest is immediately after the crack has crossed IF2, see Fig. 5.3b. In the following, the critical position for possible crack arrest is referred to as the CA position. The crack driving force and the material inhomogeneity terms for a crack located at CA position are referred to $J_{\mathrm{tip}}^{\mathrm{CA}}$ and $C_{\mathrm{inh1}}^{\mathrm{CA}}, C_{\mathrm{inh2}}^{\mathrm{CA}}$. Adopting a simple, quasi-static consideration, the crack driving force $J_{\mathrm{tip}}^{\mathrm{CA}}$ must be less than the crack growth resistance R of the bulk material in order to arrest the crack. Otherwise, the crack continues growing and, because J_{tip} is always larger than R for all subsequent steps, crack growth becomes unstable and the specimen fractures catastrophically. An improved assessment of crack arrest would take into account the kinetic energy of the specimen and a possible rate dependence of the crack growth resistance, see Freund (1990).

Clearly, the optimum effectiveness of a soft interlayer can be achieved if $J_{\mathrm{tip}}^{\mathrm{CA}} / J_{\mathrm{far}}$ becomes a minimum. Therefore, in order to find the optimum thickness and the yield stress of the soft interlayer, the influence of the thickness and the yield stress of the soft interlayer on $J_{\mathrm{tip}}^{\mathrm{CA}} / J_{\mathrm{far}}$ should be quantified.

5.7.1 Optimum interlayer thickness

The analytical results in Kolednik (2000) showed that the maximum effectiveness of a soft interlayer can be achieved when the interlayer has approximately a thickness equal to the radius of the plastic zone in the interlayer. Fig. 5.11a compares the $J_{\mathrm{tip}}/J_{\mathrm{far}}$-values, which are plotted against L_1, for an elastic–plastic single interlayer specimen with the standard material combination and t = 0.3 mm for three different J_{far}-values, J_{far} = 0.8, 6.6 and 130 kJ/m^2. Fig. 5.11b shows the shapes of the plastic zone for those values of J_{far} when the crack tip is at CA position where L_2 = 2 µm. For J_{far} = 0.8 kJ/m^2, the size of the plastic zone in the interlayer is much lower than the interlayer thickness; $r_{\mathrm{y}}^{\mathrm{IL}}$ calculated by Eq. (5.4) is 0.08 mm. As it can be seen, for J_{far} = 6.6 kJ/m^2, the plastic zone size in the direction normal to the interfaces is identical to the interlayer thickness; $r_{\mathrm{y}}^{\mathrm{IL}}$ calculated by Eq. (5.4) is 0.67 mm. For J_{far} = 130 kJ/m^2, the size of the plastic zone in the soft interlayer is much higher than the interlayer thickness; $r_{\mathrm{y}}^{\mathrm{IL}} = 13$ mm. Table 5.1 compares the normalized material inhomogeneity terms of IF1 and IF2, and the resulting values of $J_{\mathrm{tip}}/J_{\mathrm{far}}$ for the three different J_{far}-values. Fig. 5.11 and Table 5.1 show that when the crack tip is at CA position, $J_{\mathrm{tip}}/J_{\mathrm{far}}$ for J_{far} = 6.6 kJ/m^2 is lower than for the other two J_{far}-values. The reason is in the following.

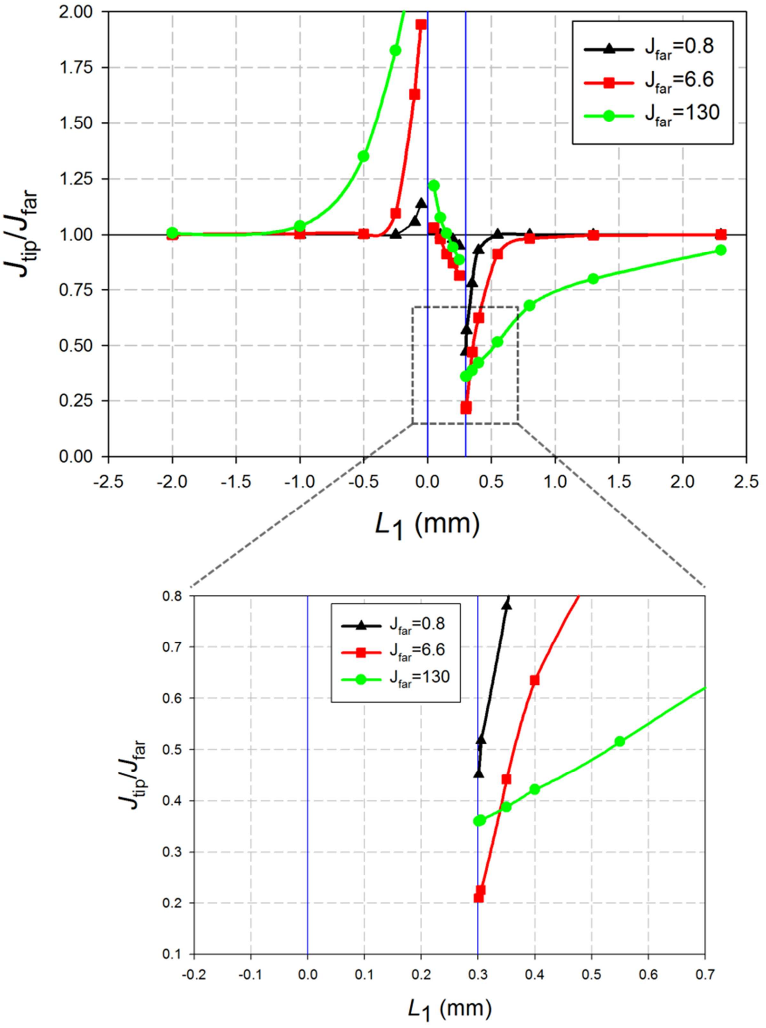

(a)

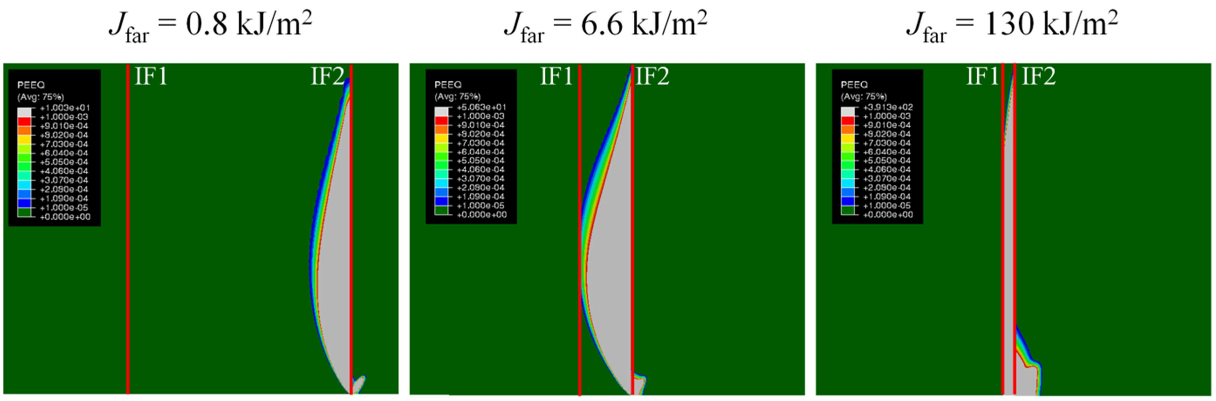
J_{far} = 0.8 kJ/m^2 J_{far} = 6.6 kJ/m^2 J_{far} = 130 kJ/m^2

(b)

Fig. 5.11 **(a)** J_{tip}/J_{far}-values plotted against L_1 and **(b)** the shapes of the plastic zone where L_2 = 2 µm for an elastic–plastic single interlayer specimen with t = 0.3 mm and three different J_{far}-values, J_{far} = 0.8, 6.6 and 130 kJ/m^2.

Table 5.1 Normalized material inhomogeneity terms and the resulting $J_{\text{tip}}/J_{\text{far}}$ for three different J_{far}-values where L_2 = 2 µm.

J_{far} (kJ/m^2)	r_y^{IL} (mm)	L_2 (µm)	L_2/r_y^{IL}	L_1 (mm)	L_1/r_y^{IL}	$C_{\text{inh1}}/J_{\text{far}}$	$C_{\text{inh2}}/J_{\text{far}}$	$J_{\text{tip}}/J_{\text{far}}$
0.8	0.08	2	0.03	0.3	3.7	0	–0.55	0.45
6.6	0.67	2	0.0029	0.3	0.45	0	–0.78	0.22
130	13	2	0.0002	0.3	0.027	0.15	–0.78	0.37

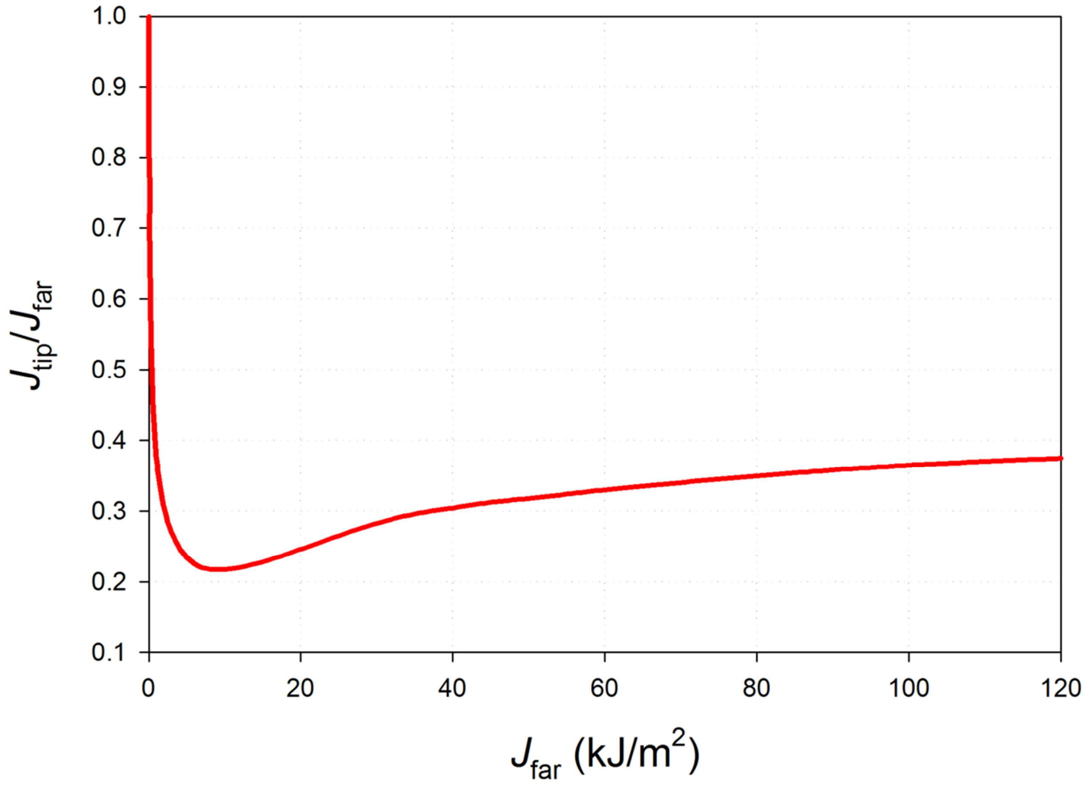

Fig. 5.12 $J_{\text{tip}}/J_{\text{far}}$ plotted against J_{far} for a single interlayer specimen with the standard material combination and t = 0.3 mm where L_2 = 2 µm.

In Fig. 5.12, $J_{\text{tip}}/J_{\text{far}}$ is plotted against J_{far} for the crack tip located at CA position, L_2 = 2 µm and L_1 = 0.302 mm. The plastic zone first touches IF2 and hence $J_{\text{tip}}/J_{\text{far}}$ decreases with increasing J_{far}. The reduction of $J_{\text{tip}}/J_{\text{far}}$ with increasing J_{far} continues until the plastic zone reaches IF1, approximately at J_{far} = 6.6 kJ/m^2. After that, with further increasing J_{far} or r_{y}^{IL}, $J_{\text{tip}}/J_{\text{far}}$ increases due to the anti-shielding effect of IF1. Therefore, $J_{\text{tip}}/J_{\text{far}}$ for a crack located at CA position reaches its minimum value when the plastic zone begins to touch IF1. This is the reason why in Fig. 5.11a, for the crack located at CA position, $J_{\text{tip}}/J_{\text{far}}$ is lower for J_{far} = 6.6 kJ/m^2 than for the other two J_{far}-values. Clearly, it can be seen from Table 5.1 that due to the anti-shielding effect of IF1, $J_{\text{tip}}/J_{\text{far}}$ becomes larger for J_{far} = 130 kJ/m^2 than for J_{far} = 6.6 kJ/m^2.

It can be concluded that the maximum reduction of $J_{\text{tip}}^{\text{CA}}/J_{\text{far}}$ is achieved, if the plasticity begins to spread over the whole interlayer. Therefore, the optimum interlayer thickness can be estimated as

$$t_{\text{opt}} \approx r_{y}^{\text{IL}} = \beta \frac{J_{\text{far}}^{\text{CA}} E}{\left(\sigma_{y}^{\text{IL}}\right)^{2} (1-\nu^{2})}, \tag{5.19}$$

where $\beta = 1/6\pi$ for plane strain conditions and $J_{\text{far}}^{\text{CA}}$ is the J_{far}-value for a crack at CA position.

5.7.2 Optimum yield stress of the soft interlayer

From Table 5.1 and the previous subsection follows that in a specimen containing a single interlayer with optimum thickness, $C_{\text{inh1}}^{\text{CA}}$ is approximately zero and one can write from Eq. (5.15),

$$\frac{J_{\text{tip}}^{\text{CA}}}{J_{\text{far}}} = 1 + \frac{C_{\text{IL}}^{\text{CA}}}{J_{\text{far}}} \approx 1 + \frac{C_{\text{inh2}}^{\text{CA}}}{J_{\text{far}}}. \tag{5.20}$$

Only the second interface has an influence on the crack driving force. The magnitude of $C_{\text{inh2}}^{\text{CA}}/J_{\text{far}}$ for different yield stress ratios $\sigma_{\text{y}}^{\text{IL}}/\sigma_{\text{y}}^{\text{M}}$, can be extracted from Fig. 5.9b, taking $L_2/r_{\text{y}}^{\text{IL}} \rightarrow 0$. These values from Fig. 5.9b are plotted against $\sigma_{\text{y}}^{\text{IL}}/\sigma_{\text{y}}^{\text{M}}$ in Fig. 5.13a. As can be seen, $C_{\text{inh2}}^{\text{CA}}/J_{\text{far}}$ decreases with decreasing $\sigma_{\text{y}}^{\text{IL}}/\sigma_{\text{y}}^{\text{M}}$, until $\sigma_{\text{y}}^{\text{IL}}/\sigma_{\text{y}}^{\text{M}} \cong 0.2$. After that, $C_{\text{inh2}}^{\text{CA}}/J_{\text{far}}$ remains constant. By inserting $C_{\text{inh2}}^{\text{CA}}/J_{\text{far}}$ into Eq. (5.20), the normalized crack driving force $J_{\text{tip}}^{\text{CA}}/J_{\text{far}}$ can be calculated, Fig. 5.13b. As Fig. 5.13b shows, the optimum yield stress of a soft interlayer becomes

$$\left(\sigma_{\text{y}}^{\text{IL}}\right)_{\text{opt}} \leq 0.2\sigma_{\text{y}}^{\text{M}}. \tag{5.21}$$

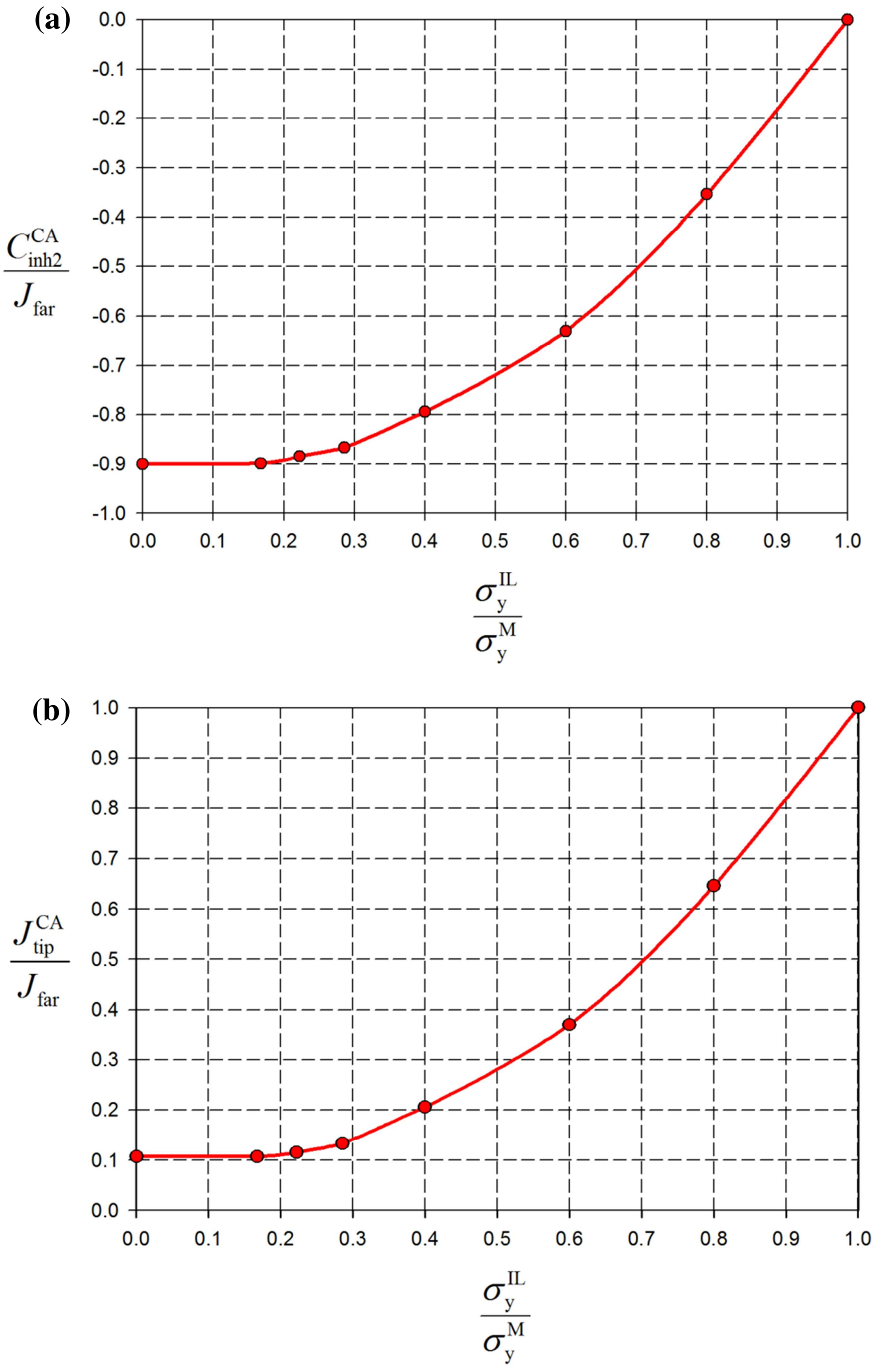

Fig. 5.13 (a) $C_{\mathrm{inh2}}^{\mathrm{CA}} / J_{\mathrm{far}}$ plotted against the yield stress ratio for a single interlayer specimen. **(b)** $J_{\mathrm{tip}}^{\mathrm{CA}} / J_{\mathrm{far}}$ plotted versus $\sigma_{\mathrm{y}}^{\mathrm{IL}} / \sigma_{\mathrm{y}}^{\mathrm{M}}$ for a specimen containing a single interlayer with optimum thickness. $J_{\mathrm{tip}}^{\mathrm{CA}} / J_{\mathrm{far}}$ reaches the minimum value when $\sigma_{\mathrm{y}}^{\mathrm{IL}} \leq 0.2\sigma_{\mathrm{y}}^{\mathrm{M}}$.

Moreover Fig. 5.13b demonstrates that a soft interlayer with optimum thickness and optimum yield stress can reduce the crack driving force of a homogenous bulk material by a factor of 10, $J_{\mathrm{tip}}^{\mathrm{CA}} / J_{\mathrm{far}} = 0.1$, which is the maximum possible reduction of the crack driving force.

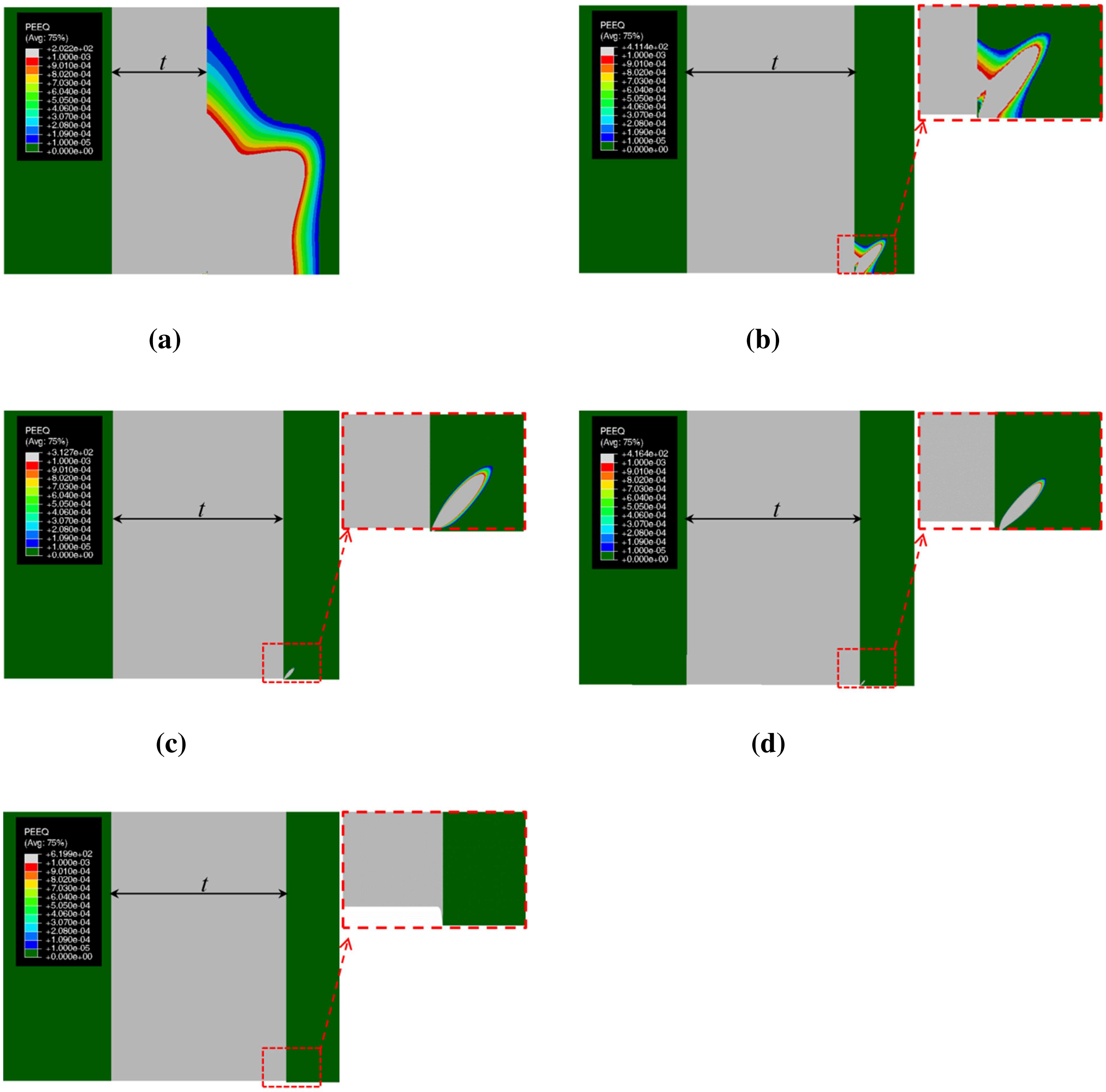

(a) **(b)**

(c) **(d)**

(e)

Fig. 5.14 The shape of the plastic zone for interlayer specimens with t = 0.3 mm, E = 70 GPa, $\sigma_{\mathrm{y}}^{\mathrm{IL}} = 200$ MPa and five different yield stress ratios where L_2 = 2 µm and $r_{\mathrm{y}}^{\mathrm{IL}} = 2.5$ mm. **(a)** $\sigma_{\mathrm{y}}^{\mathrm{IL}} / \sigma_{\mathrm{y}}^{\mathrm{M}} = 0.4$, **(b)** $\sigma_{\mathrm{y}}^{\mathrm{IL}} / \sigma_{\mathrm{y}}^{\mathrm{M}} = 0.22$, **(c)** $\sigma_{\mathrm{y}}^{\mathrm{IL}} / \sigma_{\mathrm{y}}^{\mathrm{M}} = 0.2$, **(d)** $\sigma_{\mathrm{y}}^{\mathrm{IL}} / \sigma_{\mathrm{y}}^{\mathrm{M}} = 0.167$, **(e)** $\sigma_{\mathrm{y}}^{\mathrm{IL}} / \sigma_{\mathrm{y}}^{\mathrm{M}} = 0$.

In order to explain why $C_{\mathrm{inh2}}^{\mathrm{CA}} / J_{\mathrm{far}}$ becomes constant for $\sigma_{\mathrm{y}}^{\mathrm{IL}} / \sigma_{\mathrm{y}}^{\mathrm{M}} \leq 0.2$ (Fig. 5.13a), the shape of the plastic zone is depicted in Fig. 5.14 for interlayer specimens with t = 0.3 mm, E = 70 GPa, $\sigma_{\mathrm{y}}^{\mathrm{IL}} = 200$ MPa and five different yield stress ratios, $\sigma_{\mathrm{y}}^{\mathrm{IL}} / \sigma_{\mathrm{y}}^{\mathrm{M}} = 0.4, 0.22, 0.2, 0.167$ and 0. For all cases, L_2 = 2 µm and $r_{\mathrm{y}}^{\mathrm{IL}} = 2.5$ mm. It is seen that the yield stress ratio influences the orientation of the plastic zone and its extension into the matrix. The plastic zone in the matrix interacts with IF2 for $\sigma_{\mathrm{y}}^{\mathrm{IL}} / \sigma_{\mathrm{y}}^{\mathrm{M}} = 0.4$ and 0.22, but not for smaller values of $\sigma_{\mathrm{y}}^{\mathrm{IL}} \big/ \sigma_{\mathrm{y}}^{\mathrm{M}}$. Since the plastic zone in the matrix does not contact IF2 for $\sigma_{\mathrm{y}}^{\mathrm{IL}} \big/ \sigma_{\mathrm{y}}^{\mathrm{M}} \leq 0.2$, the jump of the strain energy density at IF2 becomes constant. Therefore, $C_{\mathrm{inh2}}^{\mathrm{CA}} \big/ J_{\mathrm{far}}$ is constant for $\sigma_{\mathrm{y}}^{\mathrm{IL}} \big/ \sigma_{\mathrm{y}}^{\mathrm{M}} \leq 0.2$.

This paper focused on the influence of a soft interlayer on the crack driving force and the optimum interlayer configurations were derived so that the maximum reduction of the crack driving force can be reached. The influence of a soft interlayer with optimum configurations on the fracture resistance of a layered composite will be investigated in a separate paper.

Finally, it should be remarked that the results in this paper have been deduced for non-hardening materials. Especially the quantitative results such as the maximum possible reduction of the crack driving force due to a soft interlayer, should not be directly transferred to (strongly) hardening materials without a check by additional numerical analyses. The mechanism for the improvement of the fracture resistance and the procedure for finding optimum configurations are valid also for hardening materials.

5.8 Summary

In the current paper, the influence of a single soft interlayer, which has equal elastic properties as the matrix but a different yield stress, on the crack driving force is examined using the configurational forces concept. The main findings are:

- The material inhomogeneity effect due to a single interlayer on the crack driving force, which is called the interlayer inhomogeneity term C_{IL}, can be quantified by the summation of the material inhomogeneity terms of the first and second interfaces of the interlayer, C_{inh1} and C_{inh2}.
- The normalized material inhomogeneity term, $C_{\mathrm{inh}} \big/ J_{\mathrm{far}}$, of each interface is a function of the two dimensionless terms, the distance between crack tip and interface related to the plastic zone size in the interlayer and the yield stress ratio.
- The normalized interlayer inhomogeneity term, $C_{\mathrm{IL}} \big/ J_{\mathrm{far}}$, is additionally dependent on a third dimensionless term, which is the interlayer thickness related to the plastic zone size in the interlayer.
- It is observed that immediately after the crack has crossed the second interface of the soft interlayer (IF2), the crack driving force becomes a minimum, and this position is the critical position for possible crack arrest.
- The optimum effectiveness of a soft interlayer is achieved if the soft interlayer fulfills certain conditions derived in this paper, i) the interlayer thickness should be equal to the

size of the plastic zone in the interlayer, and ii) the yield stress of the soft interlayer should be approximately equal to or smaller than 0.2 times the yield stress of the matrix.

- By inserting a soft interlayer with the derived conditions, the crack driving force of a bulk material can be reduced by a factor of 10, which is the maximum possible reduction of the crack driving force. This effect is basically different from the delamination effect in composites with weak interlayers.

Acknowledgements

Financial support by the Austrian Federal Government and the Styrian provincial Government within the research activities of the K2 Competence Center “Integrated Research in Materials, Processing and Product Engineering’’, under the frame of the Austrian COMET Competence Center Program, is gratefully acknowledged (Project A4.20-WP1).

6 Improving fracture stress by yield stress inhomogeneity effect

Paper I focused on the influence of a single soft interlayer, which has equal elastic properties as the matrix but a different yield stress, on the crack driving force. Using numerical modeling and application of the concept of the configurational forces, it was shown that a soft interlayer works as a very efficient crack arrester in materials. The optimum interlayer configurations were derived so that the maximum reduction of the crack driving force can be reached.

In Paper II it is shown that the introduction of thin, soft interlayers can greatly improve the strength of inherently brittle materials. The effect occurs due to the strong decrease of the crack driving force when the crack tip is located in the interlayer region, near the boundary to the hard matrix material. The strength, i.e. the fracture stress in a tensile test, of intrinsically brittle materials is determined by the initiation and growth of small defects. Therefore, the introduction of a large number of thin, soft interlayers in a brittle matrix material provides many crack stopping positions and, hence, the strength of the multilayer becomes much higher than that of the homogeneous material.

The decisive parameters influencing the effectiveness of soft interlayers as crack arresters are the interlayer spacing (the wavelength of the yield stress variation), the interlayer thickness and the yield stress ratio between interlayer and matrix, see Fig. 6.4a. Paper II performs a comprehensive numerical case study, for a multilayer symmetric middle crack tension (MT) specimen with a short inherent crack, in order to quantify the effectiveness of soft interlayers in multilayer composites as a function of multilayer architectural parameters. The results are used to find, for a given matrix material and load, the optimum multilayer architecture.

The most important findings of this paper can be highlighted as:

- The effectiveness of soft interlayers as crack arrester in multilayer composites is a function of the material properties and the architecture (t, λ) of the composite, compare Fig. 6.4a.
- For an optimum effect, the ratio of the yield stress between interlayer- and matrix material should be 1/5 or smaller.
- The strength of a multilayer composite depends on three length parameters: interlayer thickness t, interlayer spacing (or wavelength) λ, and the radius of the

crack-tip plastic zone in the interlayer r_y^{IL} (which depends on the yield strength of the interlayer material, the crack length and the applied load).

- A simple fracture mechanical consideration enables us to derive the optimum wavelength of the composite, which exhibits an inverse dependency on the applied stress, $\lambda_{opt} \sim 1/\sigma_{appl}^2$. A similar relation is derived for multilayered composites with spatial variations in Young's modulus.
- An iterative procedure is outlined in order to find, for a given matrix material and load, the optimum multilayer architecture, leading to great improvement of fracture stress.

Paper II:

Improving strength and toughness of materials by utilizing spatial variations of the yield stress

M. Sistaninia, O. Kolednik

published in

Acta Materialia (2017) 122:207–219

http://dx.doi.org/10.1016/j.actamat.2016.09.044

Abstract

The introduction of thin interlayers with low yield stress can greatly improve the strength and the fracture toughness of inherently brittle materials. The reason is that the spatial yield stress variation affects the crack driving force, which strongly decreases when the crack tip is located in the interlayer region, near the boundary to the hard matrix material. This can lead to crack arrest. The material inhomogeneity effect appears without previous delamination of the interlayer. The decisive parameters influencing the effect are the interlayer spacing (the wavelength of the yield stress variation), the interlayer thickness and the yield stress ratio between interlayer and matrix. Based on numerical simulations with the configurational forces concept, it is demonstrated how the architectural parameters of the multilayer must be chosen in order to enhance the fracture stress and the fracture toughness of the material. An iterative procedure is proposed to find the optimum configuration. It is found that the optimum wavelength is inversely proportional to the square of the applied stress. A similar relation is given for composites with spatial variations in Young's modulus.

Keywords: Multilayers; Composites; Crack driving force; Configurational forces; Finite element modeling; Fracture stress.

6.1 Introduction

The design of stronger and tougher materials has been in the focus of researchers throughout the last decades. In particular, the introduction of layered structures has been proposed as a promising way for the material improvement. The most relevant mechanisms behind the improvements are

- Interface delamination: In structures with weak interfaces, the hydrostatic stress state strongly decreases due to the opening of the interface, which leads to a reduction of the crack driving force. In addition, the sharpness of the crack tip is lost when the crack grows into the delaminated interface. The increase in fracture toughness is especially high for a crack arrester configuration, i.e. when the interfaces are perpendicular to the nominal crack plane (Cook and Gordon 1964; Embury et al. 1967; Lesuer et al. 1996; Tariolle et al. 2005; Wang et al. 2000).
- Crack deflection: The interface delamination can result in crack deflection which significantly reduces the Mode I component of the local stress intensity factor and enhances the fracture toughness (Faber and Evans 1983; Suresh 1983; Suresh 1985; Lesuer et al. 1996).
- Compressive residual stresses: In multilayered structures with tailored residual stress variations, layers under compressive residual stresses act as barriers to crack propagation due to the reduction of the crack driving force (Rao et al. 1999; Lugovy et al. 2004; Sglavo et al. 2005; Lugovy et al. 2005; Bermejo et al. 2006; Chen et al. 2007).
- Reduction of defect probability: Based on Weibull's theory (Weibull 1951), the average fracture stress of intrinsically brittle materials increases with decreasing specimen volume, since the probability for the presence of a defect with critical size decreases. Therefore, the strength of a material increases when replacing a compact material by a layered structure (Ashby and Bréchet 2003; Kolednik et al. 2014a).

There exist numerous literatures where the strength or the fracture toughness of layered composites is investigated as a function of the layer geometry and the material properties. However, in most of these studies, e.g. Cook and Gordon (1964), Embury et al. (1967), Lesuer et al. (1996), Rao et al. (1999), Wang et al. (2000), Lugovy et al. (2004), Sglavo et al. (2005), Lugovy et al. (2005), Tariolle et al. (2005), Bermejo et al. (2006), interface delamination and/or residual stresses are utilized in order to increase the fracture resistance. The current paper concentrates on an alternative method for designing new fracture-resistant and flaw-tolerant materials: the utilization of the material inhomogeneity effect. The effect is based on the fact that a spatial variation of material properties in the direction of crack extension leads to a spatial variation of the crack driving force and, thus, affects the fracture toughness (Kolednik 2000; Fratzl et al. 2007; Kolednik et al. 2009; Kolednik et al. 2011; Fischer et al. 2012a; Zechner and Kolednik 2013a,b; Kolednik et al. 2014a; Sistaninia and Kolednik 2014). For example, the crack driving force decreases, if a crack grows from a material with lower elastic modulus towards a material with higher elastic modulus. Due to the lower crack driving force, a higher load is required for crack propagation compared to the situation in a homogeneous material. In other words, a compliant/stiff transition provides a crack tip shielding effect. In contrast, a stiff/compliant transition provides anti-shielding effect. For the quantification of the material inhomogeneity effect, the concept of configurational forces has been applied (Simha et al. 2003; Simha et al. 2005; Kolednik et al. 2005; Kolednik et al. 2009; Kolednik et al. 2010; Kolednik et al. 2011; Sistaninia and Kolednik 2014). Note that the material inhomogeneity effect does not require interface opening; it even occurs, if the Young's modulus exhibits a smooth variation (Kolednik 2000; Simha et al. 2003). Therefore, it is fundamentally different from the above mentioned effects of interface delamination.

Especially interesting for materials design is the introduction of thin, *compliant* interlayers in high-strength matrix materials with low intrinsic toughness (Kolednik et al. 2011; Kolednik et al. 2014a; Kolednik et al. 2016; Zechner and Kolednik 2013a). Anti-shielding and shielding appear pairwise at the two interfaces of the interlayer, compare Fig. 6.1. If the material properties, the thickness and the spacing of the interlayers are appropriately chosen, the strong decrease of the crack driving force at the second interface of the interlayer leads to crack arrest, and fracture toughness and strength of the composite become much higher than the values of the homogeneous matrix material (Kolednik et al. 2011; Kolednik et al. 2014a). Since the interlayers are thin, the stiffness of the composite almost equals that of the matrix.

It is worth noting that the material inhomogeneity effect can be also utilized to improve the toughness of materials against interfacial cracking. Theoretical studies and tape peeling experiments by Kendall (1975), discussed in (Atkins and Mai 1985), showed that a crack tip shielding effect occurs when an interface crack propagates from a more compliant (or thinner) tape to a stiffer (or thicker) tape. This idea can be applied for the design of tough surface coating composites where failure occurs by peeling (Kendall 1975).

It was shown that a *soft* interlayer, i.e. an interlayer with the same Young's modulus but a lower yield stress than the matrix material, also works as effective crack arrester, provided that the difference in yield stress and the thickness of the interlayer are appropriately chosen (Sistaninia and Kolednik 2014). The reason is that a soft/hard transition also delivers a crack tip shielding effect, and vice versa (Kolednik 2000; Simha et al. 2005; Predan et al. 2007; Kolednik et al. 2010). The yield stress inhomogeneity effect opens additional possibilities for the design of tough, strong and damage-tolerant composites by inserting soft interlayers in high-strength, brittle matrix materials. Therefore, in the current paper the anti-shielding and shielding effects in a material with soft interlayers shall be investigated and a procedure shall be introduced how to find, for a given matrix material, the architectural parameters of the composite, i.e. yield strength, thickness and spacing of the soft interlayers (compare Fig. 6.4a), so that the properties improve.

The following section presents a short review of the influence of a single soft interlayer on the crack driving force. Then the effects of a single-interlayer specimen and a multilayer configuration are studied. Fracture mechanical considerations are then used to derive a criterion for finding the optimum spacing of the interlayers. The criterion is applied for various types of composite materials and loading scenarios; examples are presented.

6.2 Influence of a single, soft interlayer on the crack driving force

The influence of a single soft interlayer on the crack driving force was examined in Sistaninia and Kolednik (2014). Their findings are briefly presented in this section.

Fig. 6.1a shows a fracture mechanics specimen that contains a single interlayer with two sharp interfaces, IF1 and IF2. The interlayer material has equal elastic properties as the matrix material, but a lower yield stress, $\sigma_{\mathrm{y}}^{\mathrm{IL}} < \sigma_{\mathrm{y}}^{\mathrm{M}}$. Both materials are homogeneous and behave elastic–ideally plastic, i.e. do not exhibit hardening. The interfaces are assumed as being perfect, i.e. no interface decohesion can occur. A straight crack is assumed lying perpendicular to the interlayer; L_1 and L_2 are the distances between the crack tip and IF1 and IF2, respectively. When the crack tip is situated left of an interface, L is negative. The distances L_1 and L_2 are related by

$$L_2 = L_1 - t, \tag{6.1}$$

where t is the interlayer thickness.

The crack driving force, expressed in terms of the near-tip J-integral J_{tip}, can be determined from the relation,

$$J_{\mathrm{tip}} = J_{\mathrm{far}} + C_{\mathrm{inh1}} + C_{\mathrm{inh2}} = J_{\mathrm{far}} + C_{\mathrm{IL}}. \tag{6.2}$$

The far-field J-integral J_{far} is a loading parameter and represents the driving force that is inserted by the applied load into the specimen.

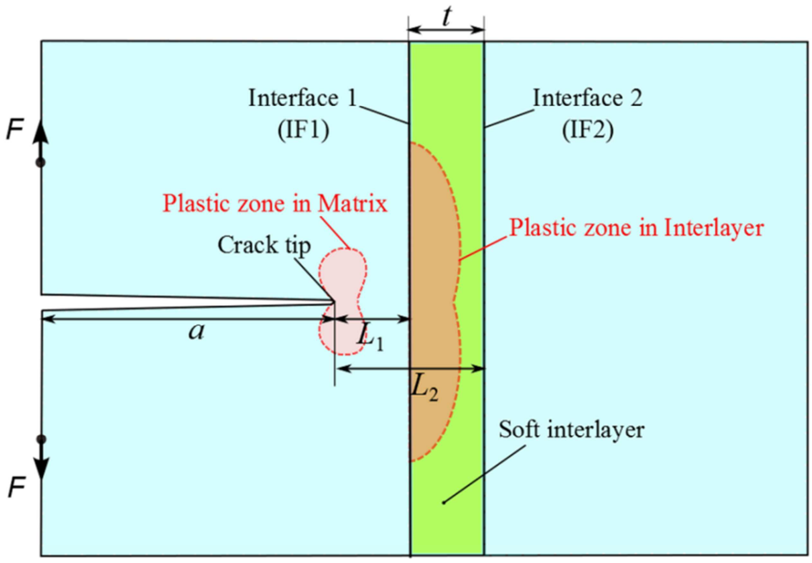

(a)

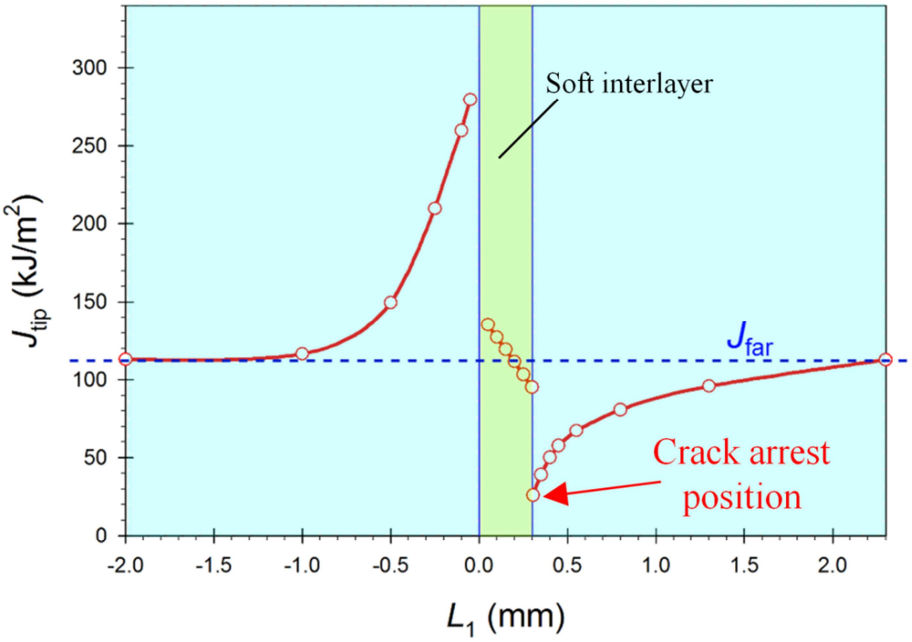

(b)

Fig. 6.1 **(a)** Fracture mechanics specimen with a long crack and a single, soft interlayer with interfaces, IF1 and IF2, perpendicular to the crack plane. **(b)** The crack driving force J_{tip} reaches a minimum value immediately after the crack tip has crossed IF2.

In a homogeneous material, $J_{\mathrm{tip}} = J_{\mathrm{far}}$. The parameters C_{inh1} and C_{inh2} are the material inhomogeneity terms of the interfaces IF1 and IF2, respectively. The term $C_{\mathrm{IL}} = C_{\mathrm{inh1}} + C_{\mathrm{inh2}}$ is called "interlayer inhomogeneity term"; it quantifies the effect of the material inhomogeneity due to the interlayer on the crack driving force.

The material inhomogeneity term caused by a single interface *i* can be calculated (for small strain theory) from the relation (Kolednik et al. 2010; Simha et al. 2003; Simha et al. 2005),

$$C_{\mathrm{inh}\,i} = -\mathbf{e} \cdot \int_{\Sigma_i} \left([[\phi]]\mathbf{I} - \langle \boldsymbol{\sigma} \rangle \cdot [[\boldsymbol{\varepsilon}]] \right) \mathbf{n}\, dl \,, \tag{6.3}$$

where ϕ is the strain energy density, **I** the identity tensor, $\boldsymbol{\sigma}$ the Cauchy stress tensor, $\boldsymbol{\varepsilon}$ the strain tensor, **e** the unit vector in the direction of crack extension, **n** the unit vector normal to the interface Σ_i, and *dl* an increment of the interface Σ_i. The symbol $[[\ ]]$ denotes the jump of a quantity at the interface, the symbol $\langle\ \rangle$ the average value of a quantity across the interface. The material inhomogeneity term C_{inh} is a scalar quantity, representing the energy that is released during a unit crack extension due to the material inhomogeneity. A negative C_{inh} leads to a reduction of the crack driving force, $J_{\mathrm{tip}} < J_{\mathrm{far}}$, i.e. the material inhomogeneity shields the crack tip.

Since the elastic properties of interlayer and matrix materials are equal, an inhomogeneity effect only appears if plastic deformation occurs, i.e. if the crack tip plastic zone touches the interface (Kolednik 2000). The radius of the crack tip plastic zone can be estimated from Irwin's model (Irwin 1961),

$$r_{\mathrm{y}} = \beta \frac{J_{\mathrm{far}} E}{\sigma_{\mathrm{y}}^2 (1 - \nu^2)} \,, \tag{6.4}$$

where *E* is the Young's modulus, σ_{y} the yield stress, ν Poisson's ratio and $\beta = 1/6\pi$ for plane strain conditions. Irwin's model assumes a circular plastic zone. In reality, the plastic zone has a complicated shape with a forward orientation, e.g. with a maximum extension at an angle of $\theta = 70^\circ$ with respect to the crack plane for a homogeneous material and plane strain conditions. In an inhomogeneous material, the angle θ changes, depending on the material inhomogeneity, its distance to the crack tip and the load. Since $\sigma_{\mathrm{y}}^{\mathrm{IL}} < \sigma_{\mathrm{y}}^{\mathrm{M}}$, the crack tip plastic zone is larger in the interlayer material, $r_{\mathrm{y}}^{\mathrm{IL}} > r_{\mathrm{y}}^{\mathrm{M}}$.

Fig. 6.1b shows schematically the variation of the crack driving force J_{tip} for constant loading, i.e. a constant value of J_{far}, and different crack tip positions: J_{tip} is plotted against the distance L_1 between crack tip and IF1. A crack far from the interface, $|L_1| > r_{\mathrm{y}}^{\mathrm{IL}}$, is not influenced by the material inhomogeneity, $J_{\mathrm{tip}} = J_{\mathrm{far}}$. If the crack tip approaches the interface from the left, J_{tip} first increases, since the plastic zone first touches IF1 (with hard/soft transition and positive material inhomogeneity term, $C_{\mathrm{inh1}} > 0$), and then decreases due to the effect of IF2 (soft/hard transition and $C_{\mathrm{inh2}} < 0$). The minimum value of the crack driving force J_{tip} is reached immediately after the crack tip has crossed IF2. This position is the critical position for possible crack arrest, and it is referred to in the following as the "CA position". The crack driving force, the far-field *J*-integral, and the material inhomogeneity terms for a crack tip located at the CA position are referred to as $J_{\mathrm{tip}}^{\mathrm{CA}}$, $J_{\mathrm{far}}^{\mathrm{CA}}$ and $C_{\mathrm{inh1}}^{\mathrm{CA}}$, $C_{\mathrm{inh2}}^{\mathrm{CA}}$.

6.3 Effectiveness of a soft interlayer as crack arrester

A numerical case study is performed to explore, under which conditions a soft interlayer is most effective as crack arrester in a given matrix material. We consider a symmetric middle crack tension (MT) specimen that contains a *short* inherent crack with initial length $2a_0$ in the matrix material and two soft interlayers left and right of the crack; λ denotes the spacing of the interlayers and t the interlayer thickness (Fig. 6.2a).

For two reasons this case study is necessary, although a similar investigation was performed in Sistaninia and Kolednik (2014) for a Compact tension (CT) specimen with *long* crack. The first reason is that the constraint situation, i.e. the hydrostatic stress state, strongly differs between a CT-specimen (high in-plane constraint) and a MT-specimen (low constraint), see e.g. Anderson (2005). The second reason is that a specimen with a long crack is required for the experimental determination and the assessment of the *fracture toughness*, while a specimen with a short crack is needed for the assessment of the *strength* of a material.

The dimensions of the specimen are chosen as: width $2W$ = 40 mm, height H = 80 mm and thickness B = 10 mm. The specimen is loaded by prescribing the vertical displacement $u_{\mathrm{appl}}/2$ at the lower and upper boundaries; the horizontal displacements at the lower and upper boundaries are free. Due to symmetry, only one quarter of the specimen is modeled, see Fig. 6.2a. Isotropic elastic–ideally plastic materials with perfect interfaces are assumed. The numerical analyses are performed with a commercial implementation of the finite element (FE) method (ABAQUS). The analyses are performed for plane strain conditions and large strain formulations. Four-node elements are used for discretizing the FE model.

After the FE stress and strain analysis, the material inhomogeneity terms, C_{inh1} and C_{inh2}, are evaluated from Eq. (6.3) for each value of u_{appl} by a post-processing routine, which is based on the papers (Müller et al. 2002; Denzer et al. 2003; Müller et al. 2004). The far-field J integral J_{far} is determined using the virtual crack extension method of ABAQUS (Simha et al. 2003; Kolednik et al. 2010; Sistaninia and Kolednik 2014). The crack driving force J_{tip} is then calculated from Eq. (6.2).

Instead of modeling crack extension, the crack driving forces of stationary cracks with increasing crack lengths are evaluated for constant values of J_{far}, resulting in J_{tip} vs. L_1-curves similar to that found in (Sistaninia and Kolednik 2014) for a specimen with a *long* crack, see Fig. 6.1b. Again the soft interlayer exerts the maximum shielding effect, at the instant when the crack tip is located immediately after IF2, i.e. at the crack arrest (CA) position. In order to

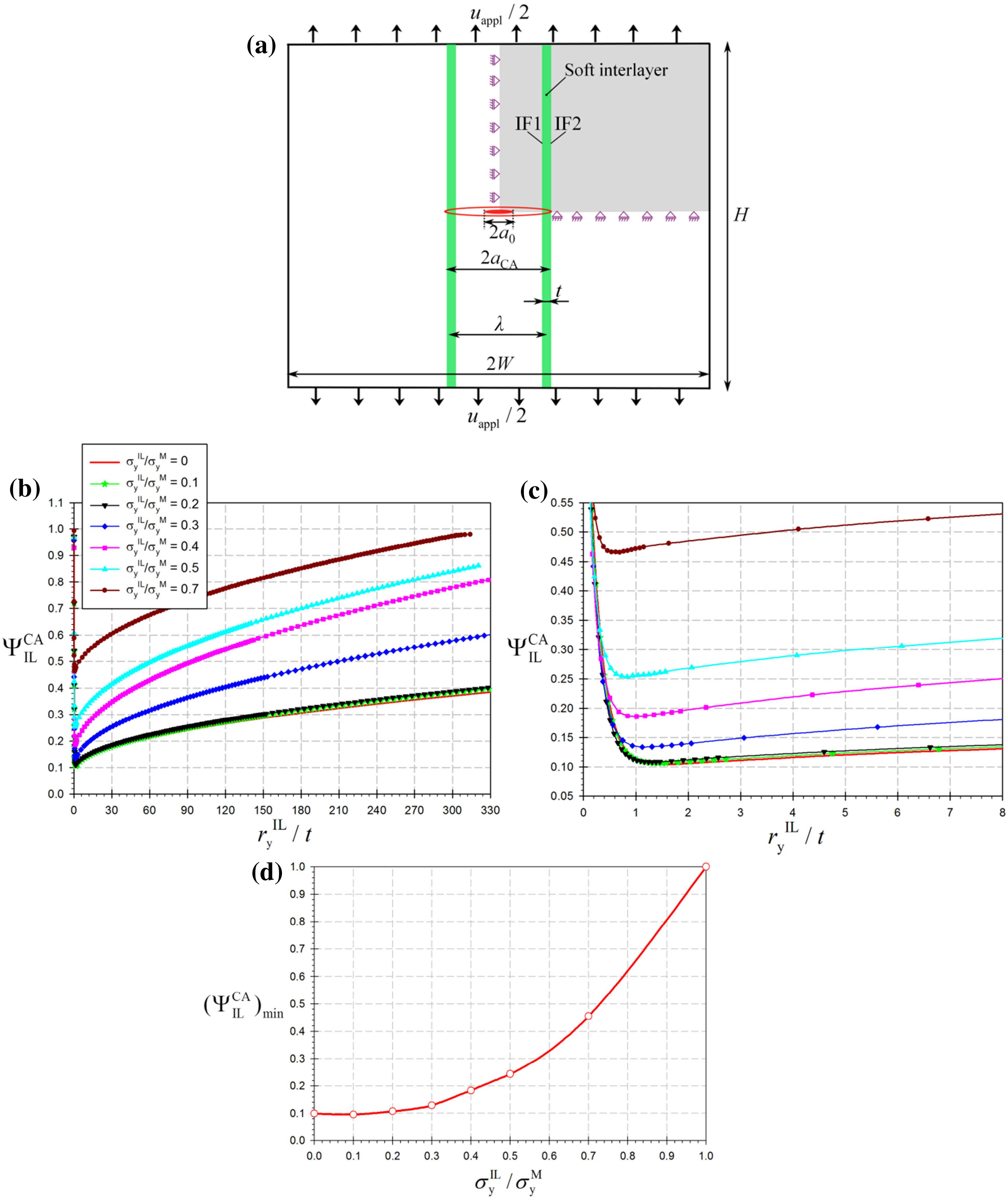

Fig. 6.2 Effectiveness of a single, soft interlayer as crack arrester: **(a)** Middle crack tension (MT) specimen with a short crack that has extended to the crack arrest (CA) position. **(b)** *J*-reduction coefficient $\Psi_{\mathrm{IL}}^{\mathrm{CA}}$ plotted against the dimensionless loading parameter $r_{\mathrm{y}}^{\mathrm{IL}}/t$ for different yield stress ratios $\sigma_{\mathrm{y}}^{\mathrm{IL}}/\sigma_{\mathrm{y}}^{\mathrm{M}}$. **(c)** Detail for $0 \le r_{\mathrm{y}}^{\mathrm{IL}}/t \le 8$. **(d)** Minimum *J*-reduction coefficient $(\Psi_{\mathrm{IL}}^{\mathrm{CA}})_{\min}$ as a function of the yield stress ratio $\sigma_{\mathrm{y}}^{\mathrm{IL}}/\sigma_{\mathrm{y}}^{\mathrm{M}}$.

evaluate accurately the crack driving force at the CA position, an FE model with a very fine mesh is used. The crack length is taken as $a_{\mathrm{CA}} = (\lambda + t)/2 + L_2$ with $L_2 = 2$ µm. For high accuracy, 10 elements are put between the crack tip and IF2. The minimum mesh size is 0.2 µm.

The effectiveness of the interlayer to work as crack arrester is quantified by a dimensionless parameter $\Psi_{\mathrm{IL}}^{\mathrm{CA}}$, called the "*J*-reduction coefficient of the single interlayer",

$$\Psi_{\mathrm{IL}}^{\mathrm{CA}} = \left.\frac{J_{\mathrm{tip}}^{\mathrm{CA}}}{J_{\mathrm{far}}^{\mathrm{CA}}}\right|_{\mathrm{IL}}, \tag{6.5}$$

where $J_{\mathrm{tip}}^{\mathrm{CA}}$ and $J_{\mathrm{far}}^{\mathrm{CA}}$ denote crack driving force and far-field *J*-integral for a crack in the CA-position and a given displacement u_{appl}. Although $\Psi_{\mathrm{IL}}^{\mathrm{CA}}$ was not defined in (Sistaninia and Kolednik 2014), it can be concluded from the results in (Sistaninia and Kolednik 2014) that $\Psi_{\mathrm{IL}}^{\mathrm{CA}}$ is a function of two dimensionless parameters, the ratio of the yield stresses of the interlayer and matrix materials and the ratio of the radius of the crack tip plastic zone in the interlayer material to the interlayer thickness,

$$\Psi_{\mathrm{IL}}^{\mathrm{CA}} = f_{\mathrm{IL}}\left(\frac{\sigma_{\mathrm{y}}^{\mathrm{IL}}}{\sigma_{\mathrm{y}}^{\mathrm{M}}}, \frac{r_{\mathrm{y}}^{\mathrm{IL}}}{t}\right). \tag{6.6}$$

Since $r_{\mathrm{y}}^{\mathrm{IL}}$ depends linearly on J_{far}, see Eq. (6.4), the ratio $r_{\mathrm{y}}^{\mathrm{IL}}/t$ can be considered as a dimensionless loading parameter.

Fig. 6.2b shows a collection of $\Psi_{\mathrm{IL}}^{\mathrm{CA}}$ vs. $r_{\mathrm{y}}^{\mathrm{IL}}/t$-curves for t = 50 µm, $\lambda = 4$ mm, W = 40 mm, and $2a_{\mathrm{CA}} = 4.054$ mm ($a/W \approx 0.05$). It is seen that, for a given yield stress ratio $\sigma_{\mathrm{y}}^{\mathrm{IL}}/\sigma_{\mathrm{y}}^{\mathrm{M}}$, the *J*-reduction coefficient $\Psi_{\mathrm{IL}}^{\mathrm{CA}}$ starts from a value of 1, then drops precipitously with increasing loading, runs through a minimum value, $(\Psi_{\mathrm{IL}}^{\mathrm{CA}})_{\min}$, and subsequently slowly increases. Fig. 6.2c shows parts of the curves in more detail, for $0 \le r_{\mathrm{y}}^{\mathrm{IL}}/t \le 8$. The *J*-reduction coefficient reaches its minimum value $(\Psi_{\mathrm{IL}}^{\mathrm{CA}})_{\min}$, i.e. the maximum reduction of the crack driving force at the CA-position appears, when the radius of the plastic zone in the interlayer has the same order of magnitude as the interlayer thickness,

$$t_{\mathrm{opt}} \approx r_{\mathrm{y}}^{\mathrm{IL}} = \beta \frac{J_{\mathrm{far}}^{\mathrm{CA}} E}{\left(\sigma_{\mathrm{y}}^{\mathrm{IL}}\right)^2 (1-\nu^2)}. \tag{6.7}$$

As explained earlier, Irwin's model, Eq. (6.4), cannot exactly estimate the real size of the plastic zone. This is the reason why the location of the minimum *J*-reduction coefficient, $(\Psi_{\mathrm{IL}}^{\mathrm{CA}})_{\min}$, does not remain constant for different values of $\sigma_{\mathrm{y}}^{\mathrm{IL}}/\sigma_{\mathrm{y}}^{\mathrm{M}}$ in Fig. 6.2c.

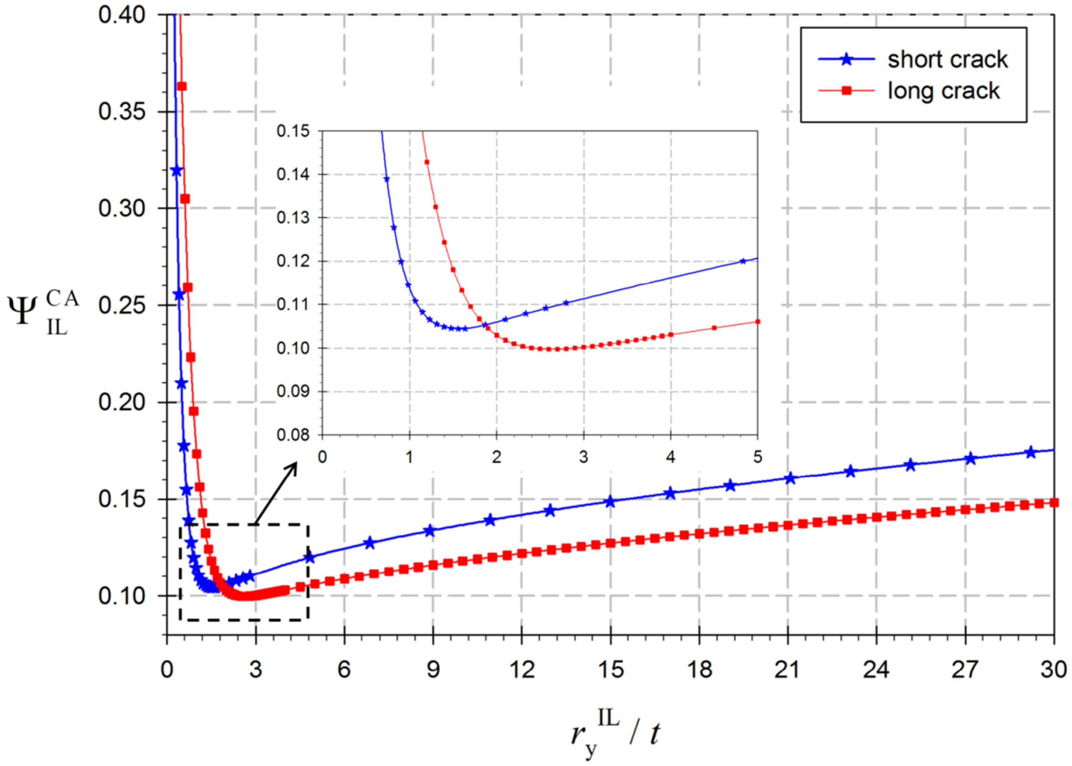

Fig. 6.3 Comparison of the single-interlayer *J*-reduction coefficients $\Psi_{\mathrm{IL}}^{\mathrm{CA}}$ for CT-specimens with long cracks and MT-specimens with short cracks and a yield stress ratio $\sigma_{\mathrm{y}}^{\mathrm{IL}} / \sigma_{\mathrm{y}}^{\mathrm{M}} = 0.1$.

A careful investigation reveals that $\Psi_{\mathrm{IL}}^{\mathrm{CA}}$ reaches its minimum, when plasticity begins to spread over the whole interlayer. In this case, the material inhomogeneity term of IF1 is approximately zero, $C_{\mathrm{inh1}}^{\mathrm{CA}} \approx 0$, and the (negative) material inhomogeneity term of IF2 reaches its maximum value, $\left(-C_{\mathrm{inh2}}^{\mathrm{CA}}\right) \to \max$.

Figs. 6.2b and 6.2c show that the levels of the $\Psi_{\mathrm{IL}}^{\mathrm{CA}}$ vs. $r_{\mathrm{y}}^{\mathrm{IL}} / t$-curves first decrease with decreasing yield stress ratio, but then seem to reach a lower saturation value. Fig. 6.2d displays the variation of $(\Psi_{\mathrm{IL}}^{\mathrm{CA}})_{\min}$ as a function of the yield stress ratio $\sigma_{\mathrm{y}}^{\mathrm{IL}} / \sigma_{\mathrm{y}}^{\mathrm{M}}$. From these curves, the optimum yield stress of a soft interlayer leading to the maximum reduction of the crack driving force is found as

$$\left(\sigma_{\mathrm{y}}^{\mathrm{IL}}\right)_{\mathrm{opt}} \leq 0.2\, \sigma_{\mathrm{y}}^{\mathrm{M}} . \tag{6.8}$$

The minimum possible value of the *J*-reduction coefficient is $\left(\Psi_{\mathrm{IL}}^{\mathrm{CA}}\right)_{\mathrm{opt}} \approx 0.105$.

The same optimum conditions for a single soft interlayer, Eqs. (6.7) and (6.8), were deduced in (Sistaninia and Kolednik 2014) for CT-specimens with long cracks. However, the magnitude of the parameter $\Psi_{\mathrm{IL}}^{\mathrm{CA}}$ differs from that of the MT-specimen with short crack. Fig.

6.3 provides a comparison of the $\Psi_{\mathrm{IL}}^{\mathrm{CA}}$-values for $\sigma_{\mathrm{y}}^{\mathrm{IL}}/\sigma_{\mathrm{y}}^{\mathrm{M}} = 0.1$. The reason for the difference in $\Psi_{\mathrm{IL}}^{\mathrm{CA}}$ is that, when the specimens are loaded to the same value of the far-field *J*-integral J_{far}, the CT-specimen has a higher level of hydrostatic stress near the crack-tip, i.e. a higher constraint, than the MT- specimen. Therefore, the real size of the plastic zone in the CT-specimen is lower than that in the MT-specimen, although the nominal value of $r_{\mathrm{y}}^{\mathrm{IL}}$ according to Eq. (6.4) is identical, see (Anderson 2005), for more information.

6.4 Effectiveness of soft interlayers as crack arresters in multilayer composites

In the previous section, the effectiveness of a single soft interlayer as crack arrester has been treated; now the effectiveness of soft interlayers as crack arrester in *multilayer* composites shall be worked out. The configuration is similar to that in Fig. 6.2a, but additional interlayers are present left and right, Fig. 6.4a. If the interlayer distance, i.e. the wavelength of the yield stress variation λ, is larger than the magnitude of the crack tip plastic zone, the material inhomogeneity effect in the multilayer equals that in a single-interlayer configuration. However, the situation changes, if the wavelength λ is so small (or the load is so high) that the crack tip plastic zone touches two or more interlayers (Kolednik 2000).

Specimen size and loading are identical to that described in Section 6.3. The crack tip is located at the CA position at IF2 of the first interlayer (IL1), i.e. the crack length is $a_{\mathrm{CA}} = (\lambda + t)/2 + L_2$ with $L_2 = 2\,\mu\mathrm{m}$. The number of interlayers in the half width of the specimen, *N*, is related to the wavelength λ by the relation, $N = W/\lambda$. After the FE stress and strain analysis, the material inhomogeneity terms, C_{inh1} and C_{inh2}, of each interlayer are evaluated from Eq. (6.3) for the considered displacements u_{appl}. Then the interlayer inhomogeneity term of the *i*-th interlayer is determined, $C_{\mathrm{IL}i} = C_{\mathrm{inh1}}^{i} + C_{\mathrm{inh2}}^{i}$, compare Eq. (6.2). After evaluating the far-field *J*-integral J_{far}, the crack driving force J_{tip} is calculated from the relation,

$$J_{\mathrm{tip}} = J_{\mathrm{far}} + \sum_{i=1}^{N} C_{\mathrm{IL}i} \,. \tag{6.9}$$

The reduction of the crack driving force due to the soft interlayers, compared to the homogeneous matrix material of the multilayer, is quantified by the dimensionless parameter,

$$\Psi_{\mathrm{ML}}^{\mathrm{CA}} = \left.\frac{J_{\mathrm{tip}}^{\mathrm{CA}}}{J_{\mathrm{far}}^{\mathrm{CA}}}\right|_{\mathrm{ML}} , \tag{6.10}$$

called the *J*-reduction coefficient of the multilayer.

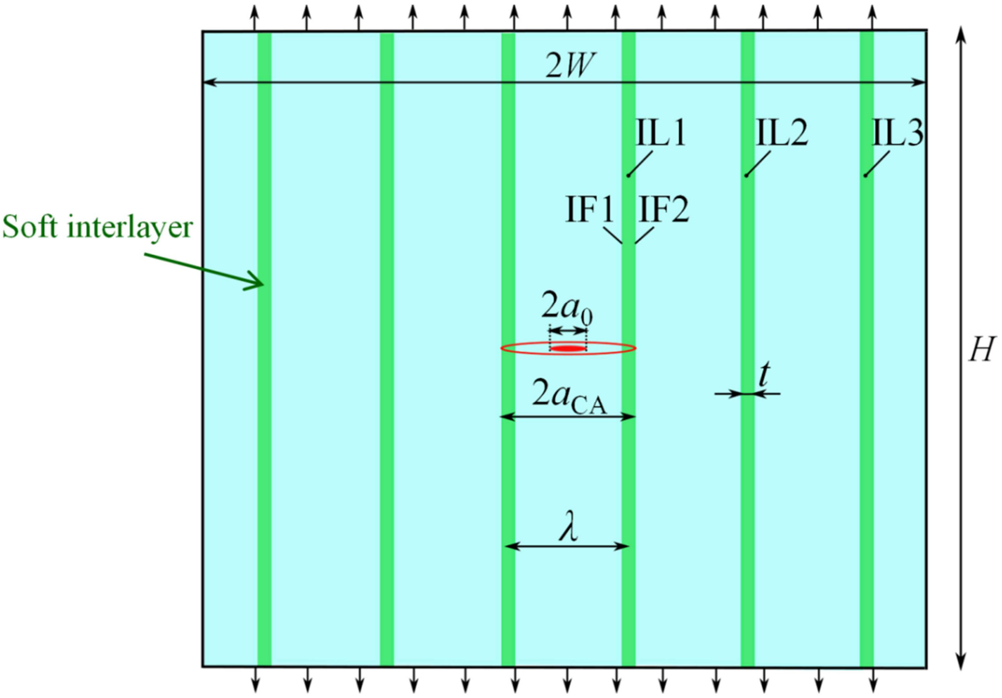

(a)

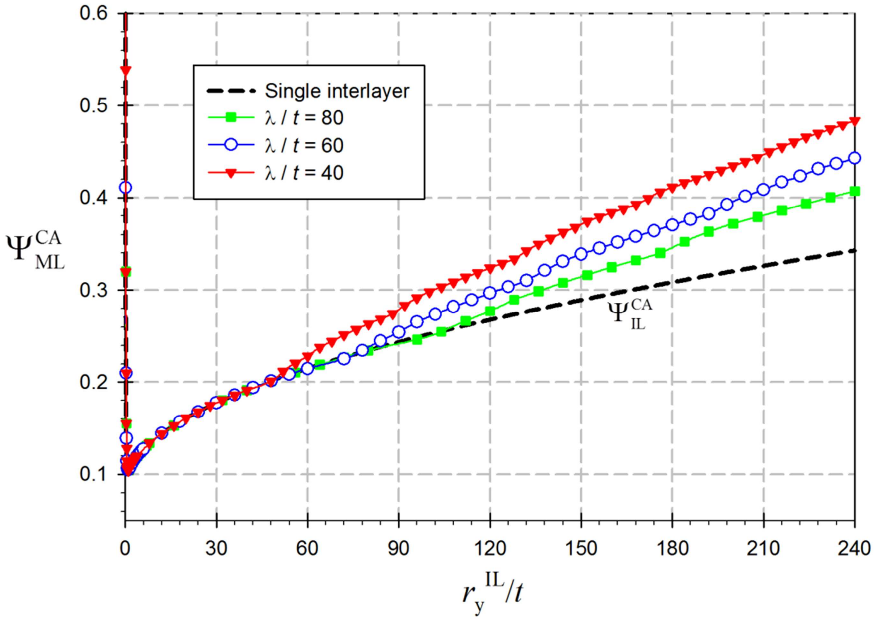

(b)

Fig. 6.4 **(a)** Multilayered MT-specimen with soft interlayers and a short crack that has arrested at the CA position (at IF2 of IL1), see Fig. 1b. **(b)** Variation of the multilayer *J*-reduction coefficient, Ψ_{ML}^{CA}, as a function of the loading parameter r_y^{IL}/t for three different wavelengths λ, $t = 0.05$ mm, $\sigma_y^M \to \infty$ and $\sigma_y^{IL} = 200$ MPa ($\sigma_y^{IL}/\sigma_y^M = 0$). Ψ_{IL}^{CA} is the *J*-reduction coefficient of a single interlayer.

Fig. 6.4b shows the variation of $\Psi_{\mathrm{ML}}^{\mathrm{CA}}$ as a function of the dimensionless loading parameter, $r_{\mathrm{y}}^{\mathrm{IL}}/t$, for a multilayer with interlayer thickness t = 0.05 mm, $\sigma_{\mathrm{y}}^{\mathrm{IL}}/\sigma_{\mathrm{y}}^{\mathrm{M}}=0$ (linear elastic matrix and $\sigma_{\mathrm{y}}^{\mathrm{IL}}=200$ MPa) and three different wavelengths, λ = 2, 3 and 4 mm. The *J*-reduction coefficient of a single interlayer $\Psi_{\mathrm{IL}}^{\mathrm{CA}}$ is plotted for comparison. The $\Psi_{\mathrm{ML}}^{\mathrm{CA}}$-curves coincide with that of $\Psi_{\mathrm{IL}}^{\mathrm{CA}}$ as long as the crack tip plastic zone does not touch the second interlayer, i.e. as long as C_{IL2} = 0. If the load increases so that $r_{\mathrm{y}}^{\mathrm{IL}}\approx\lambda$, the crack tip plastic zone starts to interact with IL2, and $\Psi_{\mathrm{ML}}^{\mathrm{CA}}$ becomes larger than $\Psi_{\mathrm{IL}}^{\mathrm{CA}}$. Note that IL2 provides an anti-shielding effect, since the hard/soft transition of IF1 is closer to the crack tip than the soft/hard transition of IF2, see Fig. 6.4a. As explained in (Sistaninia and Kolednik 2014), the absolute value of C_{inh} is inversely related to the distance between the crack tip and the interface. If $r_{\mathrm{y}}^{\mathrm{IL}}\approx 2\lambda$, $r_{\mathrm{y}}^{\mathrm{IL}}\approx 3\lambda$, etc., the crack tip plastic zone starts to interact with IL3, IL4, etc., and the $\Psi_{\mathrm{ML}}^{\mathrm{CA}}$-curve exhibits a steeper increase with $r_{\mathrm{y}}^{\mathrm{IL}}/t$, see Fig. 6.4b.

As explained in Section 6.3, $\Psi_{\mathrm{IL}}^{\mathrm{CA}}$ depends on the two dimensionless parameters $\sigma_{\mathrm{y}}^{\mathrm{IL}}/\sigma_{\mathrm{y}}^{\mathrm{M}}$ and $r_{\mathrm{y}}^{\mathrm{IL}}/t$, Eq. (6.6). It is clear from the previous paragraph that the *J*-reduction coefficient of a multilayer $\Psi_{\mathrm{ML}}^{\mathrm{CA}}$ depends additionally on the loading parameter $r_{\mathrm{y}}^{\mathrm{IL}}/\lambda$, and we can write

$$\Psi_{\mathrm{ML}}^{\mathrm{CA}}=f_{\mathrm{ML}}\left(\frac{\sigma_{\mathrm{y}}^{\mathrm{IL}}}{\sigma_{\mathrm{y}}^{\mathrm{M}}},\frac{r_{\mathrm{y}}^{\mathrm{IL}}}{t},\frac{r_{\mathrm{y}}^{\mathrm{IL}}}{\lambda}\right). \tag{6.11}$$

It is useful to consider the ratio $\Psi_{\mathrm{ML}}^{\mathrm{CA}}/\Psi_{\mathrm{IL}}^{\mathrm{CA}}$. This ratio gives the relative increase of the crack driving force in a multilayer compared to a single-interlayer specimen, both for a crack in the CA-position.

In Fig. 6.5a, the ratio $\Psi_{\mathrm{ML}}^{\mathrm{CA}}/\Psi_{\mathrm{IL}}^{\mathrm{CA}}$ is plotted against the dimensionless loading parameter $r_{\mathrm{y}}^{\mathrm{IL}}/\lambda$ for an interlayer thickness t = 0.05 mm, yield stress ratio $\sigma_{\mathrm{y}}^{\mathrm{IL}}/\sigma_{\mathrm{y}}^{\mathrm{M}}=0$ and three wavelengths, λ = 2, 3 and 4 mm. The three curves nearly coincide. $\Psi_{\mathrm{ML}}^{\mathrm{CA}}/\Psi_{\mathrm{IL}}^{\mathrm{CA}}=1$ until the crack tip plastic zone reaches IL2, $r_{\mathrm{y}}^{\mathrm{IL}}/\lambda\approx 1$. Subsequently, the ratio $\Psi_{\mathrm{ML}}^{\mathrm{CA}}/\Psi_{\mathrm{IL}}^{\mathrm{CA}}$ increases due to the anti-shielding effect of IL2. If with further loading the crack tip plastic zone starts to interact with IL3, IL4, etc., the $\Psi_{\mathrm{ML}}^{\mathrm{CA}}/\Psi_{\mathrm{IL}}^{\mathrm{CA}}$-curve exhibits a steeper increase with loading, compare also Fig. 6.4b.

Fig. 6.5b shows $\Psi_{\mathrm{ML}}^{\mathrm{CA}}/\Psi_{\mathrm{IL}}^{\mathrm{CA}}$ vs. $r_{\mathrm{y}}^{\mathrm{IL}}/\lambda$-curves for λ = 2 mm, $\sigma_{\mathrm{y}}^{\mathrm{IL}}/\sigma_{\mathrm{y}}^{\mathrm{M}}=0$ and t = 0.025, 0.05 and 0.1 mm. Again the curves coincide. Therefore, we can conclude that the ratio $\Psi_{\mathrm{ML}}^{\mathrm{CA}}/\Psi_{\mathrm{IL}}^{\mathrm{CA}}$ does not depend on the dimensionless parameter $r_{\mathrm{y}}^{\mathrm{IL}}/t$. The reason might be that both $\Psi_{\mathrm{ML}}^{\mathrm{CA}}$ and $\Psi_{\mathrm{IL}}^{\mathrm{CA}}$ depend on the parameter $r_{\mathrm{y}}^{\mathrm{IL}}/t$, but the ratio $\Psi_{\mathrm{ML}}^{\mathrm{CA}}/\Psi_{\mathrm{IL}}^{\mathrm{CA}}$ is independent of this parameter. Therefore, the *J*-reduction coefficient of a multilayer, $\Psi_{\mathrm{ML}}^{\mathrm{CA}}$ from Eq. (6.11), can be rewritten as,

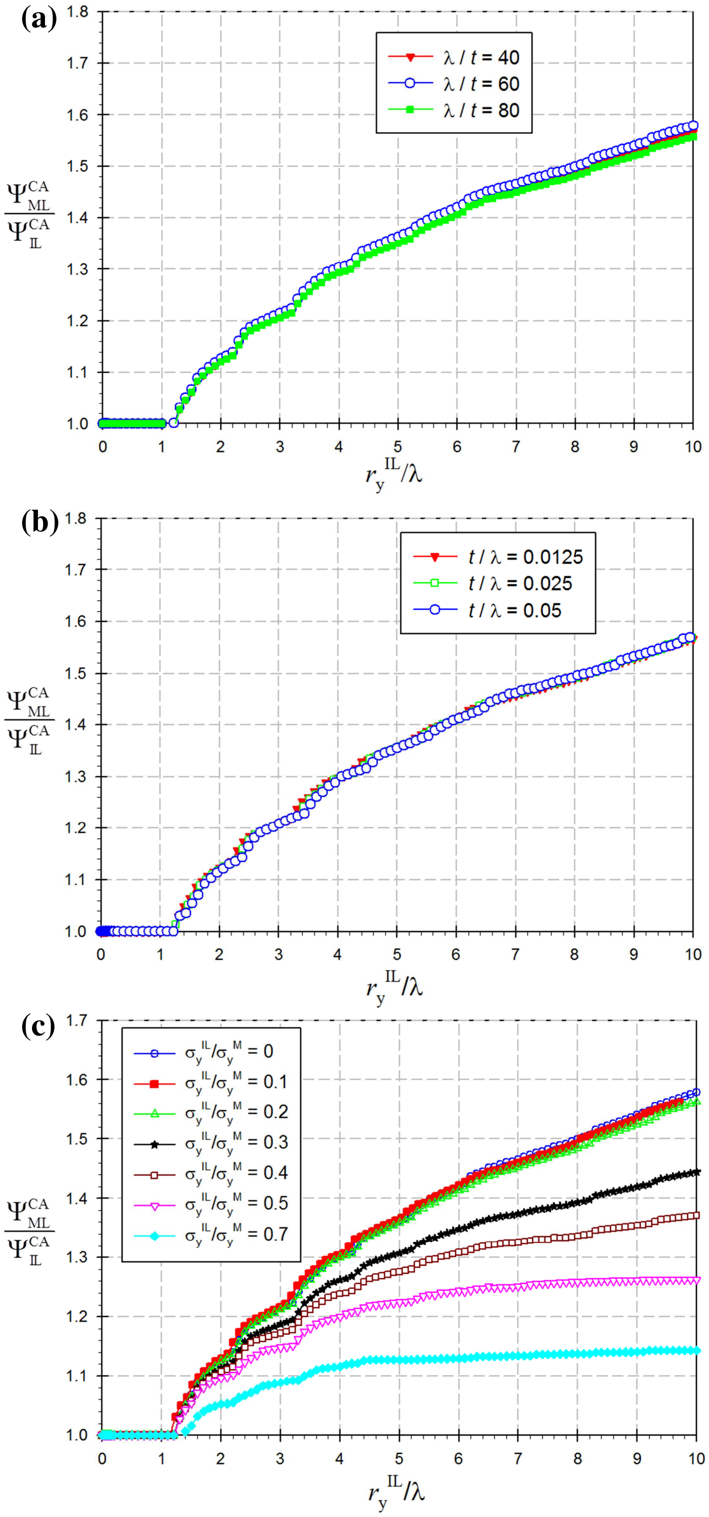

Fig. 6.5 Ratio $\Psi_{\mathrm{ML}}^{\mathrm{CA}} / \Psi_{\mathrm{IL}}^{\mathrm{CA}}$ plotted against the loading parameter $r_{\mathrm{y}}^{\mathrm{IL}} / \lambda$ for various multilayer configurations: **(a)** Multilayers with t = 0.05 mm, $\sigma_{\mathrm{y}}^{\mathrm{IL}} / \sigma_{\mathrm{y}}^{\mathrm{M}} = 0$ and three different wavelengths, λ = 2, 3 and 4 mm; the curves nearly coincide. **(b)** Multilayers with λ = 2 mm, $\sigma_{\mathrm{y}}^{\mathrm{IL}} / \sigma_{\mathrm{y}}^{\mathrm{M}} = 0$ and three different interlayer thicknesses, t = 0.025, 0.05 and 0.10 mm. **(c)** Multilayers with t = 0.05 mm, λ = 2 mm and seven different yield stress ratios $\sigma_{\mathrm{y}}^{\mathrm{IL}} / \sigma_{\mathrm{y}}^{\mathrm{M}}$ between 0 and 0.7.

$$\Psi_{\mathrm{ML}}^{\mathrm{CA}}\left(\frac{\sigma_{\mathrm{y}}^{\mathrm{IL}}}{\sigma_{\mathrm{y}}^{\mathrm{M}}},\frac{r_{\mathrm{y}}^{\mathrm{IL}}}{t},\frac{r_{\mathrm{y}}^{\mathrm{IL}}}{\lambda}\right)=\Psi_{\mathrm{IL}}^{\mathrm{CA}}\left(\frac{\sigma_{\mathrm{y}}^{\mathrm{IL}}}{\sigma_{\mathrm{y}}^{\mathrm{M}}},\frac{r_{\mathrm{y}}^{\mathrm{IL}}}{t}\right)\cdot\frac{\Psi_{\mathrm{ML}}^{\mathrm{CA}}}{\Psi_{\mathrm{IL}}^{\mathrm{CA}}}\left(\frac{\sigma_{\mathrm{y}}^{\mathrm{IL}}}{\sigma_{\mathrm{y}}^{\mathrm{M}}},\frac{r_{\mathrm{y}}^{\mathrm{IL}}}{\lambda}\right). \tag{6.12}$$

Fig. 6.5c shows the influence of the yield stress ratio $\sigma_{\mathrm{y}}^{\mathrm{IL}}/\sigma_{\mathrm{y}}^{\mathrm{M}}$ on the ratio $\Psi_{\mathrm{ML}}^{\mathrm{CA}}/\Psi_{\mathrm{IL}}^{\mathrm{CA}}$, for $t = 0.05$ mm and $\lambda = 2$ mm. The ratio $\Psi_{\mathrm{ML}}^{\mathrm{CA}}/\Psi_{\mathrm{IL}}^{\mathrm{CA}}$ increases with decreasing $\sigma_{\mathrm{y}}^{\mathrm{IL}}/\sigma_{\mathrm{y}}^{\mathrm{M}}$, but remains approximately constant for $\sigma_{\mathrm{y}}^{\mathrm{IL}}/\sigma_{\mathrm{y}}^{\mathrm{M}} \leq 0.2$, i.e. when the optimum yield stress of the interlayer is reached. One has to keep in mind that, although the ratio $\Psi_{\mathrm{ML}}^{\mathrm{CA}}/\Psi_{\mathrm{IL}}^{\mathrm{CA}}$ increases, the value of $\Psi_{\mathrm{ML}}^{\mathrm{CA}}$ decreases with decreasing $\sigma_{\mathrm{y}}^{\mathrm{IL}}/\sigma_{\mathrm{y}}^{\mathrm{M}}$. The reason is that the $\Psi_{\mathrm{IL}}^{\mathrm{CA}}$-values strongly decrease with decreasing $\sigma_{\mathrm{y}}^{\mathrm{IL}}/\sigma_{\mathrm{y}}^{\mathrm{M}}$, see Fig. 6.2b and Eq. (6.12).

From the results of this section, the effectiveness of soft interlayers as crack arresters in multilayer composites can be quantified as a function of the material properties ($\sigma_{\mathrm{y}}^{\mathrm{IL}}/\sigma_{\mathrm{y}}^{\mathrm{M}}$) and the architecture ($t$, λ) of the composite, and the magnitude of loading. First the values of $\Psi_{\mathrm{IL}}^{\mathrm{CA}}$ and $\Psi_{\mathrm{ML}}^{\mathrm{CA}}/\Psi_{\mathrm{IL}}^{\mathrm{CA}}$ are determined from Figs. 6.2b and 6.5c, respectively, and then the value of $\Psi_{\mathrm{ML}}^{\mathrm{CA}}$ is calculated from Eq. (6.12). It is outlined in the following section how this knowledge can be used for the design of strong and tough composites.

6.5 A wavelength criterion for strong and tough multilayers

When an inherent crack in a brittle homogeneous material starts to grow, it usually does not stop growing until the whole specimen is fractured. However, in the multilayer composite (Fig. 6.4a), soft interlayers can provide crack arrest at the CA position. The multilayer will exhibit a higher fracture stress than the homogeneous material, if the applied load for re-initiation of the arrested crack with length,

$$a_{\mathrm{CA}} = (\lambda + t)/2 \approx \lambda/2, \tag{6.13}$$

is higher than the load required to initiate growth of the inherent crack with length a_{n} in the homogeneous material.

If $\sigma_{\mathrm{fr}}^{\mathrm{M}}$ is the fracture stress of the homogeneous matrix material in the tensile test and $K_{\mathrm{c}}^{\mathrm{M}}$ its critical stress intensity factor, i.e. its fracture initiation toughness, determined by a fracture mechanics experiment, the inherent defect size $a_{\mathrm{n}}^{\mathrm{M}}$ can be determined as (Kolednik et al. 2011; Kolednik et al. 2014a),

$$a_{\mathrm{n}}^{\mathrm{M}} = \frac{1}{\pi}\left(\frac{K_{\mathrm{c}}^{\mathrm{M}}}{\sigma_{\mathrm{fr}}^{\mathrm{M}}}\right)^2. \tag{6.14}$$

Eq. (6.14) assumes that the inherent defect size is much smaller than the width or diameter of the tensile specimen. The condition for the initiation of crack growth is

$$J_{\mathrm{tip}} \geq J_{\mathrm{c}}^{\mathrm{M}} = (K_{\mathrm{c}}^{\mathrm{M}})^2 / E'. \tag{6.15}$$

In Eq. (6.15), J_{tip} denotes the crack driving force, $J_{\mathrm{c}}^{\mathrm{M}}$ is the fracture initiation toughness of the homogeneous matrix material in terms of the J-integral, and $E' = E$ for plane stress conditions and $E' = E/(1-\nu^2)$ for plane strain conditions (Anderson 2005).

The far-field J-integral J_{far} of a homogeneous specimen with an interior crack of length $2a$ can be written as (Anderson 2005; Gross and Seelig 2007)

$$J_{\mathrm{far}}^{\mathrm{hom}} = J_{\mathrm{tip}}^{\mathrm{hom}} = \frac{\left(\sigma_{\mathrm{appl}}\right)^2 (1-\nu^2)}{E} \pi a, \tag{6.16}$$

where σ_{appl} is the applied global stress. Eq. (6.16) is valid for linear elastic and small-scale yielding conditions. The far-field J-integral of the arrested crack in the multilayer can be approximated from Eq. (6.16), with the crack length a replaced by the length of the arrested crack a_{CA},

$$J_{\mathrm{far}}^{\mathrm{CA}} \approx \frac{\left(\sigma_{\mathrm{appl}}\right)^2 (1-\nu^2)}{E} \pi \frac{\lambda}{2}, \tag{6.17}$$

The approximation is valid, if the interlayer thickness is much smaller than the wavelength of the multilayer, $\lambda \gg t$. The crack driving force of the arrested crack can be estimated by inserting Eq. (6.17) into Eq. (6.10), yielding

$$J_{\mathrm{tip}}^{\mathrm{CA}} = \Psi_{\mathrm{ML}}^{\mathrm{CA}} J_{\mathrm{far}}^{\mathrm{CA}} \approx \Psi_{\mathrm{ML}}^{\mathrm{CA}} \frac{\pi}{2} \frac{\left(\sigma_{\mathrm{appl}}\right)^2 (1-\nu^2)}{E} \lambda. \tag{6.18}$$

In order to prevent the re-initiation of growth of the arrested crack, the crack driving force must remain smaller than the fracture initiation toughness of the matrix material, $J_{\mathrm{tip}}^{\mathrm{CA}} < J_{\mathrm{c}}^{\mathrm{M}}$. Hereby it is assumed that the fracture initiation toughness of the matrix material in the multilayer equals that of the homogeneous matrix material. By inserting the inequality $J_{\mathrm{tip}}^{\mathrm{CA}} < J_{\mathrm{c}}^{\mathrm{M}}$ into Eq. (6.18), we get a criterion for preventing growth of the arrested crack in the form,

$$\lambda < \frac{2}{\pi \Psi_{\mathrm{ML}}^{\mathrm{CA}}} \frac{J_{\mathrm{c}}^{\mathrm{M}} E}{\left(\sigma_{\mathrm{appl}}\right)^2 (1-\nu^2)}. \tag{6.19}$$

Eq. (6.19) shows that the necessary wavelength for preventing fracture of the multilayer is inversely proportional to the square of the applied stress, i.e. a high applied stress requires a small wavelength λ, and vice versa. Eq. (6.19) can be used as an architectural criterion for the design of strong multilayered composites, utilizing the yield stress inhomogeneity effect.

A similar criterion can be derived for multilayered, elastic composites with spatial variations in Young's modulus, see Appendix 6.A.

Fig. 6.6, from (Aizenberg et al. 2005), shows the cross section of a segment of the skeleton of the glass sponge *Euplectella sp.* Each rod consists of cylindrical layers made of bio-glass, connected by very thin layers of protein. Although bio-glass is very brittle, the structure exhibits a high strength and exorbitant toughness. The reason for these properties lies in the material inhomogeneity effect, for the first time noted in (Kolednik et al. 2011). The structure is mainly loaded by (impact-) bending where the bending stress linearly increases with the radius, $\sigma_{\mathrm{appl}} \sim r$. It is seen from Fig. 6.6 that the wavelength λ decreases with the radius from the center of the rod to the periphery, which is reasonable according to Eq. (6.19) or Eq. (6.A2). Other bio-inspired strategies for materials design can be found in Fratzl et al. (2016).

6.6 Procedure for finding optimum multilayer configurations

There is an interplay of three length parameters in the multilayer: interlayer thickness t, interlayer spacing (or wavelength) λ, and the radius of the crack-tip plastic zone in the interlayer $r_{\mathrm{y}}^{\mathrm{IL}}$ (which depends on the yield strength of the interlayer material, the crack length and the applied load). We demonstrate in the following that it is possible to deduce an optimum composite architecture.

Let us assume that the matrix material is known with its properties, E^{M}, ν, $\sigma_{\mathrm{y}}^{\mathrm{M}}$ and $J_{\mathrm{c}}^{\mathrm{M}}$. We select an appropriate interlayer material, which should ideally have a yield stress, $\left(\sigma_{\mathrm{y}}^{\mathrm{IL}}\right)_{\mathrm{opt}} \leq 0.2\,\sigma_{\mathrm{y}}^{\mathrm{M}}$, according to Eq. (6.8). If the applied stress σ_{appl} is known, the optimum wavelength λ_{opt} is evaluated from Eq. (6.19) by introducing a "fracture toughness safety factor" $s_{\mathrm{f}} \geq 1$,

$$\lambda_{\mathrm{opt}} = \frac{2}{\pi \Psi_{\mathrm{ML}}^{\mathrm{CA}}} \frac{(J_{\mathrm{c}}^{\mathrm{M}} / s_{\mathrm{f}}) E}{\sigma_{\mathrm{appl}}^{2} (1-\nu^{2})}. \tag{6.20}$$

The fracture toughness safety factor s_{f} should be chosen, depending on the scatter of the fracture toughness of the matrix material, so that the inequality $J_{\mathrm{tip}}^{\mathrm{CA}} < J_{\mathrm{c}}^{\mathrm{M}}$ is guaranteed in all cases. A possible uncertainty in the applied stress should be also taken into account.

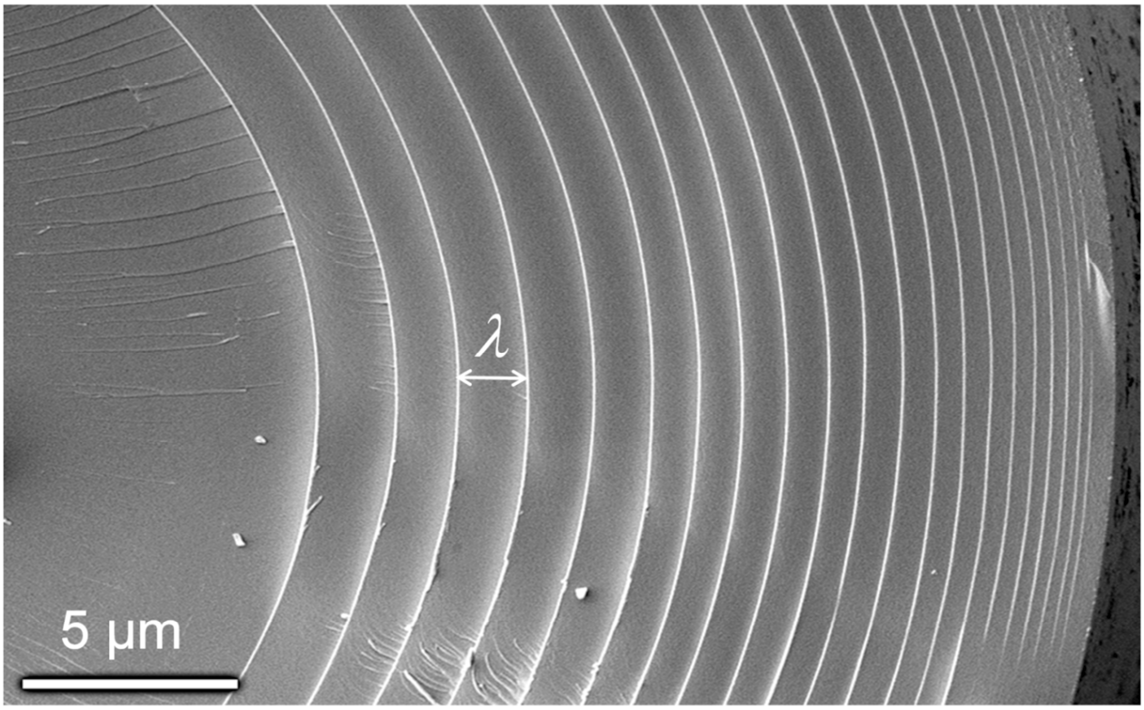

Fig. 6.6 Cross section of a segment of the skeleton of the glass sponge *Euplectella as.*, from (Aizenberg et al. 2005). Thin, soft protein layers lie between the cylindrical bioglass layers. The wavelength λ of the multilayer decreases from the center of the rod to the periphery.

A problem with application of Eq. (6.20) is that the magnitude of the *J*-reduction coefficient of a multilayer $\Psi_{\mathrm{ML}}^{\mathrm{CA}}$ is not known per se. Note that for given material properties and wavelength, the *J*-reduction coefficient of a multilayer $\Psi_{\mathrm{ML}}^{\mathrm{CA}}$ depends for a given yield stress ratio $\sigma_{\mathrm{y}}^{\mathrm{IL}}/\sigma_{\mathrm{y}}^{\mathrm{M}}$ on the load, i.e. on the factor r_{y}/λ, and on the interlayer thickness, i.e. the factor r_{y}/t, see Eqs. (6.11) and (6.12). In general, an iterative procedure must be applied in order to find the correct $\Psi_{\mathrm{ML}}^{\mathrm{CA}}$ and the optimum wavelength λ_{opt}. This procedure is outlined in the following example.

6.6.1 Procedure for composite design

Consider a brittle ceramic material, such as an yttria-stabilized zirconia (Y-TZP). The material data of TZP are: elastic modulus $E^{\mathrm{M}} \approx 200$ GPa (Jung et al. 1997; Fischer et al. 2003; Bartolomé et al. 2007), Poisson's ratio $\nu \approx 0.3$, fracture strength in the bend test (piston-on-3-ball technique (ASTM 1996)) $\sigma_{\mathrm{fr}}^{\mathrm{M}} = 608$ MPa, Weibull modulus $M = 3.9$ (Kosmač et al. 1999). The fracture initiation toughness was measured as $J_{\mathrm{c}}^{\mathrm{M}} = 0.10$ kJ/m^2 ($K_{\mathrm{c}}^{\mathrm{M}} = 4.7\ \mathrm{MPa}\sqrt{\mathrm{m}}$) (Kosmač et al. 1999). The *R*-curve behavior of TZP due to transformation toughening, i.e. the increasing crack growth resistance with crack extension

Δa, is neglected. The inherent defect size of TZP, determined from Eq. (6.14), is $a_{\mathrm{n}} = 19\,\mu\mathrm{m}$. We want to improve the fracture strength of the material by inserting soft interlayers, such as made of iron. The material data of ARMCO-iron are $E^{\mathrm{IL}} = 196$ GPa and $\sigma_{\mathrm{y}}^{\mathrm{IL}} \approx 208$ MPa (Srinivas et al. 1994). The matrix- and interlayer materials have nearly the same Young's modulus. As the TZP can be considered as linear elastic material, $\sigma_{\mathrm{y}}^{\mathrm{M}} \to \infty$, the condition $\sigma_{\mathrm{y}}^{\mathrm{IL}} < 0.2\,\sigma_{\mathrm{y}}^{\mathrm{M}}$, Eq. (6.8), is fulfilled.

Let us assume that we want to find the composite architecture for an improvement of the fracture strength by a factor 1.5, i.e. the applied stress shall be at least $\sigma_{\mathrm{appl}} = 1.5\sigma_{\mathrm{fr}}^{\mathrm{M}} = 912$ MPa at the moment of fracture. First, it is useful to calculate the radius of the plastic zone in the interlayer material. Inserting Eq. (6.17) into Eq. (6.7) leads to the relation,

$$r_{\mathrm{y}}^{\mathrm{IL}} = \frac{\beta\pi}{2}\left(\frac{\sigma_{\mathrm{appl}}}{\sigma_{\mathrm{y}}^{\mathrm{IL}}}\right)^{2}\lambda. \tag{6.21}$$

For plane strain conditions, $\beta = 1/6\pi$, the pre-factor is 1/12, and we get a relation, $r_{\mathrm{y}}^{\mathrm{IL}} = 1.60\,\lambda$. Since this value is so high, the introduction of interlayers with optimum thickness, $t_{\mathrm{opt}} \approx r_{\mathrm{y}}^{\mathrm{IL}}$, Eq. (6.7), would not make much sense because we want to have a high-strength multilayer. Therefore, we should neglect t_{opt} and select a desired value for the interlayer thickness, which fulfils the condition $\lambda \gg t$. Since $r_{\mathrm{y}}^{\mathrm{IL}} / t \gg 1$, the *J*-reduction coefficients, $\Psi_{\mathrm{IL}}^{\mathrm{CA}}$ and $\Psi_{\mathrm{ML}}^{\mathrm{CA}}$, will lie well above the minimum values, $\left(\Psi_{\mathrm{ML}}^{\mathrm{CA}}\right)_{\mathrm{opt}} \approx \left(\Psi_{\mathrm{IL}}^{\mathrm{CA}}\right)_{\mathrm{opt}} \approx 0.1$, see Figs. 6.2b and 6.4b. In our example, we select $t = 0.1\,\mu\mathrm{m}$ and a guessed starting value for the wavelength $\lambda = 20\,\mu\mathrm{m}$, or $r_{\mathrm{y}}^{\mathrm{IL}} / t = 320$. This leads to a value $\Psi_{\mathrm{IL}}^{\mathrm{CA}} = 0.38$ from Fig. 6.2b. From Fig. 6.5 we read a value $\Psi_{\mathrm{ML}}^{\mathrm{CA}} / \Psi_{\mathrm{IL}}^{\mathrm{CA}} = 1.09$ for $r_{\mathrm{y}}^{\mathrm{IL}} / \lambda = 1.6$; note that the magnitudes of t and λ do not play a role, see Eq. (6.12). The *J*-reduction coefficient of the multilayer is $\Psi_{\mathrm{ML}}^{\mathrm{CA}} = 0.41$, Eq. (6.12), and the first iteration of the optimum wavelength, from Eq. (6.20) with a fracture toughness safety factor of $s_{\mathrm{f}} = 1.4$, yields $\lambda_{\mathrm{opt}} = 29\,\mu\mathrm{m}$. These values and the values of the following iterations are collected in Table 6.1. After four iterations, the final value of the optimum wavelength of the TZP/Fe-multilayer, $\lambda_{\mathrm{opt}} = 26.3\,\mu\mathrm{m}$, is found. Other starting values for the wavelength λ lead to the same result.

The procedure can be repeated for other values of the applied stress σ_{appl}. The optimum wavelength λ_{opt} decreases for higher σ_{appl}-values, e.g. $\lambda_{\mathrm{opt}} = 4.8\,\mu\mathrm{m}$ for $\sigma_{\mathrm{appl}} = 3\sigma_{\mathrm{fr}}^{\mathrm{M}}$, or $\lambda_{\mathrm{opt}} = 1.5\,\mu\mathrm{m}$ for $\sigma_{\mathrm{appl}} = 5\sigma_{\mathrm{fr}}^{\mathrm{M}}$, see the red curve in Fig. 6.7.

6.6.2 Limiting value of fracture stress

A transformation of Eq. (6.20) with $s_{\mathrm{f}} = 1$ gives the fracture stress of the ceramic multilayer $\sigma_{\mathrm{fr}}^{\mathrm{ML}}$ as a function of the wavelength λ,

$$\sigma_{\mathrm{fr}}^{\mathrm{ML}} = \sqrt{\frac{2}{\pi(1-\nu^2)} \frac{J_{\mathrm{c}}^{\mathrm{M}} E_{\mathrm{ML}}}{\Psi_{\mathrm{ML}}^{\mathrm{CA}} \lambda}}. \tag{6.22}$$

The fracture stress of the homogeneous matrix material $\sigma_{\mathrm{fr}}^{\mathrm{M}}$ is found from Eq. (6.16) and the condition for initiation of crack growth, $J_{\mathrm{tip}} = J_{\mathrm{c}}^{\mathrm{M}}$, as

$$\sigma_{\mathrm{fr}}^{\mathrm{M}} = \sqrt{\frac{1}{\pi} \frac{J_{\mathrm{c}}^{\mathrm{M}} E_{\mathrm{M}}}{a_{\mathrm{n}}^{\mathrm{M}}(1-\nu^2)}}, \tag{6.23}$$

where $a_{\mathrm{n}}^{\mathrm{M}}$ is the inherent defect size, Eq. (6.14). Since $E_{\mathrm{ML}} \approx E_{\mathrm{M}}$ for $\lambda \gg t$, Eq. (6.22) and Eq. (6.23) can be combined in the form,

$$\frac{\sigma_{\mathrm{fr}}^{\mathrm{ML}}}{\sigma_{\mathrm{fr}}^{\mathrm{M}}} = \sqrt{\frac{2}{\Psi_{\mathrm{ML}}^{\mathrm{CA}}} \frac{a_{\mathrm{n}}^{\mathrm{M}}}{\lambda}}, \tag{6.24}$$

to get the ratio of the fracture stresses between multilayer and homogeneous matrix material.[6] As $\Psi_{\mathrm{ML}}^{\mathrm{CA}}$ depends on $\sigma_{\mathrm{fr}}^{\mathrm{ML}}$ and λ, Eq. (6.12), an iterative process is necessary to determine the fracture stress ratio.

Table 6.1 Iterative procedure to find the *J*-reduction coefficient $\Psi_{\mathrm{ML}}^{\mathrm{CA}}$ and the optimum wavelength λ_{opt} of a ceramic/metal multilayer with t = 0.1 μm interlayer thickness and an applied stress larger than the fracture stress of the homogeneous ceramic material, $\sigma_{\mathrm{appl}} = 1.5\sigma_{\mathrm{fr}}^{\mathrm{M}}$.

t (μm)	λ (μm)	$r_{\mathrm{y}}^{\mathrm{IL}}$ (μm) Eq. (6.21)	$r_{\mathrm{y}}^{\mathrm{IL}} / t$	$r_{\mathrm{y}}^{\mathrm{IL}} / \lambda$	$\Psi_{\mathrm{IL}}^{\mathrm{CA}}$ Fig. 6.2b	$\Psi_{\mathrm{ML}}^{\mathrm{CA}} / \Psi_{\mathrm{IL}}^{\mathrm{CA}}$ Fig. 6.5c	$\Psi_{\mathrm{ML}}^{\mathrm{CA}}$	λ_{opt} (μm) Eq. (6.20)
0.1	20	32	320	1.6	0.379	1.09	0.41	29
0.1	29	46	464	1.6	0.439	1.09	0.47	25
0.1	25	40	400	1.6	0.415	1.09	0.45	26.5
0.1	26	41	410	1.6	0.416	1.09	0.453	**26.3**

---

[6] If $J_{\mathrm{c}}^{\mathrm{M}}$ were replaced by the term $J_{\mathrm{c}}^{\mathrm{M}} / s_{\mathrm{f}}$ in Eq. (6.22), but not in Eq. (6.23) for the homogeneous material, Eq. (6.24) would take the form, $\sigma_{\mathrm{fr}}^{\mathrm{ML}} / \sigma_{\mathrm{fr}}^{\mathrm{M}} = \sqrt{2a_{\mathrm{n}} / s_{\mathrm{f}} \Psi_{\mathrm{ML}}^{\mathrm{CA}} \lambda}$. The resulting curve is identical to the red curve in Fig. 6.7.

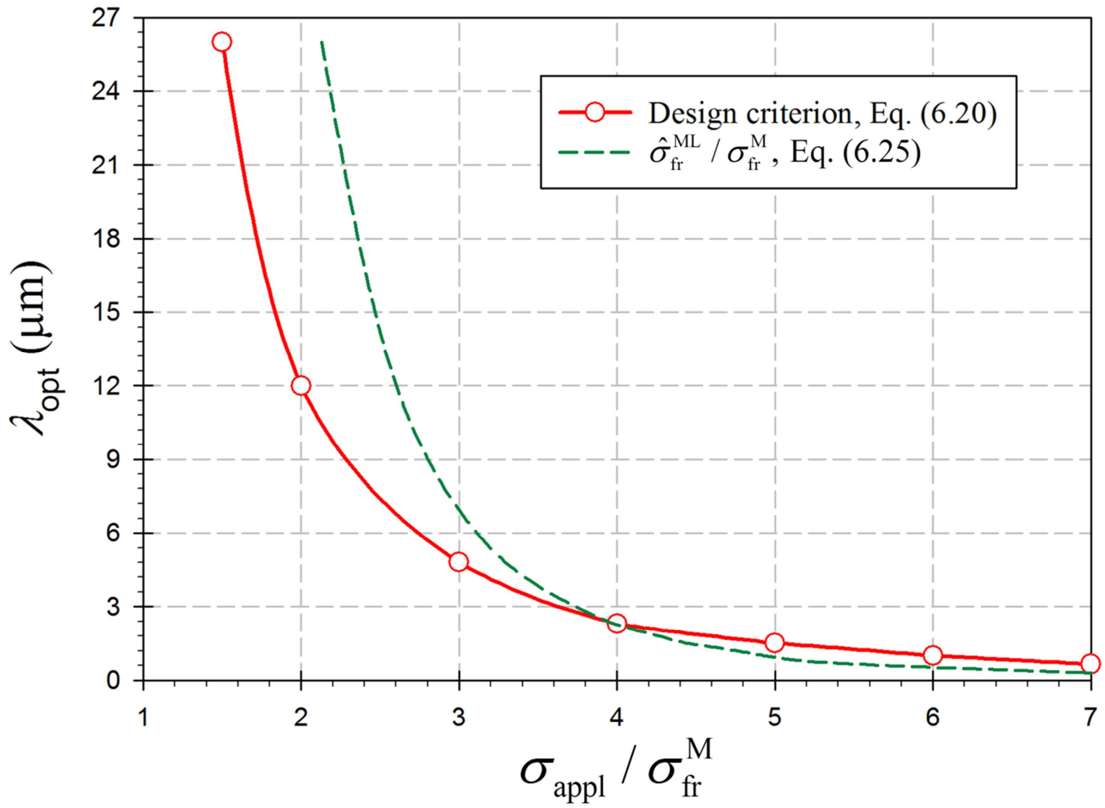

Fig. 6.7 Ceramic/metal multilayer with interlayer thickness $t = 0.1\,\mu\mathrm{m}$. Variation of the optimum wavelength λ_{opt}, Eq. (6.20), as a function of the applied load, related to the fracture stress of the homogeneous material, $\sigma_{\mathrm{appl}} / \sigma_{\mathrm{fr}}^{\mathrm{M}}$. The upper limit of the fracture stress of the multilayer $\hat{\sigma}_{\mathrm{fr}}^{\mathrm{ML}} / \sigma_{\mathrm{fr}}^{\mathrm{M}}$, Eq. (6.25), is also indicated.

Eq. (6.22) yields very high fracture stresses for small wavelengths of the multilayer. An upper limit of the fracture stress of the multilayer $\hat{\sigma}_{\mathrm{fr}}^{\mathrm{ML}}$ was derived in (Kolednik et al. 2014a) for inherently brittle matrix materials, based on the weakest link concept,

$$\hat{\sigma}_{\mathrm{fr}}^{\mathrm{ML}} = \sigma_{\mathrm{fr}}^{\mathrm{M}} \left(\frac{W}{\lambda} \right)^{\frac{1}{M}} . \tag{6.25}$$

Eq. (6.25) assumes two tensile specimens of same thickness *B*, width *W*, and length *L*. One specimen consists of homogeneous matrix material, the other one of the multilayer with wavelength $\lambda \gg t$. The parameter *M* denotes the Weibull modulus of the matrix material (Weibull 1951). Eq. (6.25) relies on the fact that, for statistically homogeneously distributed defects, the probability to find a defect with critical size in a body increases with its volume.

The limit stress of the multilayer $\hat{\sigma}_{\mathrm{fr}}^{\mathrm{ML}}$ is schematically indicated as dashed curve in Fig. 6.7; here we assumed $M = 3.9$ (Kosmač et al. 1999) and a value $W = 500\,\mu\mathrm{m}$ for TZP. It is seen that Eq. (6.20) is applicable only for $\sigma_{\mathrm{appl}} \leq 4\,\sigma_{\mathrm{fr}}^{\mathrm{M}}$. For higher applied loads, the fracture stress is limited by $\hat{\sigma}_{\mathrm{fr}}^{\mathrm{ML}}$.

6.6.3 Other possible applications

Not only the fracture stress, but also the fracture toughness of inherently brittle materials can be significantly improved by the introduction of soft interlayers. The improvement of the critical fracture toughness, i.e. the fracture toughness measured at maximum load during the fracture mechanics experiment (Kolednik et al. 2014a), can be estimated from the relation,

$$J_{\mathrm{c}}^{\mathrm{ML}} \approx J_{\mathrm{c}}^{\mathrm{M}} \big/ \Psi_{\mathrm{ML,long\ crack}}^{\mathrm{CA}} \tag{6.26}$$

Eq. (6.26) is deduced from the condition for initiation of crack growth, Eq. (6.15), Eq. (6.18), and the relation, $J_{\mathrm{far}}^{\mathrm{ML}} = J_{\mathrm{far}}^{\mathrm{M}}$. Note that fracture toughness is determined on specimens with *long* cracks. Since the *J*-reduction coefficients differ for small and long cracks, compare Fig. 6.3, the magnitude of the parameter $\Psi_{\mathrm{ML,long\ crack}}^{\mathrm{CA}}$ will be determined in a forthcoming paper. If the crack is completely arrested by the interlayer as shown in (Zechner and Kolednik 2013a), the fracture mechanics specimen behaves like a tensile specimen; the critical fracture toughness for this case was derived in (Kolednik et al. 2014a).

The procedure for composite design and the derivation of Eq. (6.19) are applicable for all matrix materials with low fracture toughness, even if it does not behave fully brittle, e.g. if the matrix material exhibits an *R*-curve effect (i.e. the crack growth resistance increases with crack extension), or if the fracture mechanism of the matrix is micro-ductile.

One example is the cleavage fracture of a body centered metal at low temperature where a crack nucleus (inherent crack) is formed during the loading of the specimen (Anderson 2005; Chen et al. 1997). One should be careful, however, if the material exhibits an elastic-plastic behavior. If the maximum load in the tensile test is determined by reaching a plastic limit load, and not by the onset of growth of an inherent crack, the fracture stress cannot be further improved. However, a significant improvement of the fracture toughness by the implementation of soft interlayers is possible, as outlined above.

An example is a high-strength aluminum alloy 7075-T6 with yield stress $\sigma_{\mathrm{y}}^{\mathrm{M}} = 520$ MPa, ultimate tensile stress $\sigma_{\mathrm{UTS}}^{\mathrm{M}} = 580$ MPa, and a value of the critical *J*-integral $J_{\mathrm{c}}^{\mathrm{M}} \approx 30$ kJ/m^2 for crack growth in thickness direction ($J_{\mathrm{c}}^{\mathrm{M}} \approx 8$ kJ/m^2 for crack growth in longitudinal direction) (Zechner and Kolednik 2013a). Introduction of soft interlayers made of pure aluminum, Al-1050 with $\sigma_{\mathrm{y}}^{\mathrm{IL}} = 105$ MPa, gave after roll bonding and T6 heat treatment a composite with interlayer thickness $t = 0.10$ mm and a wavelength $\lambda = 1.21$ mm. The multilayer showed a value of the *J*-integral measured at maximum load of $J_{\max}^{\mathrm{ML}} \approx 900$ kJ/m^2 (Kolednik et al. 2016).

The improvement of the fatigue resistance due to the introduction of soft (and soft plus compliant) interlayers was studied in (Kolednik et al. 2016). The maximum applied load is usually low in fatigue, so that it might be possible to insert interlayers with optimum thickness, t_{opt} from Eq. (6.7), and minimum *J*-reduction coefficient, $\left(\Psi_{\mathrm{ML}}^{\mathrm{CA}}\right)_{\mathrm{opt}} \approx 0.1$, in such cases.

6.7 Summary

It is possible to improve the strength and the fracture toughness of inherently brittle matrix materials by the introduction of thin interlayers that have the same Young's modulus but lower yield stress than the matrix. The reason is that, caused by the strong decrease of the crack driving force, a crack arrests near the interface to the hard matrix material. This effect appears without previous delamination of the interlayer. The crack driving force is characterized by the near-tip *J*-integral J_{tip}. The effectiveness of a soft interlayer as crack arrester is quantified by the *J*-reduction coefficient of the multilayer $\Psi_{\mathrm{ML}}^{\mathrm{CA}}$, Eq. (6.10). The parameters, which determine the magnitude of $\Psi_{\mathrm{ML}}^{\mathrm{CA}}$, have been found by a numerical case study, based on the application of the configurational forces concept.

It is shown that, for an optimum effect, the ratio of the yield stress between interlayer- and matrix material should be 1/5 or smaller. The most important architectural parameter of the multilayer is the interlayer spacing, i.e. the wavelength λ of the yield stress variation. A simple fracture mechanical consideration has enabled us to derive the optimum wavelength, which exhibits an inverse dependency on the applied stress, $\lambda_{\mathrm{opt}} \sim 1/\sigma_{\mathrm{appl}}^{2}$, Eq. (6.20). A similar relation has been derived for multilayered composites with spatial variations in Young's modulus. An iterative procedure has been outlined in order to find, for a given matrix material and load, the optimum multilayer architecture, leading to great improvements of fracture stress and/or fracture toughness. The design concept presented in this paper can be applied for different types of multilayers.

Acknowledgements

Financial support by the Austrian Federal Government and the Styrian provincial Government within the research activities of the K2 Competence Center “Integrated Research in Materials, Processing and Product Engineering’’, under the frame of the Austrian COMET Competence Center Program, is gratefully acknowledged (Project A4.20-WP1).

Appendix A. Design criterion for multilayers with spatial variations in Young's modulus

Assume a composite with thin interlayers as depicted in Fig. 6.4. Both matrix and interlayer are elastic; the Young's modulus of the interlayer material E^{IL} is significantly lower than that of the matrix material E^{M}. The driving force of a crack located at the crack arrest position, $a_{\mathrm{CA}} \approx \lambda / 2$, is given by (Kolednik et al. 2014a)

$$J_{\mathrm{tip}}^{\mathrm{CA}} \approx \psi_{\mathrm{ML}}^{\mathrm{CA}} E^{\mathrm{IL}} \left(1-\nu^2\right) \pi \frac{\lambda}{2} \frac{\sigma_{\mathrm{appl}}^2}{\bar{E}^2} . \tag{6.A1}$$

In Eq. (6.A1), $\bar{E}$ denotes the average Young's modulus of the composite and $\psi_{\mathrm{ML}}^{\mathrm{CA}}$ is a non-dimensional parameter resulting from the numerical analysis. Compared to the equation given in (Kolednik et al. 2014a), the applied strain has been substituted by $\varepsilon_{\mathrm{appl}} = \sigma_{\mathrm{appl}} / \bar{E}$, and the term $\left(1-\nu^2\right)$ appears, since plane strain- and not plane stress conditions prevail.

The derivation of the wavelength criterion analogously to Section 6.5 leads to the inequality,

$$\lambda < \frac{2}{\pi \psi_{\mathrm{ML}}^{\mathrm{CA}}} \frac{J_{\mathrm{c}}^{\mathrm{M}} \bar{E}^2}{E^{\mathrm{IL}} \sigma_{\mathrm{appl}}^2 \left(1-\nu^2\right)} , \tag{6.A2}$$

compare Eq. (6.19). It has been demonstrated in (Kolednik et al. 2014a) that very thin interlayers are sufficient for crack arrest, which means that the loss in stiffness is almost negligible, $\bar{E} \approx E^{\mathrm{M}}$. The effectiveness of a compliant interlayer as crack arrester in a multilayer can be quantified, according to Eq. (6.10), by the *J*-reduction coefficient,

$$\left(\Psi_{\mathrm{ML}}^{\mathrm{CA}}\right)_{E\text{-inh}} = \frac{E^{\mathrm{IL}}}{\psi_{\mathrm{ML}}^{\mathrm{CA}} \bar{E}} \approx \frac{E^{\mathrm{IL}}}{\psi_{\mathrm{ML}}^{\mathrm{CA}} E^{\mathrm{M}}} . \tag{6.A3}$$

The correctness of Eq. (6.A3) is easily seen when comparing Eq. (6.18) to Eq. (6.A1), or Eq. (6.19) to Eq. (6.A2). The numerical results in (Kolednik et al. 2014a) resulted $\psi_{\mathrm{ML}}^{\mathrm{CA}} \approx 1.3$. However, a dependency of $\psi_{\mathrm{ML}}^{\mathrm{CA}}$ on the *E*-variation, the load, the interlayer thickness, and the wavelength cannot be excluded.

Analogously to Eq. (6.20), the optimum wavelength of the multilayer for a given applied stress is found with Eq. (6.A3) and by introducing a safety factor s_{f} in the form,

$$\lambda_{\mathrm{opt}} = \frac{2}{\pi \left(\Psi_{\mathrm{ML}}^{\mathrm{CA}}\right)_{E\text{-inh}}} \frac{\left(J_{\mathrm{c}}^{\mathrm{M}} / s_{\mathrm{f}}\right) \bar{E}}{\left(\sigma_{\mathrm{appl}}\right)^2 \left(1-\nu^2\right)} . \tag{6.A4}$$

Appendix B. List of symbols

a	Crack length
a_{CA}	Length of arrested crack
$a_{\mathrm{n}}^{\mathrm{M}}$	Inherent defect size in matrix material, Eq. (6.14)
C_{inh}	Material inhomogeneity term
E	Young’s modulus
$J_{\mathrm{tip}}^{\mathrm{CA}}$	Near-tip *J*-integral for a crack at crack arrest position
$J_{\mathrm{far}}^{\mathrm{CA}}$	Far-field *J*-integral for a crack at crack arrest position
$J_{\mathrm{c}}^{\mathrm{M}}$	Fracture initiation toughness of the matrix material
r_{y}	Radius of the crack tip plastic zone, Eq. (6.4)
$r_{\mathrm{y}}^{\mathrm{IL}}$	Radius of the plastic zone in the interlayer material
s_{f}	Safety factor
t	Interlayer thickness
β	Constant related to the radius of the crack tip plastic zone
λ	Spacing of interlayers, i.e. wavelength of multilayer
v	Poisson’s ratio
σ_{y}	Yield stress
σ_{appl}	Applied global stress
$\sigma_{\mathrm{fr}}^{\mathrm{M}}$	Fracture stress of the matrix material
$\hat{\sigma}_{\mathrm{fr}}^{\mathrm{ML}}$	Upper limit of fracture stress of the multilayer
$\Psi_{\mathrm{IL}}^{\mathrm{CA}}$	*J*-reduction coefficient of a single interlayer, Eq. (6.5)
$\Psi_{\mathrm{ML}}^{\mathrm{CA}}$	*J*-reduction coefficient of the multilayer, Eq. (6.10)

7 Improving fracture toughness by yield stress inhomogeneity effect

In Paper II, we have shown that the strength, i.e. the fracture stress in a tensile test, of intrinsically brittle materials can be greatly improved by the introduction of thin, soft interlayers in high-strength matrix materials with low intrinsic toughness. An iterative procedure has been worked out to find, for given matrix material and applied stress, the optimum yield stress of soft interlayers, as well as the optimum multilayer architecture, which is determined by interlayer thickness t and interlayer spacing (wavelength) λ.

Paper III shows that not only the strength, but also the fracture toughness of inherently brittle materials can be significantly improved by the introduction of soft interlayers.

The fracture toughness of a material is determined by fracture mechanics experiments on specimens with long cracks. Therefore, Paper III first performs a comprehensive case study, for a multilayer single-edge notch tension (SENT) specimen that contains a long crack, in order to quantify the influence of soft interlayers on the crack driving force of multilayers with long cracks; the concept of configurational forces, in combination with a finite element (FE) stress and strain analysis, is used for this quantification. Fracture mechanical considerations are then used to derive a model for predicting the improvement of the fracture toughness in multilayer structures as a function of the multilayer architectural parameters (the interlayer spacing, the interlayer thickness and the yield stress ratio between interlayer and matrix) and the fracture toughness of the homogeneous matrix material. Finally, the findings are compared to experimental results of fracture tests conducted on a compound made of high-strength steel as matrix and low-strength steel as interlayer material.

Our investigations lead to the following conclusions of Paper III:

- Spatial variations of the yield stress by the implementation of thin, soft interlayers significantly improve the fracture toughness of brittle matrix materials, if the architectural parameters of the multilayers are appropriately chosen.
- An iterative procedure is presented for predicting the fracture toughness of the multilayer.
- Experiments with steel compounds, consisting of a tool steel as matrix and a low-carbon steel as interlayer material, confirm our findings.

- From the results of fracture tests and numerical simulations, it is found that the intrinsic fracture initiation toughness of the matrix material in the multilayer equals that of the homogeneous matrix material.
- It is shown that, in addition to the crack arresting effect of soft interlayers, compressive thermal residual stresses, which develop in the matrix during the production process of the steel multilayers, lead to a further improvement in fracture toughness.

Paper III:

Design of highly fracture-resistant composites by the application of the yield stress inhomogeneity effect

M. Sistaninia, R. Kasberger, O. Kolednik

submitted to

Composite Structures

Abstract

Improvement of the fracture toughness by the introduction of thin, soft interlayers is investigated. The mechanism is the strong decrease of the crack driving force when the crack tip is located in the soft region. Based on numerical simulations with the configurational forces concept, it is demonstrated that the fracture toughness of brittle materials can be greatly improved by the introduction of soft interlayers, if the architectural parameters of the multilayer are appropriately chosen. The findings are compared to experimental results of fracture tests conducted on compounds made of high-strength steel as matrix and low-strength steel as interlayer material. The design concept presented in this paper can be applied for various types of composite materials.

Keywords: Multilayer composites; Material inhomogeneity effect; Finite element modeling; Fracture toughness; Steel composite.

7.1 Introduction

Increasing strength leads to a decrease in fracture toughness. This general rule applies to most engineering materials and alloys. A new and innovative method to break this rule is to utilize the *material inhomogeneity effect* (Fratzl et al. 2007; Kolednik et al. 2011; Kolednik et al. 2014a; Sistaninia and Kolednik 2017) by inserting soft interlayers into the material. The interlayers act as crack arresters so that the fracture toughness strongly increases. If the soft interlayers are thin, the loss in strength is almost negligible.

The material inhomogeneity effect is based on the fact that spatial variations in material properties have a large influence on the crack driving force, i.e. a material inhomogeneity can hinder or promote crack propagation (Kolednik 2000; Chen et al. 2007; Fratzl et al. 2007; Kolednik et al. 2009; Kolednik et al. 2011; Fischer et al. 2012a; Kolednik 2012; Zechner and Kolednik 2013a; Fischer et al. 2014; Kolednik et al. 2014a; Sistaninia and Kolednik 2014; Kolednik et al. 2016; Sistaninia and Kolednik 2017). For example, the crack driving force decreases, if a crack grows from a region with lower Young's modulus towards a region with higher Young's modulus. The same occurs, if a crack grows from a region with lower yield stress towards a region with higher yield stress. In our terminology, compliant/stiff and soft/hard transitions provide a crack-tip shielding effect, which hinders crack propagation. In contrast, stiff/compliant and hard/soft transitions provide an increase of the crack driving force, i.e. anti-shielding, which promotes crack propagation. Experimental evidence of the material inhomogeneity effect has been presented, e.g. in (Pippan et al. 2000; Suresh et al. 1993; Suresh et al. 1992; Zechner and Kolednik 2013a; Zechner and Kolednik 2013b). The material inhomogeneity effect works for both abrupt and smooth spatial variations of material properties and is fundamentally different from other toughening mechanisms in composite materials, such as interface delamination (Cook and Gordon 1964; Embury et al. 1967; Lesuer et al. 1996; Tariolle et al. 2005), crack deflection (Lesuer et al. 1996) and compressive residual stresses (Lugovy et al. 2005; Rao et al. 1999; Sglavo and Bertoldi 2006).

The strength, i.e. the fracture stress in a tensile test, of intrinsically brittle materials is determined by the initiation and growth of *small* defects – in contrast to ductile materials where the strength is determined by a plastic limit load. In previous papers, we derived models for predicting the *strength* of multilayers consisting of intrinsically brittle matrix materials and thin, compliant (Kolednik et al. 2011; Kolednik et al. 2014a) or soft (Sistaninia and Kolednik 2017) interlayers. It was shown that the introduction of thin, compliant or soft interlayers can significantly improve the strength of brittle materials. An iterative procedure has been outlined in Sistaninia and Kolednik (2017) in order to find, for a given matrix material and applied load, the optimum multilayer architecture, which is determined by interlayer thickness t and interlayer spacing (wavelength) λ.

Contrary to strength, *fracture toughness* is determined by fracture mechanics experiments on specimens with *long* cracks. It was demonstrated in (Kolednik et al. 2014a) that a linear elastic material with spatial variation of the Young's modulus exhibits significantly higher fracture toughness than a corresponding homogeneous material. It was shown that the improvement depends on the amplitude of the E-variation; however, a quantification of the effect was not possible at that time.

In the current paper, the fracture toughness of a multilayer with constant Young's modulus E and spatial variation of the yield stress σ_{y} is considered. By numerical simulations and fracture mechanical considerations, the improvement in fracture toughness of such a multilayer structure is quantified as a function of the variation of σ_{y}, the architectural parameters of the multilayer (interlayer thickness t and -spacing λ), and the fracture toughness of the homogeneous matrix material. An iterative procedure is presented for predicting the fracture toughness of the multilayer. This procedure shall be applicable for designing fracture-resistant composites based on the yield stress inhomogeneity effect. The findings are compared to results of experiments conducted on steel compounds consisting of a high-strength steel as matrix and a low-strength steel as interlayer material.

7.2 Estimate of the fracture toughness for multilayers with thin, soft interlayers

7.2.1 Condition for initiation of crack growth

Assume a homogeneous specimen consisting of a brittle material with an initial crack of length a_0, Fig. 7.1a. When the crack starts to grow, it usually does not stop growing until the whole specimen is fractured. The condition for initiation of crack growth is,

$$J_{\mathrm{tip}} \geq J_{\mathrm{c}}^{\mathrm{M}}, \tag{7.1}$$

where $J_{\mathrm{c}}^{\mathrm{M}}$ is the fracture initiation toughness of the material in terms of the J-integral, determined by a fracture mechanics experiment (Anderson 2005), and the near-tip J-integral J_{tip} characterizes the crack driving force. The J-integral is path-independent in homogenous materials. The J-integral of the homogeneous specimen can be expressed via the stress intensity factor K as (Anderson 2005),

$$J_{\mathrm{far}}^{\mathrm{hom}} = J_{\mathrm{tip}}^{\mathrm{hom}} = \frac{K^2(1-\nu^2)}{E} = \frac{\sigma_{\mathrm{appl}}^2(1-\nu^2)}{E}\pi a_0 \left[f_K\left(\frac{a_0}{W}\right)\right]^2, \tag{7.2}$$

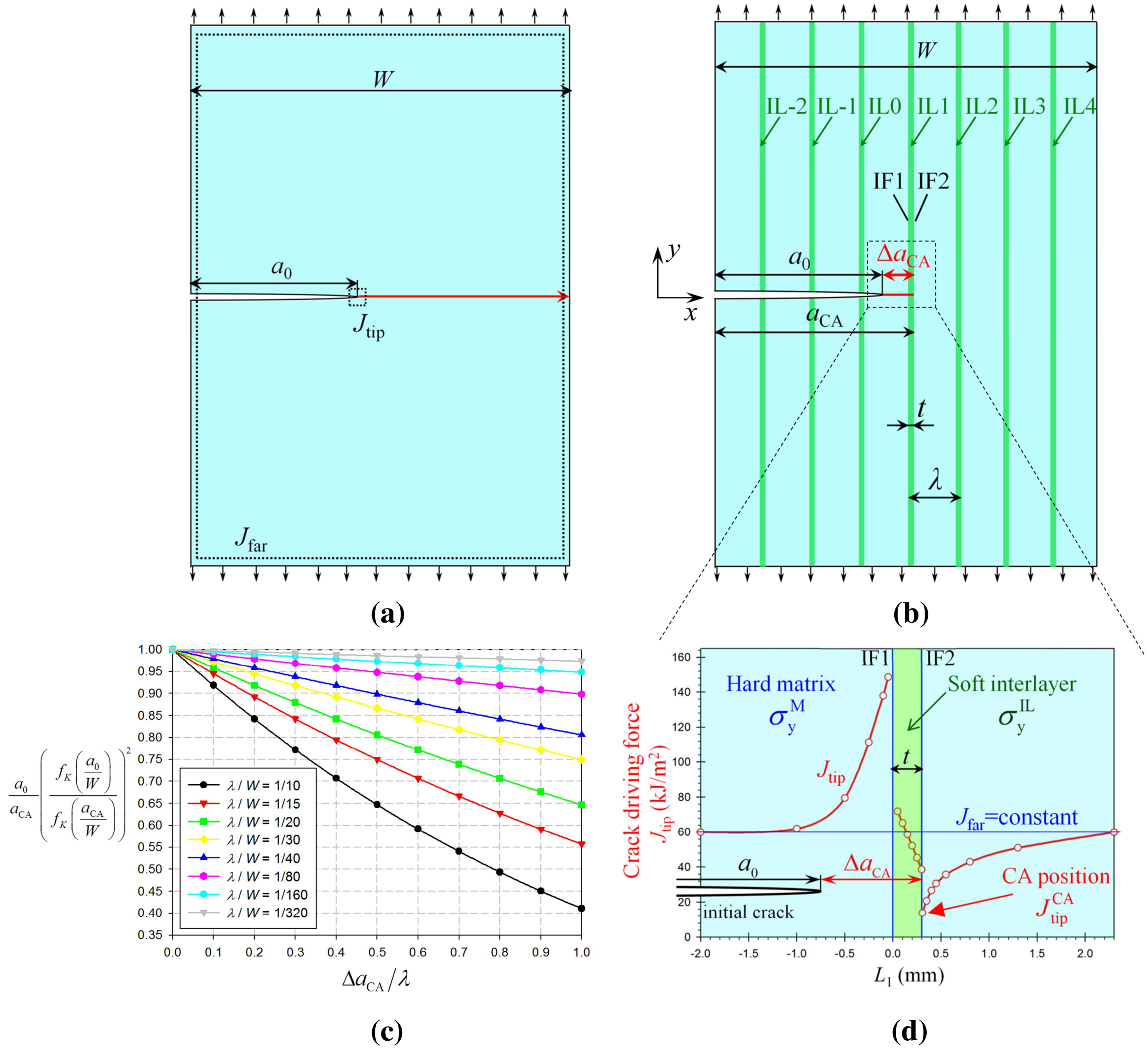

Fig. 7.1 **(a)** Specimen made of brittle, homogeneous material with a crack of initial length a_0: After crack growth has been initiated, the crack does not stop growing until the whole specimen is fractured. **(b)** Multilayered specimen with soft interlayers: The crack propagates to the next interlayer and arrests at the CA position. **(c)** Crack length correction term, i.e. the second term on the right hand side of Eq. (7.8), plotted against $\Delta a_{CA}/\lambda$ for different λ/W-values. **(d)** The strong decrease of the crack driving force in the soft interlayer leads to crack arrest at the CA position and is responsible for the high fracture toughness of the multilayer.

where σ_{appl} denotes the applied global stress, E the Young's modulus, ν Poisson's ratio, W the width of the specimen, and f_K is a dimensionless geometry parameter. Eq. (7.2) is valid for linear elastic and small-scale yielding conditions.

7.2.2 Soft interlayer as a crack arrester

Now assume that the specimen is made of a multilayer consisting of the same matrix material and thin, soft interlayers (ILs), as depicted in Fig. 7.1b. IL1 to IL4 lie in front of the crack tip, IL0 to IL-2 behind it. Since the IL-material has equal elastic properties as the matrix material (M), but a lower yield stress, $\sigma_{\mathrm{y}}^{\mathrm{IL}} < \sigma_{\mathrm{y}}^{\mathrm{M}}$, a material inhomogeneity effect only appears if plastic deformation occurs, i.e. if the crack-tip plastic zone touches an interlayer (Kolednik 2000). Then the *J*-integral becomes path-dependent, and the far-field *J*-integral, J_{far}, which characterizes the driving force that is inserted by the applied load into the body, differs from the crack driving force, J_{tip} (Kolednik 2012).

Since $\sigma_{\mathrm{y}}^{\mathrm{IL}} < \sigma_{\mathrm{y}}^{\mathrm{M}}$, the crack-tip plastic zone is larger in the interlayer material than in the matrix, $r_{\mathrm{y}}^{\mathrm{IL}} > r_{\mathrm{y}}^{\mathrm{M}}$. The radius of the plastic zone in the interlayer material can be estimated from Irwin's model (Irwin 1961),

$$r_{\mathrm{y}}^{\mathrm{IL}} = \beta \frac{J_{\mathrm{far}} E}{\left(1-\nu^2\right)(\sigma_{\mathrm{y}}^{\mathrm{IL}})^2}, \tag{7.3}$$

where $\beta = 1/(6\pi)$ for plane strain conditions. Each interlayer has two sharp interfaces, IF1 and IF2, see Fig. 7.1d. The hard/soft transition of IF1 always induces anti-shielding effect, the soft/hard transition at IF2 crack-tip shielding.

Fig. 7.1d shows, for a specimen with a single interlayer, schematically the variation of the crack driving force J_{tip} for a constant J_{far} and various crack tip positions: J_{tip} is plotted against the distance L_1 between crack tip and IF1. A crack far from the interlayer is not influenced by the material inhomogeneity, $J_{\mathrm{tip}} = J_{\mathrm{far}}$ for $|L_1| > r_{\mathrm{y}}^{\mathrm{IL}}$. When the crack approaches the interlayer from the left, J_{tip} first increases, since IF1 is closer to the crack tip than IF2; therefore, crack growth is promoted. Subsequently, J_{tip} precipitously decreases due to the shielding effect of IF2. The minimum value of J_{tip} is reached immediately after the crack tip has crossed IF2. This position, referred to as the "crack arrest (CA-) position", is critical for the fracture toughness of the composite, since the crack must overcome this position for further crack growth. The crack is arrested, if the crack driving force for a crack tip located at the CA position, $J_{\mathrm{tip}}^{\mathrm{CA}}$, is smaller than the fracture initiation toughness of the matrix material, $J_{\mathrm{tip}}^{\mathrm{CA}} < J_{\mathrm{c}}^{\mathrm{M}}$; hereby it is assumed that the fracture initiation toughness of the matrix material in the multilayer equals that of the homogeneous matrix material. The arrested crack will start to grow again and the single-interlayer composite will fracture completely, if the load increases so that $J_{\mathrm{tip}}^{\mathrm{CA}} = J_{\mathrm{c}}^{\mathrm{M}}$.

The situation in the multilayer is similar: It will fracture, if the crack is able to overcome the CA-position of the first interlayer, IL1, in front of the crack tip, Fig. 7.1b. In the following, the fracture toughness of the multilayer, $J_{\mathrm{c}}^{\mathrm{ML}}$, shall be estimated.

7.2.3 Fracture toughness of multilayers

If the volume fraction of the interlayer material is low, i.e. for $t \ll \lambda$ (Fig. 7.1b), the far-field J-integral of the arrested crack in the multilayer, $J_{\text{far}}^{\text{CA}}$, can be approximated from Eq. (7.2), but with the crack length a_0 replaced by the length of the arrested crack, $a_{\text{CA}} = a_0 + \Delta a_{\text{CA}}$, yielding

$$J_{\text{far}}^{\text{CA}} = \frac{\sigma_{\text{appl}}^2 (1-\nu^2)}{E} \pi a_{\text{CA}} \left[f_K \left(\frac{a_{\text{CA}}}{W} \right) \right]^2 . \tag{7.4}$$

The crack driving force of the arrested crack, $J_{\text{tip}}^{\text{CA}}$, can be determined from the relation,

$$J_{\text{tip}}^{\text{CA}} = \Psi_{\text{ML}}^{\text{CA}} J_{\text{far}}^{\text{CA}} . \tag{7.5}$$

The dimensionless parameter $\Psi_{\text{ML}}^{\text{CA}}$ in Eq. (7.5) gives, for the crack in the CA-position, the reduction of the crack driving force in the multilayer, compared to the homogeneous matrix material; it was called "J-reduction coefficient of the multilayer" (Sistaninia and Kolednik 2017). By inserting $J_{\text{far}}^{\text{CA}}$ from Eq. (7.4) into Eq. (7.5), $J_{\text{tip}}^{\text{CA}}$ can be evaluated as,

$$J_{\text{tip}}^{\text{CA}} = \Psi_{\text{ML}}^{\text{CA}} J_{\text{far}}^{\text{CA}} = \Psi_{\text{ML}}^{\text{CA}} \frac{\sigma_{\text{appl}}^2 (1-\nu^2)}{E} \pi a_{\text{CA}} \left[f_K \left(\frac{a_{\text{CA}}}{W} \right) \right]^2 . \tag{7.6}$$

The condition for re-initiation of the arrested crack in the multilayer is $J_{\text{tip}}^{\text{CA}} = J_{\text{c}}^{\text{M}}$. The corresponding critical far-field J-integral in the multilayer is,

$$J_{\text{far,c}}^{\text{CA}} = J_{\text{c}}^{\text{ML}} = \frac{J_{\text{c}}^{\text{M}}}{\Psi_{\text{ML}}^{\text{CA}}} , \tag{7.7}$$

compare Eq. (7.5). Note that this value, $J_{\text{far,c}}^{\text{CA}} = J_{\text{c}}^{\text{ML}}$, is the fracture toughness of the multilayer, which can be measured experimentally in a fracture mechanics test (Fischer et al. 2014). From Eq. (7.7), it can be concluded that the ratio of the fracture toughness of the multilayer to that of the homogeneous material is $J_{\text{c}}^{\text{ML}} / J_{\text{c}}^{\text{M}} = 1 / \Psi_{\text{ML}}^{\text{CA}}$; however, this is true only in case that the crack length of the arrested crack equals the initial crack length, $a_{\text{CA}} = a_0$, i.e. $\Delta a_{\text{CA}} = 0$. Since this is not so in general, a crack-length correction term must be inserted, compare Eq. (7.2), resulting finally in the solution,

$$\frac{J_{\text{c}}^{\text{ML}}}{J_{\text{c}}^{\text{M}}} \approx \frac{1}{\Psi_{\text{ML}}^{\text{CA}}} \frac{a_0 \left[f_K \left(\frac{a_0}{W} \right) \right]^2}{a_{\text{CA}} \left[f_K \left(\frac{a_{\text{CA}}}{W} \right) \right]^2} . \tag{7.8}$$

The first term on the right hand side of Eq. (7.8), $1/\Psi_{\mathrm{ML}}^{\mathrm{CA}}$, results from the reduction of the crack driving force due to the interlayers; it must be determined numerically, see Section 7.3. The crack-length correction term is limited by the wavelength, $0 \le \Delta a_{\mathrm{CA}} \le \lambda$. This term is easily evaluated, if the function $f_{\mathrm{K}}(a/W)$ is known for common specimen types, see e.g. (Anderson 2005). For the example of single-edge notch tension (SENT) specimens loaded by a constant applied stress, the function $f_{\mathrm{K}}(a/W)$ is given by (Tada et al. 2000),

$$f_K = 1.122 - 0.231\left(\frac{a}{W}\right) + 10.55\left(\frac{a}{W}\right)^2 - 21.71\left(\frac{a}{W}\right)^3 + 30.382\left(\frac{a}{W}\right)^4. \qquad (7.9)$$

Fig. 7.1c shows the magnitude of this term for $a_0/W = 0.5$.

It should be noted that the fracture toughness estimate, Eq. (7.8), has been deduced under the assumption of (engineering) linear elastic fracture mechanics, i.e. small-scale yielding conditions should prevail.

7.3 Effectiveness of soft interlayers as crack arresters

The effectiveness of soft interlayers as crack arrester in multilayer composites is quantified by the *J*-reduction coefficient of the multilayer, Eq. (7.5), $\Psi_{\mathrm{ML}}^{\mathrm{CA}} = J_{\mathrm{tip}}^{\mathrm{CA}} / J_{\mathrm{far}}^{\mathrm{CA}}\big|_{\mathrm{ML}}$. The parameter $\Psi_{\mathrm{ML}}^{\mathrm{CA}}$ can be also seen as the ratio of the crack driving force in the multilayer in the arrest position to that in the homogeneous matrix material for the same crack length (Sistaninia and Kolednik 2017). The *J*-reduction coefficient $\Psi_{\mathrm{ML}}^{\mathrm{CA}}$ is determined by performing numerical analyses with a commercial implementation of the finite element (FE) method (ABAQUS).

We consider a SENT specimen with dimensions, width W = 20 mm, height H = 80 mm, thickness B = 10 mm, crack length a_0 = 10 mm. Due to symmetry, only the upper half of the SENT specimen is modeled under plane strain conditions and large strain formulations. Four-node elements are used for discretizing the FE model. The nodes on the symmetry plane $y = 0$ (y denotes the axis in the vertical direction, see Fig. 7.1b), except the nodes on the crack flank, are constrained in the y-direction, but unconstrained in the x-direction. A crack located at the CA-position of IL1, see Fig. 7.1b, is considered; the distance between the crack tip and IF2 is 3 μm and 10 elements are put between the crack tip and IF2. Isotropic elastic–ideally plastic materials with perfect interfaces are assumed, i.e. interface decohesion is impossible. The Young's modulus of both materials is $E = 200\,\mathrm{GPa}$. The yield stress of the interlayer material is taken as $\sigma_{\mathrm{y}}^{\mathrm{IL}} = 200\,\mathrm{MPa}$; the yield stress of the matrix material is varied.

The crack driving force $J_{\mathrm{tip}}^{\mathrm{CA}}$ is determined by the summation of the far-field *J*-integral $J_{\mathrm{far}}^{\mathrm{CA}}$ and the material inhomogeneity terms of all interfaces within the specimen (Kolednik et al. 2014a; Sistaninia and Kolednik 2014,2017). The material inhomogeneity term C_{inh} represents the driving force term induced by the material inhomogeneity at an interface, see e.g. (Kolednik et al. 2009; Kolednik et al. 2014a; Sistaninia and Kolednik 2014,2017). After the FE stress and strain analysis, C_{inh} of each interface and $J_{\text{far}}^{\text{CA}}$, and the resulting $J_{\text{tip}}^{\text{CA}}$, are evaluated by a configurational force post-processing routine, which is based on the papers (Denzer et al. 2003; Müller et al. 2004; Müller et al. 2002). More details about the procedure for evaluating $J_{\text{far}}^{\text{CA}}$ and $J_{\text{tip}}^{\text{CA}}$ are given in Sistaninia and Kolednik (2017) where the magnitude of $\Psi_{\text{ML}}^{\text{CA}}$ was determined for middle crack tension (MT) specimens with short cracks. We cannot use the results of (Sistaninia and Kolednik 2017) here, since the hydrostatic stress state strongly differs between a SENT-specimen with long crack (high in-plane constraint) and an MT-specimen with short crack (low constraint), e.g. (Anderson 2005).

It is useful to determine first the *J*-reduction coefficient for a specimen with a *single* soft interlayer; $\Psi_{\text{IL}}^{\text{CA}} = J_{\text{tip}}^{\text{CA}} / J_{\text{far}}^{\text{CA}}\big|_{\text{IL}}$ is called the "*J*-reduction coefficient of a single interlayer". For non-hardening materials, $\Psi_{\text{IL}}^{\text{CA}}$ depends on two parameters, $\Psi_{\text{IL}}^{\text{CA}} = f_{\text{IL}}\left(\sigma_{\text{y}}^{\text{IL}} / \sigma_{\text{y}}^{\text{M}}, r_{\text{y}}^{\text{IL}} / t\right)$, see (Sistaninia and Kolednik 2014,2017). Since r_{y}^{IL} depends on J_{far}, Eq. (7.3), the ratio $r_{\text{y}}^{\text{IL}} / t$ can be considered as dimensionless loading parameter of the crack. Fig. 7.2a shows $\Psi_{\text{IL}}^{\text{CA}}$ plotted against $r_{\text{y}}^{\text{IL}} / t$ for an interlayer thickness, $t = 0.05$ mm, and different $\sigma_{\text{y}}^{\text{IL}} / \sigma_{\text{y}}^{\text{M}}$ -values.

For a given yield stress ratio, $\Psi_{\text{IL}}^{\text{CA}}$ drops from unity, runs through a minimum and increases with increasing loading. The minimum value appears when plasticity begins to spread over the whole interlayer, $t \approx r_{\text{y}}^{\text{IL}}$. Fig. 7.2a further shows that $\Psi_{\text{IL}}^{\text{CA}}$ decreases with decreasing yield stress ratio; however, a limit value is reached for $\sigma_{\text{y}}^{\text{IL}} \le 0.2\,\sigma_{\text{y}}^{\text{M}}$ (Sistaninia and Kolednik 2014). Therefore, $t_{\text{opt}} = r_{\text{y}}^{\text{IL}}$ can be seen as optimum thickness and $\left(\sigma_{\text{y}}^{\text{IL}}\right)_{\text{opt}} \le 0.2\,\sigma_{\text{y}}^{\text{M}}$ as optimum yield stress of a single, soft interlayer, leading to the maximum possible reduction of the crack driving force. It will be seen later that the optimum interlayer thickness can be rarely utilized in practice.

In a multilayer, interlayers behind the crack tip are weakly loaded and have barely an effect. Interlayers in front of the tip, such as IL2, influence the driving force of the crack located at the CA-position of IL1. Since IF1 is closer to the tip than IF2, each interlayer will exert an anti-shielding effect (Sistaninia and Kolednik 2017). The smaller the wavelength λ is, the higher will be the influence of IL2 on the crack driving force. This is seen in Fig. 7.2b for a multilayer with $t = 0.05\,\text{mm}$, $\sigma_{\text{y}}^{\text{IL}} / \sigma_{\text{y}}^{\text{M}} = 0.1$ and three different wavelengths. $\Psi_{\text{ML}}^{\text{CA}}$ coincides with $\Psi_{\text{IL}}^{\text{CA}}$ as long as the crack-tip plastic zone does not touch IL2. Jumps in the slopes of the curves appear when the crack-tip plastic zone touches the next interlayer.

The ratio $\Psi_{\text{ML}}^{\text{CA}} / \Psi_{\text{IL}}^{\text{CA}}$ is plotted against $r_{\text{y}}^{\text{IL}} / \lambda$ in Fig. 7.2c for different yield-stress ratios. The ratio $\Psi_{\text{ML}}^{\text{CA}} / \Psi_{\text{IL}}^{\text{CA}}$ depends on two parameters, $\sigma_{\text{y}}^{\text{IL}} / \sigma_{\text{y}}^{\text{M}}$ and $r_{\text{y}}^{\text{IL}} / \lambda$, see (Sistaninia and Kolednik 2017). $\Psi_{\text{ML}}^{\text{CA}}$ is determined using the relation, $\Psi_{\text{ML}}^{\text{CA}} = \Psi_{\text{IL}}^{\text{CA}}\left(\Psi_{\text{ML}}^{\text{CA}} / \Psi_{\text{IL}}^{\text{CA}}\right)$, i.e. by first estimating the value of $\Psi_{\text{IL}}^{\text{CA}}$ from Fig. 7.2a and then reading the ratio $\Psi_{\text{ML}}^{\text{CA}} / \Psi_{\text{IL}}^{\text{CA}}$ from Fig. 7.2c.

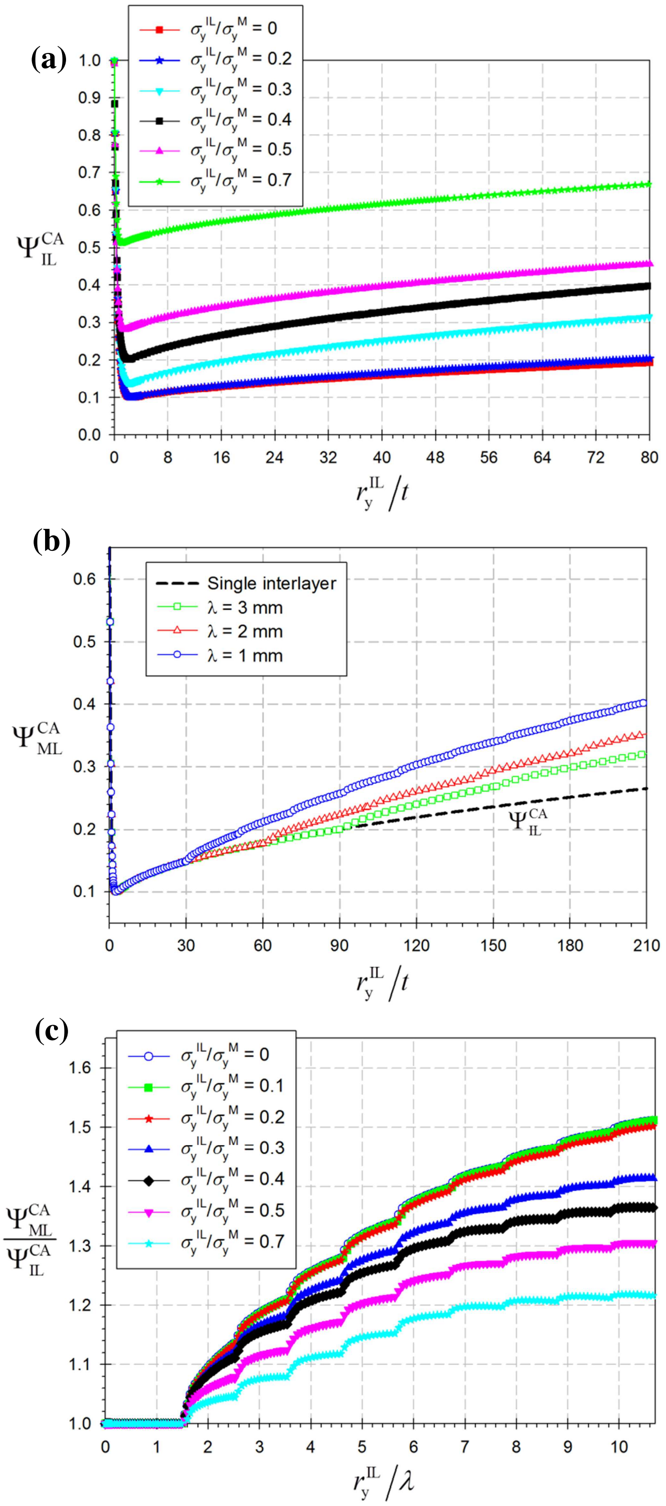

Fig. 7.2 Diagrams for the determination of the *J*-reduction coefficient of the multilayer, $\Psi_{\mathrm{ML}}^{\mathrm{CA}}$: **(a)** *J*-reduction coefficient of a single interlayer, $\Psi_{\mathrm{IL}}^{\mathrm{CA}}$, plotted against the loading parameter, $r_{\mathrm{y}}^{\mathrm{IL}}/t$, for different yield stress ratios, $\sigma_{\mathrm{y}}^{\mathrm{IL}}/\sigma_{\mathrm{y}}^{\mathrm{M}}$. **(b)** $\Psi_{\mathrm{ML}}^{\mathrm{CA}}$ for three different wavelengths *λ*, interlayer thickness *t* = 0.05 mm, $\sigma_{\mathrm{y}}^{\mathrm{IL}}/\sigma_{\mathrm{y}}^{\mathrm{M}} = 0.1$ and $\sigma_{\mathrm{y}}^{\mathrm{IL}} = 200$ MPa; $\Psi_{\mathrm{IL}}^{\mathrm{CA}}$ is plotted for comparison. **(c)** Ratio $\Psi_{\mathrm{ML}}^{\mathrm{CA}}/\Psi_{\mathrm{IL}}^{\mathrm{CA}}$ plotted against the term $r_{\mathrm{y}}^{\mathrm{IL}}/\lambda$ for different yield stress ratios, $\sigma_{\mathrm{y}}^{\mathrm{IL}}/\sigma_{\mathrm{y}}^{\mathrm{M}}$.

From the results of this section, the *J*-reduction factor $\Psi_{\mathrm{ML}}^{\mathrm{CA}}$ can be quantified for a given composite with known material properties and geometry. The improvement in fracture toughness, $J_{\mathrm{c}}^{\mathrm{ML}}/J_{\mathrm{c}}^{\mathrm{M}}$, is then estimated by inserting $\Psi_{\mathrm{ML}}^{\mathrm{CA}}$ in Eq. (7.8). Examples will be presented below, how this knowledge can be used for the design of tough multilayer composites.

7.4 Fracture mechanics experiments

Fracture mechanics tests are conducted in order to experimentally investigate the improvement of fracture toughness by the introduction of thin, soft interlayers. Experiments are carried out on SENT specimens with one, two and four interlayers (1IL-, 2IL- and 4IL-specimens), see Fig. 7.3. The specimens consist of high-strength tool steel, X210CrW12, as matrix and low-strength deep-drawing steel, DC04, as interlayer material. The chemical compositions of the steels are given in Table 7.1. The X210CrW12 has a microstructure with primary carbides, and the DC04 has a very low carbon content so that it does not harden. The specimens are manufactured from DC04 sheets sandwiched between X210CrW12 sheets. Joining of the steel compounds is performed by hot-forging with a hydraulic press at 980 °C. The thickness t and the spacing λ of the interlayers after forging are given in Table 7.2.

The SENT specimens with thickness B = 5 mm are machined (Fig. 7.3a); the width W of specimens is presented in Table 7.2. The specimens are heat treated (austenitizing 15 minutes, 980 °C; air cooling to room temperature; annealing 500 °C, 2h) to ensure high hardness

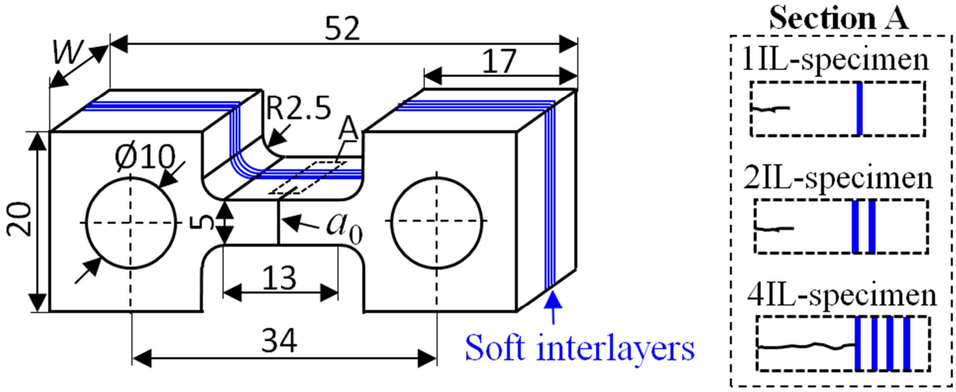

(a) **(b)**

Fig. 7.3 Fracture mechanics experiments are conducted on SENT specimens made of high-strength steel as matrix and low-strength steel as interlayer material. **(a)** Geometry of SENT specimens. **(b)** SENT specimens with one, two and four interlayers (1IL-, 2IL- and 4IL-specimens).

Table 7.1 Chemical compositions of the constituents of the steel-multilayer in weight-%.

	C	Si	Mn	P	S	Cr	W
X210CrW12	2.11	0.25	0.41	0.019	0.0003	11.21	0.65
DC04	0.04	-	0.2	0.01	0.01	-	-

difference between matrix (Vickers hardness $\text{HV0.2} = 650$) and interlayer ($\text{HV0.2} = 160$). From the relation between the yield strength and hardness given in (Pavlina and Van Tyne 2008), the yield stresses are estimated as $\sigma_{\text{y}}^{\text{M}} = 1835 \text{ MPa}$ and $\sigma_{\text{y}}^{\text{IL}} = 390 \text{ MPa}$, respectively, resulting in a yield stress ratio $\sigma_{\text{y}}^{\text{IL}} / \sigma_{\text{y}}^{\text{M}} = 0.21$. The Young's modulus is $E = 210 \text{ GPa}$ for both matrix and interlayer. The specimens are notched and pre-fatigued before testing. The initial crack length is $a_0 = 4.92 \text{ mm}$ and the distance between crack tip and IF1 is $L_1 = 1.09 \text{ mm}$ in the 1IL-specimen; $a_0 = 3.67 \text{ mm}$ and $L_1 = 1.11 \text{ mm}$ for the 2IL-specimen. In the 4IL-specimen, the initial crack tip is already located at the CA-position of IL1, $a_0 = a_{\text{CA}} = 4.71 \text{ mm}$.

The fracture mechanics experiments are analyzed by plotting experimental *J*-integral vs. crack extension (*J*–Δ*a*) curves. For the determination of *J*–Δ*a*-curve for the steel composites, the specimens are tested at a constant crosshead displacement rate of 0.3 mm/min using a Zwick tensile testing machine with a 100 kN load cell. In these tests, the crack extension Δ*a* is measured both optically and by using the direct current potential drop technique according to the International Standard [ISO-12135-02 2002]. For each crack tip position, the value of *J*-integral is determined by inserting the values of applied stress and crack length $a = a_0 + \Delta a$ into Eq. (7.2). The *J*–Δ*a* curve is then plotted for each specimen.

Table 7.2 Results of fracture mechanics tests and of the numerical analyses of the specimens with and without thermal residual stresses. J_{c}^{M} denotes the fracture toughness of the homogeneous matrix material, J_{c}^{ML} that of the specimens with interlayer(s), $J_{\text{tip,c}}^{\text{CA}}$ the critical crack driving force at the fracture load F_{max}.

	Fracture mechanics tests							Numerical simulations		
									$J_{\text{tip,c}}^{\text{CA}}$ [kJ/m^2]	
Specimen	W (mm)	t (μm)	λ (μm)	F_{max} [kN]	J_{c}^{M} [kJ/m^2]	J_{c}^{ML} [kJ/m^2]	$J_{\text{c}}^{\text{ML}} / J_{\text{c}}^{\text{M}}$	$J_{\text{c}}^{\text{ML}} = J_{\text{far,c}}^{\text{CA}}$ [kJ/m^2]	without residual stresses	with residual stresses
1IL	12.59	88	–	9.10	3.64	12.9*	3.55	15.9$^+$	3.63	3.24
2IL	9.93	88	162	10.82	4.88	24.0*	4.92	33.9$^+$	14.8	4.47
4IL	9.95	93	240	11.62	4.88	23.3*	4.76	35.2$^+$	16.4	5.24

* values calculated from Eq. (7.2) $^+$ values from FEM-computation

7.5 Results and discussion

7.5.1 Results of fracture mechanics tests

Fig. 7.4a shows the experimental *J*-integral vs. normalized crack extension, $\Delta a/(L_1 + t)$, curves for the 1IL- and 2IL-specimens; the result of the 4IL-specimen is also indicated. The numbers correspond to stages of crack propagation; the digital photographs in Fig. 7.4b show these stages for the 1IL-specimen. The *J*-integral at Point 1, for $\Delta a \approx 0.2\,\mathrm{mm}$, gives the fracture initiation toughness of the matrix material, J_c^M; since the crack tip plastic zone is distant from the interlayer ($|L_1| > r_\mathrm{y}^\mathrm{IL}$), the yield stress inhomogeneity has no effect, $J_\mathrm{tip} = J_\mathrm{far}$. The subsequent crack growth is very fast; the crack jumps to the interlayer, Point 2. Hereby the *J*-value increases due to the increase in crack length, Eq. (7.2). During further loading, crack extension is very slow[7] until crack growth is re-initiated at the maximum load F_max (Point 3) and the specimen completely fractures (Point 4). Therefore, the *J*-integral at Point 3 gives the fracture toughness of the composite, J_c^ML.

For the 1IL-specimen (red curve in Fig. 7.4a), the fracture initiation toughness of the matrix material is determined as $J_\mathrm{c}^\mathrm{M} = 3.64\ \mathrm{kJ/m^2}$, and the fracture toughness of the composite as $J_\mathrm{c}^\mathrm{ML} = 12.91\ \mathrm{kJ/m^2}$. Thus we can conclude that the soft interlayer caused an improvement in fracture toughness by a factor $J_\mathrm{c}^\mathrm{ML}/J_\mathrm{c}^\mathrm{M} = 3.55$.

Fig. 7.4a shows that for the 2IL-specimen $J_\mathrm{c}^\mathrm{M} = 4.88$ kJ/m^2 and $J_\mathrm{c}^\mathrm{ML} = 23.99$ kJ/m^2; the fracture toughness is improved by a factor of $J_\mathrm{c}^\mathrm{ML}/J_\mathrm{c}^\mathrm{M} = 4.92$. The 4IL-specimen fractures at $J_\mathrm{c}^\mathrm{ML} = 23.25\ \mathrm{kJ/m^2}$; under the assumption that J_c^M of the 4IL-specimen equals that of the 2IL-specimen, the soft interlayers cause an improvement in fracture toughness by a factor $J_\mathrm{c}^\mathrm{ML}/J_\mathrm{c}^\mathrm{M} = 4.76$.

The results of the fracture mechanics experiments are summarized in Table 7.2. It should be noted that no interface delamination is observed in the three tests.

The scanning electron microscope (SEM) micrograph of the fracture surface of the 1IL-specimen in Fig. 7.5 shows that the fracture mechanism of the matrix is micro-ductile; the fracture surface consists of shallow dimples, whereas the large primary carbides in the matrix fail by brittle, transcrystalline fracture. Very interesting is that the interlayer material exhibits cleavage fracture. This cleavage fracture, which is also observed in the 2IL- and 4IL-specimens, is promoted by carbon diffusion from the matrix material during manufacture and

---

[7] The exact values of Δa and the increase in Δa between Points 2 and 3 are somewhat uncertain. The reason is that the calibration of the direct current potential drop technique, which is applied for the measurement of crack extension, is difficult and, e.g., blunting of an arrested crack results in a change in the electric potential, too.

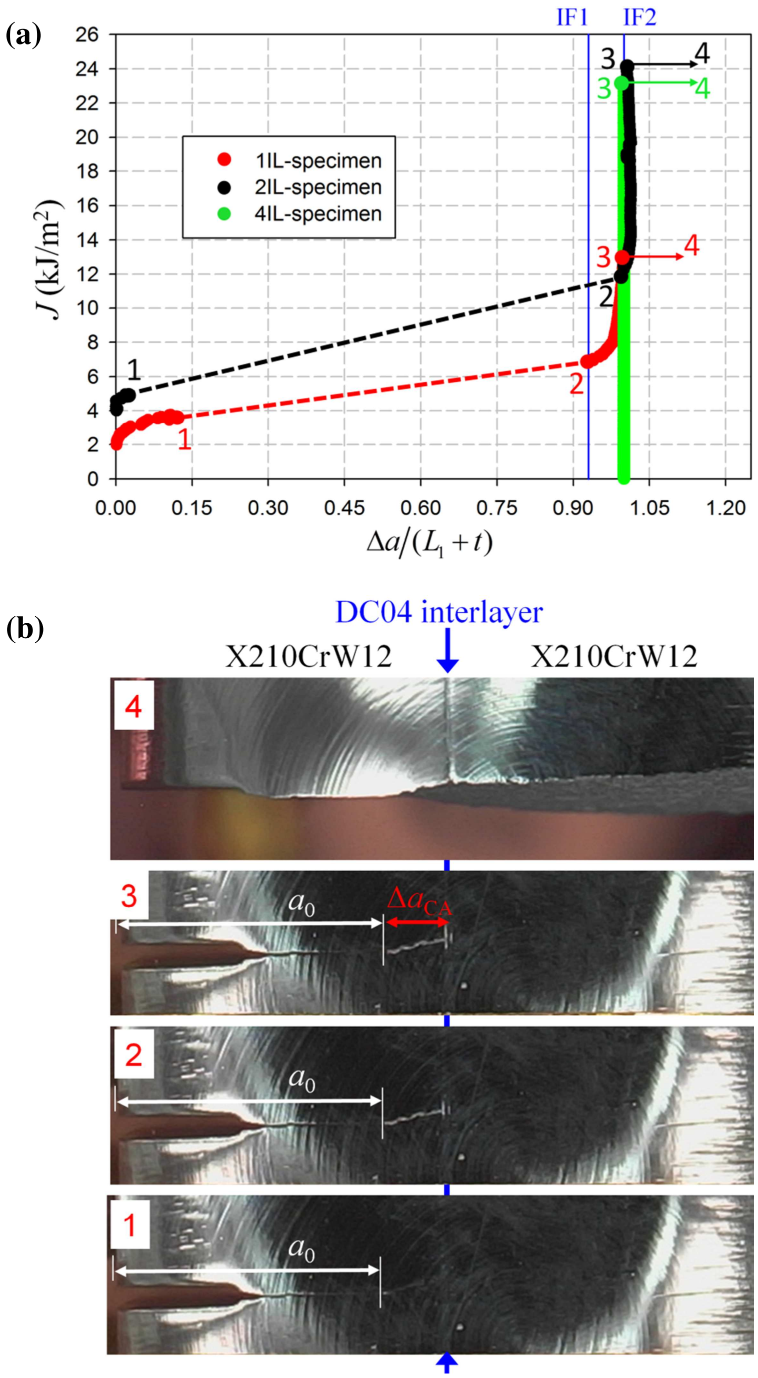

Fig. 7.4 **(a)** Experimental curves J-integral vs. normalized crack extension, $\Delta a/(L_1+t)$, for the single-interlayer (1IL-) and multilayer (2IL- and 4IL-) specimens. The numbers correspond to stages of crack propagation: **1** initiation of crack extension in matrix material, **2** crack reaches the soft interlayer, **3** re-initiation of crack growth at interlayer, **4** fracture of the specimen. **(b)** 1IL-specimen during testing. The labels of the images correspond to the numbers in (a).

heat treatment, tensile residual stresses (see below), the high hydrostatic stress state in the 90 μm thin interlayers, and the rapid crack propagation through the interlayer.

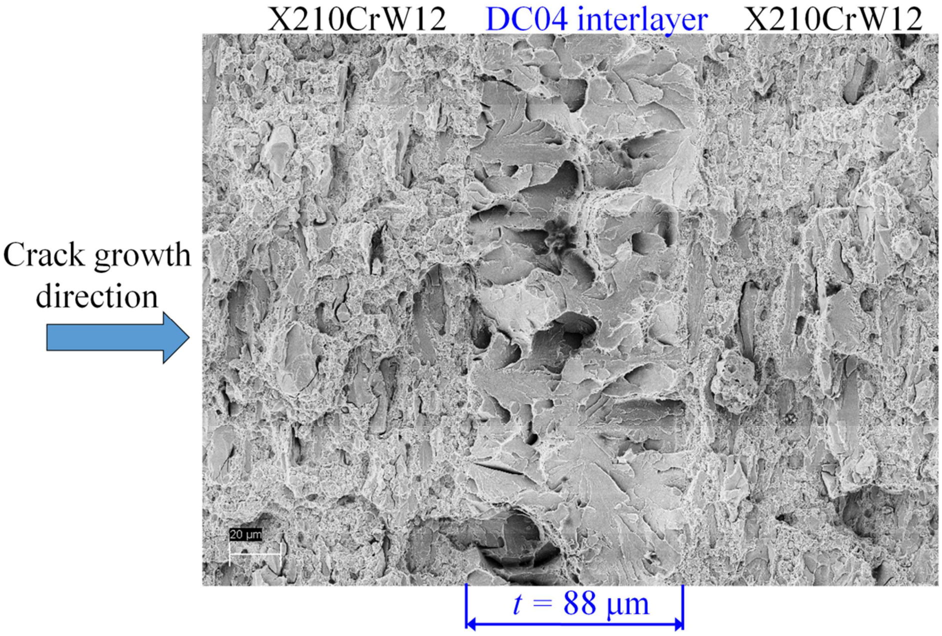

Fig. 7.5 SEM micrograph of the fracture surface of the 1IL-specimen showing cleavage of interlayer material.

The fracture surface appearance suggests that the intrinsic crack growth resistance of the interlayer material is lower than that of the matrix material. This is in our opinion a striking evidence for the effectiveness of the material inhomogeneity effect: The fracture toughness strongly increases by the insertion of thin, soft interlayers, although the interlayers fracture in a very brittle mode.

7.5.2 Procedure for predicting the fracture toughness of multilayer composites

The experimental improvement factors of the fracture toughness of the three specimens, $J_{\mathrm{c}}^{\mathrm{ML}}/J_{\mathrm{c}}^{\mathrm{M}}$, are in the following compared to the theoretical values deduced from Eq. (7.8).

The result of the 1IL-specimen can be compared to an estimate deduced from Eq. (7.8), with the *J*-reduction factor of the multilayer, $\Psi_{\mathrm{ML}}^{\mathrm{CA}}$, replaced by the *J*-reduction factor of the single interlayer, $\Psi_{\mathrm{IL}}^{\mathrm{CA}}$. By inserting the data of the specimen geometry, with $a_0 = 4.92$ and $a_{\mathrm{CA}} = a_0 + L_1 + t_1 = 6.10\,\mathrm{mm}$, the crack-length correction term in Eq. (7.8) results 0.48. In order to determine the value of $\Psi_{\mathrm{IL}}^{\mathrm{CA}}$ from Fig. 7.2a, the plastic zone radius at the maximum load, $\left(r_{\mathrm{y}}^{\mathrm{IL}}\right)_{\mathrm{c}}$, must be known where crack growth is re-initiated. $\left(r_{\mathrm{y}}^{\mathrm{IL}}\right)_{\mathrm{c}}$ is determined from Eq. (7.3) by replacing J_{far} with $J_{\mathrm{c}}^{\mathrm{ML}}$. Since the value of $J_{\mathrm{c}}^{\mathrm{ML}}$ is unknown, an iterative procedure must be applied:

> We select a guessed starting value, e.g. $J_{\mathrm{c}}^{\mathrm{ML}}/J_{\mathrm{c}}^{\mathrm{M}} = 2$ or $J_{\mathrm{c}}^{\mathrm{ML}} = 7.28\ \mathrm{kJ/m^2}$. This leads to $\left(r_{\mathrm{y}}^{\mathrm{IL}}\right)_{\mathrm{c}} = 0.59\,\mathrm{mm}$, $\left(r_{\mathrm{y}}^{\mathrm{IL}}\right)_{\mathrm{c}}/t = 6.66$, and $\Psi_{\mathrm{IL}}^{\mathrm{CA}} = 0.11$ from Fig. 7.2a for a yield stress ratio $\sigma_{\mathrm{y}}^{\mathrm{IL}}/\sigma_{\mathrm{y}}^{\mathrm{M}} = 0.2$. Inserting $\Psi_{\mathrm{IL}}^{\mathrm{CA}}$ into Eq. (7.8) gives $J_{\mathrm{c}}^{\mathrm{ML}}/J_{\mathrm{c}}^{\mathrm{M}} = 4.34$ after the first

iteration. These values and the values of the following iterations are collected in Table 7.3. After four iterations, the final value of the fracture toughness ratio is found: $J_{\mathrm{c}}^{\mathrm{ML}}/J_{\mathrm{c}}^{\mathrm{M}} = 3.86$, which is in good agreement to the experimental value of 3.55.

Fig. 7.6 shows the experimental $J_{\mathrm{c}}^{\mathrm{ML}}/J_{\mathrm{c}}^{\mathrm{M}}$-value (blue dot) and the results of the procedure for arbitrary interlayer positions with respect to the crack tip (blue curve). The fracture toughness ratio $J_{\mathrm{c}}^{\mathrm{ML}}/J_{\mathrm{c}}^{\mathrm{M}}$ increases with decreasing $\Delta a_{\mathrm{CA}} = L_1 + t$.

Table 7.3 Iterative procedure to find the *J*-reduction factor of a single interlayer, $\Psi_{\mathrm{IL}}^{\mathrm{CA}}$, and the fracture toughness ratio between composite and homogeneous matrix material, $J_{\mathrm{c}}^{\mathrm{ML}}/J_{\mathrm{c}}^{\mathrm{M}}$.

t (μm)	$J_{\mathrm{c}}^{\mathrm{M}}$ (kJ/m^2)	$J_{\mathrm{c}}^{\mathrm{ML}}$ (kJ/m^2)	$\left(r_{\mathrm{y}}^{\mathrm{IL}}\right)_{\mathrm{c}}$ (mm)	$\left(r_{\mathrm{y}}^{\mathrm{IL}}\right)_{\mathrm{c}}/t$	$\Psi_{\mathrm{IL}}^{\mathrm{CA}}$ Fig. 7.2a	$J_{\mathrm{c}}^{\mathrm{ML}}/J_{\mathrm{c}}^{\mathrm{M}}$ Eq. (7.8)
88	3.64	7.28	0.59	6.66	0.110	4.34
88	3.64	15.80	1.27	14.45	0.127	3.76
88	3.64	13.69	1.10	12.52	0.123	3.88
88	3.64	14.12	1.14	12.92	0.124	**3.86**

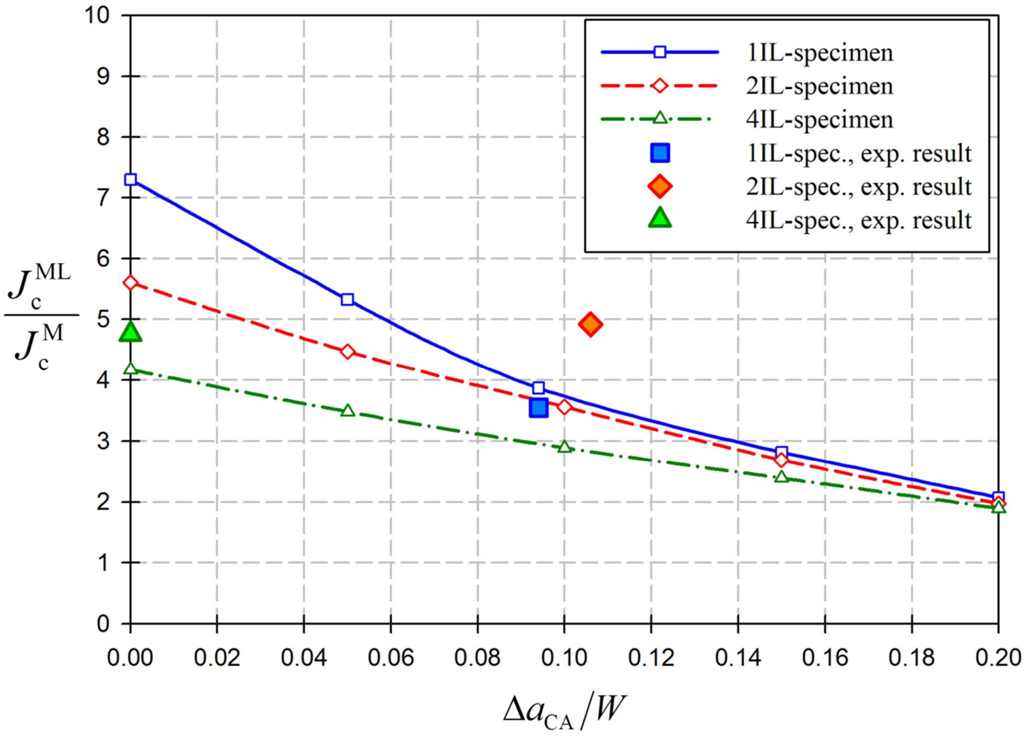

Fig. 7.6 Curves of the predicted fracture toughness ratio between composite and homogeneous matrix material, $J_{\mathrm{c}}^{\mathrm{ML}}/J_{\mathrm{c}}^{\mathrm{M}}$, for the 1IL-, 2IL- and 4IL-specimen plotted against the distance between crack arrest position and initial crack tip location, $\Delta a_{\mathrm{CA}} = L_1 + t$. The experimental values of $J_{\mathrm{c}}^{\mathrm{ML}}/J_{\mathrm{c}}^{\mathrm{M}}$ are marked as dots.

In order to predict the fracture toughness ratio $J_{\mathrm{c}}^{\mathrm{ML}}/J_{\mathrm{c}}^{\mathrm{M}}$ of the 2IL- and 4IL-specimens, an iterative procedure similar to that explained for the single-interlayer case is applied to determine the *J*-reduction factor of the multilayer, $\Psi_{\mathrm{ML}}^{\mathrm{CA}}$, and the ratio $J_{\mathrm{c}}^{\mathrm{ML}}/J_{\mathrm{c}}^{\mathrm{M}}$ from Eq. (7.8). In each iteration, the term $\left(r_{\mathrm{y}}^{\mathrm{IL}}\right)_{\mathrm{c}}/\lambda$ is evaluated additionally, which is needed to determine the ratio $\Psi_{\mathrm{ML}}^{\mathrm{CA}}/\Psi_{\mathrm{IL}}^{\mathrm{CA}}$ from Fig. 7.2c and the magnitude of $\Psi_{\mathrm{ML}}^{\mathrm{CA}}=\Psi_{\mathrm{IL}}^{\mathrm{CA}}\,\Psi_{\mathrm{ML}}^{\mathrm{CA}}/\Psi_{\mathrm{IL}}^{\mathrm{CA}}$. The predicted $J_{\mathrm{c}}^{\mathrm{ML}}/J_{\mathrm{c}}^{\mathrm{M}}$-ratios for the 2IL- and 4IL-specimen are plotted against $\Delta a_{\mathrm{CA}}/W$ as red and green curves in Fig. 7.6; the corresponding experimental values are marked as red and green dots. The experimental results lie somewhat higher, but are still in satisfactory agreement with the numerical predictions. The reason for the deviations between the numerical predictions and the experimental results, for the 2IL- and 4IL-specimen, is discussed in the following.

7.5.3 *Influence of thermal residual stresses*

Since the plastic zone size in the matrix material reaches approximately the magnitude of the interlayer spacing at maximum load $F_{\max}$, small-scale yielding conditions are not fulfilled for the 2IL- and 4IL-specimens. This means that linear elastic fracture mechanics is not valid any more, and the fracture toughness estimate, Eq. (7.8), might become inaccurate. Therefore, numerical analyses are performed to determine more accurately the critical values of the far-field *J*-integral $J_{\mathrm{far}}^{\mathrm{CA}}$ and the crack driving force $J_{\mathrm{tip}}^{\mathrm{CA}}$ at the experimentally measured fracture loads $F_{\max}$, using the configurational forces concept (Kolednik et al. 2014a; Sistaninia and Kolednik 2014,2017). These critical values are denominated as $J_{\mathrm{far,c}}^{\mathrm{CA}}=J_{\mathrm{c}}^{\mathrm{ML}}$ and $J_{\mathrm{tip,c}}^{\mathrm{CA}}$, see Section 2.

FE models of the 1IL-, 2IL- and 4IL-specimens are generated for the stress–strain analysis and the subsequent configurational force post-processing for the determination of $J_{\mathrm{tip}}^{\mathrm{CA}}$. Modeling details are given in Section 3. The specimens are loaded by prescribing the load until to the fracture load $F_{\max}$. The values of $J_{\mathrm{far,c}}^{\mathrm{CA}}$ and $J_{\mathrm{tip,c}}^{\mathrm{CA}}$ at the fracture load $F_{\max}$ are inserted into Table 7.2. Whereas the condition $J_{\mathrm{tip,c}}^{\mathrm{CA}}=J_{\mathrm{c}}^{\mathrm{M}}$ is fulfilled for the 1IL-specimen, this is not so for the 2IL- and 4IL-specimens: $J_{\mathrm{tip,c}}^{\mathrm{CA}}>>J_{\mathrm{c}}^{\mathrm{M}}$, see the penultimate column in Table 7.2. This is due to the presence of residual stresses, as discussed in the following.

The coefficient of thermal expansion differs between the interlayer and matrix material, $\alpha^{\mathrm{IL}}=13.31\times10^{-6}\ \mathrm{K}^{-1}$ and $\alpha^{\mathrm{M}}=10.67\times10^{-6}\ \mathrm{K}^{-1}$ (average values for the temperature range $20\,^{\circ}\mathrm{C}-500\,^{\circ}\mathrm{C}$) (Spittel and Spittel 2009). Therefore, it can be expected that cooling from the annealing temperature (500 °C) to room temperature will introduce in *y*- and *z*-direction tensile residual stresses in the interlayers and compressive residual stresses in the matrix, compare Fig. 7.1b.

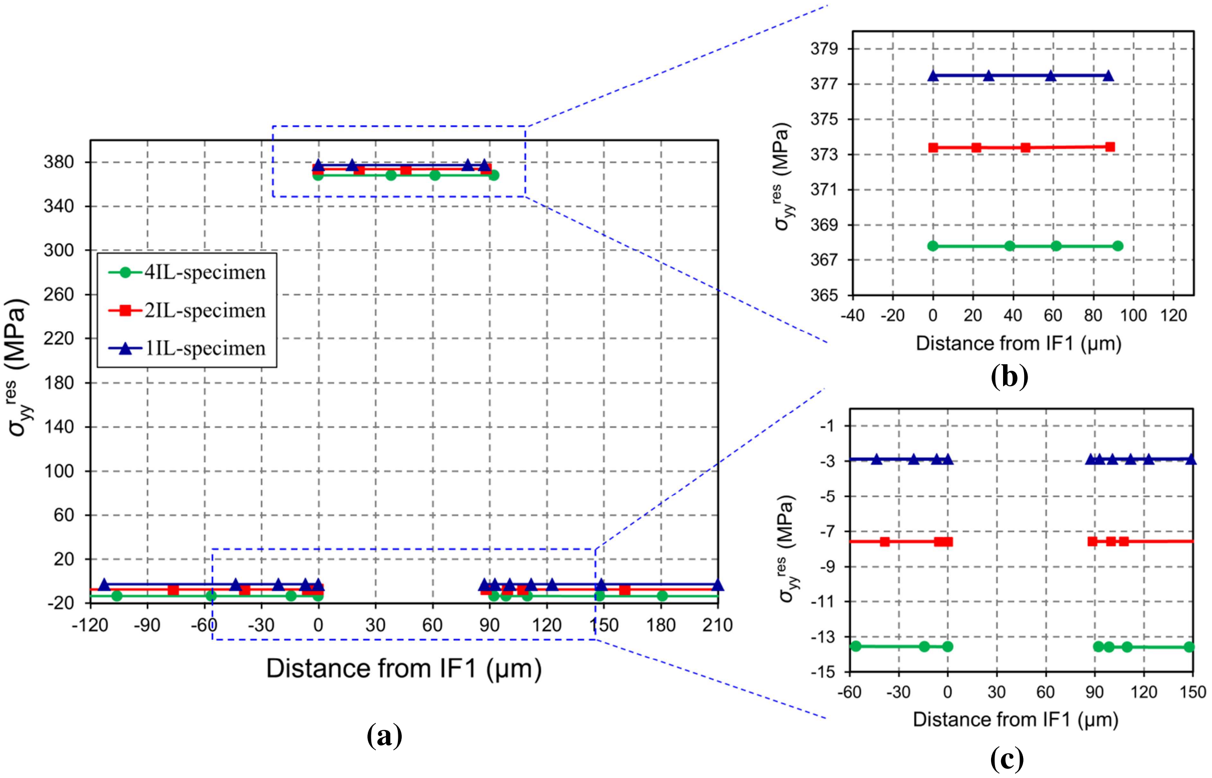

(a)

(b)

(c)

Fig. 7.7 **(a)** Residual stresses $\sigma_{yy}^{\mathrm{res}}$ in the plane $y = 0$ for the uncracked specimens after cooling from the annealing temperature, plotted against the distance from IF1 of IL1. **(b)** Details of the high tensile residual stresses in the interlayers, **(c)** of the low compressive residual stresses in the matrix.

In order to determine the residual stresses and to quantify their effect on $J_{\mathrm{tip,c}}^{\mathrm{CA}}$, new numerical analyses are performed under the assumption of generalized plane strain conditions. The following procedure is applied: (i) the uncracked and unloaded specimen is subjected to thermal loading by a temperature difference $\Delta T = -480\,°\mathrm{C}$. (ii) A crack located at the CA-position of IL1 is introduced using the node-release technique (Malluck and King 1980). (iii) The specimen is mechanically loaded to the experimentally measured fracture load $F_{\max}$. The critical crack driving force $J_{\mathrm{tip,c}}^{\mathrm{CA}}$ and the critical far-field *J*-integral $J_{\mathrm{far,c}}^{\mathrm{CA}}$ are then evaluated for the load $F_{\max}$ by using the configurational forces concept.

The thermal residual stresses $\sigma_{yy}^{\mathrm{res}}$ on the symmetry plane of the specimens, $y = 0$, before and after introduction of the crack are depicted in Figs. 7.7 and 7.8, respectively. Fig. 7.7 shows that high tensile residual stresses of about 370 MPa are generated in the interlayers after cooling from the annealing temperature, while the compressive residual stresses in the matrix are very low, of the order of 10 MPa. The normal stresses in *z*-direction are of equal size, whereas the normal stresses in *x*-direction are zero. After the implementation of the crack with its tip located at the CA-position of IL1, the tensile residual stresses in IL1 are released due to the normal stress-free crack surface. The relaxation of tensile residual stresses

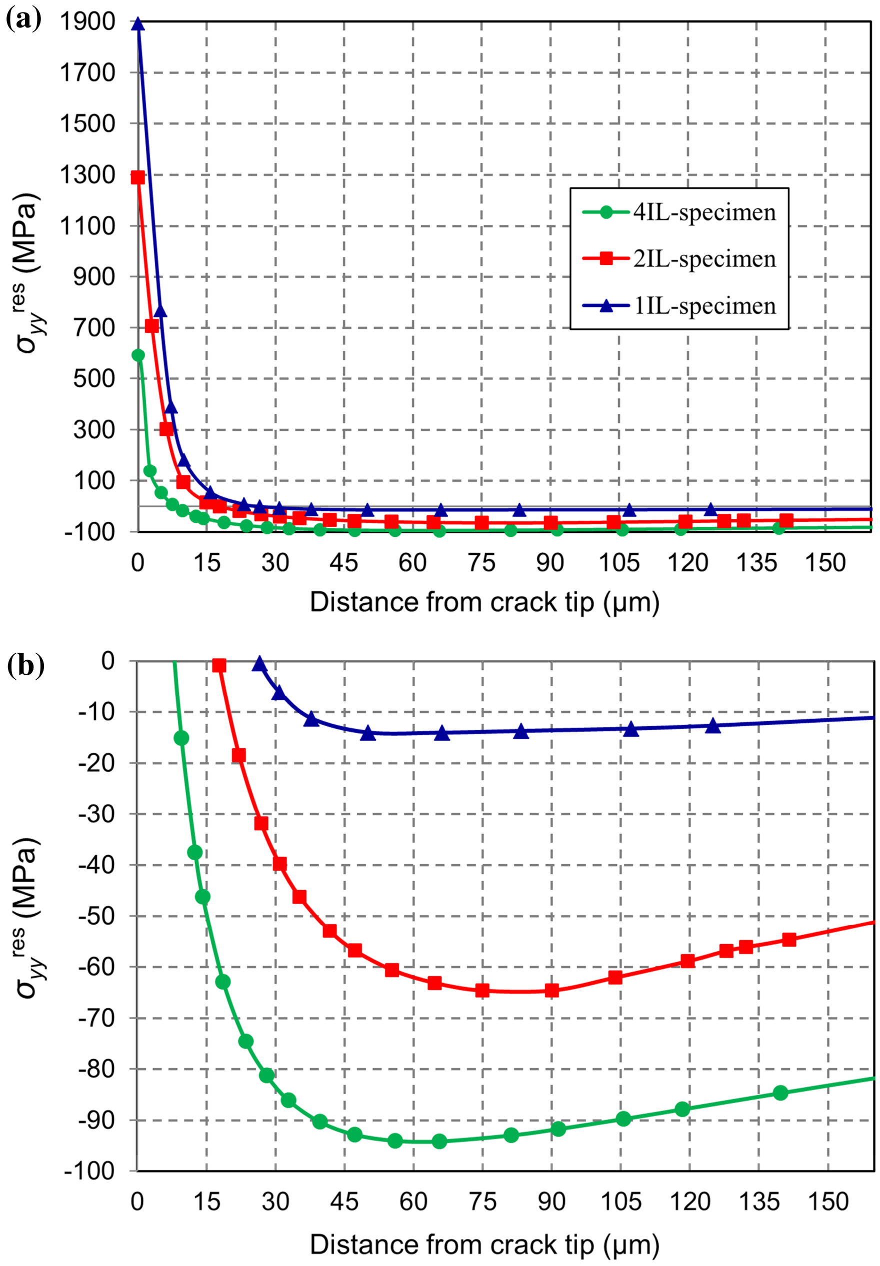

Fig. 7.8 **(a)** Residual stresses σ_{yy}^{res} after cooling and implementation of a crack located at the CA-position of IL1, plotted against the distance from the crack tip. **(b)** Detail of the curves in the region of compressive residual stresses.

leads to the contraction of IL1 in *y*-direction and to a redistribution of the stresses in the matrix front of the crack tip. High tensile residual stresses appear in a small region (3 to 8 μm) in front of the crack tip, Fig. 7.8a. Also the tensile stresses in *x*- and *z*-direction are high in this region. This hydrostatic stress state is highest for the 1IL- and lowest for the 4IL-specimen. In contrast, a zone of compressive residual stresses (in *y*-, *z*- and *x*-direction) appears at larger distances from the crack tip, Fig. 7.8b. The maximum values of the compressive residual stresses are $\sigma^{\mathrm{res}}_{yy,\max} = -14$, -65 and -94 MPa for the 1IL-, 2IL- and 4IL-specimens, respectively.

Fig. 7.8 depicts the stress state in the unloaded fracture mechanics specimen, i.e. before starting the test. The lower hydrostatic stress states in the 2IL- and 4IL-specimens explain why higher loads $F_{\max}$ are required in these specimens to achieve re-initiation of crack growth, compared to the 1IL-specimen. In other words, the presence of additional interlayers leads to a decrease of the hydrostatic stress state near the crack tip and, thus, increases the fracture toughness.

The critical values of the far-field *J*-integral, $J^{\mathrm{CA}}_{\mathrm{far,c}} = J^{\mathrm{ML}}_{\mathrm{c}}$, are equal for the cases with and without taking into account the residual stresses. However, the critical values of the crack driving force, $J^{\mathrm{CA}}_{\mathrm{tip,c}}$, change significantly, compare the last two columns in Table 7.2. It is seen that especially the $J^{\mathrm{CA}}_{\mathrm{tip,c}}$-values for the 2IL- and 4IL-specimens are strongly reduced due to the presence of residual stresses, so that they approach the magnitudes of the fracture toughness of the homogeneous matrix material, $J^{\mathrm{M}}_{\mathrm{c}}$.

Two remarks shall be made concerning the still existing misfit between the $J^{\mathrm{CA}}_{\mathrm{tip,c}}$- and $J^{\mathrm{M}}_{\mathrm{c}}$-values and the scatter of the $J^{\mathrm{M}}_{\mathrm{c}}$-values: (i) A significant scatter of the measured fracture toughness is not unusual for a tool steel with low toughness and large primary carbides. (ii) Accurate computation of the thermal residual stresses in the multilayer compounds is difficult, since it is not known whether all primary residual stresses, which occur during hot-forging, disappear during the annealing at 500°C, as is assumed in the modelling.

This section can be concluded by stating that an excellent agreement has been achieved between the experimentally measured fracture behavior of the compounds and the numerical modeling results after consideration of thermal residual stresses: Final fracture of the multilayer compounds always occurs when the crack driving force $J^{\mathrm{CA}}_{\mathrm{tip}}$ reaches $J^{\mathrm{M}}_{\mathrm{c}}$.

7.6 Summary

This paper demonstrates that spatial variations of the yield stress by the implementation of thin, soft interlayers significantly improve the fracture toughness of brittle matrix materials, if the architectural parameters of the multilayers are appropriately chosen. An iterative procedure is presented for predicting the fracture toughness of the multilayer. This procedure helps to select the most appropriate multilayer geometry. Experiments with steel compounds, consisting of a tool steel as matrix and a low-strength steel as interlayer material, confirm the modeling predictions. From the results of fracture tests and numerical simulations, it is found that the intrinsic fracture initiation toughness of the matrix material in the multilayer equals that of the homogeneous matrix material. Furthermore, it is shown that thermal residual stresses, which develop in the multilayers during the production process, may lead to further improvement in fracture toughness of the multilayers. The knowledge presented in this paper can be used for the future design of highly fracture resistant multilayer compounds.

Acknowledgements

Financial support by the Austrian Federal Government and the Styrian provincial Government within the research activities of the K2 Competence Center “Integrated Research in Materials, Processing and Product Engineering’’, under the frame of the Austrian COMET Competence Center Program, is gratefully acknowledged (Project A4.20-WP1 and WP2).

“There are sadistic scientists who hurry to hunt down errors instead of establishing the truth.”

Marie Curie

Part III

Physically correct evaluation of the crack driving force in magnesia-spinel refractories with configurational forces concept

8 Thermal shock resistance of magnesia-spinel refractories

Paper IV, which is an output of a co-operation project with Chair of Ceramics at Montanuniversität Leoben, deals with the thermal shock resistance of magnesia-spinel refractories.

In magnesia-spinel refractories, spinel inclusions are embedded in a magnesia matrix in order to increase the thermal shock resistance by micro-crack toughening. Due to the thermal mismatch between spinel inclusions and matrix, damage processes are initiated during the cooling at the end of the production process. The damage initiation is intended because it increases the thermal shock resistance due to the reduction of the tensile strength and the increase in the specific fracture energy caused by the formation of a fracture process zone.

The development of the damage zone between spinel grains during the cooling can be simulated by a sophisticated numerical analysis, with the concrete damaged plasticity (CDP) model. It is clear that in cases where the CDP-model is used in order to reflect the damage evolution process in the matrix, the conditions of proportional loading are disturbed and the conventional J-integral, see Section 3.5, is not applicable anymore for evaluating the crack driving force (see Section 4.4); the crack driving force is used for the characterization of the thermal shock resistance. The crack driving force must be evaluated from the elastic–plastic configurational forces and the incremental plasticity J-integral, see Section 4.4.

Paper IV presents a new methodology for the physically correct evaluation of the crack driving force in coarse grained refractories, such as magnesia-spinel refractories. The methodology consists in numerical investigations with the finite element (FE) method, based on the following steps:

- Application of the concrete damaged plasticity (CDP) model for the modelling of the micro-crack initiation and formation during the cooling of the magnesia spinel refractory.
- Application of the concept of configurational forces and the elastic–plastic J-integral concept for the evaluation of the crack driving force.

Our results lead to the following conclusions of Paper IV:

- Evaluations show the strong influence of an inherent matrix crack on the damage evolution: Damage initiation happens at lower ΔT for the cases with an inherent crack, the magnitude and shape of the quasi-plastic damage zone are different.
- J-integral evaluated with the concept of configurational forces according to the incremental theory of plasticity (leading to the incremental plasticity J-integral J^{ep}) enables the physically correct evaluation of the crack driving force for the concrete damage plasticity model.
- The results demonstrate that, for the material data given, inherent matrix cracks are unable to grow during the cooling, since the crack driving force is smaller than the specific work for fracture. Instead a quasi-plastic damage zone appears between the grains, which consumes energy and decreases the driving forces of possible inherent cracks, without showing pronounced damage localization. This behaviour is the main reason for the good thermal shock resistance of magnesia spinel materials.

Paper IV:

Thermal shock resistance of magnesia spinel refractories—Investigation with the concept of configurational forces

Dietmar Gruber, Masoud Sistaninia, Christoph Fasching, Otmar Kolednik

published in

Journal of the European Ceramic Society (2016) 36:4301–4308
http://dx.doi.org/10.1016/j.jeurceramsoc.2016.07.001

Abstract

In magnesia-spinel refractories, spinel inclusions are embedded in a magnesia matrix in order to increase the thermal shock resistance by micro-crack toughening. The paper investigates damage evolution in the material during the cooling at the end of the production process by a sophisticated numerical analysis. After a stress-strain analysis on a large representative volume element, the development of the damage zone between spinel grains is simulated with the concrete damaged plasticity model of ABAQUS. Application of the concept of configurational forces allows the physically correct determination of the driving force for cracks in the elastic quasi-plastic matrix material. The results demonstrate that inherent matrix cracks are unable to grow during the cooling, but they strongly influence the initiation and development of the damage zone. The pronounced damage initiation, in combination with the low crack driving force, is the main reason for the good thermal shock resistance of magnesia spinel refractories.

Keywords: Magnesia spinel refractory; Configurational force concept; *J*-integral; concrete damaged plasticity; damage evolution.

8.1 Introduction

According to the theories of Kingery (1955) and Hasselman (1969), two routes appear possible in order to improve thermal shock behaviour. On the one hand crack initiation could be prevented at all; on the other hand the crack propagation could be hindered. For many refractories, the latter route is preferred because stresses are too high to prevent crack initiation completely. Several figures of merit have been proposed for the characterization of the thermal shock resistance. The Hasselman parameter R'''' based on the ratio of elastic strain to work of fracture reads as follows (Hasselman 1969),

$$R'''' = \frac{\gamma E}{\sigma_\mathrm{t}^2}. \tag{8.1}$$

Here, γ is the specific fracture surface energy, σ_t the tensile strength and E the Young's modulus. High specific fracture energy $G_\mathrm{f} = 2\gamma$ and low tensile strength σ_t is increasing R''''. The so-called characteristic length (Hillerborg 1983),

$$l_\mathrm{ch} = \frac{G_\mathrm{f} E}{\sigma_\mathrm{t}^2}, \tag{8.2}$$

is closely related to R'''' in the form,

$$l_\mathrm{ch} = 2R''''. \tag{8.3}$$

High values for l_ch indicate low brittleness because it means a relatively high specific work of fracture compared to the stored elastic strain energy density. This results in more stable crack propagation and higher resistance against crack propagation, i.e. higher thermal shock resistance.

The main idea behind the addition of spinel ($MgAl_2O_3$) to pure magnesia (MgO) refractories is to improve the thermal shock behaviour by increasing the crack growth resistance. Due to the thermal mismatch between spinel inclusions and matrix, damage processes are initiated during the cooling at the end of the production process. The damage initiation is intended because it increases the thermal shock resistance due to the reduction of the tensile strength and the increase in the specific fracture energy caused by the formation of a fracture process zone (Harmuth and Tschegg 1997). This has been observed also in the works of Aksel et al. (2002; 2004a,b) and Aksel and Warren (2003a,b), who investigated the influence of different spinel contents with grain sizes <30 µm in very fine grained magnesia. In a similar study, Grasset-Bourdel et al. (2013) investigated the influence of coarse spinel grains with sizes between 1 and 3 mm in MgO with a grain size varying between 1 µm to 3 mm. The addition of 5 wt% spinel to pure magnesia nearly doubled the characteristic length and the specific fracture energy. At the same time, strength and Young's modulus were significantly reduced. Higher spinel contents of up to 25 wt% yielded similar results for the specific fracture energy, while the strength was further reduced (Grasset-Bourdel et al. 2013).

This paper investigates the damage evolution in the magnesia matrix between the spinel inclusions during the cooling process by a sophisticated numerical analysis. A Finite Element modelling is performed in two steps. First a stress-strain analysis is conducted on a large representative volume element of the refractory. Subsequently, damage evolution is modelled in detail on a fine-meshed sub-model taken from a critical region of the material. Since the presence of defects in the magnesia matrix cannot be excluded, cases without and with inherent cracks between the spinel grains are considered. Additionally, a new, modern tool of mechanics is applied for this investigation, the concept of configurational forces. A short outline of this concept is given in the following section.

8.2 The concept of configurational forces

Configurational forces are thermodynamic forces acting on defects in materials, such as cracks or interfaces (Eshelby 1970; Maugin 1999; Gurtin 2000). A configurational force on a considered defect arises, if the total energy of the system varies for different positions of the defect in the material. The defect experiences a driving force to move in such a direction so that the total energy decreases. An outline of the concept of configurational forces is found in the books of Maugin (1999), Gurtin (2000), or Kienzler and Herrmann (2000). The great versatility is shown, for example, in the references (Maugin 1995; Simha 2000; Gross et al. 2002; Menzel et al. 2005).

A configurational force appears on such positions in the material where the divergence of the configurational stress tensor **C** is different from zero. The configurational force vector **f** is given by the relation,

$$\mathbf{f} = -\nabla . \mathbf{C} = -\nabla \left(\phi \mathbf{I} - \mathbf{F}^{\mathrm{T}} \mathbf{S} \right), \tag{8.4}$$

where the symbol ∇ denotes the Lagrangian gradient operator, ϕ the strain energy density, **I** the identity tensor, $\mathbf{F}^{\mathrm{T}}$ the transposed of the deformation gradient **F**, and **S** the first Piola-Kirchhoff stress. The configurational stress $\mathbf{C}$ is a second rank tensor, which was introduced by Eshelby as "energy momentum tensor" (Eshelby 1970).

The crack driving force is a well-known example for a configurational force. The configurational force vector at the crack tip is given by (Simha et al. 2003; Kolednik et al. 2010)

$$\mathbf{f}_{\text{tip}} = -\lim_{r\to 0}\int_{\Gamma_r}\left(\phi\mathbf{I}-\mathbf{F}^{\text{T}}\mathbf{S}\right)\mathbf{m}\,dl. \tag{8.5}$$

The vector $\mathbf{m}$ is the unit normal vector to a circle Γ_r with radius r centred at the crack tip. It is possible to calculate the scalar near tip J-integral from the configurational force at the crack tip,

$$J_{\text{tip}} = \mathbf{e}.\left(-\mathbf{f}_{\text{tip}}\right), \tag{8.6}$$

with $\mathbf{e}$ as the unit vector in the direction of crack growth. It is seen from Eq. (8.6) that the vector $\mathbf{f}_{\text{tip}}$ points into the negative crack growth direction.

It is also well-known that a material inhomogeneity influences both the crack driving force and the crack path, see e.g. Simha et al. (2005). The reason is that configurational forces are induced at the boundary of the inhomogeneity, and they influence magnitude and direction of the configurational force vector at the crack tip, $\mathbf{f}_{\text{tip}}$. The configurational force along a sharp interface $\mathbf{f}_{\Sigma}$ is determined by the jumps of the strain energy density and the deformation gradient at the interface (Chen et al. 2007),

$$\mathbf{f}_{\Sigma} = -\left([[\phi]]\mathbf{I} - [[\mathbf{F}^{\text{T}}]].\langle\mathbf{S}\rangle\right)\mathbf{n}. \tag{8.7}$$

In Eq. (8.7), the symbol ⟦ ⟧ denotes the jump and ⟨ ⟩ the mean value of a quantity, calculated from the limiting values on either side of the interface; $\mathbf{n}$ is the unit normal vector to the interface Σ. An example for the application of this concept in order to predict the fracture toughness of a ceramic multilayer has been presented in (Chen et al. 2007).

The main advantage of the use of the configurational force concept is that it allows the evaluation of the crack driving force independent of the constitutive relations of the material (Simha et al. 2008; Kolednik et al. 2014b). If the material is (non-linear) elastic, the total strain energy density ϕ is recoverable and the "non-linear elastic configurational force" $\mathbf{f}^{\text{nlel}}$ is given by Eq. (8.4). Since no bulk configurational forces exist in a homogeneous elastic material, $\mathbf{f}^{\text{nlel}} = \mathbf{0}$, the non-linear elastic J-integral is path-independent, $J^{\text{nlel}}_{\text{tip}} = J^{\text{nlel}}_{\Gamma} = J^{\text{nlel}}_{\text{far}}$, where J_{Γ} is the J-integral for an arbitrary contour Γ and J_{far} is the far-field J-integral, and the scalar crack driving force is given by Eq. (8.6). The non-linear elastic J-integral deduced from configurational forces J^{nlel} is identical to the conventional J-integral derived by Rice (1968b,c).

Path independence also applies for elastic–plastic materials that are described by deformation theory of plasticity (Rice 1968b,c; Simha et al. 2008; Kolednik et al. 2014b). In elastic-plastic materials with incremental theory of plasticity, the total strain energy density consists of an elastic and a plastic part, $\phi = \phi_{\text{e}} + \phi_{\text{p}}$. Only the elastic part of the strain energy density ϕ_{e} is recoverable. Therefore, the "elastic-plastic configurational force" $\mathbf{f}^{\text{ep}}$ (Simha et al. 2008; Kolednik et al. 2014b) is given by Eq. (8.4), but with ϕ replaced by ϕ_{e}. The scalar, near-tip incremental plasticity *J*-integral is given by the relation $J_{\mathrm{tip}}^{\mathrm{ep}} = \mathbf{e}\cdot\left(-\mathbf{f}_{\mathrm{tip}}^{\mathrm{ep}}\right)$, analogously to Eq. (8.6). Since bulk configurational forces emerge in the plastically deformed regions of the material, the incremental plasticity *J*-integral is path dependent. The incremental plasticity *J*-integral for an arbitrary contour Γ is evaluated from the equation (Simha et al. 2008; Kolednik et al. 2014b),

$$J_{\Gamma}^{\mathrm{ep}} = -\mathbf{e}\cdot\left(\mathbf{f}_{\mathrm{tip}}^{\mathrm{ep}} + \int_{\mathcal{D}} \mathbf{f}^{\mathrm{ep}}\, dA\right), \tag{8.8}$$

where $\mathcal{D}$ denotes the region between the crack tip and the contour Γ.

It has been found in (Kolednik et al. 2014b) that the crack driving force of a stationary crack under monotonic loading is characterised by the parameter $J_{\mathrm{PZ}}^{\mathrm{ep}}$, i.e. the incremental plasticity *J*-integral for an integration path Γ_{PZ}, which encloses completely the crack tip plastic zone. Note that the conventional *J*-integral approach, or the non-linear elastic *J*-integral J^{nlel}, do, in general, *not* provide a measure of the crack driving force for elastic-plastic materials (Rice 1968b,c; Kolednik et al. 2014b). However, the incremental plasticity *J*-integral $J_{\mathrm{PZ}}^{\mathrm{ep}}$ and the conventional *J*-integral are equal under certain conditions (Kolednik et al. 2014b).

A big advantage of the configurational forces approach is that it enables the evaluation of the crack driving force even for growing cracks in elastic-plastic materials under monotonic or cyclic loads (Kolednik et al. 2014b; Ochensberger and Kolednik 2016). From the foregoing it becomes clear that the elastic-plastic configurational forces and the incremental plasticity *J*-integral are applicable also to ceramic materials with quasi-plastic behaviour, as described by the Concrete Damaged Plasticity (CPD) model, see below.

8.3 The finite element model

In order to simulate the damage evolution in a magnesia spinel refractory during the cooling process, a model similar to that in (Fasching et al. 2015) was used (Fig. 8.1). The model consists of circular spinel inclusions in a homogeneous magnesia matrix. The 2-dimensional representative volume element (RVE) was very large in order to correctly reflect the size distribution of the spinel grains. The size distribution of the inclusions was chosen according the Dinger-Funk's function (Dinger and Funk 1997) where the percentage of grains smaller than a given grain size d is calculated from the relation,

$$P(d)=\frac{d^m-d_{\min}^m}{d_{\max}^m-d_{\min}^m}100\%. \tag{8.9}$$

The parameter m denotes the distribution modulus; $d_{\min}$ is the minimum and $d_{\max}$ the maximum grain size. A value of m close to 1 gives a uniform grain size distribution; for $m < 1$ the smaller grain sizes are dominant.

In our model we chose a spinel content of 10 vol.%, and the parameters were $d_{\min} = 1$ mm, $d_{\max} = 5$ mm and $m = 0.37$, which corresponds to the optimum value for a dense packing of the spherical grains (Chen et al. 2007). The model was meshed automatically by ABAQUS using the advanced front algorithm and quad-dominated linear generalized plane strain coupled thermal-displacement elements (CPEG4T). The average mesh size l_{el} was approximately 0.33 mm. Periodic boundary conditions were assumed. For the details of the model generation and the random arrangement of the spinel grains, see Fasching et al. (2015).

Only tensile cracking in the matrix was permitted; cracking of particles and interfaces was not considered. It was decided to neglect the thermomechanical strains above 1200 °C, since the material relaxes to a nearly stress-free state at these temperatures within short time (Jin et al. 2014). The material was only thermally loaded. Because of the low cooling rate, a homogeneous temperature distribution was assumed in the RVE. The calculation started with a homogeneous cooling from 1200 °C, assuming a stress free initial state. Hereby small strain theory and generalized plane strain conditions were assumed.

After the finite element stress and strain analysis with ABAQUS, the non-linear elastic and elastic-plastic bulk configurational forces, $\mathbf{f}^{\mathrm{nlel}}$ and $\mathbf{f}^{\mathrm{ep}}$, and the configurational forces at the interfaces $\mathbf{f}_{\Sigma}$ were evaluated from the equations given in the preceding section by a self-written post-processing routine based on (Müller et al. 2002; Denzer et al. 2003; Müller et al. 2004). Subsequently, the non-linear elastic and the incremental plasticity *J*-integrals $J_{\Gamma}^{\mathrm{nlel}}$ and J_{Γ}^{ep} were calculated from the configurational forces, Eq. (8.8). Note that the evaluation of the conventional *J*-integral in ABAQUS is not possible for generalized plane strain conditions.

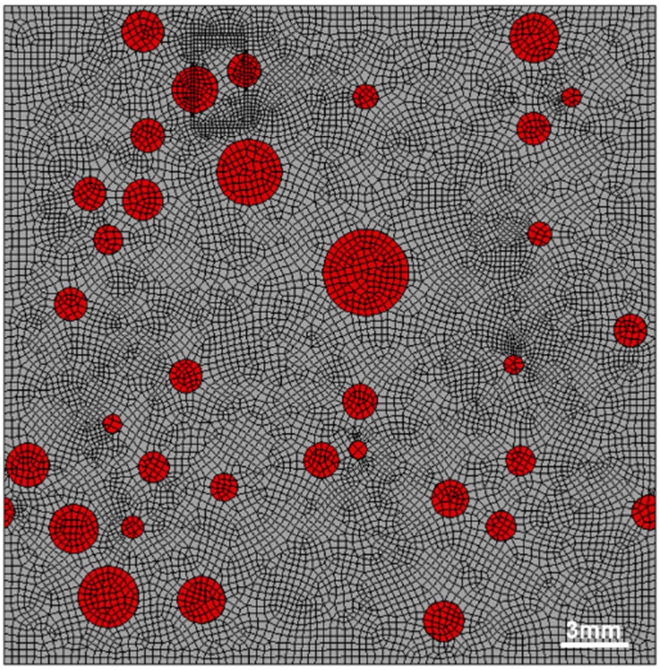

Fig. 8.1 Global model of the magnesia spinel refractory with circular spinel inclusions (red) in a homogeneous magnesia matrix.

Table 8.1 Material properties used for the simulations.

Material	E [GPa]	σ_t [MPa]	α [10^{-6} K^{-1}]	G_f [J/m^2]	ν
Matrix	110	7	13.6	100	0.2
MA-spinel	210	-	7.5	-	0.2

8.4 Material behaviour

The spinel grains were assumed as linear elastic. The behaviour of the magnesia matrix was modelled with the Concrete Damaged Plasticity (CDP) model. The CDP model in ABAQUS provides the capability of modelling the inelastic behaviour during the cooling of the refractory. It is based on the works of Lubliner et al. (1989) and Lee and Fenves (1998) and Hillerborg's fictitious crack model (Hillerborg et al. 1976). A possible normal stress versus crack-opening displacement, σ vs. x, response of the material is shown in Fig. 8.2a. The stress increases linearly until the tensile strength σ_t is reached. A damage process is initiated at this point, which leads to a decrease of the stress with further opening. For an opening equal or larger than x_{ult}, the stress is reduced to zero. The σ vs. x relationship is mainly characterised by σ_t and the specific fracture energy G_f, which is given by

$$G_\mathrm{f} = \int_0^{x_\mathrm{ult}} \sigma(x)\, dx \, . \tag{8.10}$$

For the CDP model, ABAQUS applies a characteristic element length l_el to transform the σ vs. x curve of Fig. 8.2a into a characteristic stress strain curve of the material, Fig. 8.2b. Hereby the strain is given by the relation

$$\varepsilon = \frac{x}{l_\mathrm{el}} \, . \tag{8.11}$$

The material behaves linear elastic until the tensile strength σ_t is reached, followed by a strain softening behaviour at larger strains. For a strain equal or larger than ε_ult, the stress is reduced to zero.

The used material properties are listed in Table 8.1; it was assumed that the values are independent from temperature. Data for the Young's modulus E, the coefficient of thermal expansion α, the specific fracture energy G_f were taken from former works of the authors and from literature (Burnett and Authority 1969; Shackelford and Alexander 2010; Grasset-Bourdel 2011; Grasset-Bourdel et al. 2012). Aksel et al. determined for low-porosity fine-grained magnesia-spinel materials similar values of the specific fracture energy, $\gamma_\mathrm{WOF} = G_\mathrm{f}/2 \approx 40\text{–}60\ \mathrm{J/m^2}$ (Aksel et al. 2004a). A Poisson's ratio $\nu = 0.2$ was assumed for both matrix and MA-spinel.

8.5 *Results and discussion*

Due to the lower thermal expansion coefficient of the spinel grains, tensile circumferential stresses develop in the matrix material during the cooling of the RVE, whereas the grains are under compression. Fig. 8.3a shows the distribution of the maximum principal stresses after a cooling of ΔT = 15K. The maximum circumferential stresses in the matrix appear near the interfaces to the grains. They can reach the magnitude of the matrix tensile strength σ_t. At some locations, where a narrow matrix corridor lies between two spinel grains, high normal stresses appear even distant from the interfaces. Such regions are most critical for damage initiation. One of the most critical regions in the RVE is marked in Fig. 8.3a and selected for further investigation, see below. Another critical matrix region is seen near the lower left corner of the RVE. More details about the effect of cooling on the mechanical behaviour of the RVE can be found in (Fasching et al. 2015).

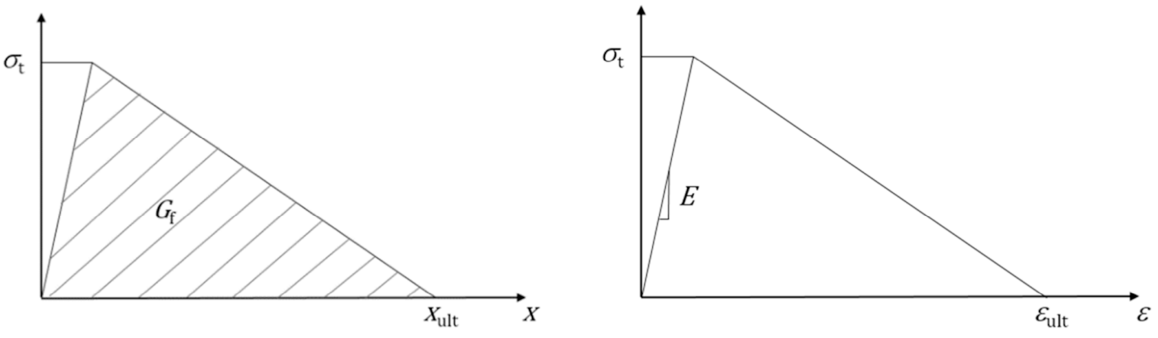

(a) **(b)**

Fig. 8.2 **(a)** Stress vs. opening displacement behaviour under tensile loading for linear softening behaviour. **(b)** corresponding stress vs. strain relationship, see Eq. (8.11).

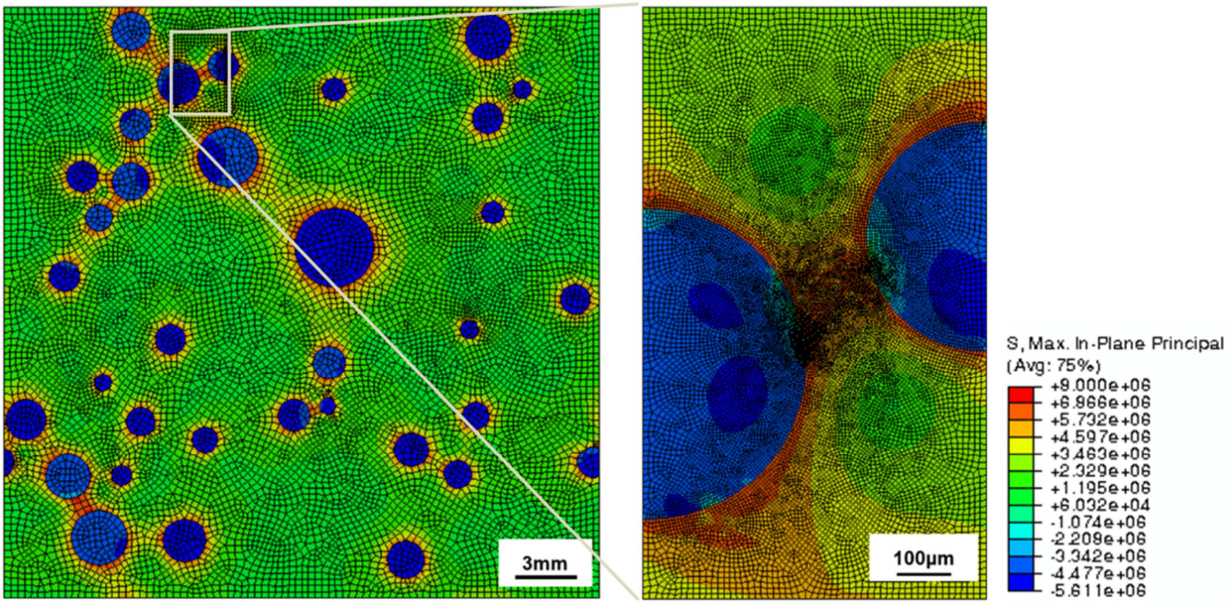

(a) **(b)**

Fig. 8.3 Maximum principal stresses after a cooling of 15K, **(a)** full model, **(b)** sub-model.

A sub-model is used to investigate in more detail the damage initiation process in the critical matrix region marked in Fig. 8.3a. The average mesh size in the sub-model is approximately 12 μm, Fig. 8.3b. The boundary conditions of the sub-model are found by interpolation of the solution from the global model .

A basic question that should be answered in the current investigation is, how the presence of an initial defect influences the process of damage initiation and crack growth in the magnesia matrix, in comparison to the undamaged matrix. Therefore, three versions of the sub-model were generated: (i) defect-free matrix, (ii) matrix with short inherent crack, crack length a_0 = 34 µm; (iii) matrix with long inherent crack, a_0 = 240 µm. The inherent cracks are located in the direction of a line connecting the centres of the two spinel grains, and they start at the surface of the left grain in Fig. 8.3b, compare also Fig. 8.5.

Fig. 8.4 shows the distribution of configurational forces $\mathbf{f}^{\mathrm{nlel}}$ in the sub-model with long inherent crack for linear elastic material behaviour, i.e. without CDP for the matrix material. The results are plotted for a cooling of ΔT = 200K. Configurational forces $\mathbf{f}_{\Sigma}$ appear at the interfaces between grains and matrix material, and at the two tips and the flanks of the inherent crack. Additional configurational forces are seen at the outer boundary of the sub-model. They indicate the effect of the boundary conditions for the sub-model. The $\mathbf{f}_{\Sigma}$-vectors on the grain-matrix interfaces are perpendicular to the grain surface and point into the matrix, the more compliant material, see Eq. (8.7).

The configurational force vectors emanating from the crack tips are pointing against the crack growth direction, Eq. (8.6). It is seen in Fig. 8.4b that the $\mathbf{f}_{\mathrm{tip}}$-vector originating from the right tip and pointing to the lower left is larger than the one originating from the left tip. The reason is that the left spinel grain provides a crack-tip shielding effect, since its Young's modulus is higher than that of the magnesia matrix, see e.g. Kolednik et al. (2005), Kolednik (2012). The $\mathbf{f}_{\mathrm{tip}}$-vectors are accompanied by a number of small **f**-vectors, which appear only due to numerical effects. They decrease to zero at a mesh-dependent distance of less than 50 µm. They should be taken into account for the evaluation of the scalar crack driving force J_{tip} with Eq. (8.6), since the bulk configurational force $\mathbf{f} = \mathbf{0}$ in a homogeneous elastic material (e.g. Simha et al. 2003, Kolednik et al. 2014b). For plane strain or plane stress conditions, the J_{tip}-value of the right tip could be also evaluated from the conventional J-integral concept by employing the virtual crack extension (VCE) method in ABAQUS . Hereby, allowing for numerical inaccuracies, an integration path of 2 or 3 elements around the crack tip should be chosen. Since the evaluation of the conventional J-integral in ABAQUS is not possible for *generalized* plane strain conditions, the computation of the J-integral from the configurational force concept is important in our case even for elastic material behaviour.

In elastic–plastic materials, or in cases where the CDP-model is used in order to reflect the damage evolution process in the matrix, the crack driving force must be evaluated from the incremental plasticity J-integral computed for an integration path Γ_{PZ} around the (quasi-) plastic zone, $J_{\mathrm{PZ}}^{\mathrm{ep}}$ (see Eq. (8.8)). The appearance of quasi-plastic strains in the matrix material simulated with the CDP-model is causing bulk configurational forces $\mathbf{f}^{\mathrm{ep}}$ in the damage zone. The damage zone is expanding with progressing cooling.

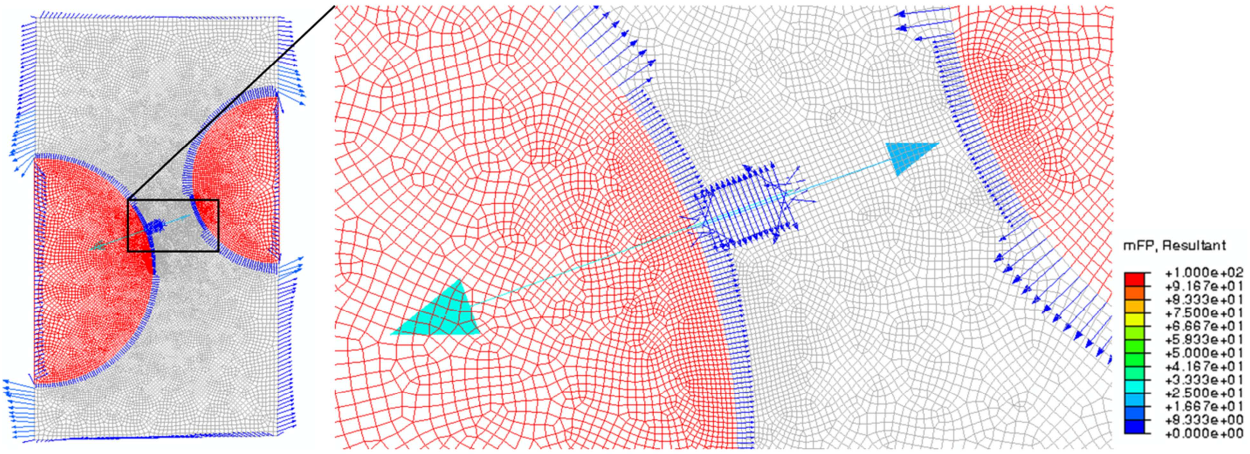

(a) **(b)**

Fig. 8.4 Configurational forces $\mathbf{f}^{\,\mathrm{nlel}}$ in the sub-model for a cooling of 200K and linear elastic material behaviour.

Fig. 8.5 shows the maximum principle quasi-plastic strains after ΔT = 10.5K for the three sub-models without inherent crack, with inherent short crack and with inherent long crack. Fig. 8.6 illustrates the same after a cooling of ΔT = 15K. For both values of ΔT, the J-integral values for the right crack tips, $J_{\mathrm{PZ}}^{\mathrm{ep}}$ and $J_{\mathrm{PZ}}^{\mathrm{nlel}}$, are listed in Table 8.2. It is seen from Fig. 8.5 that after a cooling of 10.5K, a damage process zone is initiated only in the cases with inherent cracks, but not in the defect-free material. It is seen that the $J_{\mathrm{PZ}}^{\mathrm{nlel}}$-values are only little larger than $J_{\mathrm{PZ}}^{\mathrm{ep}}$; the reason is that the damage zone ends far from the interface of the right spinel grain.

After a cooling of ΔT = 15K, all sub-models exhibit a pronounced damage zone, crossing the whole matrix corridor between the two spinel grains, Fig. 8.6. Since the damage zone reaches the interface of the right grain, the $J_{\mathrm{PZ}}^{\mathrm{nlel}}$-values are significantly larger than the $J_{\mathrm{PZ}}^{\mathrm{ep}}$-values and not reliable anymore. The comparison of the three sub-models shows that the pattern of the damage zone is strongly influenced even by the presence of a very small crack.

It is seen from Table 8.2 that the values of the crack driving force, $J_{\mathrm{PZ}}^{\mathrm{ep}}$, are very small, much smaller than the magnitude of the specific fracture energy, $G_{\mathrm{f}} = 100\,\mathrm{J/m^2}$, which would be required for crack propagation. Therefore, the inherent cracks are not able to propagate during the initial stages of cooling. Instead, the matrix material is increasingly damaged by the growth of the damage zone, i.e. when the maximum normal stress exceeds the tensile strength σ_{t} of the matrix.

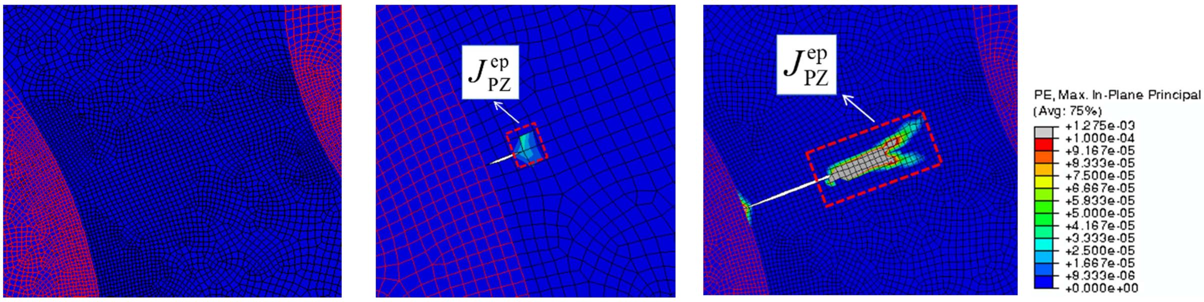

(a) **(b)** **(c)**

Fig. 8.5 Maximum principle quasi-plastic strains after a cooling of 10.5K for the models **(a)** without inherent crack, **(b)** with inherent short crack, **(c)** with inherent long crack.

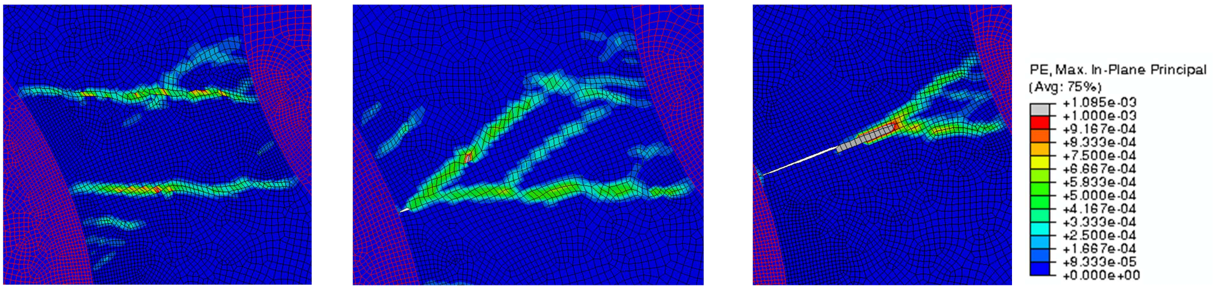

(a) **(b)** **(c)**

Fig. 8.6 Maximum principle quasi-plastic strains after a cooling of 15K for the models **(a)** without inherent crack, **(b)** with inherent short crack, **(c)** with inherent long crack.

Table 8.2 Results of the *J*-integral evaluation for the right tips of the inherent matrix cracks.

	J [J/m^2]			
	short crack, $a_0 = 0.034$ mm		long crack, $a_0 = 0.240$ mm	
ΔT [K]	$J_{\mathrm{PZ}}^{\mathrm{ep}}$	$J_{\mathrm{PZ}}^{\mathrm{nlel}}$	$J_{\mathrm{PZ}}^{\mathrm{ep}}$	$J_{\mathrm{PZ}}^{\mathrm{nlel}}$
10.5	0.0132	0.0134	0.100	0.113
15.0	-	-	0.131	0.293

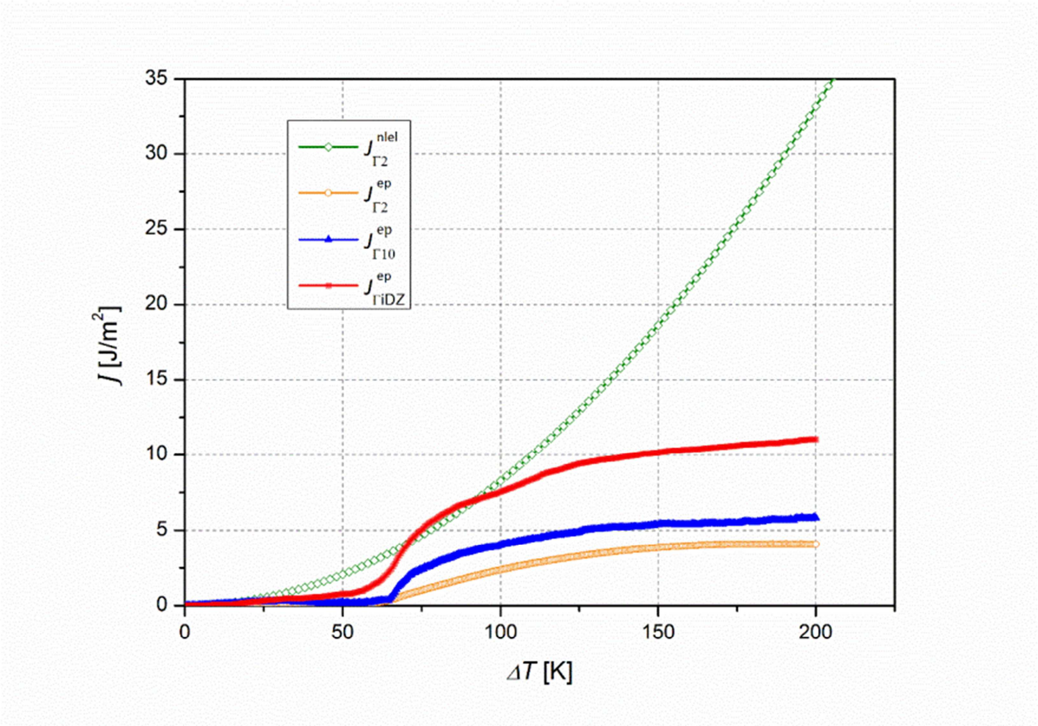

Fig. 8.7 Variation of J-integrals with increasing cooling ΔT for the sub-model with inherent long crack.

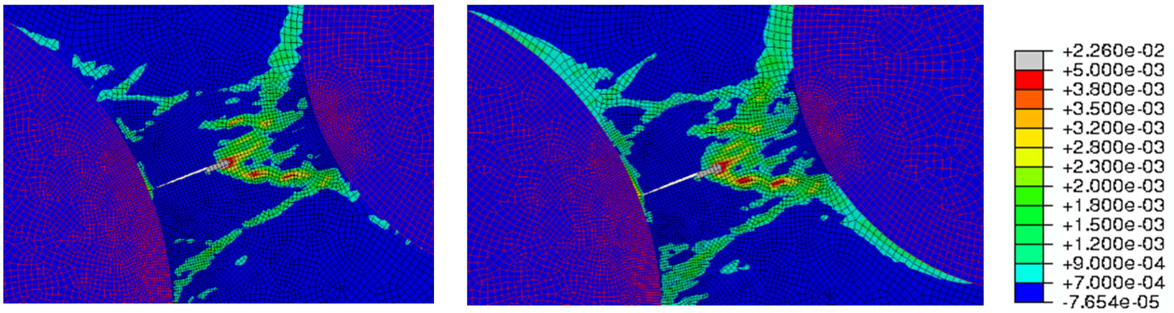

(a) **(b)**

Fig. 8.8 Maximum principal plastic strains after a cooling of **(a)** 57K and **(b)** 60K for the model with the inherent long crack.

Fig. 8.7 shows the development of various J-integral values for a long inherent crack with increasing cooling temperature. The upper curve shows the variation of $J^{\mathrm{nlel}}_{\Gamma 2}$ for the linear elastic matrix material, i.e. without CDP. The index Γ2 means that the J-integral is computed along a contour drawn 2 elements around the crack tip. A cooling of $\Delta T \approx$ 350K would be required to reach the condition for crack growth, $J^{\mathrm{nlel}}_{\Gamma 2} = G_{\mathrm{f}}$. The lower curves in Fig. 8.7 show the variations of $J^{\mathrm{ep}}_{\Gamma 2}$, $J^{\mathrm{ep}}_{\Gamma 10}$ and $J^{\mathrm{ep}}_{\Gamma \mathrm{iDZ}}$ for the matrix material with CDP. The contour Γ_{iDZ} represents the "inner damage zone"; it extends 11 elements directly in front of the inherent crack and one row of elements above and below these 11 elements. It can be deduced from the J^{ep}-curves in Fig. 8.7 that the increasing damage in the matrix material leads to a decrease of the crack driving force so that the condition for crack growth for an inherent crack is never reached. Instead, the quasi-plastic damage zone between the grains consumes energy, without showing pronounced damage localization. This behaviour might be the main reason for the good thermal shock resistance of magnesia spinel materials. Also the experimental results in (Harmuth and Tschegg 1997) and (Aksel and Warren 2003b) support this finding, see Introduction. It is clear that the behaviour might change, if the matrix material had a higher tensile strength σ_{t} and a lower specific fracture energy G_{f}.

Here it is important to understand the physical meaning of the incremental-plasticity *J*-integral calculated around a specific contour Γ: The term J_{Γ}^{ep} gives the driving force for the combined translational movement of the crack tip plus that part of the quasi-plastic zone, which is enclosed by the contour Γ. The term $J_{\mathrm{tip}}^{\mathrm{ep}}$ would give the driving force for the crack tip alone, which is, in general, not relevant, since the crack tip cannot move without the simultaneous movement of the process- or quasi-plastic zone around the crack tip (Kolednik et al. 2014b). The term $J_{\mathrm{PZ}}^{\mathrm{ep}}$ includes the *whole* quasi-plastic damage zone. This term is reasonable for characterizing the crack driving force for the cases depicted in Fig. 8.5b and 8.c. However, this is not so for the cases depicted in Fig. 8.6. The reason is that in Fig. 8.6 the damage zone already reaches the interface of the right grain. Therefore, a further translational movement of the whole damage zone to the right is not possible anymore. However, a movement of the crack tip within the "inner" or "near-tip" process zone, as reflected by $J_{\Gamma\mathrm{iDZ}}^{\mathrm{ep}}$, is still possible. More detailed analyses would be required to determine the magnitude of this zone.

It can be also deduced from Fig. 8.7 that the right grain provides a shielding effect, which leads to a flattening of all the J^{ep}-curves for high ΔT-values. It would be interesting to conduct a comparative study where the right grain would be replaced by matrix material. However, this would require also a change of the boundary conditions of the sub-model.

Of interest is also the increase of the $J_{\Gamma 2}^{\mathrm{ep}}$- and $J_{\Gamma\mathrm{iDZ}}^{\mathrm{ep}}$-values between a cooling of 55 and 60K, whereas these J^{ep}-values are very low at lower ΔT. From Fig. 8.8 it is noticed that the damage zones form "bridges" between the two grains in this temperature range, and a significant increase in quasi-plastic strain near the interfaces is observed.

The distribution of the maximum principal quasi-plastic strain after a cooling of ΔT = 200K is shown for the defect-free matrix in Fig. 8.9a and for the inherent long crack in Fig. 8.9b. Fig. 8.10 presents the distribution of configurational forces $\mathbf{f}^{\mathrm{ep}}$ for the two cases. The figures indicate some fundamental differences. Because of the stress concentration at the tip of the inherent crack, damage initiation is happening earlier, i.e. at a lower temperature difference. A region with very high quasi-plastic strain extends in crack growth direction and ends only a few elements from the interface to the right grain. Main part of the damage zone in Figs. 8.9b and 8.10b lies in a triangle formed by the crack tip and the two tangents to the right grain. In contrast, damage appears far more distributed in the defect-free matrix, Fig. 8.9a. In Figs. 8.9b and 8.10b very high quasi-plastic strains and large $\mathbf{f}^{ep}$-vectors are seen in the matrix regions close to the interfaces to both grains, whereas this is less significant in Figs. 8.9a and 8.10a. This means that matrix fracture near the interfaces of the grains seems to be strongly promoted by the presence of the crack.

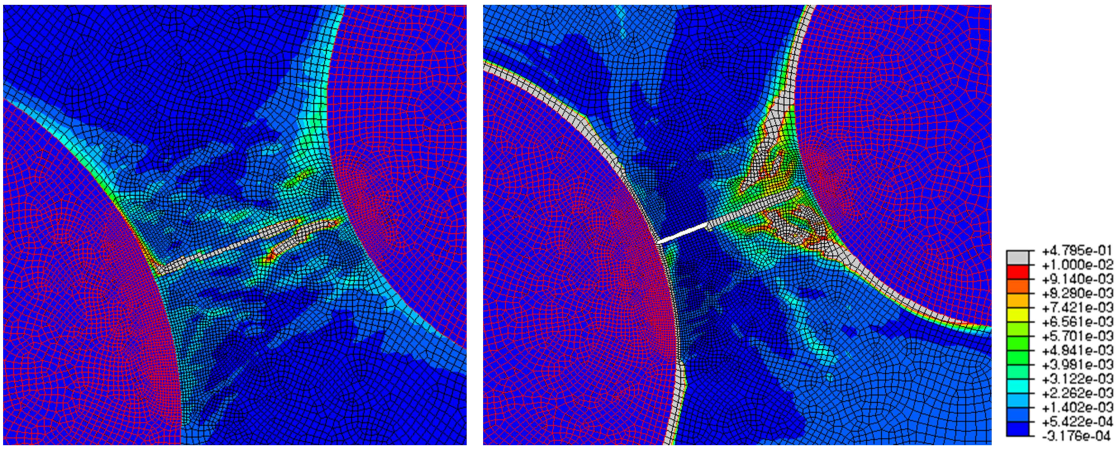

(a) **(b)**

Fig. 8.9 Maximum principle in-plane quasi-plastic strains for a cooling of ΔT = 200K in the sub-models **(a)** without inherent crack, **(b)** with inherent long crack.

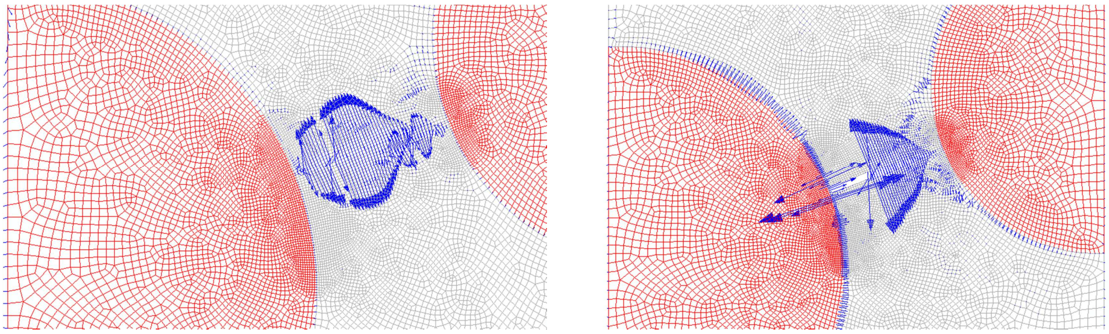

(a) **(b)**

Fig 8.10 Distribution of configurational forces $\mathbf{f}^{ep}$ for a cooling of ΔT = 200K in the sub-models **(a)** without inherent crack, **(b)** with inherent long crack.

8.6 Conclusions

The concrete damaged plasticity model and the concept of configurational forces were applied for the investigation of crack initiation of magnesia spinel products during the cooling from the burning temperature. Evaluations show the strong influence of an inherent matrix crack on the damage evolution: Damage initiation happens at lower ΔT for the cases with an inherent crack, the magnitude and shape of the quasi-plastic damage zone are different. Moreover, a strong influence on the possible formation of near-interface damage was demonstrated. For further investigations, it is recommended to consider also heterogeneities in the matrix.

With the concept of configurational forces, the J-integral can be evaluated either according to the theory of deformation plasticity (resulting in the conventional J-integral J^{nlel}) or according to the incremental theory of plasticity (leading to the incremental plasticity J-integral J^{ep}). Only the latter term enables the physically correct evaluation of the crack driving force, not only for the concrete damage plasticity model but for arbitrary non-elastic constitutive relations. The results demonstrated that, for the material data given, inherent matrix cracks are unable to grow during the cooling, since the crack driving force is smaller than the specific work for fracture. Instead a quasi-plastic damage zone appears between the grains, which consumes energy and decreases the driving forces of possible inherent cracks, without showing pronounced damage localization. This behaviour is the main reason for the good thermal shock resistance of magnesia spinel materials.

Acknowledgements

Financial support by the Austrian Federal Government (in particular from Bundesministerium für Verkehr, Innovation und Technologie and Bundesministerium für Wissenschaft, Forschung und Wirtschaft) represented by Österreichische Forschungs-förderungsgesellschaft mbH and the Styrian and the Tyrolean Provincial Government, represented by Steirische Wirtschaftsförderungsgesellschaft mbH and Standortagentur Tirol, within the framework of the COMET Funding Programme is gratefully acknowledged (K2 MPPE strategic project A4.20 work packages WP1 and WP5).

9 Discussion

In Part II of this thesis, it has been demonstrated that the yield stress inhomogeneity effect (σ_Y-inhomogeneity effect) can be applied as an innovative method for designing new, tough and flaw-tolerant materials. We demonstrated that multilayer structures with thin, soft interlayers (σ_Y-inhomogeneity effect) can have highly improved fracture strength and fracture toughness compared to the homogeneous bulk material. As explained in Part II of the thesis, the mechanism is the strong reduction of the crack driving force in the soft interlayer, which can lead to crack arrest.

Other types of material inhomogeneity, especially (E+σ_Y)-inhomogeneity, shall be investigated in future studies. In Section 9.3, it is shown that the (E+σ_Y)-inhomogeneity effect is the most effective as crack arrester in a given matrix material and, therefore, it opens additional possibilities for the design of tough and strong composites by inserting interlayers in brittle matrix materials.

It is mentioned that in Sections 9.1–9.3, the FE analyses are implemented for a standard CT specimen that has an interlayer with two sharp interfaces, interface 1 (IF1) and interface 2 (IF2), as presented in Section 5.4. In Section 9.4, a SENT specimen is used for the FE analyses.

9.1 Effectiveness of a compliant interlayer as crack arrester in linear elastic materials

Fig. 9.1a shows the variation of the crack driving force, J_tip, for a linear elastic single interlayer specimen with $t = 0.3$ mm and four different values of J_far between 10 and 90 kJ/m^2, where Young's modulus of the matrix and iterlayer are $E^\mathrm{M} = 210$ GPa and $E^\mathrm{IL} = 70$ GPa, respectively, $E^\mathrm{IL}/E^\mathrm{M} = 0.33$. As it can be seen, when the crack approaches the soft interlayer, the crack driving force first increases at IF1 and then decreases at IF2. The minimum value of J_tip occurs when the crack tip is located inside the interlayer at the second interface to the matrix material. Therefore, the critical position for possible crack arrest, CA position, is located inside the interlayer at IF2. Consequently, a compliant interlayer, the E-inhomogeneity effect, works as an efficient crack arrester in linear elastic materials. Fig. 9.1b shows the normalized crack driving force $J_\mathrm{tip}/J_\mathrm{far}$ plotted against the normalized distance L_1/t for different values of J_far. As one can see, the normalized crack driving force $J_\mathrm{tip}/J_\mathrm{far}$ is independent of the J_far-value.

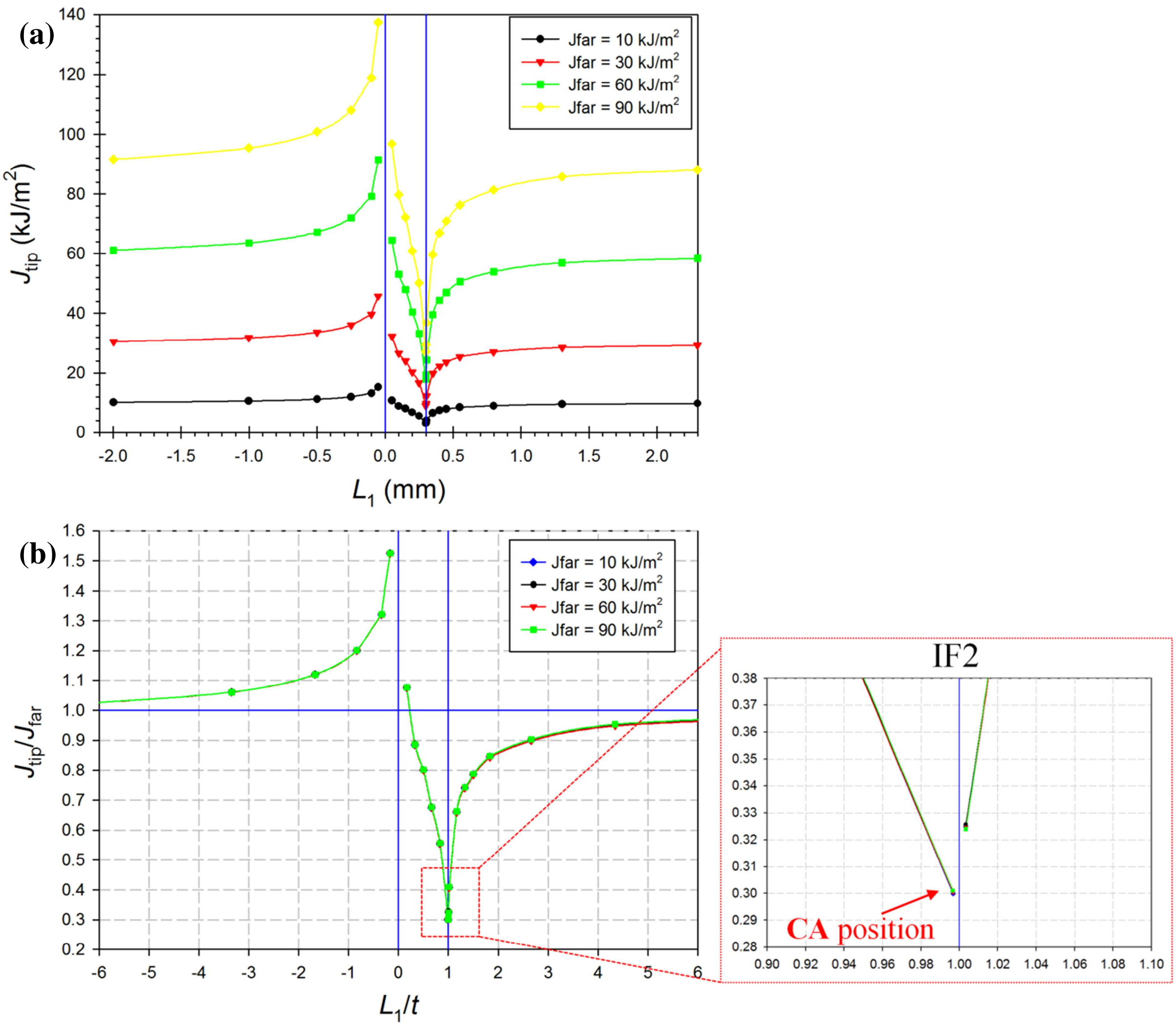

Fig. 9.1 **(a)** Crack driving force J_{tip} plotted against the distance between crack tip and IF1 L_1 for a linear elastic single interlayer specimen with four different values of J_{far}. **(b)** Normalized crack driving force $J_{\mathrm{tip}}/J_{\mathrm{far}}$ plotted against the normalized distance L_1/t. $J_{\mathrm{tip}}/J_{\mathrm{far}}$ is independent of the J_{far}-value. The crack driving force J_{tip} reaches a minimum value when the crack tip is located inside the interlayer at the second interface to the matrix material.

As explained in Sections 6.3 and 7.3, the effectiveness of the interlayer to work as crack arrester is quantified by the dimensionless parameter $\Psi_{\mathrm{IL}}^{\mathrm{CA}} = J_{\mathrm{tip}}^{\mathrm{CA}} / J_{\mathrm{far}}^{\mathrm{CA}}$, called the "*J*-reduction coefficient of the single interlayer". From Fig. 9.1b it can be concluded that the dimensionless parameter $\Psi_{\mathrm{IL}}^{\mathrm{CA}}$ is not load-dependent for linear elastic materials with *E*-inhomogeneity; this is in contrast to the σ_{y}-inhomogeneity case (see Sections 6.3 and 7.3). The *J*-reduction coefficient $\Psi_{\mathrm{IL}}^{\mathrm{CA}}$ for linear elastic materials with a compliant interlayer is a function of $E^{\mathrm{IL}}/E^{\mathrm{M}}$, the ratio of Young's modulus of the interlayer and matrix materials, and the ratio of the interlayer thickness to the width of specimen, t/W, $\Psi_{\mathrm{IL}}^{\mathrm{CA}} = f\left(E^{\mathrm{IL}}/E^{\mathrm{M}}, t/W\right)$.

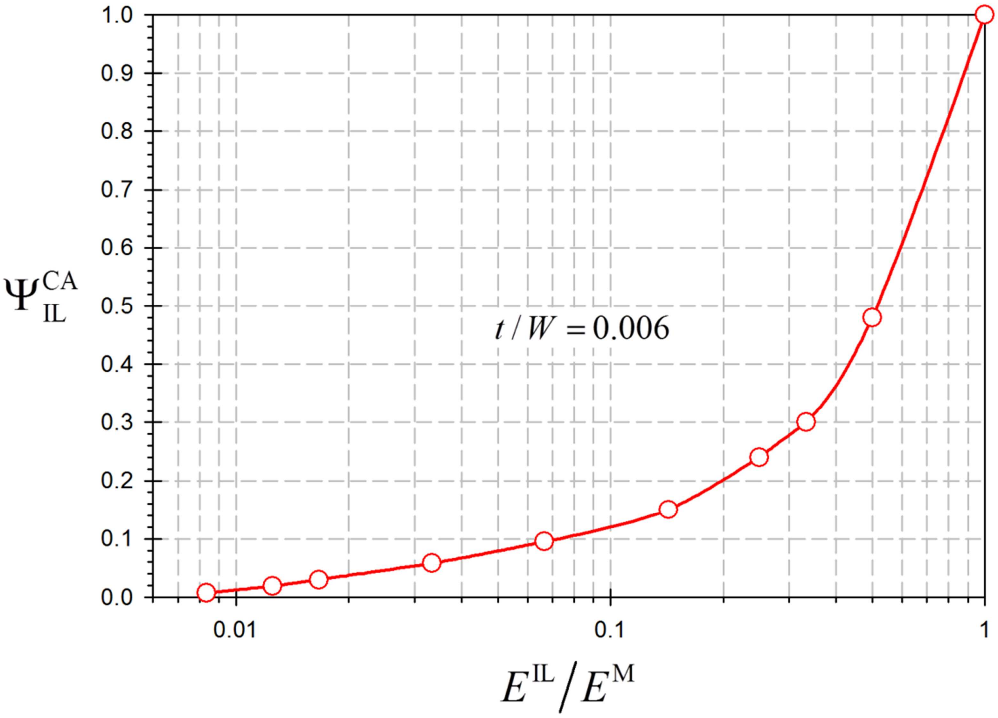

Fig. 9.2 Effectiveness of a compliant interlayer as crack arrester. *J*-reduction coefficient $\Psi_{\mathrm{IL}}^{\mathrm{CA}}$ plotted against $E^{\mathrm{IL}}/E^{\mathrm{M}}$ for a thin interlayer $t/W = 0.006$. The log scale in the x axis is chosen so as to reveal more clearly the influence of $E^{\mathrm{IL}}/E^{\mathrm{M}}$ on $\Psi_{\mathrm{IL}}^{\mathrm{CA}}$.

The effectiveness of a compliant interlayer as a function of $E^{\mathrm{IL}}/E^{\mathrm{M}}$ can be seen in Fig. 9.2; $\Psi_{\mathrm{IL}}^{\mathrm{CA}}$ is plotted against $E^{\mathrm{IL}}/E^{\mathrm{M}}$ for a thin interlayer where $t/W = 0.006$. $\Psi_{\mathrm{IL}}^{\mathrm{CA}}$ decreases with decreasing $E^{\mathrm{IL}}/E^{\mathrm{M}}$ and it tends to zero for a very small value of $E^{\mathrm{IL}}/E^{\mathrm{M}}$; the effectiveness of the compliant interlayer as crack arrester increases with decreasing $E^{\mathrm{IL}}/E^{\mathrm{M}}$.

For future work, we plan to quantify the effectiveness of the compliant interlayer for a wide range of iterlayer thicknesses (to plot Fig. 9.2 for different values of *t*/*W*).

9.2 Effectiveness of a compliant interlayer as crack arrester in elastic–plastic materials

A numerical case study is performed to work out the effectiveness of a compliant interlayer in elastic–plastic materials. The interlayer material has an equal yield stress as the matrix material, $\sigma_{\mathrm{y}}^{\mathrm{IL}} = \sigma_{\mathrm{y}}^{\mathrm{M}} = 500$ MPa, but a lower Young's modulus, $E^{\mathrm{M}} = 210$ GPa and $E^{\mathrm{IL}} = 70$ GPa. Fig. 9.3a shows the variation of the normalized crack driving force, $J_{\mathrm{tip}}/J_{\mathrm{far}}$, for four different values of the crack tip plastic zone, $r_{\mathrm{y}}^{\mathrm{IL}} = 0.17, 0.49, 0.98$ and 1.47 mm, where $t = 0.3$ mm; $r_{\mathrm{y}}^{\mathrm{IL}}$ is calculated from Irwin's model. $J_{\mathrm{tip}}/J_{\mathrm{far}}$ of the linear elastic single interlayer specimen is also plotted for comparison. In contrast to the linear elastic case, see Fig. 9.1b, $J_{\mathrm{tip}}/J_{\mathrm{far}}$ of the elastic–plastic single interlayer specimen is load-dependent.

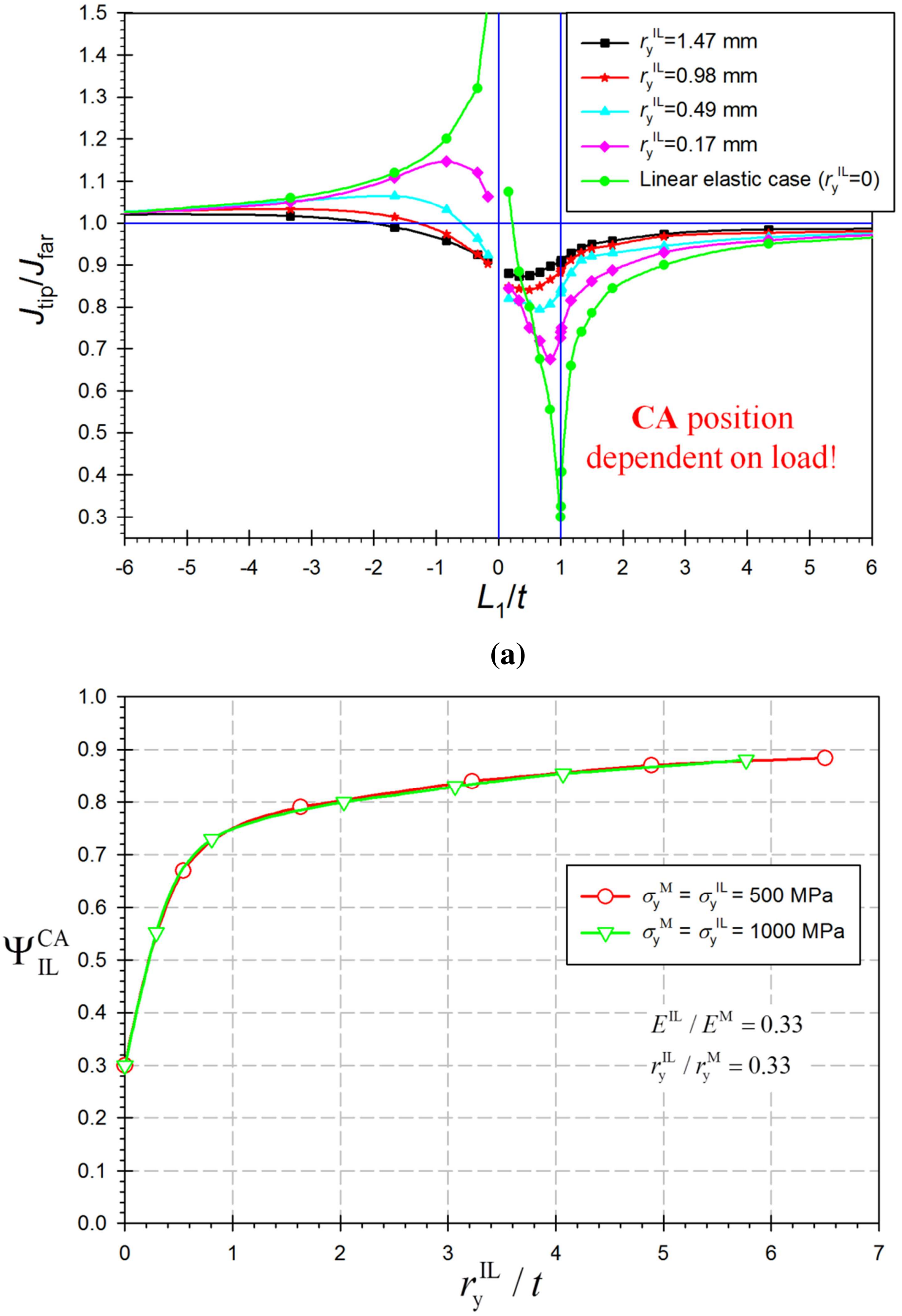

(a)

(b)

Fig. 9.3 **(a)** Normalized crack driving force $J_{\text{tip}}\big/J_{\text{far}}$ plotted against the normalized distance L_1/t for an elastic–plastic single interlayer specimen with four different r_{y}^{IL}-values, where $E^{\text{IL}}\big/E^{\text{M}} = 0.33$. $J_{\text{tip}}\big/J_{\text{far}}$ of a linear elastic single interlayer specimen is plotted for comparison. **(b)** $\Psi_{\text{IL}}^{\text{CA}}$ as a function of the loading parameter $r_{\text{y}}^{\text{IL}}\big/t$ for the elastic–plastic single interlayer specimen. $\Psi_{\text{IL}}^{\text{CA}}$ increases with increasing the load.

Fig. 9.3a shows that the CA position, where the minimum value of J_{tip} or $J_{\text{tip}}\big/J_{\text{far}}$ is reached, depends on the r_{y}^{IL}-value; the CA position is located at IF2 when $r_{\text{y}}^{\text{IL}} = 0$ (linear elastic case), but it approaches IF1 for high $r_{\mathrm{y}}^{\mathrm{IL}}$-values. The value of $J_{\mathrm{tip}}/J_{\mathrm{far}}$ at the CA position, $\Psi_{\mathrm{IL}}^{\mathrm{CA}}$, increases with increasing $r_{\mathrm{y}}^{\mathrm{IL}}$ or load. Fig. 9.3b shows the variation of $\Psi_{\mathrm{IL}}^{\mathrm{CA}}$ as a function of the dimensionless loading parameter $r_{\mathrm{y}}^{\mathrm{IL}}/t$. We can conclude from Fig. 9.3b that a compliant interlayer in elastic–plastic materials can work as effective crack arrester only when the crack tip plastic zone is very small. Fig. 9.3b demonstrates that $\Psi_{\mathrm{IL}}^{\mathrm{CA}}$ depends on $r_{\mathrm{y}}^{\mathrm{IL}}$, but not on the yield stress value; the $\Psi_{\mathrm{IL}}^{\mathrm{CA}}$-curve for $\sigma_{\mathrm{y}} = 500$ MPa coincides with the curve for $\sigma_{\mathrm{y}} = 1000$ MPa.

For future work, the curve $\Psi_{\mathrm{IL}}^{\mathrm{CA}}$ vs. $r_{\mathrm{y}}^{\mathrm{IL}}/t$, which gives the effectiveness of a compliant interlayer in elastic–plastic materials, shall be determined for different values of $E^{\mathrm{IL}}/E^{\mathrm{M}}$; Fig. 9.3b shows only the curve for $E^{\mathrm{IL}}/E^{\mathrm{M}} = 0.33$.

9.3 Effectiveness of an interlayer with (E+σ_y)-inhomogeneity as crack arrester

Fig. 9.4 compares the variations of the crack driving force for single interlayer specimens with E-, σ_y- and (E+σ_y)-inhomogeneity. As explained in Section 9.1, for linear elastic materials with E-inhomogeneity, the minimum value of J_{tip} occurs when the crack tip is located inside the interlayer at the second interface to the matrix material. For σ_y- and (E+σ_y)-inhomogeneity, the minimum of J_{tip} appears after the crack tip has crossed the interlayer and just re-enters the matrix material. The minimum J_{tip}-value is smaller for the (E+σ_y)-inhomogeneity than for the other cases. Therefore, the (E+σ_y)-inhomogeneity is most effective as crack arrester in a given matrix material.

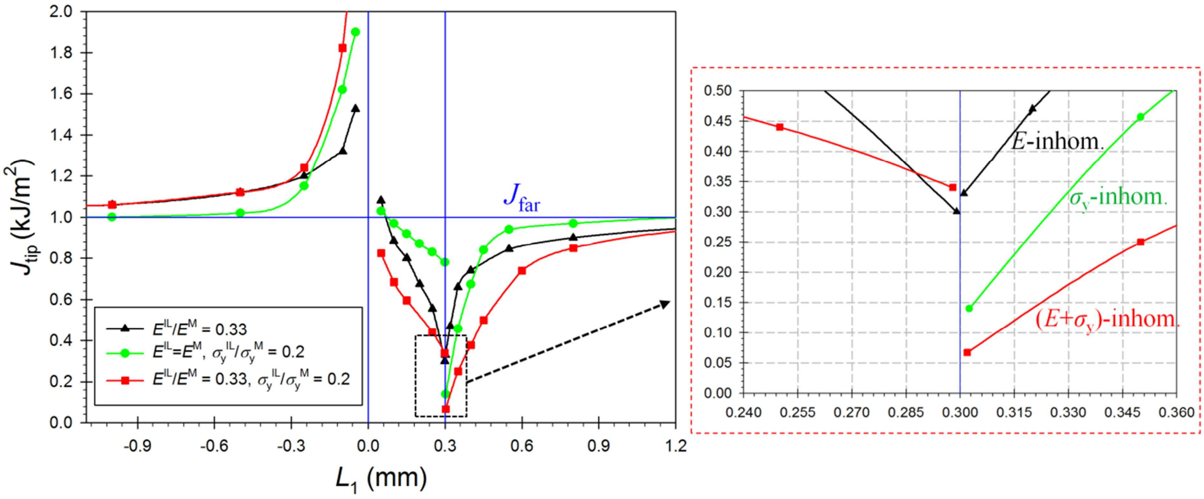

Fig. 9.4 Variation of the crack driving force of single interlayer specimens with σ_y-inhomogeneity, E-inhomogeneity and (E+σ_y)-inhomogeneity.

As it has been shown in Sections 6 and 7, it is possible to improve the strength and the fracture toughness of inherently brittle matrix materials by the application of the yield stress inhomogeneity effect, if the architectural parameters of the multilayer structure fulfill the derived design rules. From Fig. 9.4, we can conclude that especially interesting for materials design is the application of the (E+σ_y)-inhomogeneity effect, which exerts a higher shielding effect on the crack tip, compared to the yield stress inhomogeneity effect. Therefore, criteria for the design of composites with highly improved strength and fracture toughness, based on the (E+σ_y)-inhomogeneity effect, shall be derived in future work.

9.4 Utilization of the yield stress inhomogeneity effect for preventing the surface crack growth

The yield stress inhomogeneity effect can also provide crack arrest for short surface-cracks, Fig. 9.5. This is especially intresting for the design of structures with a higher fatigue life. Fatigue cracks usually start at a free surface of the structure. Therefore, by introduction of a thin, soft interlayer near to the surface, Fig. 9.5, fatigue cracks are arrested at the CA position, at the second interface of the interlayer, and the fatigue life becomes higher than that of the homogeneous matrix material.

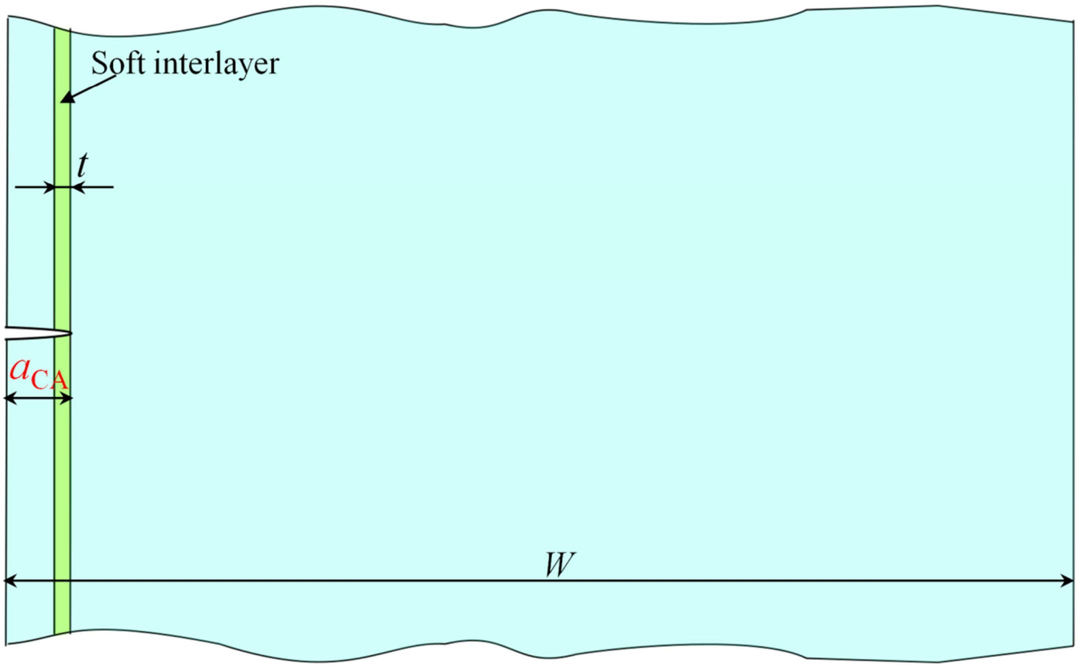

Fig. 9.5 Introduction of a thin interlayer with low yield stress near to the surface of specimen. A fatigue crack, which starts usually from the surface, propagates to the interlayer and arrests at the CA position.

A problem is, however, that the design rules derived in Sections 6 and 7 can not be used for this case. In order to work out rules for the design of multilayered materials with highly improved fatigue life, it is necessary to quantify the effectiveness of a soft interlayer as crack arrester in specimens with short surface-cracks. Fig. 9.6 shows the *J*-reduction coefficient $\Psi_{\mathrm{IL}}^{\mathrm{CA}}$ plotted against the loading parameter $r_{\mathrm{y}}^{\mathrm{IL}}/t$ for different lengths of the arrested crack, a_{CA}, see Fig. 9.5. These numerical results are obtained from FE computations performed for a SENT specimen with a single soft interlayer, where $W = 20$ mm , height $H = 80$ mm, $t = 0.3$ mm, $E = 210$ GPa, $\sigma_{\mathrm{y}}^{\mathrm{IL}} = 200$ MPa and $\sigma_{\mathrm{y}}^{\mathrm{M}} = 1000$ MPa; the crack length a_{CA} is varried. As it can be seen in Fig. 9.6, the effectiveness of the soft interlayer as crack arrester decreases with decreasing the length of the arrested crack; $\Psi_{\mathrm{IL}}^{\mathrm{CA}}$ increases with decreasing a_{CA}/W.

For future work, additional computations are required in order to quantify the effectiveness of soft interlayers, in multilayer specimens with short surface-cracks, as a function of the architectural parameters of the composite and the crack length a_{CA}. The knowledge can be used for the design of multilayer composites with a higher fatigue life.

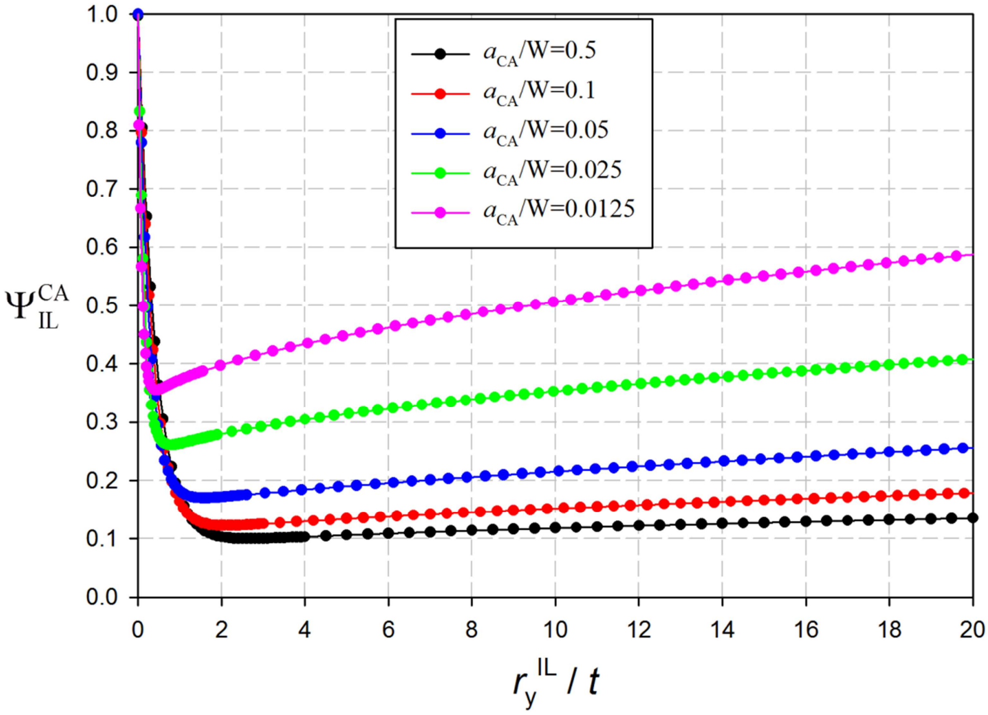

Fig. 9.6 *J*-reduction coefficient $\Psi_{\mathrm{IL}}^{\mathrm{CA}}$ plotted against the dimensionless loading parameter $r_{\mathrm{y}}^{\mathrm{IL}}/t$ for different lengths of the arrested crack. The effectiveness of the soft interlayer as crack arrester decreases with decreasing the length of the arrested crack.

10 Summary

The material inhomogeneity effect opens new possibilities for the development of new damage-tolerant and fracture-resistant materials and components, inspired by the multilayered architecture of certain biological materials. This idea can be transferred to elastic–plastic technical materials by the application of the yield stress inhomogeneity effect.

The aim of the current thesis has been the derivation of validated concepts for optimized design of future tough, strong and damage-tolerant materials and components, based on the yield stress inhomogeneity effect. This thesis concentrates mostly on theoretical and numerical aspects, with the application of the configurational forces concept, in order to reach this aim.

The methodological approach, applied for this challenge, consists in:

- performing a comprehensive numerical case study to work out the effect of soft interlayers on the variation of the crack driving force,
- quantifying the effectiveness of soft interlayers to work as crack arrester in multilayer composites,
- deriving design rules for optimum multilayer configurations for various types of composite materials and loading scenarios,
- comparing the findings to experimental results of fracture tests conducted on compounds made of high-strength steel as matrix and low-strength steel as interlayer material.

The main conclusions of the thesis are:

- it is observed that, immediately after the crack has crossed the soft interlayer and just re-enters the matrix material, the crack driving force strongly decreases and this position is the critical position for possible crack arrest; this effect appears without previous delamination of the interlayer;
- from the numerical results, conditions for maximum effectiveness of a soft interlayer as crack arrester are derived; for a given matrix material and load the magnitudes of thickness and yield stress of the soft interlayer are determined so that the crack driving force exhibits a minimum;
- by inserting a soft interlayer with the derived conditions, the maximum effectiveness of the soft interlayer as crack arrester can be achieved;

- the effectiveness of soft interlayers as crack arresters in multilayer composites with inherent small cracks is quantified as a function of multilayer architectural parameters;
- the fracture stress of multilayer composites depends on three length parameters: interlayer thickness t, interlayer spacing (or wavelength) λ, and the radius of the crack-tip plastic zone in the interlayer $r_{\mathrm{y}}^{\mathrm{IL}}$ (which depends on the yield strength of the interlayer material, the crack length and the applied load);
- based on numerical simulations with the configurational forces concept, it is demonstrated how the architectural parameters of the multilayer must be chosen in order to greatly improve the fracture stress of the matrix material;
- an iterative procedure is proposed to find the optimum configuration;
- it is found that the optimum wavelength, i.e. the interlayer spacing, is inversely proportional to the square of the applied stress;
- the effectiveness of soft interlayers to improve the fracture toughness of multilayer composites is quantified as a function of the architectural parameters of multilayer composites;
- a simple fracture mechanical consideration allows deriving a model for estimating the fracture toughness of a multilayer as a function of its geometry and the fracture toughness of the homogeneous matrix material;
- a multilayer composite, with spatial variation in the yield stress, may show a much higher fracture toughness than a comparable homogeneous material, if the architectural parameters of the multilayer are appropriately chosen;
- an iterative procedure is presented for predicting the fracture toughness of the multilayer;
- experimental results of fracture tests conducted on steel composites, consisting of a tool steel as matrix and a low-carbon steel as interlayer material, confirm our findings;
- fracture tests and numerical simulations show that the intrinsic fracture initiation toughness of the matrix material in the multilayer composite equals that of the homogeneous matrix material.

11 References

Aizenberg J (2010) New Nanofabrication Strategies: Inspired by Biomineralization. MRS Bull 35:323–330.

Aizenberg J, Weaver JC, Thanawala MS, Sundar VC, Morse DE, Fratzl P (2005) Skeleton of Euplectella sp.: Structural Hierarchy from the Nanoscale to the Macroscale. Science 309:275–278.

Aksel C, Rand B, Riley FL, Warren PD (2002) Mechanical properties of magnesia-spinel composites. J Eur Ceram Soc 22:745–754.

Aksel C, Rand B, Riley FL, Warren PD (2004a) Thermal shock behaviour of magnesia–spinel composites. J Eur Ceram Soc 24:2839–2845.

Aksel C, Warren PD (2003a) Thermal shock parameters [R, R''' and R''''] of magnesia–spinel composites. J Eur Ceram Soc 23:301–308.

Aksel C, Warren PD (2003b) Work of fracture and fracture surface energy of magnesia-spinel composites. Compos Sci Technol 63:1433–1440.

Aksel C, Warren PD, Riley FL (2004b) Magnesia–spinel microcomposites. J Eur Ceram Soc 24:3119–3128.

Anderson TL (2005) Fracture mechanics: fundamentals and applications. 3rd edn. Taylor & Francis, Boca Raton.

Ashby MF, Bréchet YJM (2003) Designing hybrid materials. Acta Mater 51:5801–5821.

ASTM E1820-05 (2005) Standard test method for measurement of fracture toughness. In: In: Annual book of ASTM standards, vol 03.01. ASTM International, West Conshohocken, PA, USA.

ASTM F (1996) 394-78, Standard test method for biaxial flexure strength (modulus of rupture) of ceramic substrates. American Society for Testing and Materials, West Conshohocken, PA (reapproved in 1996), USA.

Atkins AG (1974) Imparting strength and toughness to brittle composites. Nature 252:116–118.

Atkins AG (1975) Intermittent bonding for high toughness/ high strength composites. J Mater Sci 10:819–832.

Atkins AG, Mai YW (1985) Elastic and plastic fracture: metals, polymers, ceramics, composites, biological materials. 1st edn. Ellis Horwood, Chicester, UK.

Bartolomé JF, Gutiérrez-González CF, Pecharromán C, Moya JS (2007) Synergistic toughening mechanism in 3Y–TZP/Nb composites. Acta Mater 55:5924–5933.

Bermejo R, Danzer R (2010) High failure resistance layered ceramics using crack bifurcation and interface delamination as reinforcement mechanisms. Engng Fract Mech 77:2126–2135.

Bermejo R, Torres Y, Baudín C, Sánchez-Herencia AJ, Pascual J, Anglada M, Llanes L. (2007) Threshold strength evaluation on an Al2O3–ZrO2 multilayered system. J Eur Ceram Soc 27:1443–1448.

Bermejo R, Torres Y, Sánchez-Herencia AJ, Baudín C, Anglada M, Llanes L (2006) Residual stresses, strength and toughness of laminates with different layer thickness ratios. Acta Mater 54:4745–4757.

Bonet J, Wood RD (2008) Nonlinear Continuum Mechanics for Finite Element Analysis. 2nd edn. Cambridge Univ Press, Cambridge, UK.

Burnett SJ, Authority UKAE (1969) Properties of Refractory Materials. Atomic Energy Research Establishment. Harwell, England.

Ceylan A, Fuierer PA (2007) Fracture toughness of alumina/lanthanum titanate laminate composites with a weak interface. Mater Lett 61:551–555.

Chadwick P (2012) Continuum Mechanics: Concise Theory and Problems. Dover Publications, Inc, Mineola, New York.

Chen CR, Pascual J, Fischer FD, Kolednik O, Danzer R (2007) Prediction of the fracture toughness of a ceramic multilayer composite - Modeling and experiments. Acta Mater 55:409–421.

Chen JH, Wang GZ, Yan C, Ma H, Zhu L (1997) Advances in the mechanism of cleavage fracture of low alloy steel at low temperature. Part I: Critical event. Int J Fract 83:105–120.

Cook J, Gordon JE (1964) A Mechanism for the Control of Crack Propagation in All-Brittle Systems. Proc Roy Soc Lond Math Phys Sci 282:508–520.

Cook TS, Erdogan F (1972) Stresses in bonded materials with a crack perpendicular to the interface. Int J Engng Sci 10:677–697.

Delfin P, Gunnars J, Stárhle P (1995) Effect of elastic mismatch on the growth of a crack initially terminated at an interface in elastic plastic bimaterials. Fatigue Fract Engng Mater 18:1201–1212.

Denzer R, Barth FJ, Steinmann P (2003) Studies in elastic fracture mechanics based on the material force method. Int J Num Meth Engng 58:1817–1835.

Dinger DR, Funk JE (1997) Particle-packing phenomena and their application in materials processing. MRS Bulletin 22:19–23.

Dunlop JWC, Fratzl P (2010) Biological composites. Annu Rev Mater Res 40:1–24.

Eftis J, Liebowitz H (1975) On fracture toughness evaluation for semi-brittle fracture. Engng Fract Mech 7:101–135.

Embury JD, Petch NJ, Wraith AE, Wright ES (1967) The fracture of mild steel laminates. Trans Metall Soc AIME 239:114–118.

Erdogan F, Biricikoglu V (1973) Two bonded half planes with a crack going through the interface. Int J Engng Sci 11:745–766.

Eshelby JD (1951) The force on an elastic singularity. Philos Trans R Soc A 244:87–112.

Eshelby JD (1970) Energy relations and the energy-momentum tensor in continuum mechanics. In: Kanninen M, Adler W, Rosenfield A, Jaffee R (eds), Inelastic behavior of solids. McGraw-Hill, New York, pp 77–115.

Eshelby JD (1975) The elastic energy-momentum tensor. J Elasticity 5:321–335.

ESIS P2-92 (1992) ESIS procedure for determining the fracture behavior of materials. European Structural Integrity Society, Delft.

Espinosa HD, Rim JE, Barthelat F, Buehler MJ (2009) Merger of structure and material in nacre and bone – Perspectives on de novo biomimetic materials. Prog Mater Sci 54:1059–1100.

Faber KT, Evans AG (1983) Crack deflection processes—I. Theory. Acta Metall 31:565–576.

Fasching C, Gruber D, Harmuth H (2015) Simulation of micro-crack formation in a magnesia spinel refractory during the production process. J Eur Ceram Soc 35:4593–4601.

Fischer FD, Predan J, Fratzl P, Kolednik O (2012a) Semi-analytical approaches to assess the crack driving force in periodically heterogeneous elastic materials. Int J Fract 173:57–70.

Fischer FD, Predan J, Müller R, Kolednik O (2014) On problems with the determination of the fracture resistance for materials with spatial variations of the Young’s modulus. Int J Fract 190:23–38.

Fischer FD, Simha NK, Predan J, Schöngrundner R, Kolednik O (2012b) On configurational forces at boundaries in fracture mechanics. Int J Fract 174:61–74.

Fischer H, Weber M, Marx R (2003) Lifetime prediction of all-ceramic bridges by computational methods. J Dent Res 82:238–242.

Fratzl P, Gupta HS, Fischer FD, Kolednik O (2007) Hindered crack propagation in materials with periodically varying young's modulus - Lessons from biological materials. Adv Mater 19:2657–2661.

Fratzl P, Kolednik O, Fischer FD, Dean MN (2016) The mechanics of tessellations–bioinspired strategies for fracture resistance. Chem Soc Rev 45:252–267.

Freund LB (1990) Dynamic Fracture Mechanics. Cambridge University Press, Cambridge, UK.

Gao H (1991) Fracture analysis of nonhomogeneous materials via a moduli-perturbation approach. Int J Solids Struct 27:1663–1682.

Grasset-Bourdel R (2011) Structure/property relations of magnesia-spinel refractories: experimental determination and simulation. PhD Thesis, Université de Limoges, France.

Grasset-Bourdel R, Alzina A, Huger M, Chotard T, Emler R, Gruber D, Harmuth H (2013) Tensile behaviour of magnesia-spinel refractories: Comparison of tensile and wedge splitting tests. J Eur Ceram Soc 33:913–923.

Grasset-Bourdel R, Alzina A, Huger M, Gruber D, Harmuth H, Chotard T (2012) Influence of thermal damage occurrence at microstructural scale on the thermomechanical behaviour of magnesia–spinel refractories. J Eur Ceram Soc 32:989–999.

Griffith A (1920) The phenomena of rupture and flow in solids. Phil. Trans. Roy. Soc. A 221:163–198.

Gross D, Kolling S, Müller R, Schmidt I (2003) Configurational forces and their application in solid mechanics. Eur J Mech A: Solids 22:669–692.

Gross D, Müller R, Kolling S (2002) Configurational forces–morphology evolution and finite elements. Mech Res Commun 29:529–536.

Gross D, Seelig T (2007) Fracture Mechanics: With an Introduction to Micromechanics. Springer, Berlin.

Gurtin ME (1982) An Introduction to Continuum Mechanics. Academic Press, New York.

Gurtin ME (1995) The nature of configurational forces. Arch Rational Mech Anal 131:67–100.

Gurtin ME (2000) Configurational Forces As Basic Concepts of Continuum Physics. Springer, Berlin.

Gurtin ME, Podio-Guidugli P (1996) Configurational forces and the basic laws for crack propagation. J Mech Phys Solids 44:905–927.

Harmuth H, Tschegg EK (1997) A fracture mechanics approach for the development of refractory materials with reduced brittleness. Fatigue Fract Engng Mater Struct 20:1585–1603.

Hasselman D (1969) Unified theory of thermal shock fracture initiation and crack propagation in brittle ceramics. J Am Ceram Soc 52:600–604.

Hattiangadi A, Siegmund T (2004) A thermomechanical cohesive zone model for bridged delamination cracks. J Mech Phys Solids 52:533–566.

Hellen T, Blackburn W (1975) The calculation of stress intensity factors for combined tensile and shear loading. Int J Fract 11:605–617.

Hencky H (1924) Zur Theorie plastischer Deformationen und der hierdurch im Material hervorgerufenen Nachspannungen. ZAMM Z Angew Math Mech 4:323–334.

Hertzberg RW (1976) Deformation and fracture mechanics of engineering materials. John Wiley & Sons, New York.

Hillerborg A (1983) Analysis of one single crack. In: Wittmann FH, editor. In: Fracture Mechanics of Concrete. Elsevier Science Publishers, Amsterdam, pp 223–249.

Hillerborg A, Modéer M, Petersson P-E (1976) Analysis of crack formation and crack growth in concrete by means of fracture mechanics and finite elements. Cem Concr Res 6:773–781.

Honein T, Herrmann G (1997) Conservation laws in nonhomogeneous plane elastostatics. J Mech Phys Solids 45:789–805.

Hutchinson JW (1968) Singular behaviour at the end of a tensile crack in a hardening material. J Mech Phys Solids 16:13–31.

Irwin G. Onset of Fast Crack Propagation in High Strength Steel and Aluminum Alloys. In: Sagamore Research Conference Proceedings. Duke University, Durham (NC), 1956. pp 289–305.

Irwin GR (1957) Analysis of stresses and strains near the end of a crack traversing a plate. ASME J Appl Mech 24:361–364.

Irwin GR. Plastic zone near a crack and fracture toughness. In: Sagamore Research Conference Proceedings. Syracuse University, New York, 1961. pp. 63–78.

ISO-12135-02 (2002) Metallic materials – unified method of test for the determination of quasistatic fracture toughness. ISO, Geneva.

Jin S, Harmuth H, Gruber D (2014) Compressive creep testing of refractories at elevated loads—Device, material law and evaluation techniques. J Eur Ceram Soc 34:4037–4042.

Joyce MR, Reed PAS, Syngellakis S (2003) Numerical modelling of crack shielding and deflection in a multi-layered material system. Mater Sci Engng A 342:11–22.

Jung Y-G, Choi S-C, Oh C-S, Paik U-G (1997) Residual stress and thermal properties of zirconia/metal (nickel, stainless steel 304) functionally graded materials fabricated by hot pressing. J Mater Sci 32:3841–3850.

Kamat S, Kessler H, Ballarini R, Nassirou M, Heuer AH (2004) Fracture mechanisms of the Strombus gigas conch shell: II-micromechanics analyses of multiple cracking and large-scale crack bridging. Acta Mater 52:2395–2406.

Kendall K (1975) Control of cracks by interfaces in composites. Proc Royal Soc London A 341:409–428.

Kienzler R, Herrmann G (2000) Mechanics in material space. Springer, Berlin.

Kim AS, Suresh S, Shih CF (1997) Plasticity effects on fracture normal to interfaces with homogeneous and graded compositions. Int J Solids Struct 34:3415–3432.

Kingery WD (1955) Factors affecting thermal stress resistance of ceramic materials. J Am Ceram Soc 38:3–15.

Kolednik O (1991) On the physical meaning of the J-Δa-curves. Engng Fract Mech 38:403–412.

Kolednik O (1993) A simple model to explain the geometry dependence of J– Δa-curves. Int J Fract 63:263–274.

Kolednik O (2000) The yield stress gradient effect in inhomogeneous materials. Int J Solids Struct 37:781–808.

Kolednik O (2012) Fracture mechanics. In: Nicolais L, Borzacchiello A (eds) Wiley Encyclopedia of Composites, vol 2. Second Edition edn. John Wiley & Sons, Hoboken, New Jersey, USA, pp 1126–1141.

Kolednik O, Predan J, Fischer FD (2010) Reprint of "Cracks in inhomogeneous materials: Comprehensive assessment using the configurational forces concept". Engng Fract Mech 77:3611–3624.

Kolednik O, Predan J, Fischer FD, Fratzl P (2011) Bioinspired design criteria for damage-resistant materials with periodically varying microstructure. Adv Funct Mater 21:3634–3641.

Kolednik O, Predan J, Fischer FD, Fratzl P (2014a) Improvements of strength and fracture resistance by spatial material property variations. Acta Mater 68:279–294.

Kolednik O, Predan J, Gubeljak N, Fischer DF (2009) Modeling fatigue crack growth in a bimaterial specimen with the configurational forces concept. Mater Sci Engng A 519:172–183.

Kolednik O, Predan J, Shan GX, Simha NK, Fischer FD (2005) On the fracture behavior of inhomogeneous materials—A case study for elastically inhomogeneous bimaterials. Int J Solids Struct 42:605–620.

Kolednik O, Schöngrundner R, Fischer FD (2014b) A new view on J-integrals in elastic–plastic materials. Int J Fract 187:77–107.

Kolednik O, Shan G, Fischer FD (1997) The energy dissipation rate—a new tool to interpret geometry and size effects. ASTM STP 1296:126–151.

Kolednik O, Zechner J, Predan J (2016) Improvement of fatigue life by compliant and soft interlayers. Scripta Mater 113:1–5.

Kosmač T, Oblak C, Jevnikar P, Funduk N, Marion L (1999) The effect of surface grinding and sandblasting on flexural strength and reliability of Y-TZP zirconia ceramic. Dent Mater 15:426–433.

Lee J, Fenves GL (1998) Plastic-Damage Model for Cyclic Loading of Concrete Structures. J Engng Mech 124:892–900.

Lesuer DR, Syn CK, Sherby OD, Wadsworth J, Lewandowski JJ, Hunt Jr WH (1996) Mechanical behaviour of laminated metal composites. Int Mater Rev 41:169–197.

Li H, Chandra N (2003) Analysis of crack growth and crack-tip plasticity in ductile materials using cohesive zone models. Int J Plasticity 19:849–882.

Liu H, Lawn BR, Hsu SM (1996) Hertzian Contact Response of Tailored Silicon Nitride Multilayers. J Am Ceram Soc 79:1009–1014.

Lubliner J (2013) Plasticity Theory. Dover Publications, Inc, Mineola, New York.

Lubliner J, Oliver J, Oller S, Oñate E (1989) A plastic-damage model for concrete. Int J Solids Struct 25:299–326.

Lugovy M, Slyunyayev V, Orlovskaya N, Blugan G, Kuebler J, Lewis M (2005) Apparent fracture toughness of Si3N4-based laminates with residual compressive or tensile stresses in surface layers. Acta Mater 53:289–296.

Lugovy M, Slyunyayev V, Subbotin V, Orlovskaya N, Gogotsi G (2004) Crack arrest in Si3N4-based layered composites with residual stress. Compos Sci Technol 64:1947–1957.

Malluck JF, King WW (1980) Fast fracture simulated by conventional finite elements: a comparison of two energy-release algorithms. Crack Arrest Methodology and Applications. ASTM STP 711:38–53.

Malvern LE (1969) Introduction to the mechanics of a continuous medium. Prentice-Hall, New Jersey.

Marsden JE, Hughes TJR (2012) Mathematical Foundations of Elasticity. Dover Publications, Inc, Mineola, New York.

Marston TU, Atkins AG, Felbeck DK (1974) Interfacial fracture energy and the toughness of composites. J Mater Sci 9:447–455.

Maugin G, Epstein M (1991) The electroelastic energy-momentum tensor. Proc Royal Soc London A 433:299–312.

Maugin G, Trimarco C (1992) Pseudomomentum and material forces in nonlinear elasticity: variational formulations and application to brittle fracture. Acta Mech 94:1–28.

Maugin GA (1995) Material forces: concepts and applications. ASME J Appl Mech Rev 48:213–245.

Maugin GA (2011) Configurational Forces: Thermomechanics, Physics, Mathematics, and Numerics. CRC Press, Boca Raton.

Menzel A, Denzer R, Steinmann P (2005) Material forces in computational single-slip crystal-plasticity. Comput Mater Sci 32:446–454.

Miyazaki N, Nakagaki M (1995) Two-dimensional finite element analysis of stably growing cracks in inhomogeneous materials. Int J Pres Vess Pip 63:249–260.

Müller R, Gross D, Maugin G (2004) Use of material forces in adaptive finite element methods. Comput Mech 33:421–434.

Müller R, Kolling S, Gross D (2002) On configurational forces in the context of the finite element method. Int J Numer Methods Engng 53:1557–1574.

Müller R, Maugin G (2002) On material forces and finite element discretizations. Comput Mech 29:52–60.

Müller R (2005) Configurational Forces in Defect Mechanics and in Computational Methods. Forschungsbericht 13, Technische Universität Darmstadt.

Muju S (2000) Crack propogation in bimaterial multilayered periodically microcracking composite media. Compos Sci Technol 60:2213–2221.

Newman JC (1976) A finite element analysis of fatigue crack closure. ASTM STP 590:281–301.

Ochensberger W (2015) Characterization of fatigue crack growth with the configurational force concept. Fortschritt-Berichte VDI, Reihe 18 Mechanik/Bruchmechanik, Nr 343, VDI-Verlag, Düsseldorf.

Ochensberger W, Kolednik O (2014) A new basis for the application of the J -integral for cyclically loaded cracks in elastic-plastic materials. Int J Fract 189:77–101.

Ochensberger W, Kolednik O (2015) Physically appropriate characterization of fatigue crack propagation rate in elastic–plastic materials using the J -integral concept. Int J Fract 192:25–45.

Ochensberger W, Kolednik O (2016) Overload effect revisited− Investigation by use of configurational forces. Int J Fatigue 83:161–173.

Parks DM (1977) The virtual crack extension method for nonlinear material behavior. Comput Methods Appl Mech Engng 12:353–364.

Pavlina EJ, Van Tyne CJ (2008) Correlation of Yield Strength and Tensile Strength with Hardness for Steels. J Mater Engng Perform 17:888–893.

Pippan R, Flechsig K, Riemelmoser FO (2000) Fatigue crack propagation behavior in the vicinity of an interface between materials with different yield stresses. Mater Sci Engng A 283:225–233.

Prechtel M, Leugering G, Steinmann P, Stingl M (2011) Towards optimization of crack resistance of composite materials by adjustment of fiber shapes. Engng Fract Mech 78:944–960.

Predan J, Gubeljak N, Kolednik O (2007) On the local variation of the crack driving force in a double mismatched weld. Engng Fract Mech 74:1739–1757.

Rakin M, Kolednik O, Medjo B, Simha NK, Fischer FD (2009) A case study on the effect of thermal residual stresses on the crack-driving force in linear-elastic bimaterials. Int J Mech Sci 51:531–540.

Rao MP, Sánchez-Herencia AJ, Beltz GE, McMeeking RM, Lange FF (1999) Laminar ceramics that exhibit a threshold strength. Science 286:102–105.

Rice JR (1968a) The elastic-plastic mechanics of crack extension. Int J Fract 4:41–47.

Rice JR (1968b) Mathematical analysis in the mechanics of fracture. In: Liebowitz H (ed) Fracture: an Advanced Treatise, Vol 2. Academic Press, New York, pp 191–311.

Rice JR (1968c) A path independent integral and the approximate analysis of strain concentration by notches and cracks. ASME J Appl Mech 35:379–386.

Rice JR, Paris P, Merkle J (1973) Some further results of J-integral analysis and estimates. ASTM STP 536:231–245.

Rice JR, Rosengren GF (1968) Plane strain deformation near a crack tip in a power-law hardening material. J Mech Phys Solids 16:1–12.

Riemelmoser F, Pippan R (2000) The J-integral at Dugdale cracks perpendicular to interfaces of materials with dissimilar yield stresses. Int J Fract 103:397–418.

Ritchie R (1988) Mechanisms of fatigue crack propagation in metals, ceramics and composites: role of crack tip shielding. Mater Sci Engng A 103:15–28.

Romano A, Marasco A (2014) Continuum Mechanics using Mathematica®: Fundamentals, Methods, and Applications. Springer, New York.

Romeo A, Ballarini R (1995) A crack very close to a bimaterial interface. J Appl Mech 62:614–619.

Rubin D, Krempl E, Lai WM (2012) Introduction to Continuum Mechanics. 3rd edn. Pergamon Press, Oxford.

Schöngrundner R (2011) Numerische Studien zur Ermittlung der risstreibenden Kraft in elastisch-plastischen Materialien bei unterschiedlichen Belastungsbedingungen. Fortschritt- Berichte VDI, Reihe 18, Nr. 329, VDI-Verlag, Düsseldorf.

Sglavo VM, Bertoldi M (2006) Design and production of ceramic laminates with high mechanical resistance and reliability. Acta Mater 54:4929–4937.

Sglavo VM, Paternoster M, Bertoldi M (2005) Tailored residual stresses in high reliability alumina-mullite ceramic laminates. J Am Ceram Soc 88:2826–2832.

Shackelford JF, Alexander W (2001) CRC materials science and engineering handbook. 3rd edn. CRC Press, Boca Raton.

Shan GX (2005) Post-processing program for calculating the configurational force with ABAQUS. Internal Report Institute of Mechanics, pp 1–10.

Shao Y, Zhao H-P, Feng X-Q, Gao H (2012) Discontinuous crack-bridging model for fracture toughness analysis of nacre. J Mech Phys Solids 60:1400–1419.

Shih CF (1991) Cracks on bimaterial interfaces: elasticity and plasticity aspects. Mater Sci Engng A 143:77–90.

Simha NK (2000) Toughening by Phase Boundary Propagation. In: Carlson DE, Chen Y-C (eds) Advances in Continuum Mechanics and Thermodynamics of Material Behavior: In Recognition of the 60th Birthday of Roger L. Fosdick. Springer, Netherlands, Dordrecht, pp 195–211.

Simha NK, Fischer FD, Kolednik O, Chen CR (2003) Inhomogeneity effects on the crack driving force in elastic and elastic-plastic materials. J Mech Phys Solids 51:209–240.

Simha NK, Fischer FD, Kolednik O, Predan J, Shan GX (2005) Crack tip shielding or anti-shielding due to smooth and discontinuous material inhomogeneities. Int J Fract 135:73–93.

Simha NK, Fischer FD, Shan GX, Chen CR, Kolednik O (2008) J-integral and crack driving force in elastic-plastic materials. J Mech Phys Solids 56:2876–2895.

Sistaninia M, Kolednik O (2014) Effect of a single soft interlayer on the crack driving force. Engng Fract Mech 130:21–41.

Sistaninia M, Kolednik O (2017) Improving strength and toughness of materials by utilizing spatial variations of the yield stress. Acta Mater 122:207–219.

Spittel M, Spittel T (2009) Steel symbol/number: DC04/1.0338 and X210Cr12/1.2080. In: Warlimont H, editor. Springer Materials-The Landolt-Börnstein Database. Springer, Berlin/Heidelberg, pp 162–167 & 396–401.

Srinivas M, Sundararajan G, Malakondaiah G, Rao PR (1994) An analysis of ductile fracture initiation toughness in iron, its binary alloys and nickel. Proc Royal Soc London A 447:237–251.

Steinmann P (2000) Application of material forces to hyperelastostatic fracture mechanics. I. Continuum mechanical setting. Int J Solids Struct 37:7371–7391.

Sugimura Y, Lim PG, Shih CF, Suresh S (1995) Fracture normal to a bimaterial interface: Effects of plasticity on crack-tip shielding and amplification. Acta Metall Mater 43:1157–1169.

Suresh S (1983) Crack deflection: Implications for the growth of long and short fatigue cracks. Metall Trans A 14:2375–2385.

Suresh S (1985) Fatigue crack deflection and fracture surface contact: Micromechanical models. Metall Trans A 16:249–260.

Suresh S, Sugimura Y, Ogawa T (1993) Fatigue cracking in materials with brittle surface coatings. Scripta Metall Mater 29:237–242.

Suresh S, Sugimura Y, Tschegg EK (1992) The growth of a fatigue crack approaching a perpendicularly-oriented, bimaterial interface. Scripta Metall Mater 27:1189–1194.

Tada H, Paris PC, Irwin GR (2000) The Stress Analysis of Cracks Handbook. 3rd edn. ASME Press, New York.

Tariolle S, Thévenot F, Chartier T, Besson JL (2005) Properties of reinforced boron carbide laminar composites. J Eur Ceram Soc 25:3639–3647.

Taylor LG, Ryder DA (1976) The fatigue and fracture toughness of laminated composites based on 7075-T6 aluminium alloy. Composites 7:27–33.

Tomaszewski H, Węglarz H, Wajler A, Boniecki M, Kalinski D (2007) Multilayer ceramic composites with high failure resistance. J Eur Ceram Soc 27:1373–1377.

Truesdell C, Noll W (1965) The Non-Linear Field Theories of Mechanics, in: S. Flügge, ed, Encyclopedia of physics. Vol III/3. Springer, Berlin.

Turner C (1990) A Re-assessment of Ductile Tearing Resistance. II. Energy Dissipation Rate and Associated R-Curves on Normalised Axes.(Retroactive Coverage). ECF 8: Fracture Behaviour and Design of Materials and Structures 2:951–968.

Turner C, Kolednik O (1994) Application of energy dissipation rate arguments to stable crack growth. Fatigue Fract Engng Mater 17:1109–1127.

Walter SL, Flinn BD, Mayer G (2007) Mechanisms of toughening of a natural rigid composite. Mater Sci Engng C 27:570–574.

Wang C, Huang Y, Zan Q, Guo H, Cai S (2000) Biomimetic structure design — a possible approach to change the brittleness of ceramics in nature. Mater Sci Engng C 11:9–12.

Wang TC, Ståhle P (1998) Stress state in front of a crack perpendicular to bimaterial interface. Engng Fract Mech 59:471–485.

Weibull W (1951) A statistical distribution function of wide applicability. J Appl Mech 18:293–297.

Weichert D, Schulz M (1993) J-integral concept for multi-phase materials. Comput Mater Sci 1:241–248.

Wells A (1963) Application of fracture mechanics at and beyond general yielding. British Welding J 10:563–570.

Wells A (1961) Unstable crack propagation in metals: cleavage and fast fracture. In: Symposium on crack propagation, Vol. 1, Cranfield, pp 210–230.

Westergaard HM (1939) Bearing pressures and cracks. J Appl Mech 6:361–364.

Williams ML (1957) On the stress distribution at the base of a stationary crack. J Appl Mech 24:109–114.

Yuan H, Brocks W (1989) Numerical investigation on the significant of *J* for large stable crack growth. Engng Fract Mech 32:459–468.

Zak AR, Williams ML (1963) Crack point singularities at a bi-material interface. J Appl Mech 30:142–143.

Zechner J, Kolednik O (2013a) Fracture resistance of aluminum multilayer composites. Engng Fract Mech 110:489–500.

Zechner J, Kolednik O (2013b) Paper multilayer with a fracture toughness of steel. J Mater Sci 48:5180–5187.